

The Pennsylvania State University

The Graduate School

College of Engineering

**SEISMIC PERFORMANCES OF A LIQUEFIABLE SAND DEPOSIT
USING 1-G SHAKE TABLE TESTING CONSIDERING AGING AND SHAKING
HISTORY EFFECTS AND THE NUMERICAL SIMULATION OF SAND
LIQUEFACTION**

A Dissertation in

Civil and Environmental Engineering

by

Jintai Wang

© 2018 Jintai Wang

Submitted in Partial Fulfillment
of the Requirements
for the Degree of

Doctor of Philosophy

August 2018

The dissertation of Jintai Wang was reviewed and approved* by the following:

Ming Xiao
Associate Professor of Civil and Environmental Engineering
Dissertation Advisor
Chair of Committee

Patrick J. Fox
John A. and Harriette K. Shaw Professor
Department Head of the Department of Civil and Environmental Engineering

Tong Qiu
Associate Professor of Civil and Environmental Engineering

Shimin Liu
Associate Professor of Energy and Mineral Engineering

*Signatures are on file in the Graduate School

ABSTRACT

Earthquake-induced liquefaction is a cause of substantial damage to geotechnical structures. The examples of liquefaction-induced damage include slope failures, foundation failures and flotation of buried structures. Underground structures embedded at shallow depths such as large underground parking garages, pipelines and manholes, can suffer significant uplift in liquefied soil. Understanding the seismic performance of a liquefiable ground during and after shaking is urgently needed. The main objectives of this research are to (1) investigate the seismic performance of a liquefiable sand deposit under a series of shaking events, (2) investigate the strength gain of the liquefied sand deposit using piezo-cone penetration (CPTu) testing, (3) simulate the shaking table testing using advanced constitutive model (PM4Sand) and understand the predictive performance of this model.

A uniform liquefiable sand deposit was air-pluviated and fully saturated in a large laminar shear box ($L \times W \times H$: 2.29 m \times 2.13 m \times 1.83 m). The sand deposit was subjected to a liquefying shaking event (1st shaking) in the laminar box. Accelerometers and piezometers were embedded at different depths to capture the seismic response of liquefied sand. The measured excess pore pressures were used to verify the occurrence of liquefaction. LVDTs were attached to different frames of the laminar shear box to monitor the lateral displacements of the soil. The test recordings from piezometer, accelerometer and LVDT were presented and discussed. Another three major shaking events were designed and performed on the sand deposit after the first shaking. The shake table test

results from different shaking events were compared to investigate the seismic response of the sand deposit under multiple shaking events.

The time-dependent liquefaction resistance of a post-liquefaction sand deposit was studied using CPTu after 1st shaking event. A series of CPTu tests were conducted to measure the cone penetration resistance, friction resistance, and pore water pressure throughout the depth of the post-liquefaction sand deposit. To capture the sand aging effect after liquefaction, CPTu tests were done at different locations over a total elapsed time of 135 days. The results suggest that (1) the cone penetration resistance of the sand deposit decreased significantly immediately after liquefaction when compared with that before liquefaction; (2) the cone penetration resistance of the post-liquefaction sand deposit increased with time. The CPTu results were normalized with respect to effective overburden stress and the relationship between normalized CPTu results of the post-liquefaction sand deposit and time was proposed.

To evaluate the predictive capabilities of the PM4Sand model, a numerical simulation of the shake table test was developed. The model was first calibrated using cyclic direct simple shear tests. The calibrated model was then used to simulate the seismic performance of the uniform soil deposit under sinusoidal seismic motions. Further insight into the strengths and limitations of the PM4Sand model gained from this research was presented.

TABLE OF CONTENTS

LIST OF FIGURES	viii
LIST OF TABLES	xii
ACKNOWLEDGEMENTS	xiii
Chapter 1 Introduction	1
1.1 Problem statement	1
1.2 Research motivation	5
1.3 Research objectives	5
1.4 Organization of the dissertation	6
Chapter 2 Literature Review	7
2.1 Shake table and centrifuge testing on soil liquefaction	7
2.1.1 Shake table testing	7
2.1.2 Centrifuge testing	9
2.1.3 Soil container for seismic testing	12
2.2 Sand aging effect on key engineering properties	14
2.3 Shaking history effect on liquefaction resistance	18
2.4 Numerical modeling of sand liquefaction	20
2.4.1 Advanced soil constitutive models for liquefaction	20
2.4.2 Numerical simulation of soil liquefaction using advanced constitutive model	22
Chapter 3 Seismic Performance of Liquefiable Ground at Shallow Depth in 1-G Shake Table Test	27
3.1 Earthquake simulation facility	27
3.1.1 Large-scale shake table at Penn State	27
3.1.2 Laminar shear box	28
3.1.3 Instrumentation and data acquisition system	31
3.2 Model construction	36
3.2.1 Soil properties	36
3.2.2 Sample preparation	37
3.2.3 Test instrumentations	41
3.3 Input motion for shake table test	44
3.4 Shake table test results (1st shaking)	44
3.4.1 Pore pressure readings	44
3.4.2 Shear strains	47
3.4.3 Lateral displacement	49

3.4.4 Acceleration.....	51
3.4.5 Settlement	54
3.5 Conclusion and summary	55
Chapter 4 Time-Dependent Cone Penetration Resistance of a Post-Liquefaction Sand Deposit at Shallow Depth.....	57
4.1 CPTu test	57
4.1.1 CPTu test design and implementation.....	57
4.1.2 Time schedule of CPTu tests.....	60
4.2 Cone resistance variation before and after liquefaction with time	61
4.2.1 CPT results before shaking.....	61
4.2.2 Pre- and post-liquefaction cone resistance variation	62
4.2.3 Post-liquefaction cone resistance gain with time	64
4.2.4 Cone resistance recovery after liquefaction	68
4.2.5 Relationship between cone penetration resistance and time	69
4.3 Normalized cone penetration resistance variation with time.....	74
4.3.1 CPTu test results normalization.....	74
4.3.2 Variation of normalized cone penetration and cyclic resistance ratio with time.....	76
4.4 Conclusions and Recommendations	79
Chapter 5 The Effect of Shaking History on Liquefaction Resistance of Sand Deposit.....	81
5.1 Multiple shaking events.....	81
5.1.1 Time schedule for multiple shaking events	81
5.1.2 Input motion for 2 nd , 3 rd and 4 th shaking	83
5.2 Shake table test results for multiple shaking events	88
5.2.1 Shake table measurement of the 2 nd shaking.....	88
5.2.2 Shake table measurement of the 3 rd shaking	93
5.2.3 Shake table measurement of the 4 th shaking	97
5.3 Discussion of the shake table test results.....	102
5.3.1 Comparison of shake table recordings in the 1 st shaking and the 4 th shaking	102
5.3.2 Comparison of shake table recordings of the 4 th shaking.....	105
5.4 Conclusion and summary	107
Chapter 6 Numerical Modelling of Sand Liquefaction for Shake Table Test using PM4Sand.....	108
6.1 Introduction of <i>FLAC</i> algorithm and PM4Sand	109
6.1.1 <i>FLAC</i> algorithm	109
6.1.2 PM4Sand constitutive model.....	112
6.2 Numerical modeling of shake table test.....	114

6.2.1 Model construction and boundary conditions	114
6.2.2 Model calibration.....	117
6.3 Comparison of simulation and shake table test results	126
6.3.1 Excess pore pressure generation during shaking.....	126
6.3.2 Pore pressure contour at different time	129
6.3.3 Shear strain	133
6.3.4 Surface settlement	135
6.4 Conclusion and summary	136
Chapter 7 Summary and Conclusions.....	138
7.1 Summary.....	138
7.2 Conclusions.....	139
7.3 Limitations of this research	141
7.4 Recommendations for future work	141
REFERENCES	143
Appendix A Design drawings of shake table.....	152
Appendix B Design drawings of laminar shear box	162
Appendix C Design drawings of pluviation system	176
Appendix D Design drawings of CPT frame.....	179

LIST OF FIGURES

Figure 1-1. Examples of severe liquefaction at shallow depths: (a) 2011 Christchurch earthquake, photo courtesy of Mark Lincoln, nzraw.co.nz. (b) 2011 Tohoku Earthquake (Yamaguchi et al. 2011),.....	2
Figure 1-2. Curve Recommended for Calculation of <i>CRR</i> from CPT Data along with empirical Liquefaction Data from Compiled Case Histories (Reproduced from Robertson and Wride 1998 by Youd et al. (2001)).....	3
Figure 3-1. Shake table at Penn State	28
Figure 3-2. The assembly mechanism of frames and pairs of slider & rail	30
Figure 3-3. The assembly of shake table and LSB	30
Figure 3-4. Piezometer by Geokon (Model 3400S-2-100 kPa)	31
Figure 3-5. Piezometer by PCB PIEZOTRONICS (Model 393A03).....	32
Figure 3-6. LVDT by TE connectivity (Model DC-EC 10000)	33
Figure 3-7 LVDT by OMEGA (Model LD621-100).....	34
Figure 3-8. Data acquisition modules: a) NI-9205; b) NI-9206	35
Figure 3-9. Overview of the data acquisition system	35
Figure 3-10. User interface of developed LabVIEW program	36
Figure 3-11. SEM image of F50 silica sand at 65x magnification (Kramer 2013)	37
Figure 3-12. Uniform deposition of sand as it passes through the pluviator system...	38
Figure 3-13. Relative density calibration curve	38
Figure 3-14. Pluviation process: a) pluviator in laminar shear box b) paths alternatively followed by the pluviator.....	39
Figure 3-15. Sand saturation: a) CO ₂ flushing b) water saturation	40
Figure 3-16. Instrumentation configuration in the shake table testing (section view)	41
Figure 3-17. Installation of piezometer and accelerometer	42

Figure 3-18. Installation of LVDTs for shake table test: (a) LVDTs for LSB (b) LVDT for settlement.....	43
Figure 3-19. Comparison between the recorded table movement and input command for actuator	44
Figure 3-20. Pore pressure readings at different depths	45
Figure 3-21. Pore pressure generation during shaking at different depths	46
Figure 3-22. Cyclic shear strain during shaking at different depths: (a) $D = 0.2$ m (b) $D = 0.45$ m (c) $D = 0.7$ m (d) $D = 0.95$ m (e) $D = 1.2$ m	49
Figure 3-23. Absolute lateral movement time histories of different LSB frames (a) 2 nd frame (b) 4 th frame (c) 6 th frame (d) 8 th frame (e) 10 th frame.....	51
Figure 3-24. Acceleration time histories during shaking at different depths: (a) $D = 0.2$ m (b) $D = 0.45$ m (c) $D = 0.7$ m (d) $D = 0.95$ m (e) $D = 1.2$ m (f) Shake table.....	54
Figure 3-25. Surface settlement time histories from top LVDT during shaking	55
Figure 4-1. CPTu test: (a) CPTu design illustration; (b) CPTu in operation; (3) CPTu plan view	59
Figure 4-2. CPTu results for CPT-1 (before liquefaction).....	62
Figure 4-4. Cone resistance of CPT-3 to CPT-9.....	65
Figure 4-5. Cone resistance contour plot with time and depth	66
Figure 4-6. Cone resistance increase with time after liquefaction at different depths	67
Figure 4-7. Cone resistance recovery with time after liquefaction.....	69
Figure 4-8. q_t variation with time at different effective overburden stresses	70
Figure 4-9. Comparison of other research using equation (4-4).....	72
Figure 4-10. Comparison of other research using power function	73
Figure 4-11. q_{c1N} of CPT-3 to CPT-9.....	76
Figure 4-12. The 95% confidence intervals and mean values for q_{c1N}	77

Figure 4-13. (a) q_{c1N} variation with time, (b) $CRR_{7.5}$ variation with time.....	78
Figure 5-1. Time schedule for multiple shaking events, the shaking events have varying acceleration amplitude and duration, and the same frequency of 1 Hz...	82
Figure 5-2. Input motion for the 2 nd shaking (0.25g, 1 Hz, 25 cycles).....	84
Figure 5-4. Input motion for shaking event (4-1) (0.4g, 1 Hz, 25 cycles).....	86
Figure 5-5. Input motion for shaking event (4-2) (0.25 g, 1 Hz, 25 cycles).....	86
Figure 5-6. Input motion for shaking event (4-3) (0.1 g, 1 Hz, 14 cycles).....	87
Figure 5-7. Input motion for shaking event (4-4) (0.25g, 1 Hz, 25 cycles).....	87
Figure 5-8. Pore pressure readings of the 2 nd shaking at different depths	89
Figure 5-9. Excess pore pressure generation during the 2 nd shaking at different depths.....	90
Figure 5-10. Absolute lateral movement time histories of different LSB frames for the 2 nd shaking (a) 2 nd frame (b) 4 th frame (c) 6 th frame (d) 8 th frame (e) 10 th frame. The elevations of the frames where LVDTs were installed are shown in Figure 3-16.....	92
Figure 5-11. Pore pressure readings of the 3 rd shaking at different depths.....	93
Figure 5-12. Excess pore pressure generation during the 3 rd shaking at different depths.....	94
Figure 5-13. Absolute lateral movement time histories of different LSB frames for the 3 rd shaking (a) 3 th frame (b) 5 th frame (c) 7 th frame (d) 9 th frame (e) 11 th frame	96
Figure 5-14. Pore pressure readings of 4 th shaking (4-1) at different depths.....	97
Figure 5-15. Excess pore pressure generation during the 4 th shaking event (4-1) at different depths	98
Figure 5-16. Absolute lateral movement time histories of different LSB frames in the 4 th shaking (a) 3 th frame (b) 5 th frame (c) 7 th frame (d) 9 th frame (e) 11 th frame	100
Figure 5-17. Excess pore pressure generation during the shaking event (4-2) at different depths	101

Figure 5-18. Excess pore pressure generation during the shaking event (4-3) at different depths	101
Figure 5-19. Excess pore pressure generation during the shaking event (4-4) at different depths	102
Figure 5-20. Average relative density of the sand deposit before each shaking event	103
Figure 5-21. Pore pressure ratio comparison between 1 st , 2 nd , 3 rd , and 4-1 shaking: (a) PZ-2 (b) PZ-4	105
Figure 5-22. Comparison of pore pressure ratios between shaking (4-2) and (4-4): (a) PZ-2 (b) PZ-4	106
Figure 6-1 Schematic of the FLAC interface element (Itasca 2016)	110
Figure 6-2 <i>FLAC</i> meshing with boundary conditions.....	116
Figure 6-3 Cyclic loading responses of sand of $D_r = 55\%$ ($\sigma'_{vo} = 100$ kPa, $CSR = 0.12$) sheared up to shear strain peak = 10% (DSS test).....	120
Figure 6-4 CSR vs. $N\gamma=3\%$ curves from DSS tests	121
Figure 6-5 Triggering calibration for PM4Sand	122
Figure 6-6 Cyclic loading responses of sand at $D_r = 55\%$ ($\sigma'_{vo} = 100$ kPa, $CSR = 0.12$) sheared up to shear strain peak = 10% (PM4Sand).....	126
Figure 6-7 Pore pressure ratio time histories at five different depths: comparison of the shake table test (1st shaking) with simulations.....	129
Figure 6-8 Contour plots of pore pressures during shaking at different time (units: Pa).....	133
Figure 6-9 Shear strain time histories at two different depths: comparison of the shake table test (1st shaking) with simulations.....	134
Figure 6-10 Surface settlement time histories: comparison of the shake table test (1st shaking) with simulations	135

LIST OF TABLES

Table 4-1. CPTu testing time schedule	61
Table 4-2. Values of constants and coefficient of determination (R^2) for Equation 4-4	70
Table 4-3. CPT resistance measurement of sand aging effect	72
Table 5-1. Time schedule for multiple shaking events	82
Table 6-1 Soil properties for PM4Sand elements	116
Table 6-2 Properties for elastic elements	116
Table 6-3 Interface parameters and their values	117
Table 6-4 Activated PM4Sand parameters in calibration	122

ACKNOWLEDGEMENTS

I was fortunate to have the privilege of conducting this research under the guidance of Dr. Ming Xiao. I can well remember the many hours we spent engaged in discussing the design of the shake table facility, the research plan and the test results. Dr. Xiao possesses an endless supply of ideas, many of which have been incorporated into this research. Without his full support and encouragement over the past four years, this research would not have been possible.

I would like to thank Dr. Tong Qiu for his help and guidance on this research. Dr. Qiu is an inspiring professor, and I am grateful to have had the opportunity to discuss the problems I had in the test and numerical simulation. Dr. Qiu's critical thinking and high standards greatly enhanced the quality of this work. I would also like to thank Dr. Patrick J. Fox and Dr. Shimin Liu, for providing me with invaluable advice for conducting the tests and for their insightful comments on my work.

This work would not have been possible without the efforts of others who assisted me while conducting this research. Dr. Katerina Ziotopoulou at the University of California Davis provided cyclic DSS results which are critical for model calibration. Dr. Jeff Evans at Bucknell University provided CPTu facility and advice in interpreting data. Mr. Dan Fura helped with almost every aspect of the test preparation. Sajjad Salam, Sudheer Prabhu, Yuetan Ma, Jack Wang, Rong Zhao, Daniel Duran and Dr. Behnoud Kermani, labored over many long days while assisting me with the experiments.

My fellow graduate students, Ben Adams, Tiffany Szeles, Mahsa Khosrojerdi, Amir Ahmadipur, Juliana Neves, Mahboubeh Zahedi and Kun Zeng offered their friendship, support, and ideas. I would also like to thank my parents for their unconditional love and support. My family was a constant source of support, encouragement and laughter. Finally, my deepest gratitude is extended to my girlfriend, Ms. Xin Wen. Her love and patience sustained me through the most difficult years of this work.

Jintai Wang

06/2018

Chapter 1

Introduction

1.1 Problem statement

Liquefaction is one of the most important, interesting, complex and controversial topics in geotechnical earthquake engineering (Kramer 1996). Earthquake-induced liquefaction is a cause of substantial damage to geotechnical structures. The 1964 Good Friday earthquake in Alaska and the Niigata earthquake in Japan produced prominent examples of liquefaction-induced damage, including but not limited to slope failures, foundation failures and flotation of buried structures (Kramer 1996; Ishihara 1993). During the recent 2011 Christchurch earthquake in New Zealand, liquefaction-induced settlement, tilt and lateral sliding of structures caused severe damages and economic losses (Cubrinovski and McCahon 2012). Underground structures embedded at shallow depths such as large underground parking garages, pipelines and manholes, suffered significant uplift in liquefied soil as observed in the 2011 Great East Japan Earthquake (Chian et al. 2014). Figure 1-1 (a) shows a severe liquefaction in a residential area during the 2011 Christchurch earthquake. The liquefaction manifested as massive sand boils and large amount of sand/silt ejecta and water littering streets and residential properties, and recreation grounds (Cubrinovski et al. 2011). Figure 1-1 (b) presents an uplift of manhole due to liquefaction during the 2011 Tohoku Earthquake in Japan.



(a)



(b)

Figure 1-1. Examples of severe liquefaction at shallow depths: (a) 2011 Christchurch earthquake, photo courtesy of Mark Lincoln, nzraw.co.nz. (b) 2011 Tohoku Earthquake (Yamaguchi et al. 2011),

In practice, liquefaction evaluation is usually based on the simplified procedure developed by Seed and Idriss (1971), summarized and updated by Youd et al. (2001), Idriss and Boulanger (2008), and Boulanger and Idriss (2011). In this method, the seismic demand on a soil layer is quantified by the cyclic stress ratio (CSR); the capacity of soil liquefaction resistance is defined as cyclic resistance ratio (CRR). Liquefaction is predicted if CSR is larger than CRR . Several widely-used liquefaction charts have been developed relating CRR to field tests such as the standard penetration test (SPT), cone penetration test (CPT), and shear-wave velocity measurements (V_s) (Andrus and Stokoe 2000; Youd et al. 2001; Cetin et al. 2004; Idriss and Boulanger 2006, 2008; Moss et al. 2006; Kayen et al. 2013; Boulanger and Idriss 2014, 2015). All these charts are empirically calibrated by field case histories, which make them reliable tools for liquefaction evaluation. Figure 1-2 shows the curve recommended for calculation of CRR from CPT Data. The compiled case histories were separated by the CPT clean sand base curve. Liquefaction was reported in most of the cases above the curve, while most of the cases below the curve did not report liquefaction.

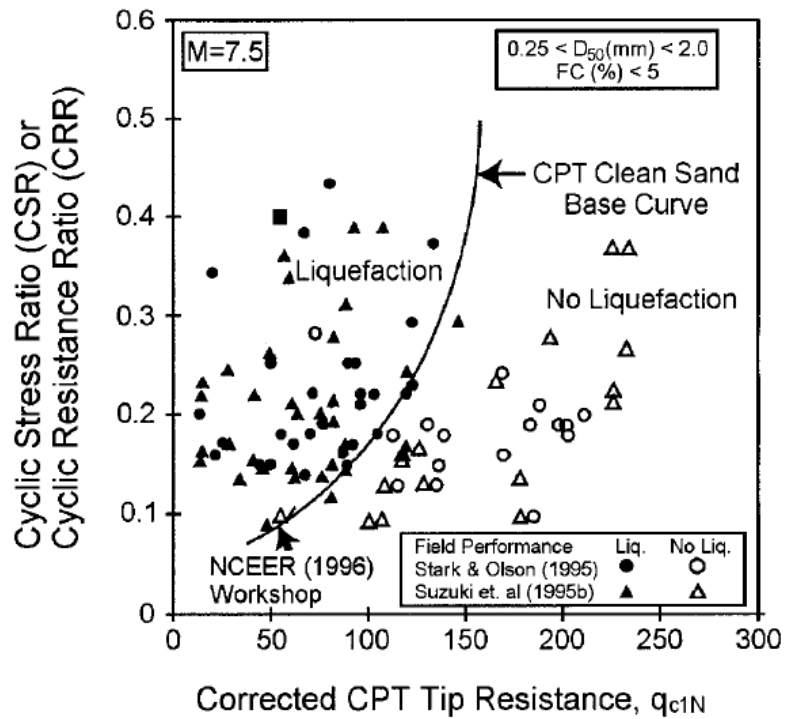


Figure 1-2. Curve Recommended for Calculation of *CRR* from CPT Data along with empirical Liquefaction Data from Compiled Case Histories (Reproduced from Robertson and Wride 1998 by Youd et al. (2001))

Although CPT has been widely accepted as a liquefaction evaluation tool and many case histories have been documented, some limitations of the empirical charts have been pointed out, such as the charts do not explicitly account for the geologic age and shaking history of the sand layer (Dobry et al. 2015; El-Sekelly et al. 2016a, 2016b). Boulanger and Idriss (2014) pointed out that the timing of CPT testing with respect to the timing of earthquake loading is not clear in some case histories. In most cases, the CPTs were likely performed after earthquake loading. There were, however, many cases where the CPT data were from site investigations performed before the earthquake in combination with some performed after the earthquake (Boulanger and Idriss 2014). The uncertainty of CPT timing

might affect the reliability of the liquefaction evaluation chart, when the time effect on liquefaction resistance is considered.

Several soil constitutive models have been developed to simulate the response of saturated sand under seismic loading. Selected examples are: the PDMY02 model (Elgamal et al. 2002 and Yang et al. 2008), the UBCSAND model (Beaty and Byrne 2011), the Dafalias-Manzari model (Dafalias and Manzari 2004) and the PM4Sand model (Boulanger and Ziotopoulou 2015, Ziotopoulou and Boulanger 2016). PDMY02 (Pressure Dependent Multi Yield 02) is an elastic-plastic model for simulating the pressure sensitive response of granular materials, described by Elgamal et al. (2002) and Yang et al. (2008). UBCSAND is an elastic-plastic material model developed for sand-like granular materials that have the potential to liquefy during cyclic loading (Beaty and Byrne 2011). The Dafalias-Manzari model is a generalized stress state, elastic-plastic material model developed from critical state and stress-ratio controlled framework (Dafalias and Manzari 2004). PM4Sand follows the stress-ratio controlled, critical state compatible, bounding surface plasticity framework that was developed by Dafalias and Manzari (2004) and was modified and further developed by Boulanger and Ziotopoulou (originally in 2012 and subsequently in 2015 and 2018) to better approximate the behavior of interest in earthquake engineering applications. Great progress has been made in liquefaction studies using advanced soil constitutive models. However, the simultaneous prediction of accelerations, generation and dissipation of excess pore pressures, and post-liquefaction settlements remains a challenge (Ramirez et al. 2017). Also, current constitutive models cannot be assumed to handle generalized conditions without structure-specific, soil-specific, and loading-specific validation studies (Bray et al. 2016).

1.2 Research motivation

The first motivation of this research is to investigate the seismic performance of liquefiable ground at shallow depth using a newly constructed shake table facility. The pore pressure generation and dissipation patterns, the acceleration and the lateral displacement of the liquefiable ground during shaking need to be investigated for understanding the seismic performance of a specific sand. The second motivation is to investigate the time-dependent cone penetration resistance of the liquefied sand deposit. Whether or not the cone penetration resistance is affected by the aging time is of great interest to understand the strength variation of a liquefied sand. The third motivation is to evaluate the predictive capabilities of an advanced constitutive model for sand using the measurements from shake table test.

1.3 Research objectives

This study has three main objectives. The first objective is to investigate the seismic performance of a liquefiable sand deposit under a series of shaking events. The second objective of this study is to investigate the strength gain of the liquefied sand deposit using a series of CPTu testing. The third objective is to simulate the shaking table test using advanced constitutive model (PM4Sand) and understand the predictive performance of this model.

1.4 Organization of the dissertation

This dissertation consists of seven chapters. Following the motivation and objective presented in this chapter, Chapter 2 presents the literature review of physical modeling of sand liquefaction, sand aging effect, shaking history effect and the numerical modelling of sand liquefaction. Chapter 3 presents the development of the 1-G shake table test for a uniform sand deposit. Chapter 4 presents a series of piezo-cone penetration testing (CPTu) performed on the liquefied sand deposit. Chapter 5 presents the shake table testing using multiple shaking events. Chapter 6 presents the development of a numerical model simulation of the shake table test. Chapter 7 of this dissertation presents the summary and conclusions derived from this study; this chapter also provides some recommendations for future research.

Chapter 2

Literature review

This chapter presents the literature review on the (1) shake table and centrifuge modeling on soil liquefaction (2) soil aging effect on key engineering properties (3) shaking history effect on liquefaction resistance (4) numerical modelling of sand liquefaction.

2.1 Shake table and centrifuge testing on soil liquefaction

2.1.1 Shake table testing

Shake table modelling of soil liquefaction has been widely reported. Sasaki and Taniguchi (1982) performed large scale shake table tests on gravel drain system as a counter-measure to liquefaction of the sand deposits. The modeled sand deposit with gravel drains and the half-buried type road model were excited by horizontal input motion. They concluded that: (1) The increase of the pore water pressure during the shaking became smaller near the gravel drain. The effective drainage area was less than 50 cm from the gravel drains. (2) The dissipation of the pore water pressure after the shaking was accelerated by the gravel drain. (3) The gravel drain system can be a good countermeasure to liquefaction if appropriately designed. Yao et al. (2004) conducted shake table tests to investigate the behavior of a soil-pile-superstructure system in liquefiable ground. A modeled two-story structure was supported by a pile group in a saturated sand deposit in a

large-scale laminar shear box. The base was subjected to a sinusoidal motion with increasing amplitude. They found that the predominant period of the pile-superstructure system became longer as excess porewater pressure was generated. The bending moment of a pile could be several times larger in the ground than at the pile head. They suggested that the stiffness against the displacement at the pile head was sufficient to represent a soil-pile system in interaction analysis. Consideration of the transient state before liquefaction in liquefiable ground was found to be important, because bending moment and earth pressure can reach maximum values at this stage.

Okamura and Teraoka (2006) performed shake table tests to investigate soil desaturation as a liquefaction countermeasure. The first series of shake table tests were performed on desaturated soil with level ground at different atmospheric pressures. In the second series, the effects of soil desaturation as a countermeasure for an existing structure were evaluated. They suggested that the use of soil desaturation as a liquefaction countermeasure technique was clearly possible in practice. The soil can be effectively desaturated during air injection. They also confirmed that volumetric strain of the voids due to seismic generation of excess pore pressure played a dominant role in increasing liquefaction resistance of soil. The settlement was remarkably reduced by the desaturation. However, desaturation was less effective for soils at shallow elevations (less than 2 m from ground surface).

Haeri et al. (2012) reported the response of a group of piles subjected to liquefaction-induced lateral spreading using a large scale 1-g shake table test. A rigid soil container was used in the shake table test. They found that the soil started to move laterally right after liquefaction and kept moving towards the downslope until the end of shaking.

The piles moved with the soil at the early stage of shaking and then bounced back gradually having a residual displacement at the end. They also found that the lateral soil pressures exerted from the laterally spreading soil varied in the individual piles of a group of piles both in transverse and longitudinal directions. The amplitude of excess pore water pressures in upslope side of the single pile was more than that of the downslope side during lateral spreading.

Otsubo et al. (2016) conducted a series of shake table tests on mitigation of liquefaction vulnerability for existing embedded lifelines. The shake table tests were based on the significant damage brought by the 2011 Tohoku Earthquake because of extensive liquefaction. Several mitigation methods, such as the horn structure method, the drain pipe method, the chemical injection method, and the insertion of a sheath pipe were evaluated in the shake table testing. They concluded that all the methods had satisfactory results. They suggested that liquefaction around a buried pipe can be mitigated by installing vertical drain pipes. The presence of a surface gravel layer could improve the drainage system in the backfill. The shake table test results also suggested that the normal operation of sewage systems was maintainable even after a strong earthquake if sheath pipes were installed. This mitigation method could prevent disasters associated with the deterioration of sewage pipes.

2.1.2 Centrifuge testing

Hushmand et al. (1988) reported a series of centrifuge liquefaction tests. Both dry and saturated sands were used and contained in a box constructed of aluminum laminae

designed to move freely on each other. Accelerometers, displacement transducers and pore pressure sensor were attached to the box and embedded in the soil at various elevations to record the response of the soil during an earthquake-like excitation. The main conclusions from the research are: (1) the placing of bearings between box layers reduced the interlayer friction coefficient to a measured value of 0.013 under the loads experienced in the centrifuge tests; (2) the apparatus was able to make detailed measurements of all the response of the soil system during precisely controlled base motion in amplitude, frequency content and duration.

Wilson et al. (2000) performed a series of dynamic centrifuge tests of pile foundations in liquefying sand. The experiments were performed using pile-supported structures founded in loose ($D_r = 35\%$) and medium dense ($D_r = 55\%$) sand profiles. Soil-pile interaction was quantified directly in terms of the observed p - y behavior through back-analysis of a well-instrumented single-pile supported structure. They reported that the back-calculated p - y behavior characteristics were consistent with the stress-strain response of liquefying sand. The lateral resistance in loose sand was usually small when the soil liquefied. In medium dense sand, the p - y relationship progressively softened during shaking as excess pore pressures, strains, and number of load cycles increased. They suggested that lateral p - y resistance of liquefied sand was shown to be significantly affected by relative density, cyclic degradation, excess pore pressures, phase transformation behavior, prior displacement history and loading rate.

Sharp et al. (2003) conducted six centrifuge model tests of liquefaction and earthquake-induced lateral spreading of fine Nevada sand using an inclined laminar box. The centrifuge tests were to simulate a gently sloping, 10 m thick stratum of saturated

homogeneous sand with a relative density range from 45 to 75%. The sand deposit was subjected to lateral base shaking with prototype peak acceleration ranging from 0.2 to 0.41 g, a frequency of 2 Hz, and duration of 22 cycles. They reported that the lateral movements stopped as soon as the shaking ended. However, much of the recorded settlement developed slowly after the shaking had ended. They also suggested that permeability played an important role in determining the liquefaction response of a homogeneous sand deposit. The permeability could affect the depth of liquefaction, the pore pressure dissipation rate and the characteristics of the ground surface settlement.

Kulasingam et al. (2004) performed twelve dynamic centrifuge modeling to study the strength loss and localization at silt interlayers in slopes of liquefied sand. The centrifuge model tests represented four different simple slope configurations, a range of initial relative densities, and three different input motions. They concluded that the potential for void redistribution induced shear localization and slope instability depended on the initial relative density, slope geometry (silt layer shape, sand layer thickness), and shaking characteristics. They suggested that the apparent residual shear strength was unlikely to correlate to pre-earthquake penetration resistance alone. It was a function of the initial shear stresses and factors affecting the process of void redistribution and localization.

Brandenberg et al. (2005) performed eight dynamic model tests on a 9 m radius centrifuge to study the behavior of single piles and pile groups in liquefiable and laterally spreading ground. The soil profile consisted of a gently sloping nonliquefied crust over liquefiable loose sand over dense sand. Each model was tested with a series of realistic earthquake motions with peak base acceleration ranging from 0.13 g to 1.0 g. They reported

that significant strains developed in the liquefiable sand, and the laterally spreading crust displaced more than the liquefiable sand. The direction of lateral loads was shown to depend on the direction of the incremental and total relative movements between the soil and piles. The displacement patterns in the soil layers and piles were identified. The liquefiable soil tended to push the piles downslope along with the crust for files that were stiff relative to the surrounding soil. For more flexible piles, the liquefiable soil produced large upslope forces. They concluded that these loading patterns were more complex than those often assumed in static and seismic analysis procedures.

Both centrifuge and shake table modeling have certain advantages and limitations. Centrifuge modeling is able to reproduce prototype stress levels in a small-scale model, while dense instrumentation may not be able to be used due to the small model size (Ecemis 2013). 1-g shaking table modeling has the advantage of well-controlled large shaking amplitude, multi-axis input motions and denser instrumentation. The use of shaking table tests has been justified if the purpose is to validate the numerical model or to understand the basic failure mechanism (Wartman et al. 2005; Paolucci et al. 2008; Antonellis et al. 2015).

2.1.3 Soil container for seismic testing

A proper soil container in seismic model test should cause stress and strain in the model similar to that in a soil layer with infinite lateral extent. Different types of soil containers have been developed to satisfy different design requirements. Design and commissioning of rigid soil containers for use on shaking table or centrifuge test have been

reported (Whitman and Lambe 1986; Adalier and Elgamal 2002; Ng et al. 2004; Wartman et al. 2005; Lin and Wang 2006). However, the main disadvantage of a rigid box is the boundary effect on the dynamic response of the soil. The study by Fishman et al. (1995) suggested that for rigid box on dynamic loading, the free field may not be realized for distances up to $1.5 H$ to $2.0 H$ from the end wall, where H was the height of the soil.

Due to the limitation of the rigid soil container, laminar shear box (LSB) was designed and widely employed in the seismic model tests. A common design of laminar shear box (LSB) is a stack of laminae that can move along the shaking direction “freely”. The design intent of LSB is to minimize the lateral stiffness of the end-walls to ensure the soil governs the behavior of the whole system. Hushmand et al. (1988), Van Laak et al. (1994), Pamuk et al. (2007) and Shen et al. (1998) described different laminar shear boxes for centrifuge tests. Single-axis laminar shear box for shaking table tests was described by Kagawa et al. (2004) and Turan et al. (2009).

Kagawa et al. (2004) reported a large-scale laminar shear box with dimensions of $11 \text{ m} \times 3.5 \text{ m} \times 6 \text{ m}$ ($L \times W \times H$). The moving parts of the shear box weighed approximately 55 tons. The weight of the box was 12% of the weight of a foundation soil model inside. This ratio was considered to be sufficiently small that the shear box could produce nearly one-dimensional wave propagation fields., i.e. free-field conditions.

Turan et al. (2009) reported the design, fabrication and commissioning of a single axis laminar shear box for use in seismic soil-structure interaction studies. The flexible container consisted of 24 horizontal laminae supported individually by linear bearings and steel guide rods. The laminae comprised solid high strength aluminum alloy box sections

bolted together to form rectangular frames. There was a 2 mm clearance between the laminae to ensure independent movement.

2.2 Sand aging effect on key engineering properties

The effect of aging on the properties of freshly deposited or densified sand has been studied by several researchers. Anderson and Stokoe (1978) used the resonant column test to show that shear moduli of sands, silts, and clays increased with time of confinement at a constant confining pressure. The time-dependent modulus increase was characterized by two phases: (1) an initial phase that resulted from primary consolidation, and (2) a second phase which occurred after completion of primary consolidation, called the “long-term time effect” (Anderson and Stokoe, 1978). Anderson and Stokoe (1978) suggested that confinement time was an important parameter that must be properly accounted for in the laboratory measurement.

Mitchell and Solymar (1984) reviewed previous field and laboratory evidence on the time-dependent behavior and concluded that freshly deposited or densified clean sand may exhibit substantial stiffening and strength increase with time up to several months. Sand deposits may experience a significant loss in strength because of disturbance, thus behaving in a manner similar to sensitive clay (Mitchell and Solymar, 1984). These phenomena must be considered when evaluating the results of laboratory tests on reconstituted samples and in the estimation of liquefaction potential. Mesri et al. (1990) observed substantial increase in stiffness and cone-penetration resistance of sand with time under drained aging conditions at constant effective vertical stress. They proposed

empirical equations for predicting the time-dependent cone resistance after ground modification. Schmertmann (1991) suggested that soil aging over engineering times can cause a general 50 to 100% improvement in many key soil properties. Improvements in properties with aging were found to be approximately linear with the logarithm of time of aging. Schmertmann (1991) also suggested that designs should include the beneficial effects of engineering aging when appropriate. For example, the designers could allow an initial lower factor of safety in an embankment or other fill if a significant time interval would pass before the loading conditions.

Charlie et al. (1992) performed a series of CPTs on a blasting site one week prior to blasting and one, three, and 18 weeks after blasting. They reported that blasting initially decreased the tip resistance by 62%, decreased the local friction by 30%, and increased the friction ratio by 100% of the pre-blast values. However, from one week to 18 weeks after blasting, the normalized tip resistance increased by 18%, the normalized local friction decreased by 39%, and the normalized friction ratio decreased by 80% of the post-blasting values. Joshi et al. (1995) studies the effect of aging on the penetration resistance of freshly deposited sands by pushing a probe periodically into the sand bed. They concluded that aging significantly increased the penetration resistance of sands and the increase rate was higher for submerged sand as compared with dry sand.

Mitchell (2008) reviewed the phenomenon of sand aging wherein disturbed natural deposits of clean sand may exhibit a sensitivity or loss of strength and then, following re-deposition and/or densification show an increase in stiffness, penetration resistance, and liquefaction resistance. The following conclusions were summarized by Mitchell (2008):

- (1) Soil aging and the associated improvements in stiffness, penetration resistance and

liquefaction resistance were ubiquitous among freshly deposited and/or densified deposits of silica sands. (2) The natural sands developed a structure over time following deposition and/or disturbance. The sand could exhibit a meta stability that was in many ways similar to sensitivity in clays. (3) The initial stiffness of clean silica sands would increase by a factor of about 1 to 3 percent per log cycle of time relative to that at an age of 1000 min. The shear modulus increase factor was greater (up to 10%) for carbonate sands. (4) Although the penetration resistance in most cases showed significant increases with time after disturbance and densification, a few cases showed no significant increase. The sand aging was referred to as “a continuing enigma” (Mitchell 2008).

Based on these investigations, different mechanisms for the aging effect have been suggested. Mitchell and Solymar (1984) reasoned that the cementation at interparticle contacts due to the dissolution and precipitation of silica would be the major factor for time-dependent strength increase. Mesri et al. (1990) explained the time effect as the continued rearrangement of sand particles during secondary compression. During drained aging of clean sands, an increased stiffness and an increase in effective horizontal stress resulted from continued rearrangement of sand particles. This resulted in an enhanced macrointerlocking of sand grains and microinterlocking of grain surface roughness (Mesri et al., 1990).

Schmertmann (1991) indicated that most engineering-time age strengthening effects resulted from increased basic soil friction, including dilatancy effects, and not from increased cohesion. The in-situ effective stresses were involved in the aging mechanisms, including grain slippage, soil-structure dispersion, increase of interlocking, and a probable internal arching of stresses. Thixotropic aging effects occurred primarily at very low

effective stresses and under undrained conditions in cohesive soils (Schmertmann, 1991). Joshi et al. (1995) suggested that the increase in penetration resistance of dry sand over time is due to macro-interlocking of particles and micro-interlocking of surface roughness. In the submerged state, besides the rearrangement of sand particles, partial cementation caused by precipitation of salts and probably also silica on the sand grains and in the pores resulted in the larger increase in the penetration resistance (Joshi et al., 1995).

The beneficial effect of geologic aging on the strength and liquefaction resistance of sand deposit has also been reported in field observations. Arango et al. (2000) analyzed the soil performance during the Charleston, South Carolina earthquake in 1886, and demonstrated that age played a major role in the field cyclic strength of sand deposits based on data from four separate site-specific investigations. The correlation that they proposed for the strength gain factor was based on an update of the correlation that was proposed earlier by Kramer and Arango (1998). The laboratory test results demonstrated a strength increase by a factor between 2 and 3. Lewis et al. (2004) reported a case history of liquefaction evaluation at the Savannah River Site. The test results showed that the soils had increased liquefaction resistance of two to three times when compared to standard literature for Holocene-age deposits. Based on the observation in Tokyo Bay after the 2011 Great East Japan earthquake, Ishihara et al. (2011) reported that young deposit was more vulnerable to liquefaction.

It has been suggested that an age correction factor be applied to CRR as follows (Arango et al. 2000; Lewis et al. 2004; Andrus et al. 2004, 2009)

$$CRR_K = CRR K_{DR} \quad (2-1)$$

where CRR_K is cyclic resistance ratio corrected for age and cementation, and K_{DR} is a factor to correct for influence of age and cementation on deposit resistance. Hayati et al. (2008) critically reviewed previous studies and suggested the following relationship

$$K_{DR} = 0.17 \log(t) + 0.83 \quad (2-2)$$

where t is the time since initial deposition or critical disturbance in years. This equation was obtained by assuming $K_{DR}=1$ at $t = 10$ years.

2.3 Shaking history effect on liquefaction resistance

Laboratory cyclic tests have shown that previous strain history affects the liquefaction resistance of the soil (Finn et al. 1970; Seed et al. 1977; Seed 1979). Finn et al. (1970) reported that partial liquefaction that occurred at small shear strains greatly increased the liquefaction resistance. However, if sand developed large shear strains, the subsequent liquefaction resistance was decreased. Finn et al. (1970) reasoned that the loss of resistance caused by larger shear strains might be the creation of a uniform metastable structure or the development of a non-uniform structure.

Oda et al. (2001) provided a microstructural interpretation for the re-liquefaction of saturated granular soil using a series of triaxial tests. They suggested that the possible mechanism for the decrease of liquefaction resistance was a development of a column-like structure, thus the microstructure of the soil was extremely unstable during the shaking. Yamada et al. (2010) performed a series of cyclic undrained triaxial tests to study the changes in anisotropy taking place during liquefaction and the effects of the anisotropy on reliquefaction behavior. They reported that liquefaction induced irreversible anisotropy to

the soil, which remained after the excess pore pressure had dissipated. As the level of induced anisotropy increased, the liquefaction resistance decreased, and the behavior of the sand resembled that of much looser sand when sheared in a certain direction, despite the increased overall density of the soil.

1-g shake table and centrifuge modelling have also been used to investigate the influence of previous liquefaction history. Ha et al. (2011) performed a series of 1-g shaking table tests using five sands with different gradation characteristic to study the liquefaction resistance of the sand. The test results showed that the number of cycles required to liquefy each sand decreased significantly following the 1st liquefaction event. They concluded that the liquefaction during the 1st shaking event destroyed the aged soil fabric, and the sand reconsolidated as a young, normally consolidated sand. They also suggested that liquefaction and liquefaction resistance did not correlate well to relative density or void ratio, D_{10} , D_{50} , or C_u .

Dobry et al. (2015) evaluated the liquefaction potential of clean and silty sands on the basis of the field measurement from the Imperial Valley of south California. They concluded that the geologically recent natural silty sand sites had significantly higher liquefaction resistance as a result of preshaking caused by the high seismic activity in the valley. Not all benefits of preshaking were necessarily lost when an earthquake liquefied the soil. This was confirmed by the centrifuge simulations by El-Sekelly (2014), where the model sand deposit showed a net gain in liquefaction resistance after being subjected to several dozen earthquakes.

El-Sekelly et al. (2016a) conducted a series of centrifuge tests on a 6-m prototype homogeneous deposit of loose saturated silty sand. Two different types of shaking events

were applied: a strong 15-cycles shaking and a weaker 5-cycle shaking. They reported that a small number of preshaking seismic events that generated excess pore pressure but did not liquefy the soil might increase its liquefaction resistance rather substantially. A larger earthquake that liquefied the soil may undo this beneficial effect of shaking, in some cases getting close to “resetting the clock”. They also concluded that the increase in liquefaction resistance with the number of earthquakes was not reflected in a corresponding increase in the shear wave velocity of the soil. El-Sekelly et al. (2016b) applied 25 additional shakings based on the work of El-Sekelly et al. (2016a). They suggested that the occurrence of extensive liquefaction resulted in significant reduction in the liquefaction resistance of the deposit. The liquefaction resistance was reduced to a level that was equal or less than that of the young deposit before it was subjected to preshaking.

The field observations by Heidari and Andrus (2012) indicated that full liquefaction may completely erase the beneficial effects of geologic aging. Thus, the geologic clock is reset, and the liquefaction resistance of the sand is brought to the liquefaction resistance it had when the sand had been just deposited.

2.4 Numerical modeling of sand liquefaction

2.4.1 Advanced soil constitutive models for liquefaction

Several soil constitutive models have been developed to simulate the response of saturated sand under seismic loading. Selected examples are: the PDMY02 model (Elgamal et al. 2002 and Yang et al. 2008), the UBCSAND model (Beatty and Byrne 2011), the

Dafalias-Manzari model (Dafalias and Manzari 2004) and the PM4Sand model (Boulanger and Ziotopoulou 2015, Ziotopoulou and Boulanger 2016).

PDMY02 (Pressure Dependent Multi Yield 02) is an elastic-plastic model for simulating the pressure sensitive response of granular materials, described by Elgamal et al. (2002) and Yang et al. (2008). UBCSAND model is an elastic-plastic material model developed for sand-like granular materials that have the potential to liquefy during cyclic loading (Beaty and Byrne 2011). The model predicts the shear stress-strain behavior of the soil using an assumed hyperbolic relationship and estimates the associated volumetric response of the soil skeleton using a flow rule. The model can be used in a fully-coupled manner that the mechanical and groundwater flow calculations are performed in parallel (Beaty and Byrne 2011). A set of input parameters have been developed to represent the response of a hypothetical generic sand for an easy use of UBCSAND in preliminary evaluations. These parameters provide reasonable estimates of stiffness of the soil and capture the liquefaction response.

The Dafalias-Manzari model is a generalized stress state, elastic-plastic material model developed from critical state and stress-ratio controlled framework (Dafalias and Manzari 2004). PM4Sand follows the stress-ratio controlled, critical state compatible, bounding surface plasticity framework that was developed by Dafalias and Manzari (2004) and was modified and further developed by Boulanger and Ziotopoulou (originally in 2012 and subsequently in 2015 and 2018) to better approximate the behavior of interest in earthquake engineering applications. The modifications included revising the fabric formation, modifying the plastic volumetric strains and the dilatancy relationships, and providing a constraint on the dilatancy during volumetric expansion. The PM4Sand has a

narrow stress-ratio based elastic cone and three other key surfaces: the bounding, dilation and critical-state surfaces. The locations of the dilation and bounding surfaces are dependent on the relative state of the soil (the difference between the relative density and the relative density at critical state for the current confining pressure), such that they both rotate when the relative state of the soil changes. As the soil is sheared towards critical state, both surfaces approach each other until they coincide at the critical state stress ratio (Kamai 2011, Boulanger and Ziotopoulou 2017). The model was coded as a user defined material (UDM) in a dynamic link library (DLL) for use with the commercial program FLAC 8.0 (Itasca 2016).

2.4.2 Numerical simulation of soil liquefaction using advanced constitutive model

The predictive capabilities of these models have been evaluated or compared based on centrifuge or 1-g shake table tests results. Byrne et al. (2004) presented the comparison of numerical modeling prediction using UBCSAND and measured centrifuge model response to investigate liquefaction at large depths. The characteristic liquefaction behavior of Nevada sand used in the numerical models was obtained from undrained cyclic simple shear tests and was the basis for the numerical predictions of the centrifuge tests. Several factors were considered to accurately predict the centrifuge results, including the change in density caused by the confining stresses induced in the centrifuge and the effects of degree of saturation. They concluded that predicted excess pore pressures were in good agreement with the measured values.

Dashti and Bray (2013) simulated centrifuge tests of structures with shallow foundations on liquefiable sand. The fully-coupled numerical simulation was performed in *FLAC-2D* using UBCSAND model. They reported that the numerical model was able to capture building settlements measured in experiments reasonably well for one scaled input motion. The soil model captured the overall contribution of deviatoric displacement mechanisms and localized volumetric strains during partially drained cyclic loading. They suggested that the limitation of the model became evident for slower rates of earthquake energy buildup. The extent of excess pore pressure generation and building displacement was overestimated by up to a factor of 4 in this case.

Ecemis (2013) simulated shake table testing on liquefaction of saturated soil in a laminar shear box. The results from numerical simulations using the UBCSAND model, including excess pore pressures, accelerations and surface settlements, were compared to shake table testing results. The measured lateral displacements were found to be slightly higher than the computed displacements during the first and second shaking tests. Ecemis (2013) reasoned that the hyperbolic relationship in UBCSAND model might cause a minor error mostly because the hyperbola was only an approximate relationship for the linear elastic and hyperbolic plastic response. The calculated maximum initial accelerations were in general agreement with the measurements before liquefaction. The computed excess pore pressures were in a good agreement with the measured values.

Karimi and Dashti (2016) used centrifuge experiment results of a shallow-founded structure on liquefiable sand to evaluate the predictive capabilities of the PDMY02 soil model. Class C, solid-fluid, fully-coupled 3D nonlinear numerical simulations of the centrifuge experiments were performed using the pressure-dependent, multiyield- surface,

nonlinear soil constitutive model (PDMY02) implemented in OpenSees 2.4.3. They reported that the simulations captured 1D, free-field site response well in terms of excess pore pressures and accelerations, particularly during less-intense motions that induced smaller strains, excess pore pressures, and soil densification. During the stronger events, however, the model cannot capture the amplified dilation cycles due to soil stiffening that produced sharp acceleration spikes and drops in excess pore pressures. Ramirez et al. (2017) compared the predictive capabilities of PDMY02 and a modified version of Manzari-Dafalias Model (Rahimi-Abkenar and Manzari, 2016) in capturing the acceleration, excess pore pressure and settlement responses of a layered soil profile in centrifuge tests. The models were first calibrated using the same set of monotonic and cyclic triaxial tests and were then used to simulate the seismic performance of a layered soil deposit to a horizontal earthquake motion. For both triaxial and centrifuge experiments, the PDMY02 model tended to overestimate material damping while Modified M&D model tended to underestimate the damping. As a result, the amplitudes of acceleration were often underestimated by PDMY02 and overestimated by Modified M&D. The Modified M&D model generally provided a better prediction of excess pore pressure generation and volumetric settlements compared to the PDMY02 model. Li et al. (2018) simulated centrifuge experiments on level and gently liquefiable slope with granular columns using PDMY02 and Manzari-Dafalias (M-D) soil constitutive model. They concluded that both models underpredicted peak ground acceleration (PGA) near the surface at different distances from the granular column, but they better predicted spectral accelerations at periods exceeding 0.5 s. However, lateral movement of the treated slope was poorly

predicted by both models due to inaccuracies in predicting the dissipation rate in the presence of drains.

The performance of the PM4Sand model for predicting the response of liquefiable sloping ground has been examined with the Liquefaction Experiments and Analyses Projects (LEAP) centrifuge tests (Ziotopoulou, 2017; Ekstrom and Ziotopoulou, 2017) as well as other centrifuge tests (e.g. Boulanger et al., 2017).

Kamai and Boulanger (2012) performed numerical simulations of a centrifuge test with lateral spreading and void redistribution effect using PM4Sand model. In the centrifuge test, the pore pressure dissipation patterns, lateral spreading, and shear strain localization were measured and recorded. The simulations were performed for four consecutive shaking events, and results were compared for both the nontreated side and the drain-treated side. They reported that the results from both individually run simulations and the in-sequence simulations yielded comparable results in terms of the dynamic response and final deformations. These two approaches were mostly different in the cumulative effects of void redistribution.

Boulanger et al. (2014) simulated two centrifuge tests using PM4Sand model in FLAC. The results of the centrifuge tests involving liquefiable sands with lower-permeability interlayers have demonstrated that void redistribution can affect shear strength losses and slope deformations. The simulations were shown to reasonably reproduce the patterns of void redistribution that were observed in physical modeling. The numerical simulations provided additional insight on the mechanisms of void redistribution. They suggested that the estimation of earthquake-induced deformations for

geotechnical structures affected by liquefaction involved significant uncertainties. The estimation of in-situ residual shear strength was a major contributor to those uncertainties.

Ziotopoulou (2017) simulated three centrifuge tests on a sloping ground of medium dense Ottawa Sand subjected to a sinusoidal acceleration input motion. Measured and recorded pore pressure dissipation patterns, accelerations, and displacements were compared to Class A and C numerical predictions performed in FLAC using PM4Sand. Ziotopoulou (2017) concluded that key observations, mechanisms, and time histories were reasonably captured by the simulations. FLAC, PM4Sand and the overall employed methodology had the capability to predict the response of liquefiable sloping ground. The soil properties were found to be the most important factor in capturing the finer details of the response. Ekstrom and Ziotopoulou (2017) presented the Class B predictions and their comparisons against the LEAP experimental measurements. The recordings of the centrifuge experiments for each facility were compared to the corresponding numerical model analysis and results were presented in terms of excess pore pressure time histories and spectral accelerations. They concluded that the numerical model can satisfactorily predict the results of the experiment for most facilities.

Chapter 3

Seismic Performance of Liquefiable Ground at Shallow Depth in 1-G Shake Table Test

This chapter presents the development of the 1-G shake table test for a uniform sand deposit. The earthquake simulation facility designed and built at Penn State is introduced. The instrumentation and data acquisition system used in the test are presented. The detailed procedure of sample preparation, including the pluviation and saturation is described. The test recordings from piezometer, accelerometer and LVDT are presented and discussed. In this chapter, the following questions are addressed: 1) What is the performance of the shake table and laminar shear box for the target input motion? 2) Will the sand liquefy at the shaking event? 3) What is the seismic response of the sand deposit during shaking? 4) Is the pore pressure ratio sensitive to cyclic shear strain? Answering these questions can provide insights for further understanding of soil liquefaction at shallow depth.

3.1 Earthquake simulation facility

3.1.1 Large-scale shake table at Penn State

A large-scale 1-D shake table was designed and constructed at Civil Infrastructure Testing and Evaluation Laboratory (CITEL). The shake table, as shown in Figure 3-1, can generate recorded historical earthquake motions or user-defined seismic motions. The

dimensions of the shake table are 3 m × 3 m and the load capacity is 133 kN (30,000 lb) at an acceleration of 1g. The table is driven in one-dimension by a 5.6 L/s (90 gpm) pump and an actuator that provides 245 kN (55 kips) hydraulic driving force through a ± 12.5 cm dynamic displacement stroke.



Figure 3-1. Shake table at Penn State

3.1.2 Laminar shear box

The laminar shear box was designed and manufactured at the Pennsylvania State University. The detailed design consideration can be summarized as: 1) each lamina should have sufficient stiffness to maintain its shape during seismic loading; 2) the laminar shear box should have small mass compared to the tested soil to minimize inertia of box on the soil specimen. The LSB was made of thirteen independent steel frames (laminates) that freely slide on top of each other through linear guide rails. Each lamina comprises of two

wide flange beams ($W 5 \times 16$) and two rectangular tubes ($TR 4 \times 3 \times 3/16$). All the four structural steels were welded into a rigid frame. Four pairs of customized slides and rails (manufactured by NSK, Ann Arbor, Michigan) were bolted between two adjacent frames. Figure 3-2 shows the assembly mechanism of frames and pairs of slider and rail. The maximum slide distance of each frame relative to the frame immediately beneath is ± 2.54 cm (± 1 inch), and the maximum lateral deformation of the top frame relative to the shake table is 30.5 cm (± 12 inch). After the assembly, the inside dimensions of the laminar shear box are 2.29 m \times 2.13 m \times 1.83 m ($L \times W \times H$). Two protection mechanisms were developed. Two L shape steel plates were welded onto each frame and over travel of each frame more than ± 2.54 cm was prevented. A protection frame was also constructed to prevent the possible flip-out of the box during shaking. A geomembrane bag was used to line the inside the LSB to house the tested specimen. The bag was able to prevent soil and water from seeping out of the box. The geomembrane bag was flexible enough to make sure the soil would govern the system response. The LSB weight was approximately 12.4% of the dry weight of the tested specimen in the box. This ratio is considered to be sufficiently small to neglect the inertial effect of the LSB (Kagawa et al. 2004). The assembly of the shake table and LSB is presented in Figure 3-3.



Figure 3-2. The assembly mechanism of frames and pairs of slider & rail

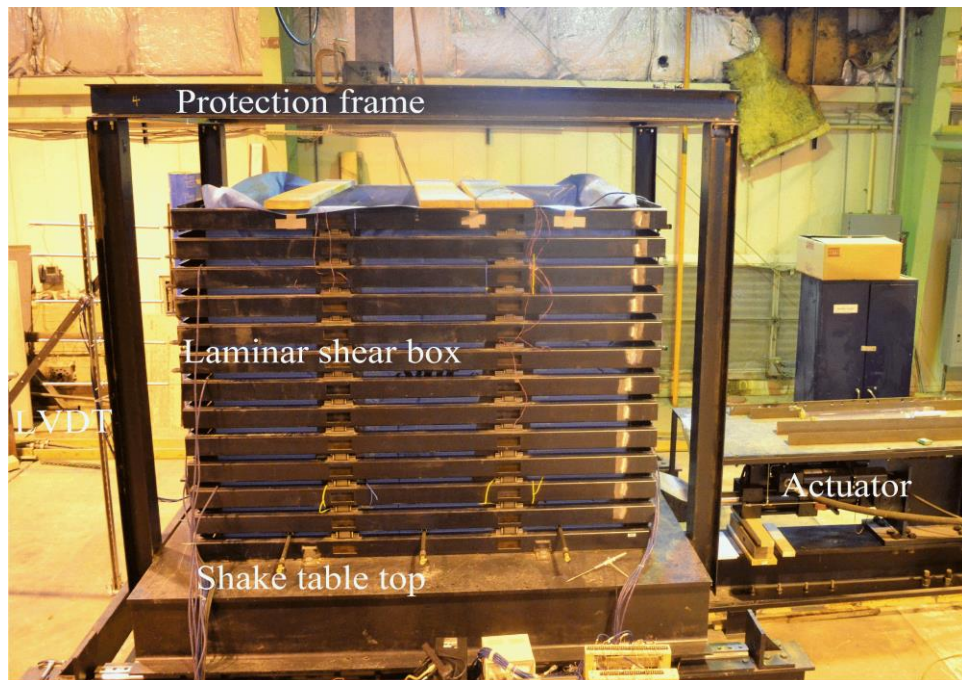


Figure 3-3. The assembly of shake table and LSB

3.1.3 Instrumentation and data acquisition system

Piezometers

As part of the test program, it was necessary to obtain piezometers that could capture the pore pressure variations during shaking. Semiconductor piezometers (model 3400S-2-100 kPa) manufactured by Geokon (Lebanon, New Hampshire) were used in this research and are as shown in Figure 3-4. Geokon Model 3400 Piezometers are intended for dynamic measurements of fluid and/or pore water pressures in standpipes, boreholes, embankments, pipelines, pressure vessels, reservoirs, etc. The output from the transducer used in this research is DC output, 0-5 volts. The pressure measurement range is 0 - 100 kPa and the accuracy is 0.1 kPa. The piezometer is able to tolerate a vibration of 35g at 5 - 2000 Hz.



Figure 3-4. Piezometer by Geokon (Model 3400S-2-100 kPa)

Accelerometers

The accelerometers must be placed in the saturated sand for a long period of time. In addition to being waterproof, the selection criteria for the accelerometers were high sensitivity, DC response, small size, and economy. Piezoelectric ICP accelerometers (model 393A03) manufactured by PCB PIEZOTRONICS (Depew, New York) were selected in this research. Powered by simple, inexpensive, constant-current signal conditioners, these sensors are easy to operate and interface with signal analysis, data acquisition and recording instruments. The measurement range is ± 2 g (peak) and the sensitivity is $\pm 5\%$ of the range. The accelerometer was fixed onto a light plastic plate to make sure that it could be placed horizontally in the sand deposit, as shown in Figure 3-5.

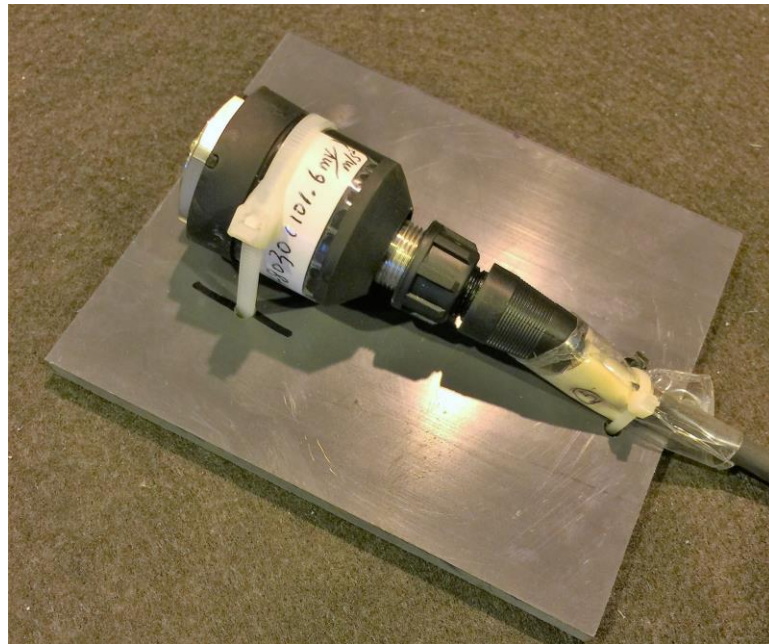


Figure 3-5. Piezometer by PCB PIEZOTRONICS (Model 393A03)

Linear variable differential transformer (LVDT)

In order to measure the displacement of the LSB at different depths and the surface settlement of the sand during shaking, two different types of LVDTs were used. Five LVDTs (Model DC-EC 10000) manufactured by TE Connectivity (Berwyn, Pennsylvania) were selected to measure the movement of LSB frames during shaking, as shown in Figure 3-6. The metal core rod of LVDT can be connected to an LSB frame and the rigidity of the core rod prevents measurement lagging. The measurement range of this LVDT is ± 10 in. (25.4 cm) and the accuracy is 0.25% of its range. This model can tolerate a vibration of 10 g up to 2 kHz.

Another LVDT (Model LD621-100) manufactured by OMEGA (Norwalk, Connecticut) was used to measure the settlement of the sand surface during shaking, shown in Figure 3-7. The measurement range of this LVDT is 0-10 cm, and the accuracy is 0.2% of its range. Both LVDT models require DC excitation and have voltage output.



Figure 3-6. LVDT by TE connectivity (Model DC-EC 10000)



Figure 3-7 LVDT by OMEGA (Model LD621-100)

Data acquisition

Two data acquisition modules (Model 9205 and 9206) manufacture by National Instruments (NI, Austin, Texas) were used as the data processor, shown in Figure 3-8. Both modules are almost identical. They are compatible with any CompactDAQ or Compact RIO system from NI. The features of the modules are: 16 differential analog inputs, 16-bit resolution and a maximum sampling rate of 250 kS/s. These two data processing modules can work simultaneously in recording displacement, acceleration and pressure data during the shake table test at a sampling frequency of 200 Hz. An overview of the data acquisition system and power supply is presented in Figure 3-9.



(a)

(b)

Figure 3-8. Data acquisition modules: a) NI-9205; b) NI-9206

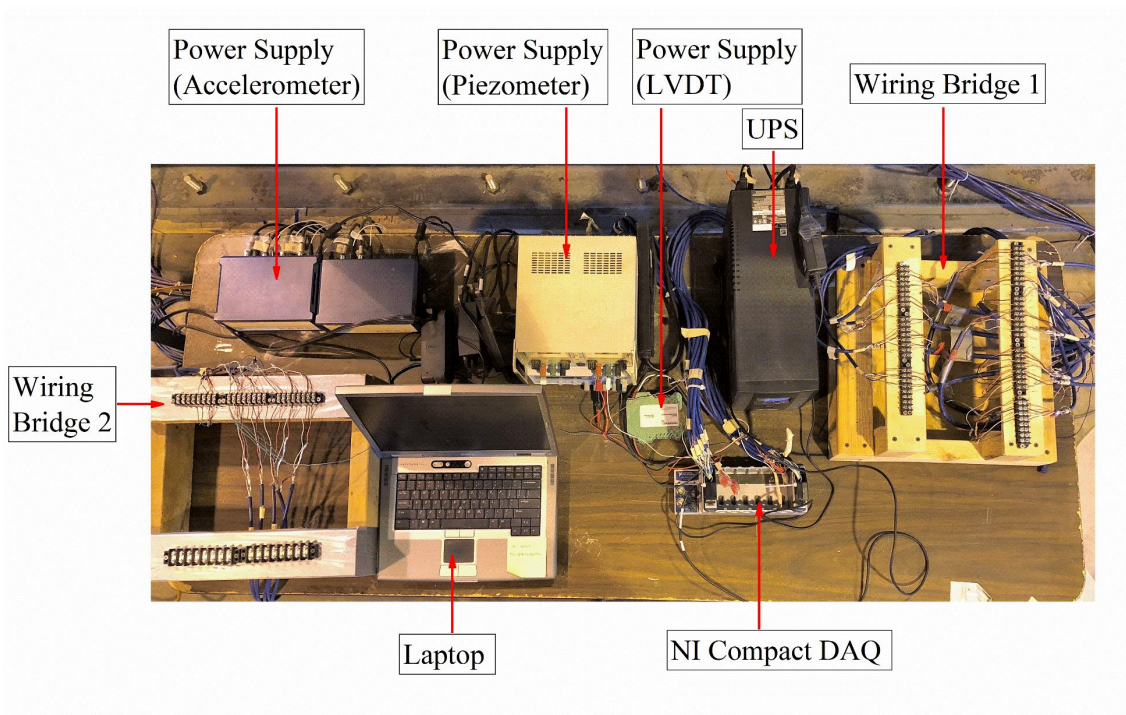


Figure 3-9. Overview of the data acquisition system

A data acquisition interface was developed for the tests using National Instrument LabVIEW 2016. In each test, this program synchronized displacement, acceleration and

pressure data together and allowed data to be written in the same spreadsheet. Calibration and parameter settings can be done on the interface, as shown in Figure 3-10.

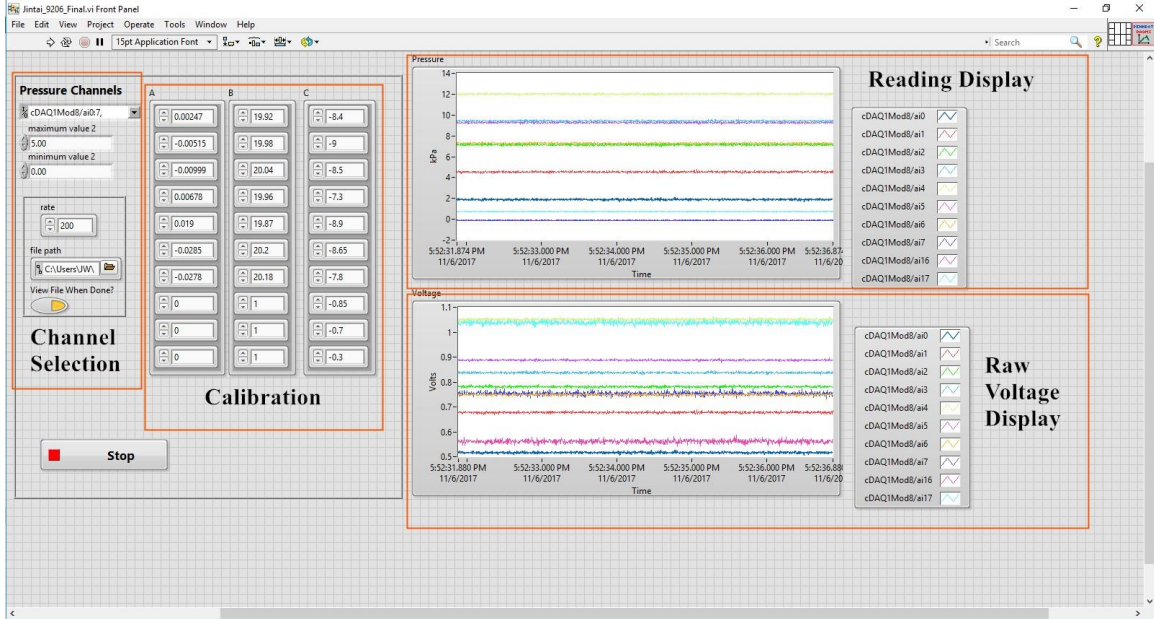


Figure 3-10. User interface of developed LabVIEW program

3.2 Model construction

3.2.1 Soil properties

Standard F50 Ottawa sand was chosen for this research. The measured properties of Ottawa sand were: mean particle size $D_{50} = 0.25$ mm, coefficient of uniformity $C_u = 1.8$, coefficient of curvature $C_c = 0.95$, specific gravity $G_s = 2.65$, maximum void ratio $e_{max} = 0.78$ and minimum void ratio $e_{min} = 0.48$. Direct shear tests suggested the critical state friction angle for the sand was 31.8° . The scanning electron microscope (SEM) image reveals a typical subangular shape for the sand particles, as shown in Figure 3-11.

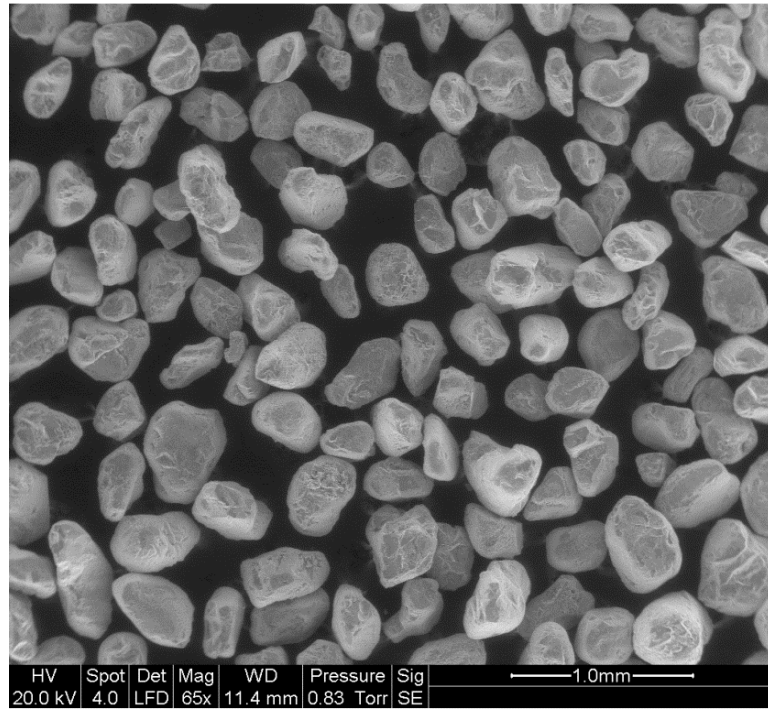


Figure 3-11. SEM image of F50 silica sand at 65x magnification (Kramer 2013)

3.2.2 Sample preparation

The dry sand was air-pluviated into the LSB by a moving pluviator, shown in Figure 3-12. The deposition intensity (i.e., the mass of soil falling per unit area per unit time) and the drop height (the distance between the pluviator bottom to the sand surface) were strictly controlled to achieve a uniform sand profile with an average relative density of 55%. According to the relative density calibration curve shown in Figure 3-13, the drop height was controlled at 26 cm during the pluviation to achieve the target relative density. As suggested by Fretti et al. (1995), crossing the moving direction of the pluviator from one stratum to another would produce higher-quality specimens than using one direction of

travel. Two travel paths were alternatively followed by the pluviator, as shown in Figure 3-14.



Figure 3-12. Uniform deposition of sand as it passes through the pluviator system

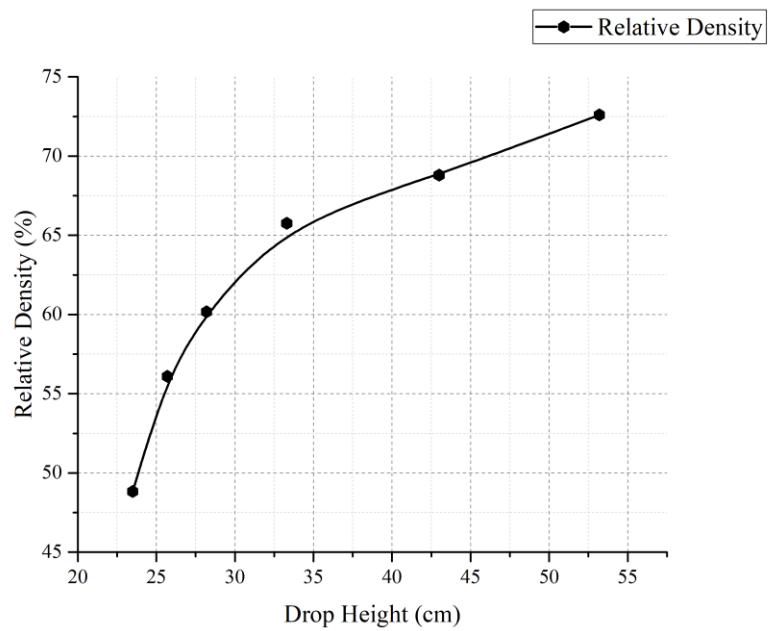
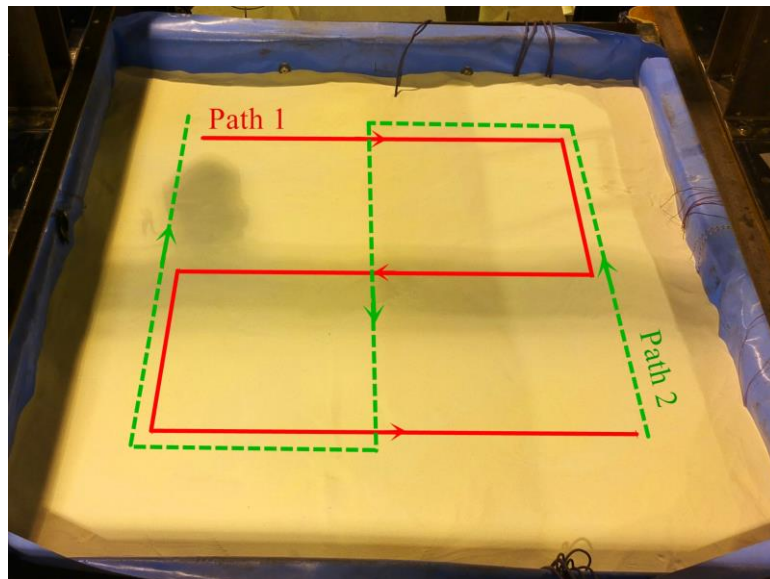


Figure 3-13. Relative density calibration curve



(a)

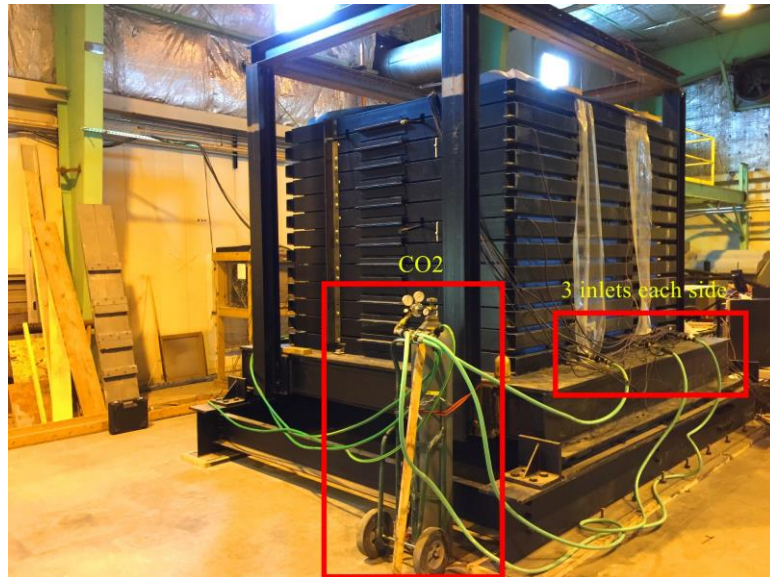


(b)

Figure 3-14. Pluviation process: a) pluviator in laminar shear box b) paths alternatively followed by the pluviator

Immediately after the pluviation, the soil was flushed with CO₂ from the bottom of the LSB for 24 hours, as shown in Figure 3-15 (a). The purpose of using CO₂ was to facilitate full saturation. After the CO₂ flushing, water was introduced from six inlets on

the geomembrane bag at the bottom at a slow flow rate and exited from the outlets at the top surface of the sand, as shown in Figure 3-15 (b). The saturation stage lasted 22 days. The volume of water collected at the outlets was 7.89 m³, over 2.5 times of the void volume of the dry sand.



(a)



(b)

Figure 3-15. Sand saturation: a) CO₂ flushing b) water saturation

3.2.3 Test instrumentations

Piezometers (PZ-1 to PZ-5) were installed at every 25-cm lift to measure the excess pore pressure during shaking. To minimize the boundary effect on the soil liquefaction and instruments' readings, the instrumentation array was set at the center of the LSB. This setup of the instrumentation is commonly used in physical modeling of liquefaction (Abdoun et al. 2013; EI-Sekelly et al. 2016). Two duplicate piezometers (PZ-6 and PZ-7) were placed 508 mm away from the center line at two depths. Five LVDTs (LVDT-1 to LVDT-5) were installed on a rigid frame adjacent to the shake table. The metal core rod of LVDT was connected to a LSB frame and the rigidity of the core rod prevented measurement lagging. The designed instrumentation configuration is shown in Figure 3-16.

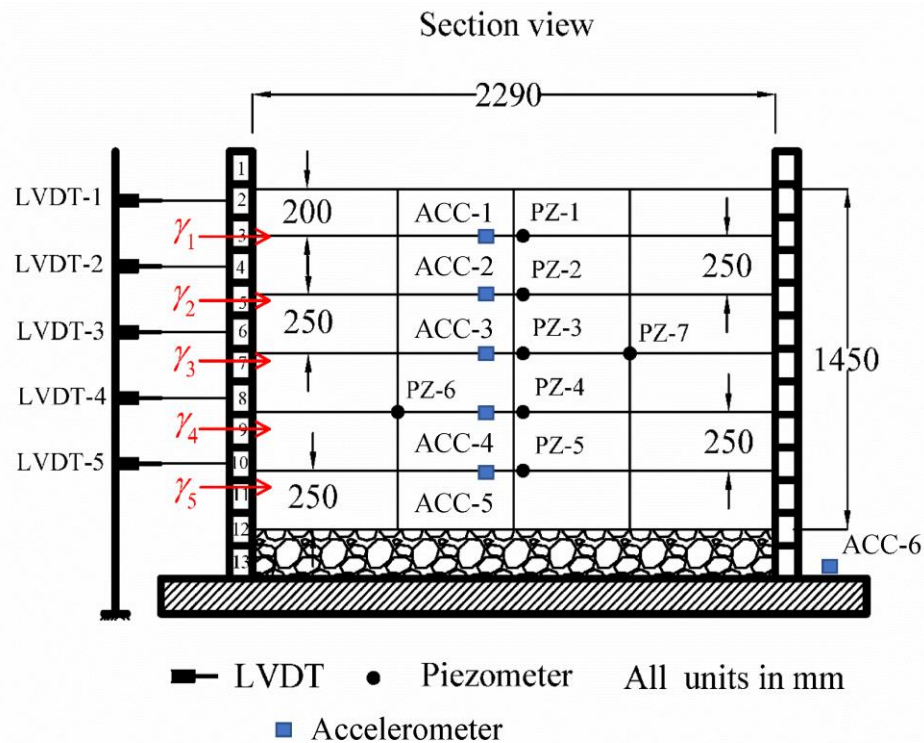


Figure 3-16. Instrumentation configuration in the shake table testing (section view)

The installation of two piezometers and one accelerometer is shown in Figure 3-17. It is worth mentioning that each piezometer has two fixing wires which would prevent sensors dropping during shaking. However, fixing wire cannot be applied to accelerometer because it might constrain the movement of accelerometer. The installation of five LVDTs on the side and top LVDT is shown in Figure 3-18.

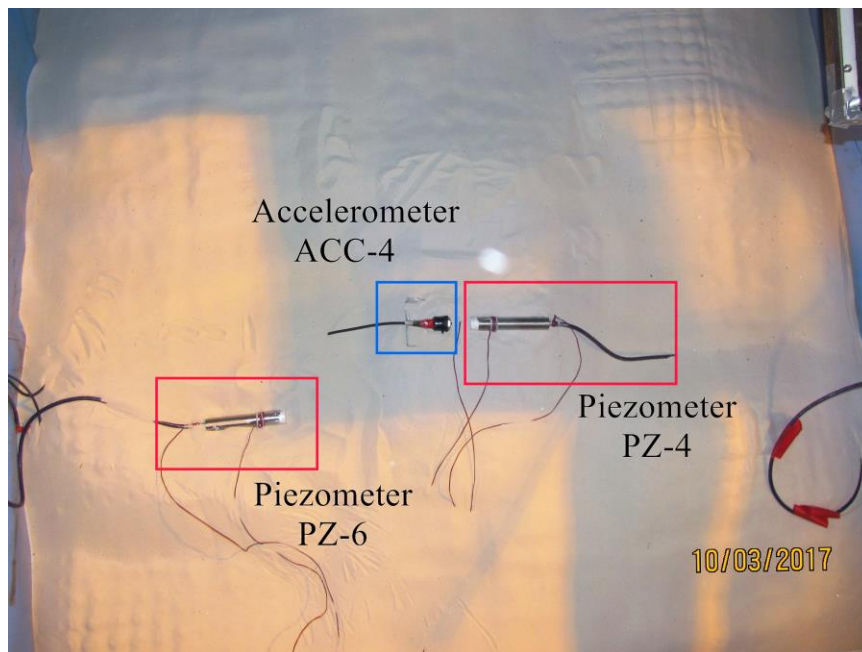
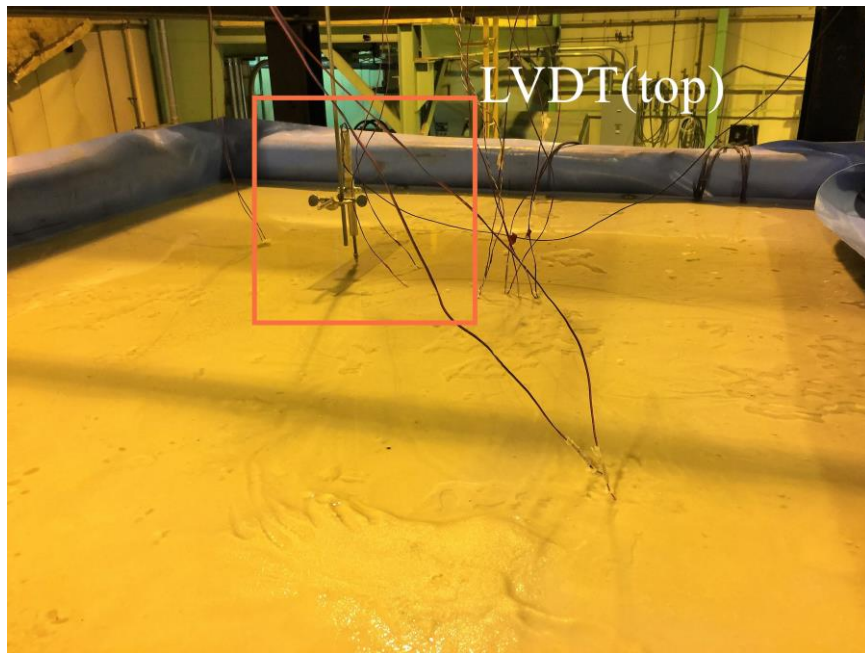


Figure 3-17. Installation of piezometer and accelerometer



(a)



(b)

Figure 3-18. Installation of LVDTs for shake table test: (a) LVDTs for LSB (b) LVDT for settlement

3.3 Input motion for shake table test

The shaking event was defined as 21 sinusoidal cycles of a maximum base acceleration of 0.25 g at 1 Hz. Two ramp-up and ramp-down cycles were added to make sure the smooth start and ending of the shake table system. Figure 3-19 shows that the measured table displacement and the input command of the actuator were almost the same, which indicates satisfactory performance of the actuator during the shaking.

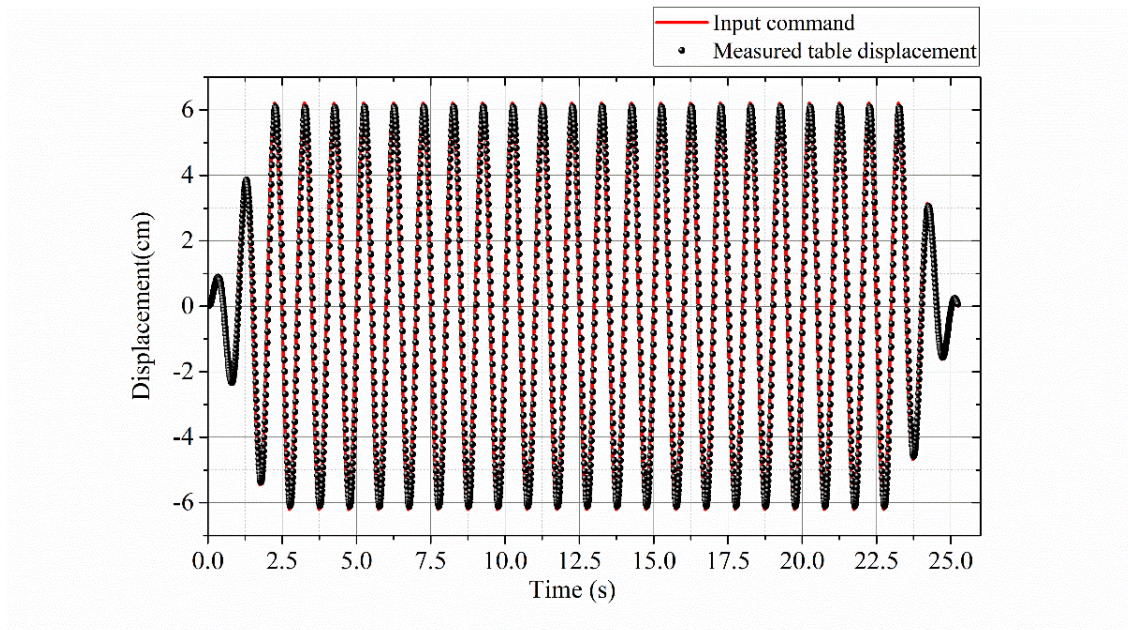


Figure 3-19. Comparison between the recorded table movement and input command for actuator

3.4 Shake table test results (1st shaking)

3.4.1 Pore pressure readings

Figure 3-20 presents the pore pressure generation during shaking and pore pressure dissipation after shaking measured by five piezometers located at five different depths. The

pore pressure data were recorded at 200 Hz. A clear excess pore pressure build-up was observed during the shaking event. After the shaking ended, a small increase of pore pressure was observed and then the excess pore pressure dissipated. 95 s after shaking, the excess pore pressure was gone. There was a slight increase of the static pore pressure at the end. The sensors might drop a bit (2-3 cm) because of the occurrence of liquefaction and sand strength loss. With the help of fixing wires, the settlement of piezometers due to soil settlement was minimized.

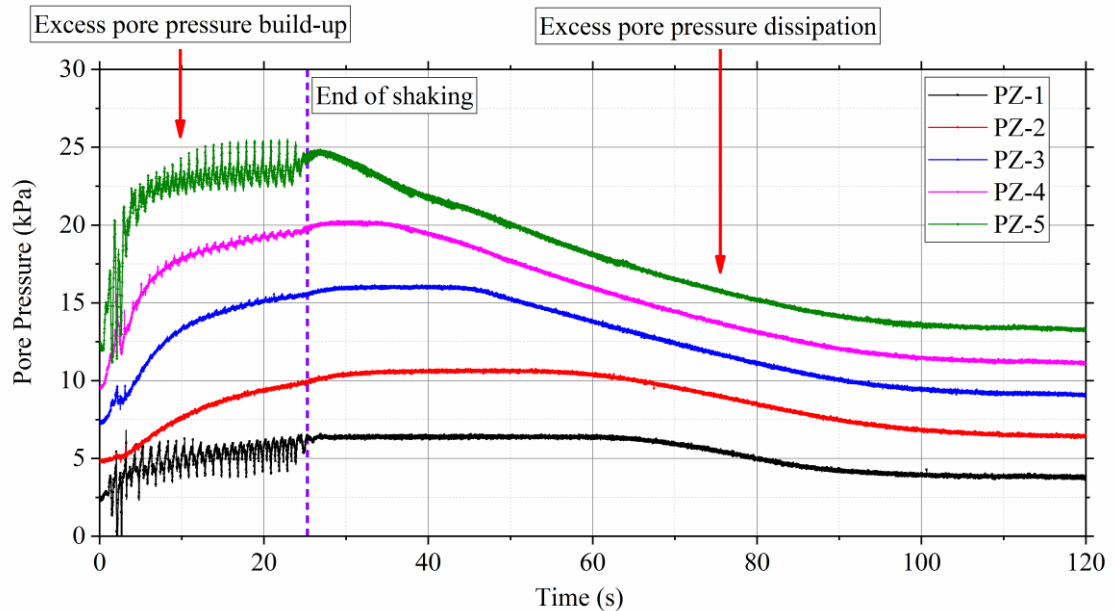


Figure 3-20. Pore pressure readings at different depths

To further look at the pore pressure generation, Figure 3-21 presents the pore pressure readings at the first 25s. A locally weighted scatterplot smoothing (LOWESS) was applied to the raw data. The solid lines in Figure 3-21 were the results after smoothing. In this research, liquefaction is defined by a pore pressure ratio $r_u = 1$, which means the excess pore pressure is equal to the initial vertical effective stress. The pore pressure of sand at

different depths all rapidly increased after the two ramp-up cycles. The pore pressure reading from PZ-1 suggested that the sand near the top liquefied at 8 seconds. PZ-2 suggested that the sand at this depth liquefied at 23 seconds. PZ-3 showed a similar pore pressure increase trend as PZ-4 and the sand at these two depths liquefied at around 20.5 seconds. The sand near the bottom of the sample had a rapidly increased pore pressure within the first 5 seconds and eventually liquefied at 25 seconds. The pore pressure readings from duplicate piezometers (PZ-6 and PZ-7) were almost the same as the readings from the piezometers in the middle (PZ-4 and PZ-3), thus were not included in Figure 3-20 for the sake of clarity. Overall, the pore pressure readings indicate the occurrence of liquefaction for the whole sand deposit.

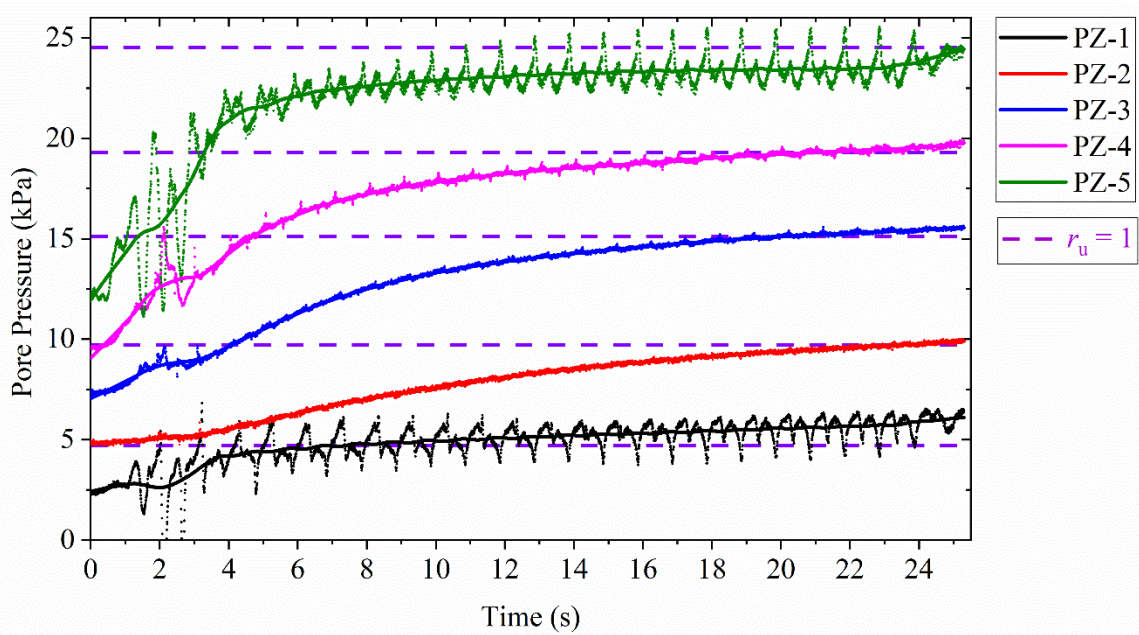
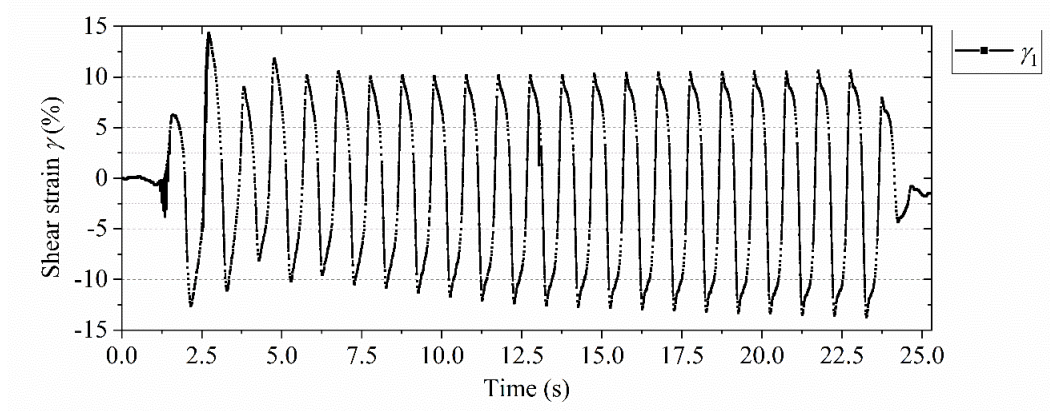


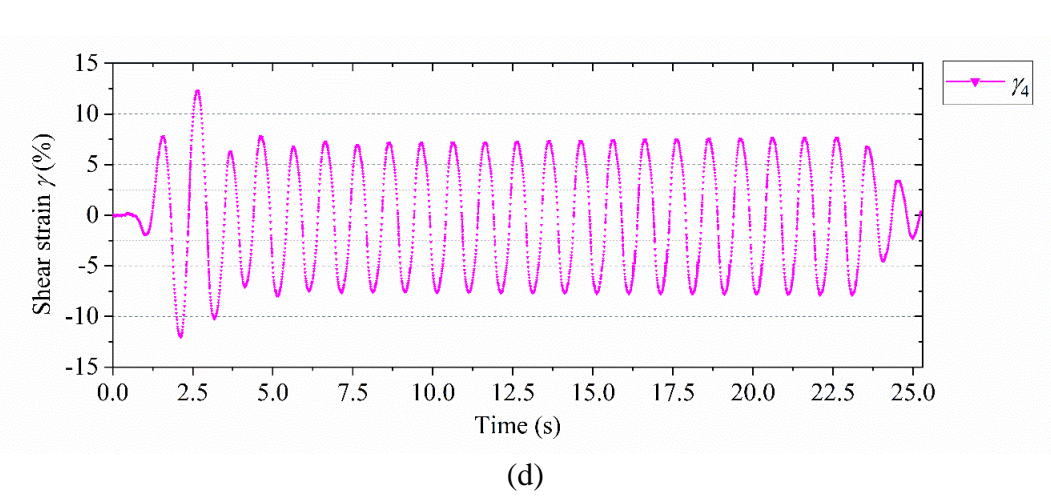
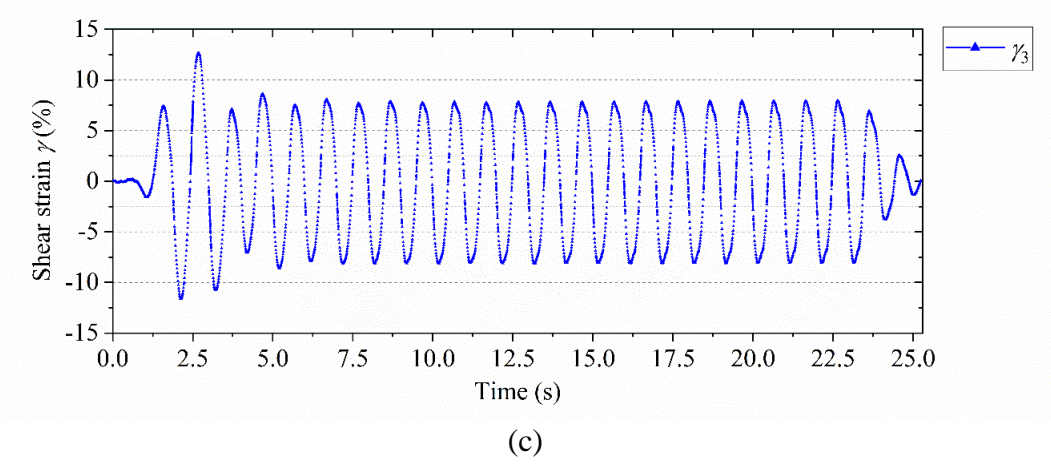
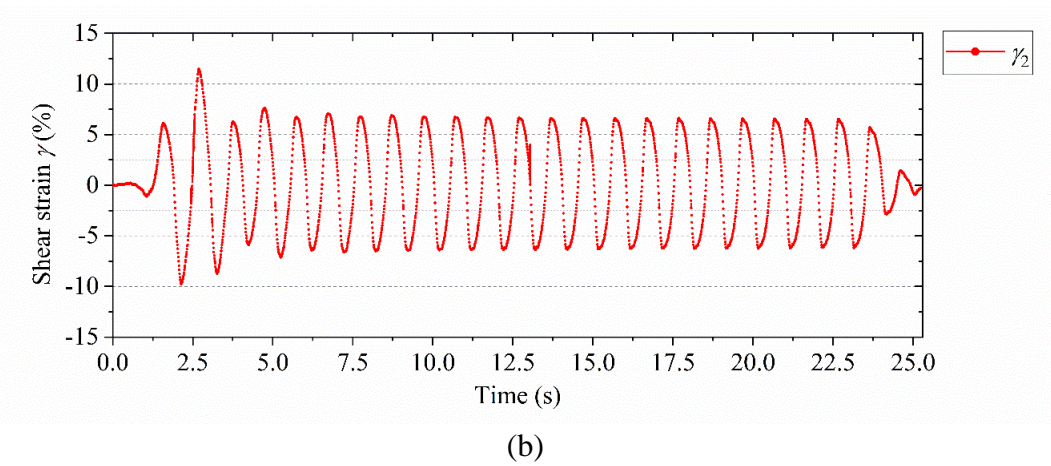
Figure 3-21. Pore pressure generation during shaking at different depths

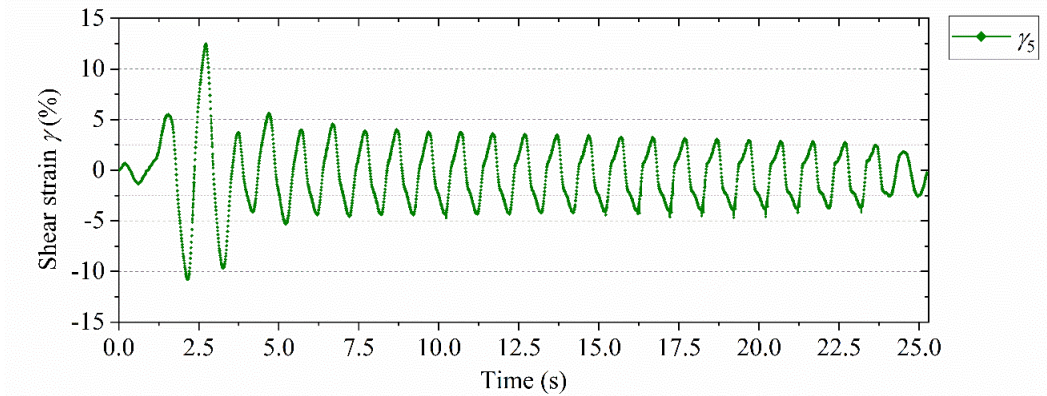
3.4.2 Shear strains

The cyclic shear strains (γ) of the soil induced by the shaking are shown in Figure 3-22. The shear strain was calculated using the LVDT readings. For example, γ_1 was calculated by the relative displacement between LVDT-1 and LVDT-2, and thus it represented the average shear strain for the sand between LVDT-1 and LVDT-2. Figure 5 suggested that all the shear strains increased rapidly as the shaking started and kept relatively constant amplitudes after 4 seconds. The shear strain amplitudes were consistent with the pore pressure readings from Figure 4. The sand at PZ-1 had the highest shear strain amplitude (more than 10%); hence, this depth liquefied first. The sand at PZ-5 had the smallest shear strain amplitude (4%); hence, this depth liquefied last. The sand at PZ-3 and PZ-4 had similar shear strain amplitude (7.5%) but slightly larger than that at PZ-2 (6.8%); hence, the sand at PZ-3 and PZ-4 liquefied at about same time and earlier than the sand at PZ-2. The results showed a correlation between pore pressure ratio and cyclic shear strain.



(a)



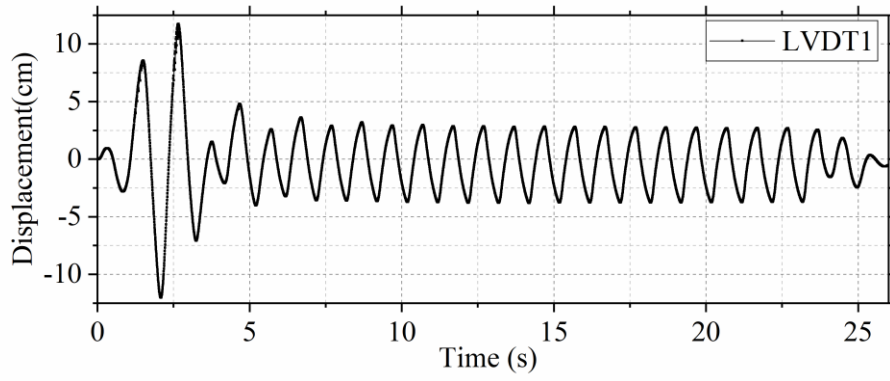


(e)

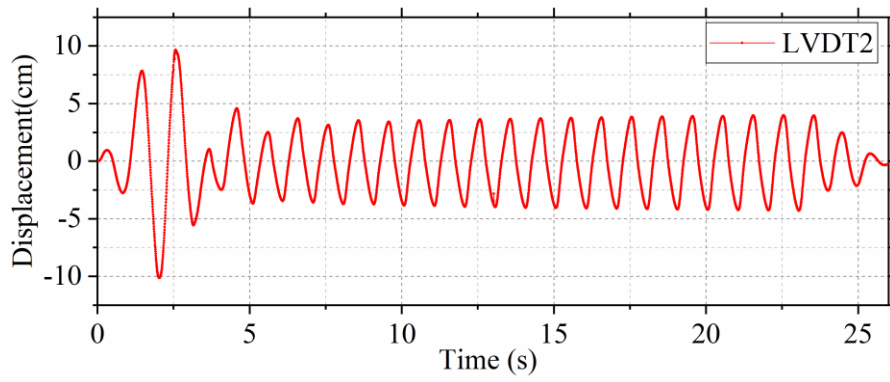
Figure 3-22. Cyclic shear strain during shaking at different depths: (a) $D = 0.2$ m (b) $D = 0.45$ m (c) $D = 0.7$ m (d) $D = 0.95$ m (e) $D = 1.2$ m

3.4.3 Lateral displacement

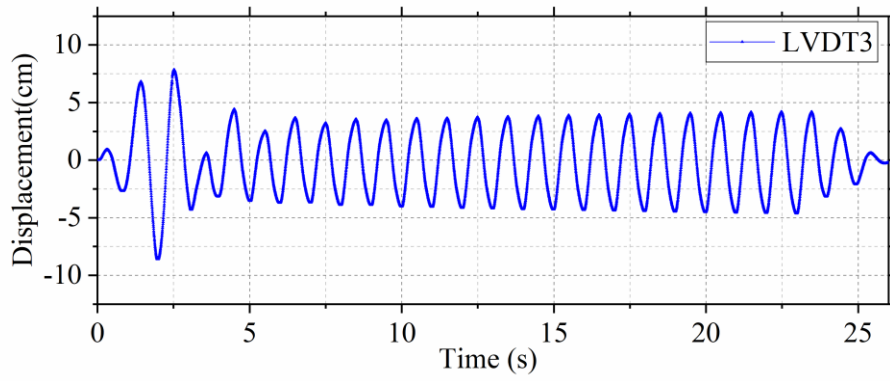
The absolute lateral movement time histories of different LSB frames are shown in Figure 3-23. The lateral movement of 10th frame (LVDT-5) was very similar to that of the table, as the location of this frame is close to the table top. The 8th frame (LVDT-4) had slight amplification at the first three cycles and kept an averaged amplitude of 5 cm. The 6th frame (LVDT-3) had more obvious amplification at the first three cycles and kept an averaged amplitude of 3.8 cm. The 4th frame (LVDT-2) had obvious amplification at the first three cycles and kept an averaged amplitude of 3.6 cm. The 2nd frame (LVDT-1) had large amplification (11.8 cm) at the first three cycles and kept an averaged amplitude of 2.7 cm.



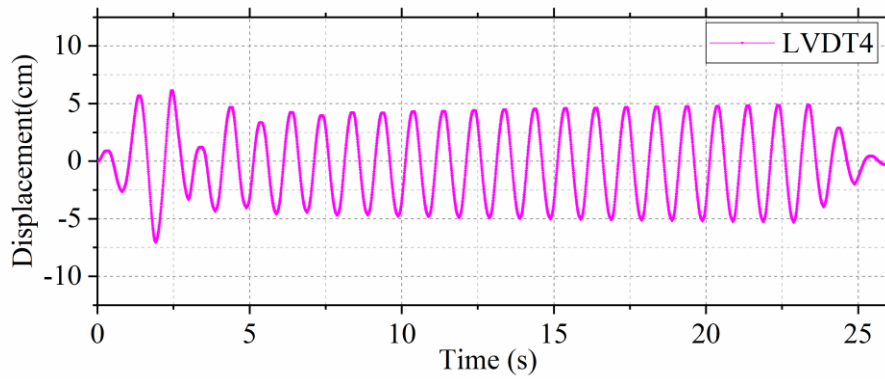
(a)



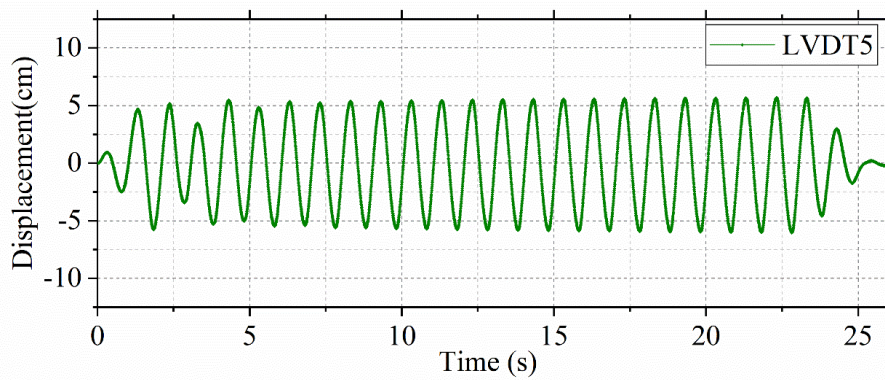
(b)



(c)



(d)



(e)

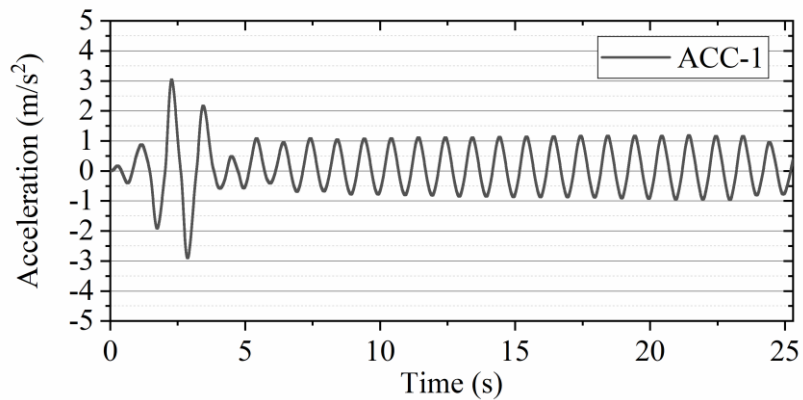
Figure 3-23. Absolute lateral movement time histories of different LSB frames (a) 2nd frame (b) 4th frame (c) 6th frame (d) 8th frame (e) 10th frame

3.4.4 Acceleration

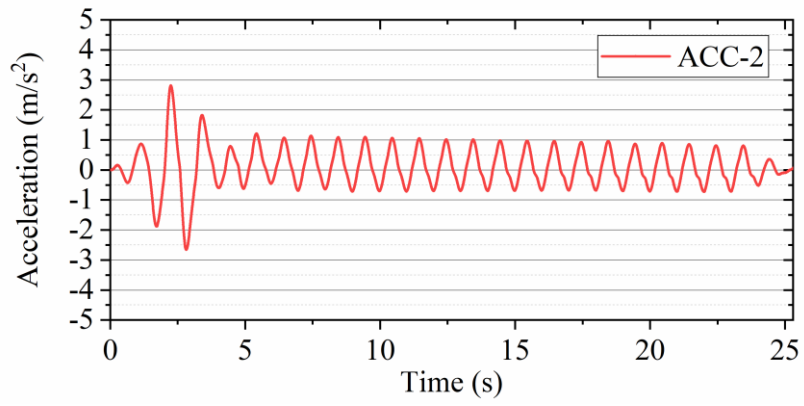
The acceleration time histories of sand at different depths are shown in Figure 3-24. The recorded signals were filtered using a 3rd order, 60 Hz Butterworth filter. This filtering was employed in a series of shake table testing by Wartman (1996). The filtered shake table acceleration recordings, as shown in Figure 3-24 (f), were consistent with the actuator feedback presented in Figure 3-19. In general, the acceleration recordings had a similar trend captured by LVDTs on the LSB. A major amplification in the first three cycles was observed at shallow depths (ACC-1, ACC-2 and ACC-3). After that, the accelerations

of the sand at these three depths kept an average amplitude of 0.1g. The average acceleration amplitudes measured by ACC-4 ($D = 0.95$ m) and ACC-5 ($D = 1.2$ m) were 0.16g and 0.21g, respectively. In general, from the bottom to the top of the soil specimen, a deamplification trend was observed. This can be explained by the liquefaction as follows.

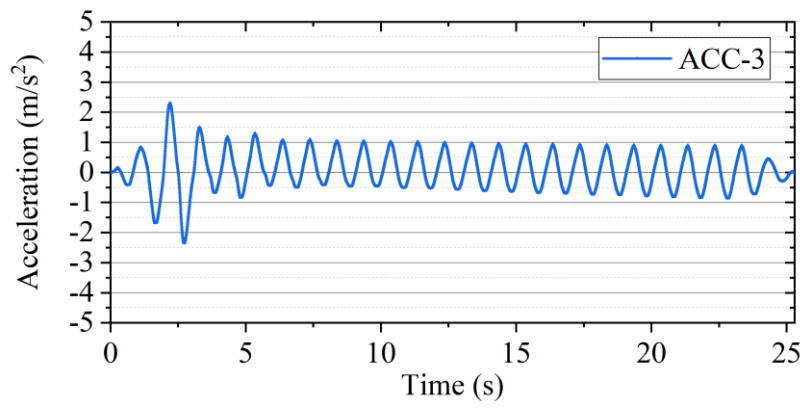
In the first several cycles, the excess pore pressure due to shaking was still small. The sand was able to maintain most of its stiffness, so that an acceleration amplification was observed at shallow depths. However, with the development of positive excess pore pressure, the soil stiffness decreased quickly and dramatically. The shake table motion cannot be transmitted to the sand surface anymore. A de-amplification of the acceleration was observed. Kramer (1996) suggested that the amplitude and frequency content of the surface motion may change considerably throughout the earthquake due to liquefaction. The development of very high pore pressures can cause the stiffness (and strength) of even a thin layer to be so low that the high-frequency components of a bedrock motion can be filtered by this layer (Kramer 1996). In this research, the frequency content of input motion is simple (1 Hz). A change of frequency content due to liquefaction was not observed. The amplitude change, however, was consistent with the evidence suggested by Kramer (1996).



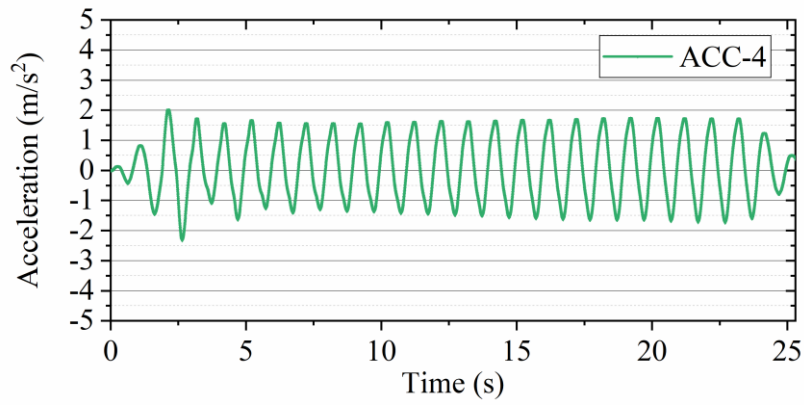
(a)



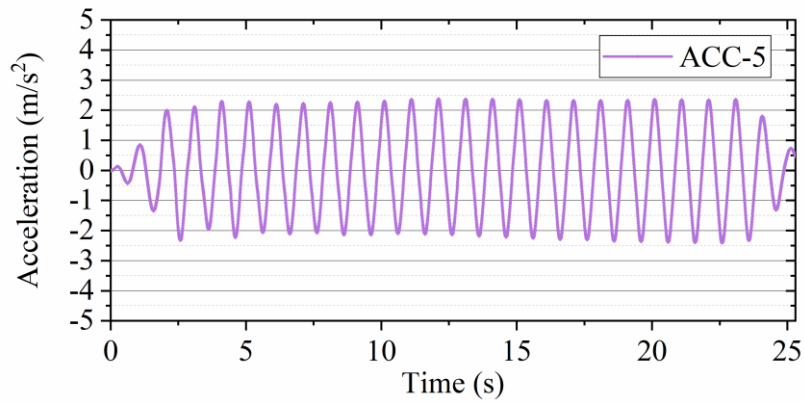
(b)



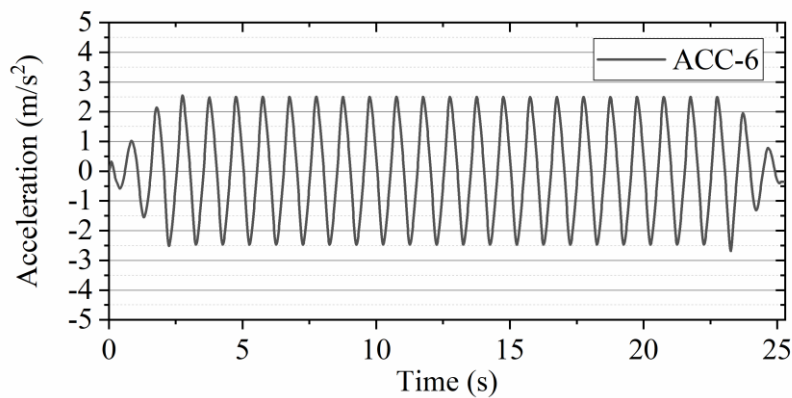
(c)



(d)



(e)



(f)

Figure 3-24. Acceleration time histories during shaking at different depths: (a) $D = 0.2$ m (b) $D = 0.45$ m (c) $D = 0.7$ m (d) $D = 0.95$ m (e) $D = 1.2$ m (f) Shake table

3.4.5 Settlement

The surface settlement time histories from the top LVDT are shown in Figure 3-25. The surface did not settle in the first two seconds. After that, the settlement rate increased, and a final settlement of 4.25 cm was observed. A large fluctuation was observed in the test. This might be due to the plastic plate which was placed between the top LVDT rod and sand surface in the shake table test. The rocking of the plate during shaking may result in significant fluctuation in LVDT measurement.

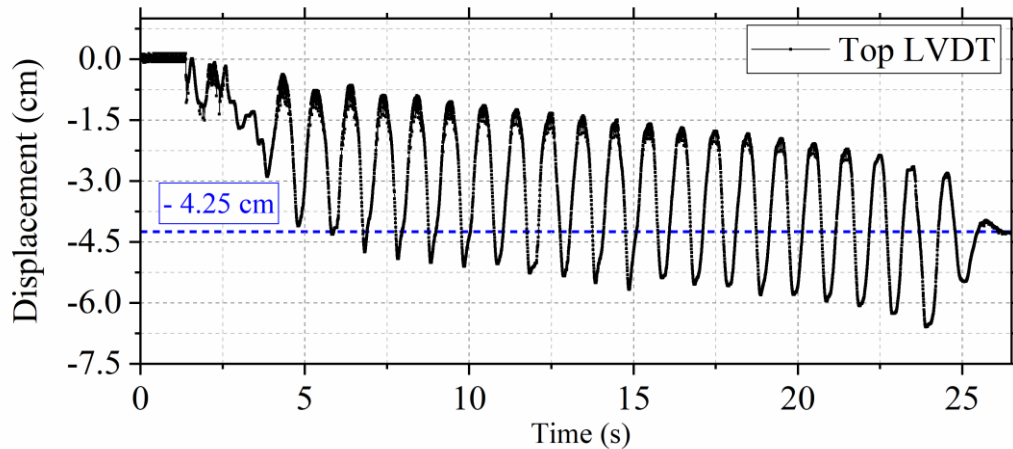


Figure 3-25. Surface settlement time histories from top LVDT during shaking

3.5 Conclusion and summary

The following conclusions and summary are based on the data, analysis and interpretation presented in this chapter.

1) The shake table has a satisfactory performance for a sinusoidal input motion with 0.25g-amplitude at 1 Hz.

2) The sand generates excess pore pressure during shaking event. The excess pore pressure starts to dissipate after the shaking ends. It takes about 95s for a total dissipation of excess pore pressure.

3) The pore pressure readings indicate the occurrence of liquefaction for the whole sand deposit. The sand near the top liquefies first (8 s) and the sand near the bottom liquefies last (25 s). The sand in between liquefies between 20.5 s to 23 s.

4) A correlation can be found between pore pressure ratio and cyclic shear strain. The sand that liquefies first shows the largest shear strain amplitude. The sand that liquefies last has the smallest shear strain amplitude.

5) Both amplification in the first 3 cycles and de-amplification after the first 3 cycles of acceleration in the soil deposit were observed in the test. The development of positive excess pore pressure can decrease the soil stiffness. The change of soil stiffness can alter the acceleration response of the soil.

Chapter 4

Time-Dependent Cone Penetration Resistance of a Post-Liquefaction Sand Deposit at Shallow Depth

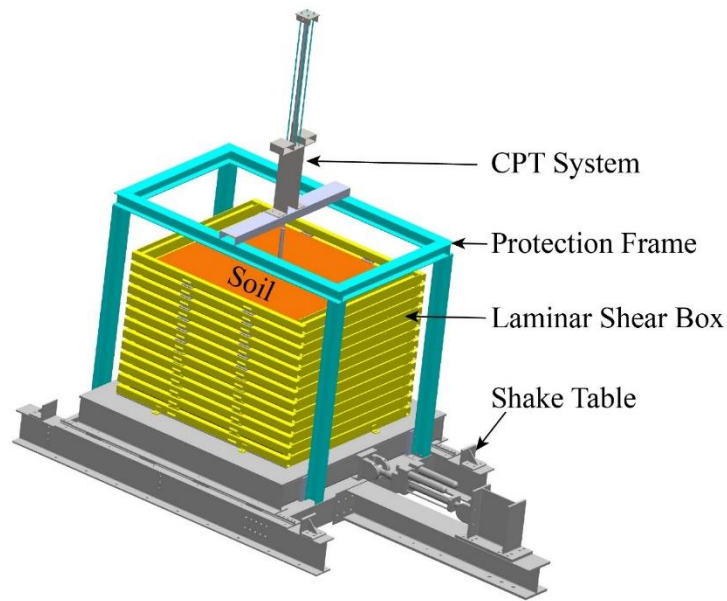
This chapter presents a series of piezo-cone penetration testing (CPTu) performed on the liquefied sand deposit from the shake table test presented in Chapter 3. The cone penetration resistance, friction resistance, and pore water pressure throughout the depth of the post-liquefaction sand deposit were measured during the CPTu. To capture the sand aging effect after liquefaction, CPTu tests were done at different locations over a total elapsed time of 135 days. The main findings of this chapter are: (1) The cone penetration resistance of the sand deposit decreased significantly immediately after liquefaction when compared with that before liquefaction; (2) the cone penetration resistance of the post-liquefaction sand deposit increased with time; a relationship between cone penetration resistance and time at different effective stresses is proposed, (3) the CPTu results were normalized with respect to effective overburden stress and the relationship between normalized CPTu results of the post-liquefaction sand deposit and time is proposed.

4.1 CPTu test

4.1.1 CPTu test design and implementation

Piezo-cone penetration testing (CPTu) was used to evaluate the liquefaction resistance of the sand deposit. In the field, the CPT or CPTu test is usually done using a

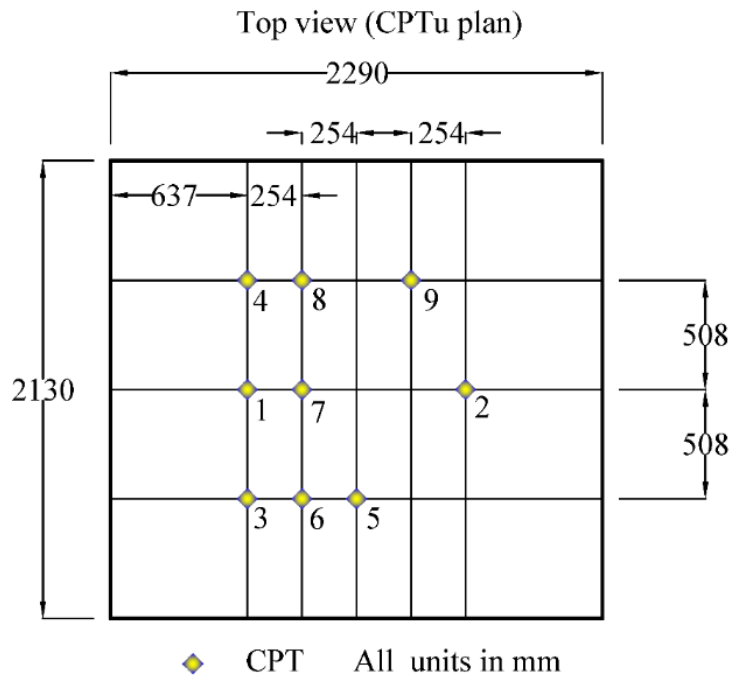
truck-based CPT push system. In this research, a customized CPTu push system was designed, built, and mounted above the LSB. As shown in Figure 4-1 (a), a reaction frame was anchored on top of the protection frame and housed a hydraulic piston, a rod and a CPTu cone (Geonor, Inc., Augusta, NJ) with a diameter of 31 mm. The hydraulic piston (Model CHIEF WC 3000, BAILEY HYDRAULICS, Knoxville, TN) and mounting system were designed and constructed to push the rod and CPTu cone into the soil at a constant speed of 1.5 cm/s for 1.27 m. The reaction frame can be bolted onto a C-channel at three different locations. By moving the C-channel on the protection frame and moving the reaction frame on the C-channel, it was possible to perform CPTu tests at different locations on the sand deposit. Figure 4-1 (b) presents the CPTu test operation.



(a)



(b)



(c)

Figure 4-1. CPTu test: (a) CPTu design illustration; (b) CPTu in operation; (3) CPTu plan view

A total number of 9 CPTu tests were planned and conducted for the soil deposit within the laminar shear box. Yang (2006) suggested the influence zone for end bearing piles in clean sand is between 1.5 and 2.5 D , where D is pile diameter. The diameter of the

CPTu cone used in this study is 31 mm. The influence zone should be between 46.5 mm and 77.5 mm. In the experimental design for this project, the spacing between each CPTu was at least 254 mm. Moreover, the CPTu cone and rod are made of stainless steel and have smoother surface compared with piles. Overall, the design is conservative enough to make sure each CPTu test is affected by others. The detailed plan for the nine CPTu locations is summarized in Figure 4-1 (c).

4.1.2 Time schedule of CPTu tests

Anderson and Stokoe (1978) reported that the low-amplitude shear modulus of soil increased approximately linearly with the logarithm of the time after primary consolidation, this was referred to as the long-term time effect. In this research, a similar time schedule for testing was adopted. The CPTu after shaking was designed to span a period from 10 mins to 2×10^5 mins. Considering the time required for preparation and installation of CPTu system immediately after shaking, 10-minute CPTu was the earliest test that can be realistically conducted. The subsequent tests were designed to be conducted at 10, 40, 1500, 30000, 50000, 100000 and 200000 mins. The actual time after liquefaction for tests were 10, 39, 1600, 33167, 51810, 100726 and 194553 mins due to the limitation of working schedules. The CPTu testing time is summarized in Table 4-1.

Table 4-1. CPTu testing time schedule

Event	CPT-Data Log	Time after liquefaction(mins)	Time after liquefaction (days)
Before liquefaction	CPT-1	N/A	N/A
	CPT-2	N/A	N/A
After liquefaction	CPT-3	10	0.007
	CPT-4	39	0.027
	CPT-5	1600	1.111
	CPT-6	33167	23.033
	CPT-7	51810	35.979
	CPT-8	100726	69.949
	CPT-9	194553	135.106

4.2 Cone resistance variation before and after liquefaction with time

4.2.1 CPT results before shaking

For CPTs in liquefaction applications, the measured cone resistance (q_c) requires correction because of unequal end area effects (Campanella et al. 1982) as:

$$q_t = q_c + (1 - a_r) u_2 \quad (4-1)$$

where q_t = the corrected cone resistance, a_r = area ratio for the cone tip (0.85 used in this research), and u_2 = measured pore pressure behind the cone tip. The measured cone resistance in this research was corrected using Equation 4-1.

The friction ratio is defined as the percentage of sleeve friction, f_s , to cone resistance, q_t , at the same depth.

$$R_f = (f_s / q_t) \times 100\% \quad (4-2)$$

The results from CPT-1(before liquefaction) are shown in Figure 4-2. The cone resistance increased with depth until 0.9 m and then maintains around 800 kPa to a depth of 1.27 m where the push ended. The sleeve friction is small with a maximum value less than 4 kPa. The friction ratio is less than 1%. The measured pore pressure during penetration is approximately equal to the static pore pressure, which confirms the full saturation of the soil profile and reliability of pore pressure measurement. Both the friction ratio and pore pressure reading indicate that the soil profile is clean sand (Robertson 1990; Robertson and Cabal 2015), which is consistent with the properties of Ottawa sand used in this research.

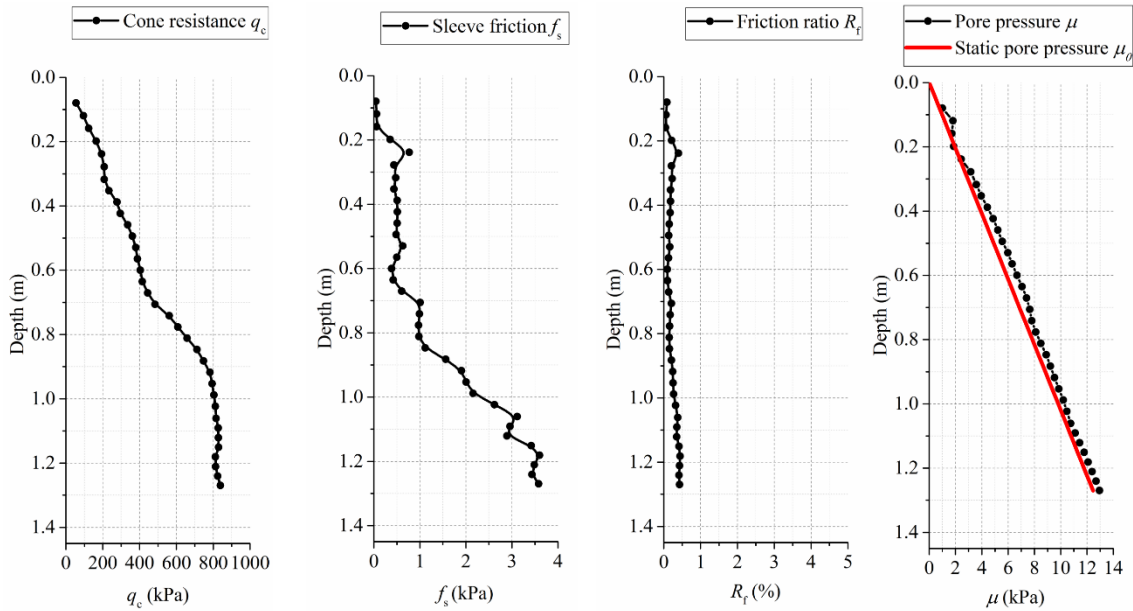


Figure 4-2. CPTu results for CPT-1 (before liquefaction)

4.2.2 Pre- and post-liquefaction cone resistance variation

To investigate the effect of liquefaction on the strength of the soil, the cone tip resistance values of sand before and after liquefaction were compared. Both CPT-1 and

CPT-2 were conducted 1 day before shaking at different locations. As shown in Figure 4-3, the CPT-1 and CPT-2 have similar cone resistance readings at similar depths, indicating that the sample preparation (sand pluviation) is consistent at different plan view locations. CPT-3 was performed 10 mins after shake table testing. The cone resistance measured by CPT-3 decreased compared with the pre-liquefaction cone tip resistance. After liquefaction, the cone resistance was reduced by 40.3%, 43%, 52.9% and 51.5%, at the depth of 0.4 m, 0.6 m, 0.8 m, and 1.0 m, respectively. On average, liquefaction reduced the cone resistance of the sand by 50%. This observation of cone resistance decrease is consistent with Ha et al. (2011). Ha et al. (2011) presented a series of shake table tests and found out the liquefaction resistance of the sand decreased significantly from the 1st to the 2nd shaking event (sand liquefied in 1st shaking), despite the increase in relative density. Oda et al. (2011) suggested that the soil undergoes large shear strain during liquefaction (> 2 - 3%), which creates a highly anisotropic, column-like structure that is highly unstable in the major principle stress direction.

Charlie et al. (1992) reported a 62% tip resistance decrease due to blasting and concluded that the natural sand deposits have an existing structure that is destroyed by the disturbance due to blasting. The 62% tip resistance decrease from Charlie et al. (1992) is comparable to the 50% decrease in this study, which indicates that both blasting and liquefaction due to shaking have extensively disturbed the soil. This comparison is interesting because blasting has been used effectively to densify cohesionless and saturated soil as a ground improvement method (Charlie et al. 1992), while liquefaction is considered as an unwelcome phenomenon. The cone resistance decrease observed in this study is a

strong evidence that the liquefaction has destroyed (at least partially) the original soil structure formed in deposition.

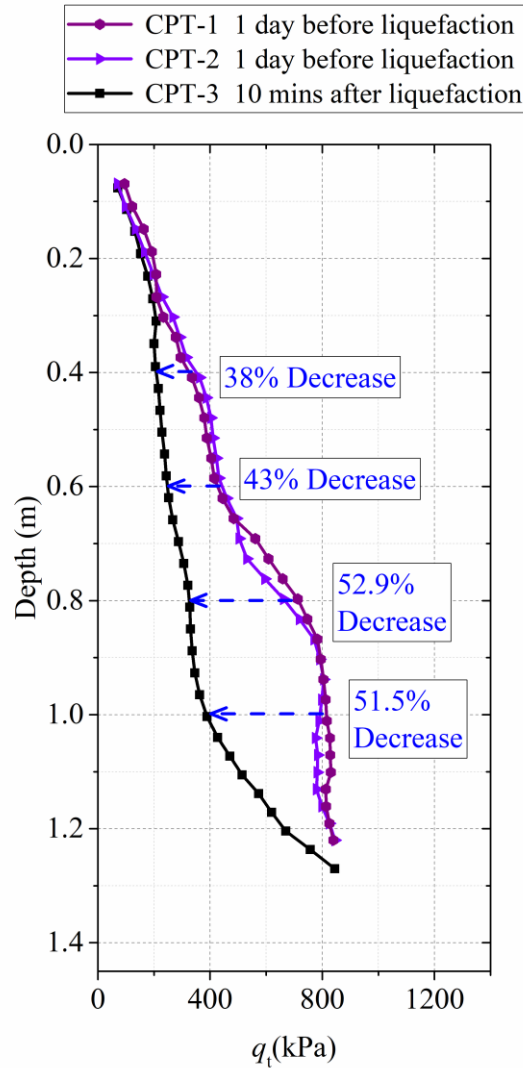


Figure 4-3. Cone resistance variation before and after liquefaction

4.2.3 Post-liquefaction cone resistance gain with time

After liquefaction, a total of seven CPTu tests (CPT-3 to CPT-9) in a span of 135 days were performed to investigate the effect of time after liquefaction on sand strength.

Figure 4-4 summarizes the cone resistance of all the CPTu tests conducted after liquefaction. From the results of CPTu tests of CPT-3 to CPT-9, the data clearly indicate that the sand deposit was gaining strength with time at all depths. All the seven curves were replotted in cone resistance contours with both depth and time and shown in Figure 4-5. From the contour plot, the smallest q_t value happens at the top left corner with the shallowest depth and shortest time. As the time and depth increase, the q_t also increases. The bottom right corner represents the maximum depth and time, which also has the maximum value of cone resistance. The relatively consistent color changing from top left corner to bottom right corner demonstrates that the cone resistance q_t varies with both effective overburden stress and time.

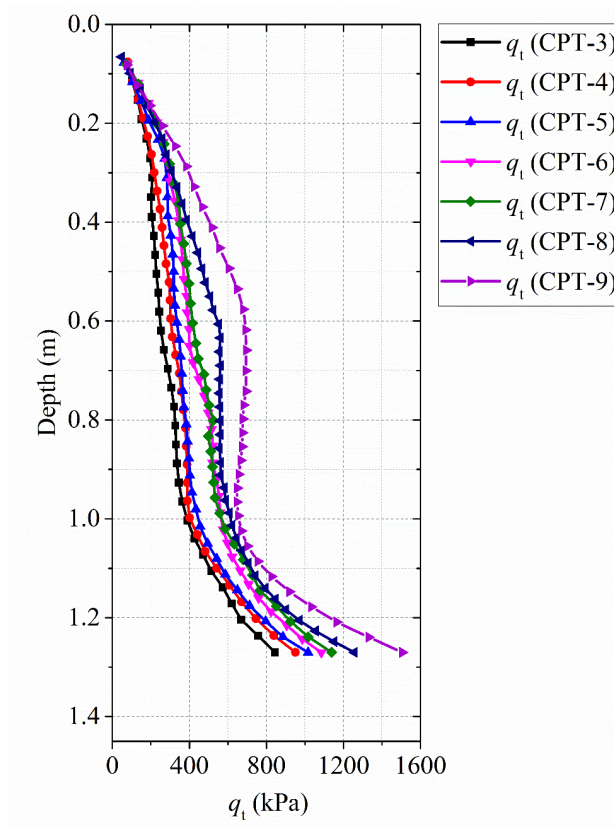


Figure 4-4. Cone resistance of CPT-3 to CPT-9

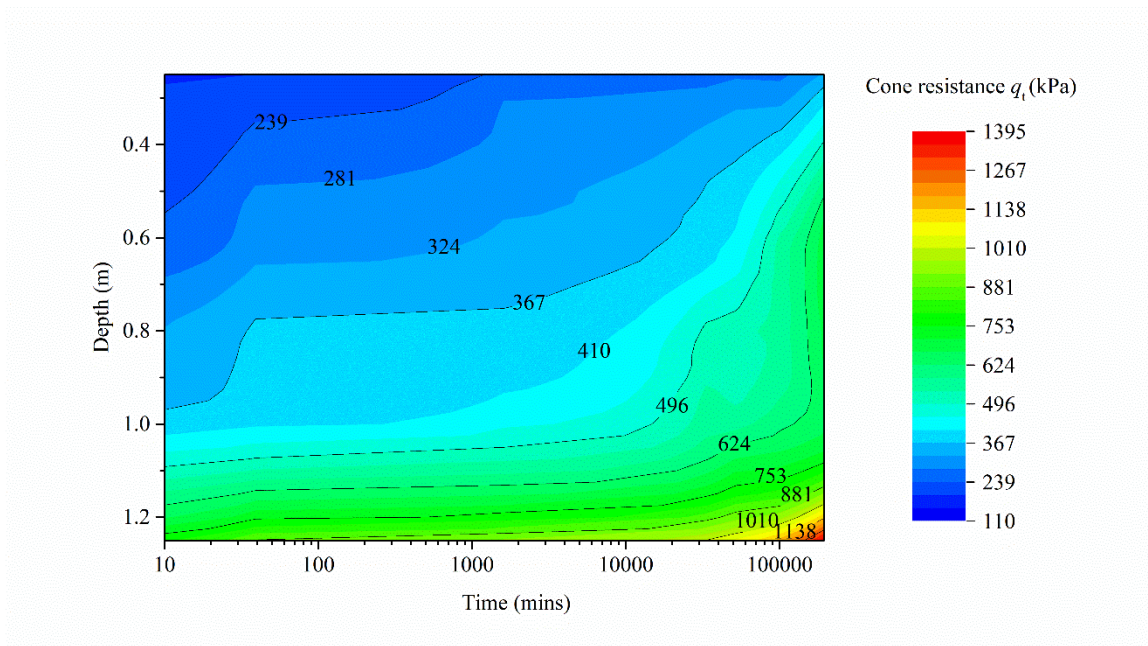


Figure 4-5. Cone resistance contour plot with time and depth

To investigate the effect of time after liquefaction on cone resistance, CPT-3 to CPT-9 were further compared at five selected depths (0.4 m, 0.6 m, 0.8 m, 1.0 m and 1.2 m). The cone resistance of sand deposit 10 mins after liquefaction (CPT-3) is considered as a base value, which is shown as 100% in Figure 4-6. At depth of 0.4 m, the cone resistance of CPT-4 to CPT-9 is 123%, 141%, 165%, 169%, 187% and 242% of that from CPT-3, showing that the sand strength was continuously increasing with time. The same trend can also be found at depths of 0.6 m, 0.8 m, 1.0 m and 1.2 m, suggesting such time effect is universal at different depths. For CPT-4, although it was conducted only 29 mins after CPT-3, the cone resistance is 123%, 123%, 115%, 104% and 112% of that from CPT-3 at depths of 0.4 m, 0.6 m, 0.8 m, 1.0 m and 1.2 m, respectively, this means the sand experienced rapid increase in strength after a major disturbance (liquefaction). After 194,553 mins (or 135 days), the cone resistance had substantial increase. The q_t is 242%,

277%, 208%, 169% and 170% of that from CPT-3, at the depths of 0.4 m, 0.6 m, 0.8 m, 1.0 m and 1.2 m, respectively. The aging time of 135 days gave an average of 113% strength increase for the sand deposit.

Other researchers also reported similar findings of the aging effect on the penetration resistance of sands. Joshi et al. (1995) pushed 10 mm diameter probes into clean sand deposit under 100 kPa. For river sand submerged in distilled water, a 40% increase in penetration resistance was reported between 1 day and 4-week tests. In this research, from CPT-5 (that was conducted at 1.1 days) to CPT-7 (that was conducted at 35.9 days), the cone penetration resistance increases by 27% on average from depth 0.2 m to 1.0 m. Schmertmann (1991) summarized several examples of the significant effects of aging on soil's engineering properties from the literature and reported a general 50 to 100 % improvement effect in many key soil properties over time from a few days to 100 years. In this paper, the average of 113% cone resistance increase in 135 days (from CPT-3 to CPT-9) is also comparable with the reported aging effect range by Schmertmann (1991).

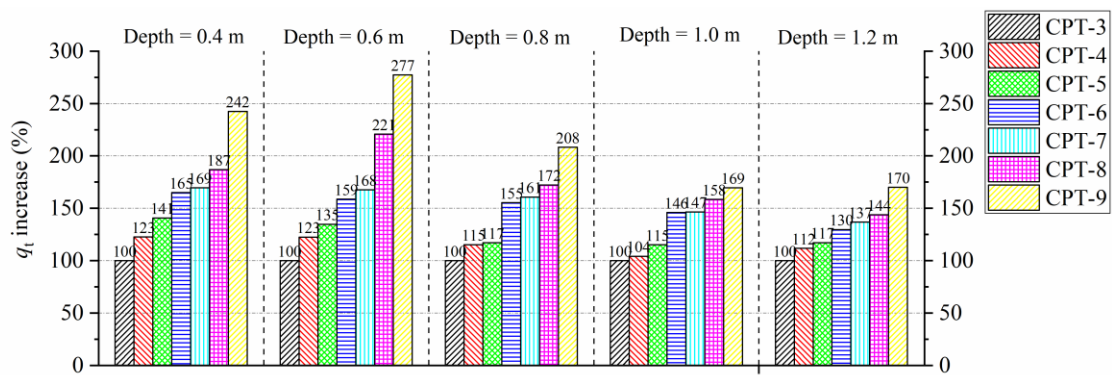


Figure 4-6. Cone resistance increase with time after liquefaction at different depths

The reason for the obvious sand strength increase with time can be explained as the continued rearrangement of sand particles during secondary compression, as suggested by

Mesri et al. (1991). The rearrangement results in an enhanced macrointerlocking of sand particles and microinterlocking of grain surface roughness. Other factors could also contribute the strength gain, such as grain slippage, soil-structure dispersion, increase of interlocking, and a probable internal arching of stresses (Schmertmann 1991). In the meanwhile, partial cementation caused by precipitation of salts and probably also silica on the sand grains and in the pores resulted in the larger increase in the penetration resistance (Joshi et al. 1995).

4.2.4 Cone resistance recovery after liquefaction

Although liquefaction reduces the cone resistance of the sand deposit, time allows sand to age and regain strength. However, whether the sand strength recovers to the same level as of before liquefaction has heretofore remained unknown. The average cone resistance of CPT-1 and CPT-2 is considered as a base value prior to liquefaction. The cone resistance recovery can be defined as:

$$q_t \text{ recovery percentage} = \frac{q_t(\text{CPT}i \text{ (}i=3-9\text{)}) - q_t(\text{Avg CPT1\&2})}{q_t(\text{Avg CPT1\&2})} \times 100\% \quad (4-3)$$

The calculated percentages of cone resistance recovery are summarized in Figure 4-7. The horizontal zero line represents the pre-liquefaction cone resistance level. The negative values below the recover line suggest the sand is still weaker than pre-liquefaction state. The positive values mean the sand has fully recovered in strength and is even stronger than the pre-liquefaction condition. At depth of 0.4 m, CPT-3 shows that the cone resistance is initially 38% less than the pre-liquefaction resistance. With time, the soil strength at this depth gradually recovered and continued to gain strength well beyond the

pre-liquefaction strength. After 33,167 mins (23 days), CPT-6 shows a 2% increase compared to CPT-1&2. After 194,553 mins (135.1 days), CPT-9 has a 49% increase compared to the pre-liquefaction resistance. At the depth of 0.6 m, it started with a 43% strength decrease right after liquefaction and ended up with a 58% increase after 194,553 mins. However, for the depths of 0.8 m and 1.0 m, the soil strength did not fully recover. Even after 194,553 mins (CPT-9), the cone resistances were still 2% and 18% less than the pre-liquefaction values at the depths of 0.8 m and 1.0 m, respectively. At the depth of 1.2 m, the soil was found to have 36% strength gain at CPT-9. The data suggest that, with time, the post-liquefaction strength will eventually return to the pre-liquefaction strength.

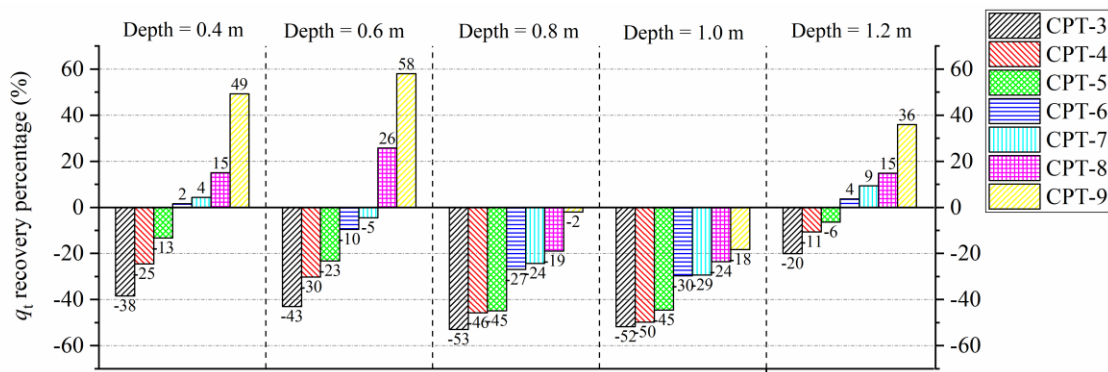


Figure 4-7. Cone resistance recovery with time after liquefaction

4.2.5 Relationship between cone penetration resistance and time

To further investigate the relationship between the cone penetration resistance (q_t) of post-liquefaction sand and time, three different effective stress levels are selected. The average q_t from three depth intervals of 0.2-0.6 m, 0.6-1.0 m, and 1.0-1.25 m, with an average effective stress level of 4.0 kPa, 8.0 kPa, and 11.3 kPa, respectively, is plotted

against time in Figure 4-8. A logarithm relationship between q_t and t can be established using:

$$q_t = k \log(t) + b \quad (t \geq 10) \quad (4-4)$$

where t is the aging time expressed in minutes; k and b are constants depending on the effective stress levels of the sand. Table 4-2 lists the values of constants and R^2 for three different effective stress levels. The R^2 of the fittings using Equation 4-4 are 0.794, 0.801 and 0.852 for effective stress level of 4.0 kPa, 8.0 kPa, and 11.3 kPa, respectively. The R^2 values indicate that Equation 4-4 can well describe the logarithm relationship between q_t and t .

Table 4-2. Values of constants and coefficient of determination (R^2) for Equation 4-4

Average effective stress σ'_v (kPa)	k	b	R ²
4.0	47.0	154.4	0.794
8.0	66.0	227.4	0.801
11.3	67.6	476.5	0.852

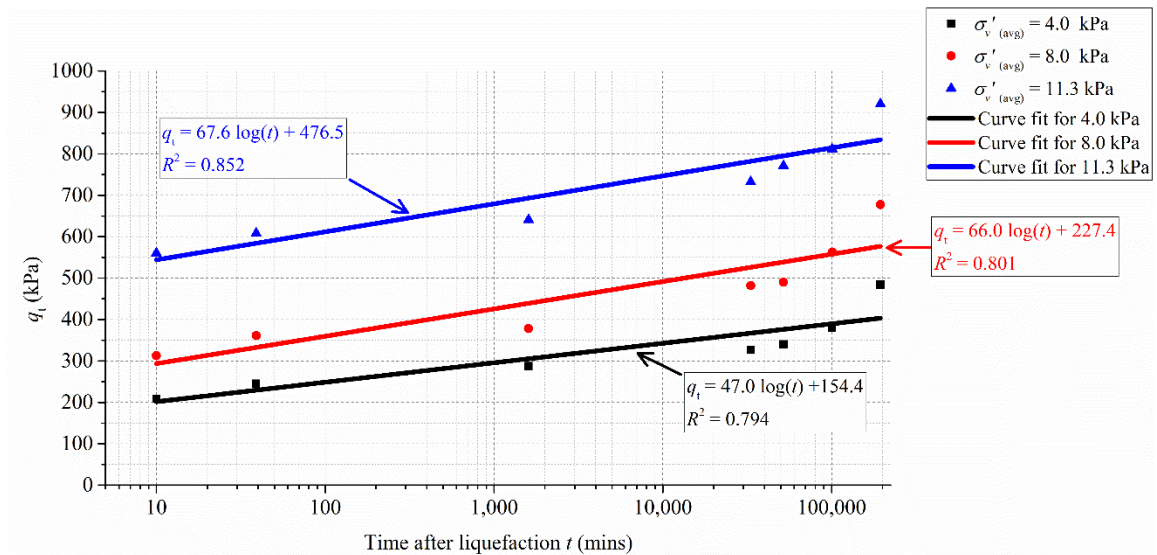


Figure 4-8. q_t variation with time at different effective overburden stresses

To investigate the predictive behaviors of Equation 4-4, Figure 4-9 compares the CPT data from the existing literature under various testing conditions and the equation proposed by this research. Equation 4-4 at 4 kPa and 11.3 kPa is included in Figure 4-9 to show the range of cone resistance increase after liquefaction from this research. The details of the previous studies by Mesri et al. (1990), Charlie et al. (1992), and Joshi et al. (1995) are summarized in Table 4-3. The test methods for the empirical equations summarized in Table 4-3 varied. For example, the equations from Mesri et al. (1990) and Joshi et al. (1995) were examined by laboratory data, while Charlie et al. (1992) presented field CPT results after blasting. All the summarized equations focus on cone penetration variation with time after major disturbance or fresh deposition.

Figure 4-9 shows that the increase of cone resistance predicted by Equation 4-4 from this research is within a reasonable range compared with others' work. It should be noted that most literature did not capture the immediate cone resistance increase after disturbance. Joshi et al. (1995) reported the first test one day after deposition while Charlie et al. (1992) conducted the first CPT one week after blasting. In this research, the first CPTu test was performed 10 mins after liquefaction. This provides further understanding of the cone resistance increase with time. The limitation of Equation 4-4 is that it only applies to relatively low effective stress levels (less than 11.3 kPa). The performance of this equation at higher stress levels needs further investigation.

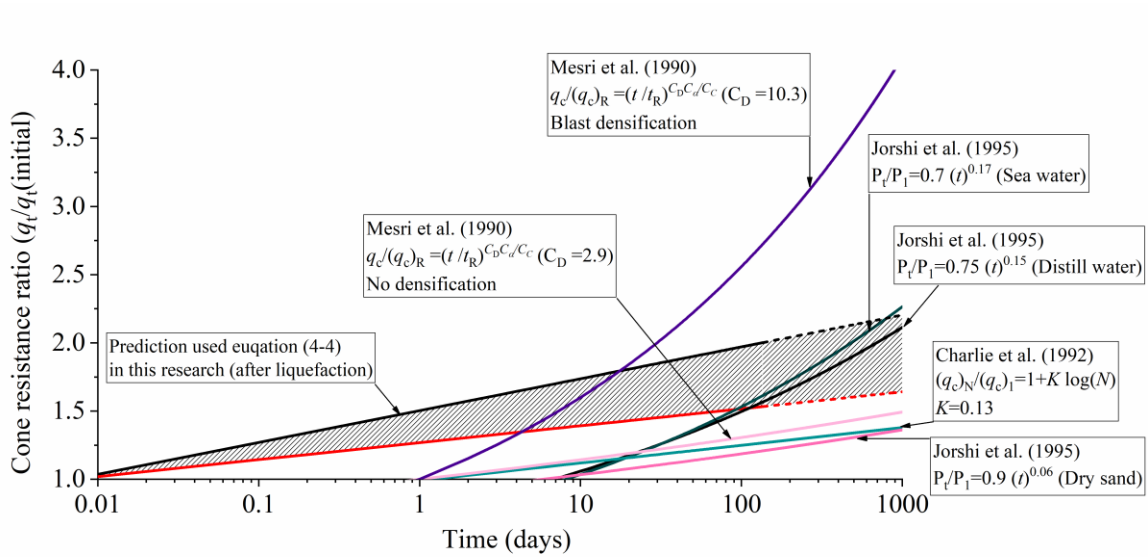


Figure 4-9. Comparison of other research using equation (4-4)

Table 4-3. CPT resistance measurement of sand aging effect

References	Type of test	Proposed equation	Notes
Mesri et al. (1990)	Lab compression tests	$q_c/(q_c)_R = (t/t_R)^{C_D C_a/C_c}$	$(q_c)_R$ is a reference penetration resistance at a time after the primary consolidation. C_c is compression index, C_a is secondary compression index, C_D is between 3 to 20, dependent on densification.
Charlie et al. (1992)	Field CPT	$(q_c)_N/(q_c)_1 = 1 + K \log(N)$	N is time in weeks. K is in the range of 0 to 1 and dependent on soil type, densification method and temperature.
Joshi et al (1995)	Lab samples aged under 100 kPa with 10 mm diameter penetrometer	$P_t/P_1 = a (t)^b$	t is aging time in days. P_t is the penetration resistance at age t . P_1 is the penetration resistance of freshly deposited sand on

			the first day. a and b are constants depending on the environmental conditions of the sand.
This research	Shake table test with CPTu test	$q_t = k \log(t) + b$	t is aging time in minutes. q_t is the cone penetration resistance.

A power function was used to fit the data as an alternative to Equation (4-4). The comparison using this power function was also compared with others' work and shown in Figure 4-10. In this fitting, the 1-day CPT results were considered as the starting values. The prediction using power function is close to the prediction by Jorshi et al. (1995) under submerged conditions.

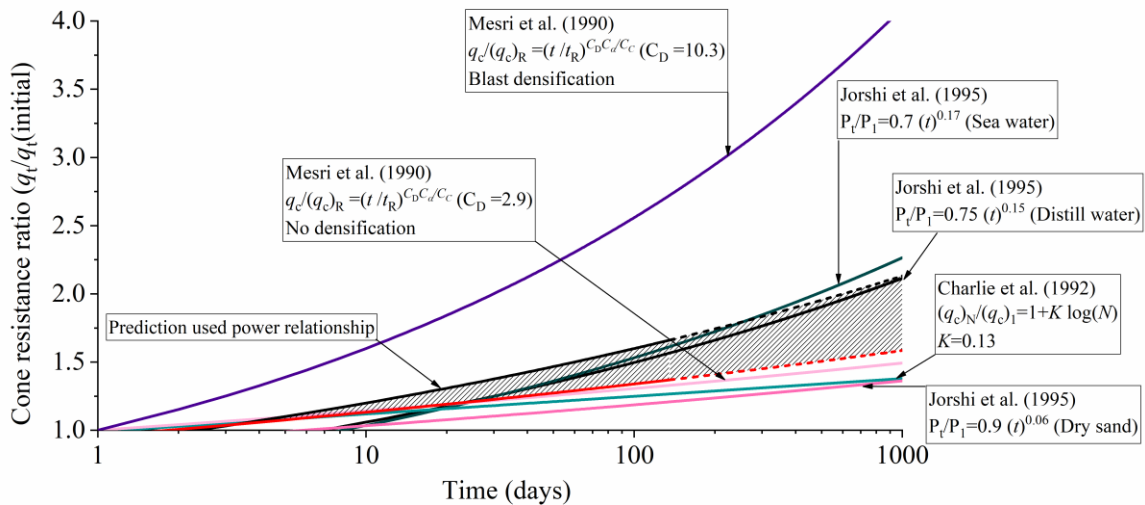


Figure 4-10. Comparison of other research using power function

4.3 Normalized cone penetration resistance variation with time

4.3.1 CPTu test results normalization

Since CPT results are one of the most widely used indices for evaluating the liquefaction characteristics of soil (Boulanger and Idriss 2014), several correlations have been proposed to estimate CRR for clean sand using CPT penetration resistance corrected for overburden pressure (e.g. Suzuki et al. 1995; Stark and Olson 1995; Robertson and Wride 1998, Boulanger and Idriss 2014). The CPTu results normalized in this paper follows the flow chart suggested by Robertson and Wride (1998).

The normalized cone penetration resistance (q_{c1N} , dimensionless) corrected for overburden stress is given by:

$$q_{c1N} = \left(\frac{q_c}{P_{a2}}\right) \left(\frac{P_a}{\sigma'_{v0}}\right)^{0.5} \quad (4-5)$$

where q_c is the measured cone tip penetration resistance; P_a is a reference pressure in the same units as σ'_{v0} (i.e., $P_a = 100$ kPa if σ'_{v0} is in kPa); and P_{a2} is a reference pressure in the same units as q_c (i.e., $P_{a2} = 0.1$ MPa if q_c is in MPa).

The soil behavior type index, I_c , is defined as follows (Robertson and Wride 1998):

$$I_c = [(3.47 - Q)^2 + (\log F + 1.22)^2]^{0.5} \quad (4-6)$$

where Q is the normalized CPT penetration resistance

$$Q = [(q_c - \sigma'_{v0}) / P_a] [(P_a / \sigma'_{v0})^n] \quad (4-7)$$

and F is the normalized friction ratio in percent

$$F = [f_s / (q_c - \sigma'_{v0})] \times 100\% \quad (4-8)$$

As suggested by Robertson and Wride (1998), an exponent value of 0.5 for n is appropriate for clean sands. The calculated I_c for all the CPTus is less than 2.6, which confirms that the soil is nonplastic and granular.

The cyclic resistance ratio (CRR for $M = 7.5$) can be estimated using the equivalent clean sand normalized penetration resistance q_{c1N} by:

$$CRR_{7.5} = 0.833 ((q_{c1N})_{cs} / 1000) + 0.05 \quad ((q_{c1N})_{cs} < 50) \quad (4-9)$$

Using the normalization equations by Robertson and Wride (1998), the normalized cone penetration resistance q_{c1N} from CPT-3 to CPT-9 is plotted in Figure 4-11. The results suggest that the q_{c1N} for all the CPTus is generally within the range from 10 to 30, which is relatively small due to the shallow depth of sand deposit. Similar to the cone resistance curves shown in Figure 4-4, an increasing trend of q_{c1N} can also be found from CPT-3 to CPT-9. The q_{c1N} curves from CPT-3 to CPT-9 indicate that the q_{c1N} of sand deposit increases with the aging time. The variation of q_{c1N} values with depths, however, is difficult to generalize. The q_{c1N} for CPT-3 to CPT-7 has small variations from depths 0.2 m to 1.0 m and starts to increase with depths from 1.0 m till 1.27 m. CPT-8 and CPT-9 have relatively large variations through the entire depth. Moreover, based on Equation 4-9, a small variation of q_{c1N} (less than 10) will only introduce very small change on $CRR_{7.5}$. This research focuses on the time effect on q_{c1N} variation.

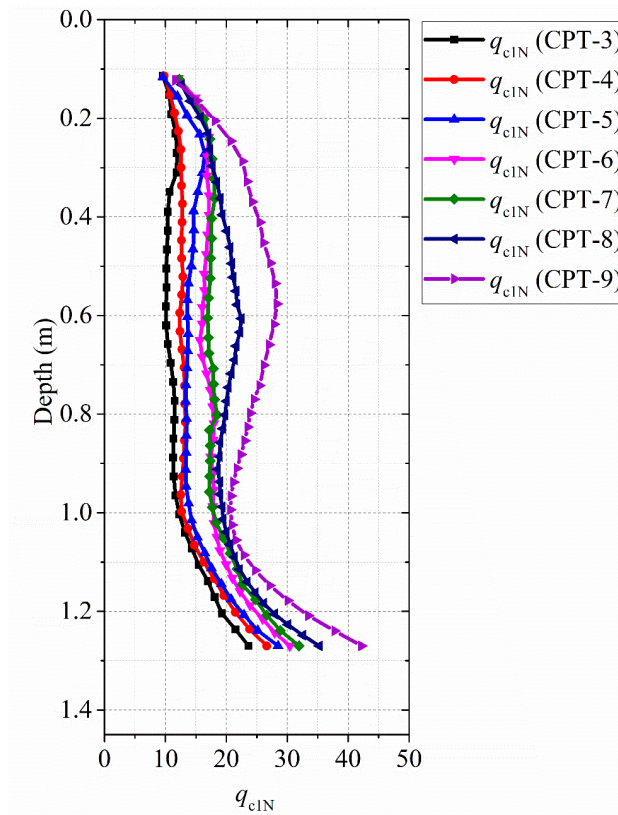


Figure 4-11. q_{cIN} of CPT-3 to CPT-9

4.3.2 Variation of normalized cone penetration and cyclic resistance ratio with time

By neglecting the q_{cIN} variation with depth, a statistical analysis with mean values and $\pm 95\%$ confidence intervals (CIs) for CPT-3 to CPT-9 is summarized in Figure 4-12. An obvious increasing trend of the mean values from CPT-3 to CPT-9 can be seen. The mean values of CPT-3 to CPT-9 are 12.7, 14.4, 15.7, 18.5, 19.1, 21.1 and 25.5 respectively. The q_{cIN} increase of CPT-9 compared with CPT-3 is 101%, which is a little less than the 127% q_t increase reported in previous section. The confidence intervals show that the CPT-9 has the greatest measurement variation while other CPTs have similar CIs.

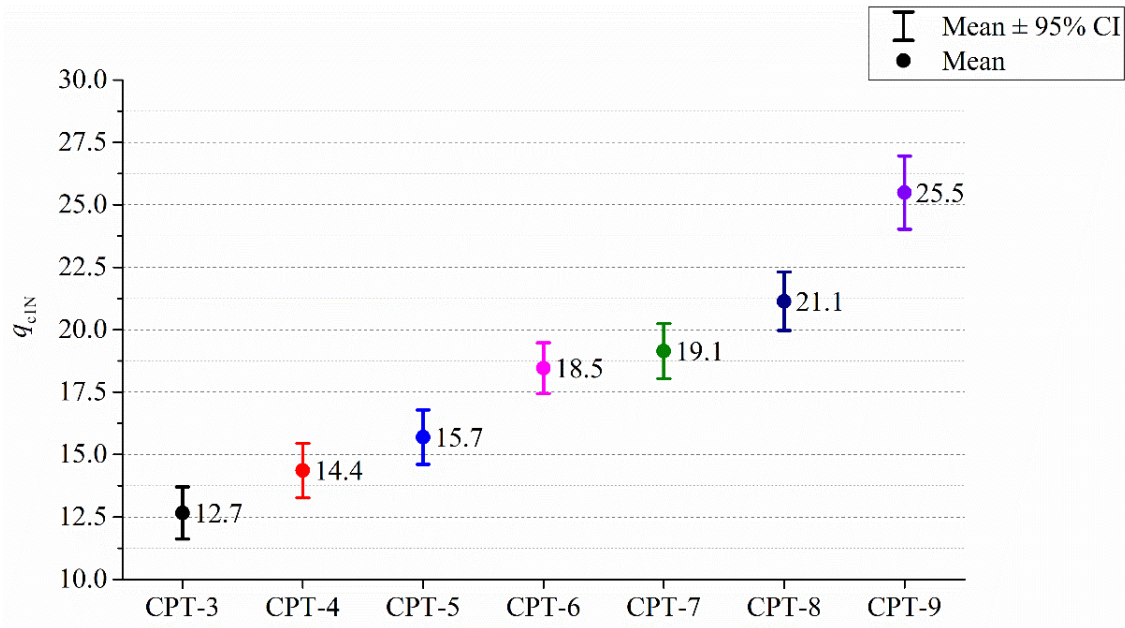


Figure 4-12. The 95% confidence intervals and mean values for q_{c1N}

The q_{c1N} can be replotted with time on logarithmic scale, as shown in Figure 4-13

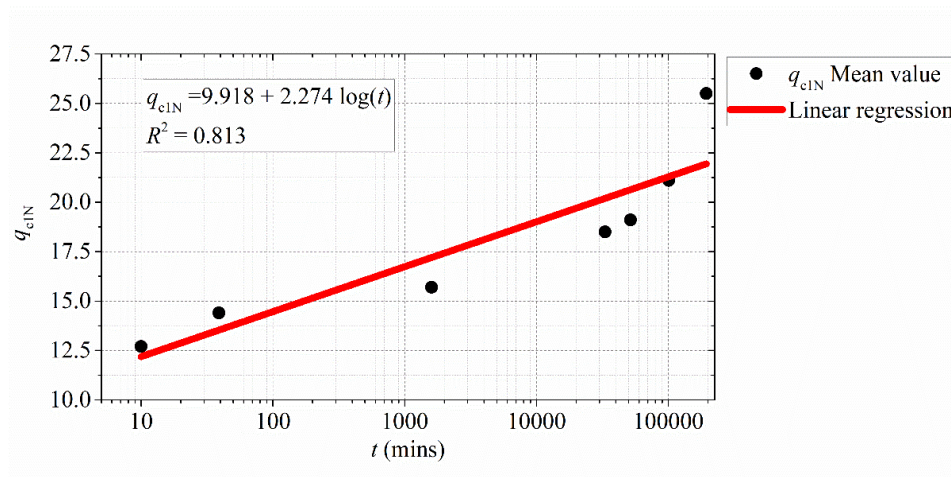
(a). A linear relationship can be established between q_{c1N} and $\log(t)$ as follows:

$$q_{c1N} = 9.918 + 2.274 \log(t) \quad (4-10)$$

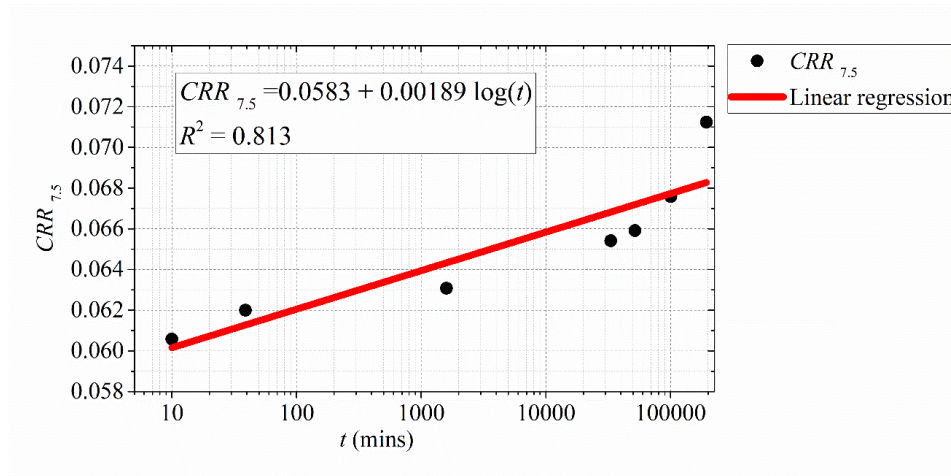
Equation 4-9 gives a linear relationship between q_{c1N} and the cyclic resistance ratio for $M = 7.5$ ($CRR_{7.5}$). Thus, the $CRR_{7.5}$ can also be linearly related to $\log(t)$ as:

$$CRR_{7.5} = 0.0583 + 0.00189 \log(t) \quad (4-11)$$

The coefficient of determination (R^2) is 0.81 for both regressions. It should be noted that the linear regression might underpredict q_{c1N} and $CRR_{7.5}$ at longer time.



(a)



(b)

Figure 4-13. (a) q_{c1N} variation with time, (b) $CRR_{7.5}$ variation with time

After the normalization of the CPTu data, a linear relationship can be established between $CRR_{7.5}$ and $\log(t)$. However, the increase of $CRR_{7.5}$ from CPT-3 to CPT-9 (4.5 months) is less obvious than the q_t or q_{c1N} increase. The $CRR_{7.5}$ is 0.06058 for CPT-3 and 0.07124 for CPT-9. The 135 days' aging gives a 17.6% increase in $CRR_{7.5}$. Compared with the 127% increase in q_t and 101% increase in q_{c1N} , this increase is much smaller.

4.4 Conclusions and Recommendations

The following conclusions and summary are based on the data, analysis and interpretation presented in this chapter.

1. Liquefaction can reduce the cone penetration resistance of a sand deposit significantly immediately after the liquefaction event. For a sand deposit from 0.2 m to 1.0 m depth, the cone penetration resistance can reduce by 50% on average due to liquefaction.

2. After liquefaction, the cone penetration resistance of a sand deposit increases with aging time. In an aging span of 4.5 months after liquefaction, an average of 113% gain in cone penetration resistance was observed. An equation relating the cone penetration resistance, effective stress and time is proposed and compared with results from the literature. The equation may under-predict strength gain at long time.

3. The cone penetration resistance of the sand deposit is able to recover to or exceed the pre-liquefaction level at certain stress levels during the test time span.

4. After the liquefaction, the normalized cone penetration resistance increases with time. In 4.5 months, a 101% gain of normalized cone penetration resistance is observed. The normalized cone penetration resistance has a linear relationship with the logarithm of time.

5. The cyclic resistance ratio for earthquake with magnitude of 7.5 increases with time after liquefaction. A 17.6% increase in $CRR_{7.5}$ is observed in the testing time span. The $CRR_{7.5}$ has a linear relationship with the logarithm of time.

6. Data, equations and discussion presented in this paper are based on the limited laboratory results for a clean sand. The effective stress levels of the sand are relatively low

as is typical in a laminar box. Further examination of the proposed equations is needed for different soil types and effective stress levels.

The following recommendation is based on the results and conclusions from this study. The CPT case history data for liquefaction study should include the timing information. Most CPTs in the current database were performed after earthquake loading and the time elapsed between an earthquake loading and penetration testing was not regularly reported. This research suggests that short period of time might have great influence on the soil properties. Aging time between earthquake and field tests cannot be neglected and should be documented for better data interpretation.

Chapter 5

The Effect of Shaking History on Liquefaction Resistance of Sand Deposit

This chapter presents the multiple shaking events performed on the sand deposit after the 1st shaking presented in Chapter 3 and CPTu testing presented in Chapter 4. Three major shaking events are designed and performed on the sand deposit after the first shaking event. The test recordings from piezometer and LVDT are presented and discussed. In this chapter, the following questions are addressed: (1) What is the liquefaction resistance of the sand deposit after the 1st shaking? Will the same shaking event liquefy the soil in the 2nd shaking? (2) What is the seismic response of the sand deposit when subjecting to shaking events with longer duration or higher acceleration amplitude? (3) Will a mild shaking event have the same effect on the liquefaction resistance as a strong shaking? Answering these questions can provide insights for further understanding of the effect of shaking history on liquefaction resistance of sand deposit.

5.1 Multiple shaking events

5.1.1 Time schedule for multiple shaking events

Three major shaking events were designed and performed on the same sand deposit after the first shaking that was presented in Chapter 3. The 2nd shaking occurred after 153 days after the 1st shaking. The 3rd shaking occurred 21 days after the 2nd shaking, and the

4th shaking occurred 21 days after the 3rd shaking. The 2nd shaking had the same input motion as the 1st shaking. The 3rd shaking had the same acceleration amplitude and frequency as in the 1st shaking, but longer durations. The 4th shaking was comprised of four sub-shaking events that are denoted as shaking 4-1, 4-2, 4-3, 4-4, the resting duration between the sub-shaking events is 5 min. The detailed time schedule for multiple shaking events is summarized in Figure 5-1 and Table 5-1.

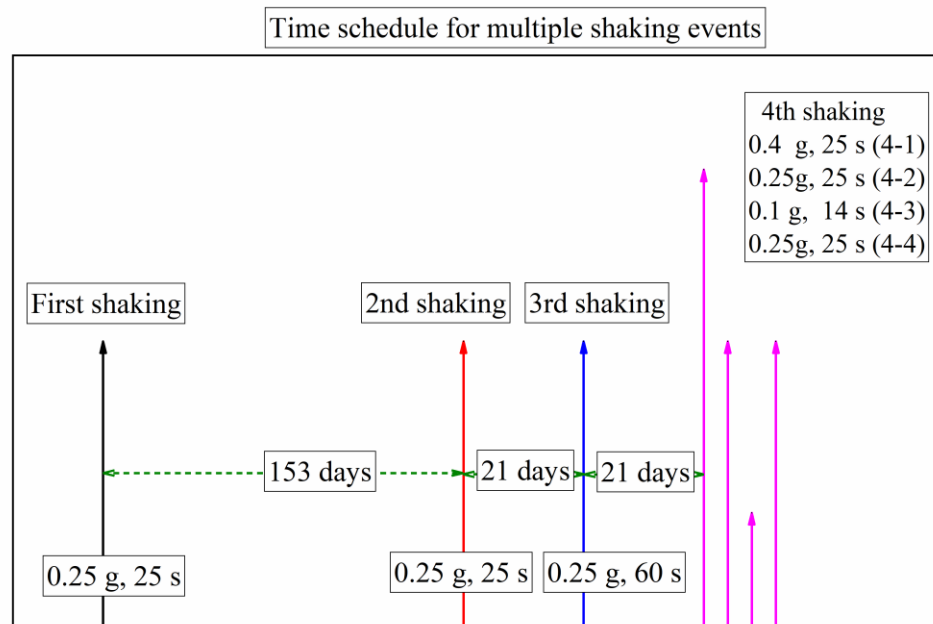


Figure 5-1. Time schedule for multiple shaking events, the shaking events have varying acceleration amplitude and duration, and the same frequency of 1 Hz.

Table 5-1. Time schedule for multiple shaking events

Shaking Event	Amplitude (g)	Duration	Time elapsed from last shaking
1st shaking	0.25	25	N/A
2nd shaking	0.25	25	153 days
3rd shaking	0.25	60	21 days

4th shaking	4-1	0.4	25	21 days
	4-2	0.25	25	5 mins
	4-3	0.1	14	5 mins
	4-4	0.25	25	5 mins

5.1.2 Input motion for 2nd, 3rd and 4th shaking

Input motion for the 2nd shaking

The input motion of the 2nd shaking was the same as the first shaking event that was presented in Chapter 3. The shaking event was defined as 21 sinusoidal cycles of a maximum base acceleration of 0.25 g at 1 Hz, as shown in Figure 5-2. Two ramp-up and ramp-down cycles were added to make sure smooth start and ending of the shake table system. The purpose of choosing such shaking was to evaluate whether the same sand deposit after 153 days of aging can still liquefy or not under the same shaking event as the 1st one.

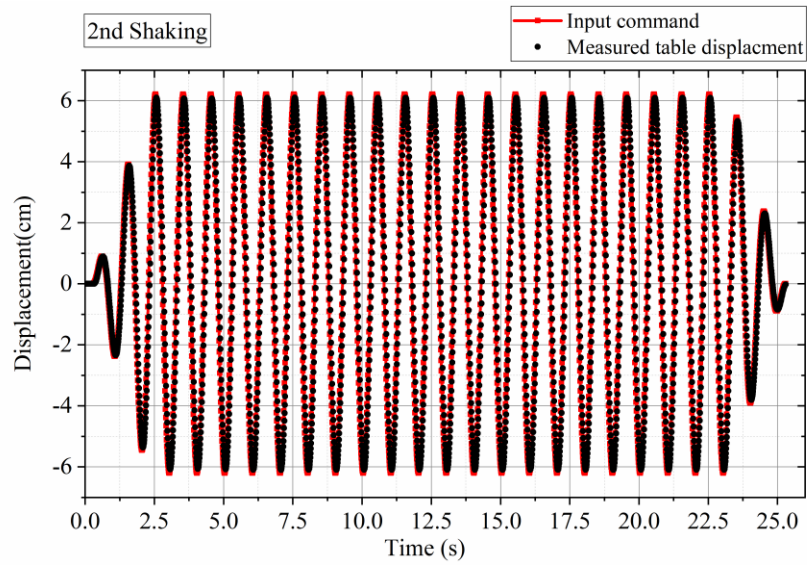


Figure 5-2. Input motion for the 2nd shaking (0.25g, 1 Hz, 25 cycles)

Input motion for the 3rd shaking

The shaking event was defined as 56 sinusoidal cycles of a maximum base acceleration of 0.25 g at 1 Hz with two ramp-up and ramp-down cycles, as shown in Figure 5-3. The design intent of this shaking event was to investigate the seismic response of sand deposit under longer shaking duration.

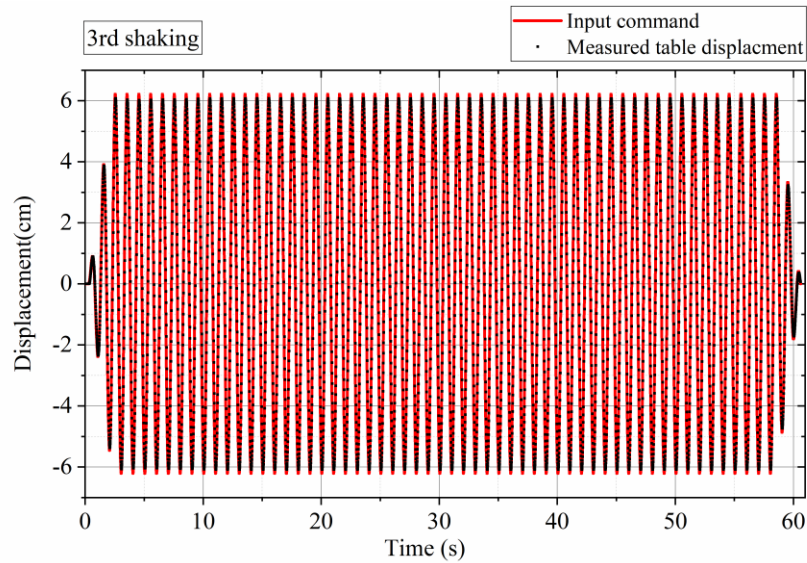


Figure 5-3. Input motion for 3rd shaking (0.25g, 1 Hz, 60 cycles)

Input motion for the 4th shaking

The shaking event (4-1) was defined as 21 sinusoidal cycles of a maximum base acceleration of 0.4 g at 1 Hz with two ramp-up and ramp-down cycles, as shown in Figure 5-4. A 0.25 cm difference between the measured table movement and the input command was observed at the peak values. This means the actual input motion was 0.39g, slightly less than the 0.4g target. The shake table actuator was still able to perform well for relative strong input motions.

The shaking events (4-2) and (4-4) were the same. Both were also the same as the input motion of the 1st and 2nd shaking. The shaking event (4-3), however, only had 0.1g and 14 cycles. This event was designed to be a mild shaking event. By comparing the seismic response from shaking events (4-2) and (4-4), the influence of a strong shaking (4-

1) and mild shaking (4-3) on the sand deposit could be investigated. The input command and measured table displacement for shaking (4-2) to shaking (4-4) are shown in Figure 5-5 to Figure 5-7, respectively.

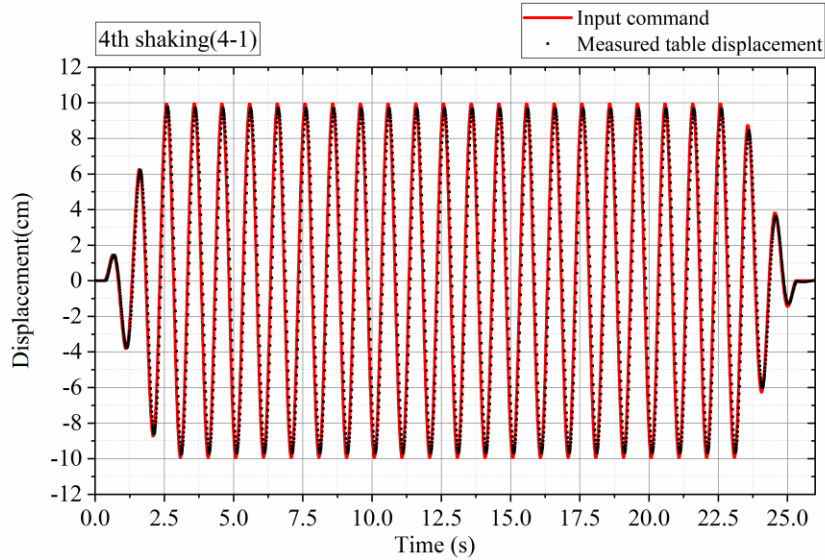


Figure 5-4. Input motion for shaking event (4-1) (0.4g, 1 Hz, 25 cycles)

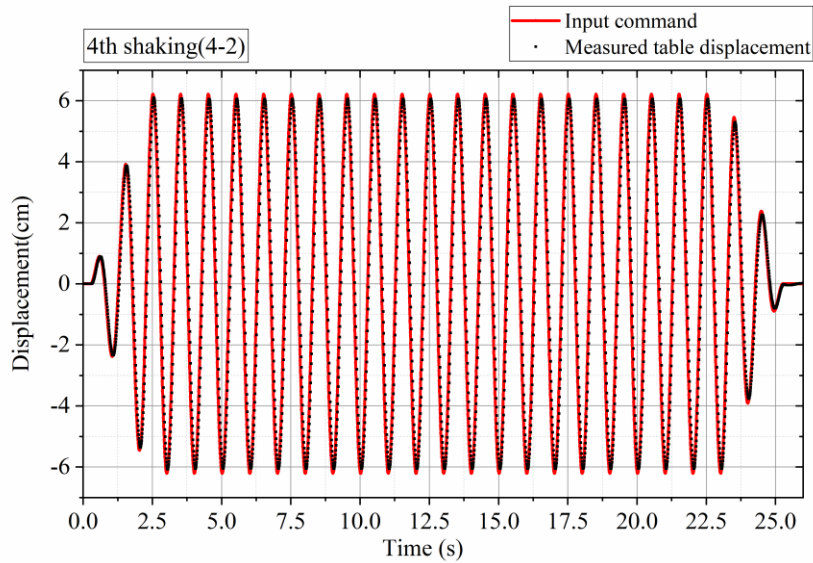


Figure 5-5. Input motion for shaking event (4-2) (0.25 g, 1 Hz, 25 cycles)

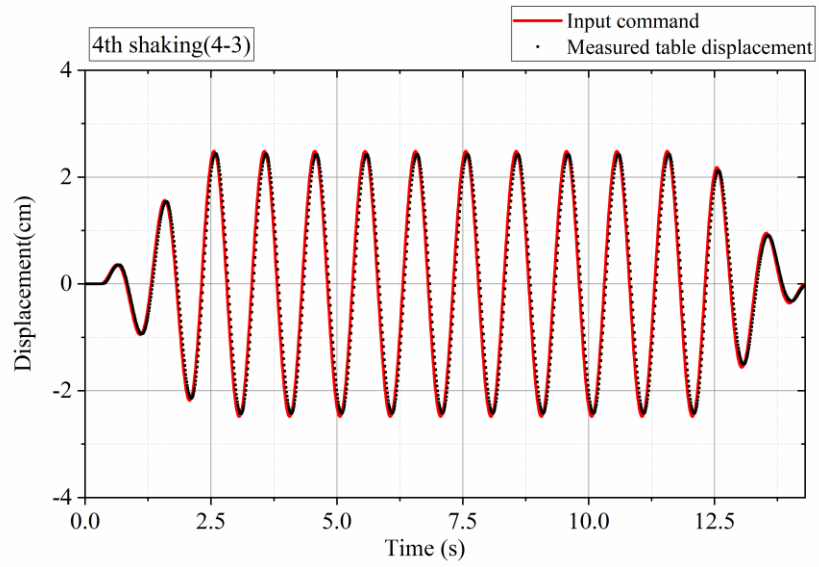


Figure 5-6. Input motion for shaking event (4-3) (0.1 g, 1 Hz, 14 cycles)

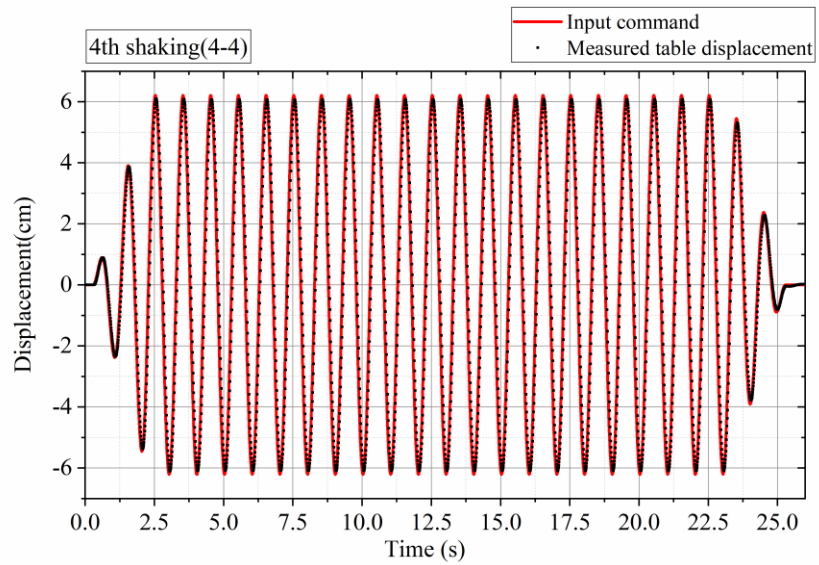


Figure 5-7. Input motion for shaking event (4-4) (0.25g, 1 Hz, 25 cycles)

5.2 Shake table test results for multiple shaking events

5.2.1 Shake table measurement of the 2nd shaking

Pore pressure readings

Figure 5-8 presents the pore pressure readings for the 2nd shaking. A clear excess pore pressure build-up was observed during the shaking event. An interesting observation was that the excess pore pressure did not start to dissipate right after shaking. A relatively obvious pore pressure increase was observed from PZ-2 to PZ-5. PZ-5 ($D = 1.2$ m) recorded its maximum reading at $t = 27.5$ s, 2.5 s after the end of shaking. PZ-4 ($D = 0.95$ m) recorded its maximum reading at $t = 32.4$ s. PZ-3 ($D = 0.7$ m) had the maximum reading at $t = 37.6$ s. PZ-2 ($D = 0.45$ m) recorded its maximum reading at $t = 52.5$ s. No pore pressure increase after shaking was observed at PZ-1 ($D = 0.2$ m). However, the excess pore pressure started to dissipate at this depth at around $t = 50$ s. The maximum values of the pore pressure readings after shaking were marked and shown in Figure 5-8. The reason that a maximum pore pressure reading did not happen right after shaking can be explained by the excess pore pressure dissipation process. Apparently, the sand at the bottom would build up the highest excess pore pressure. As the excess pore pressure started to dissipate, a water flow might be developed from the bottom to top because of the water head difference. The water flew to the top gradually. This caused the maximum pore pressure to occur at different time for different sand layers. Another evidence for this explanation is that the sand near the bottom (PZ-5) was the first one finishing excess pore pressure

dissipation while sand near the top (PZ-2) finished the dissipation last. However, this trend was not observed in the PZ-1 readings.

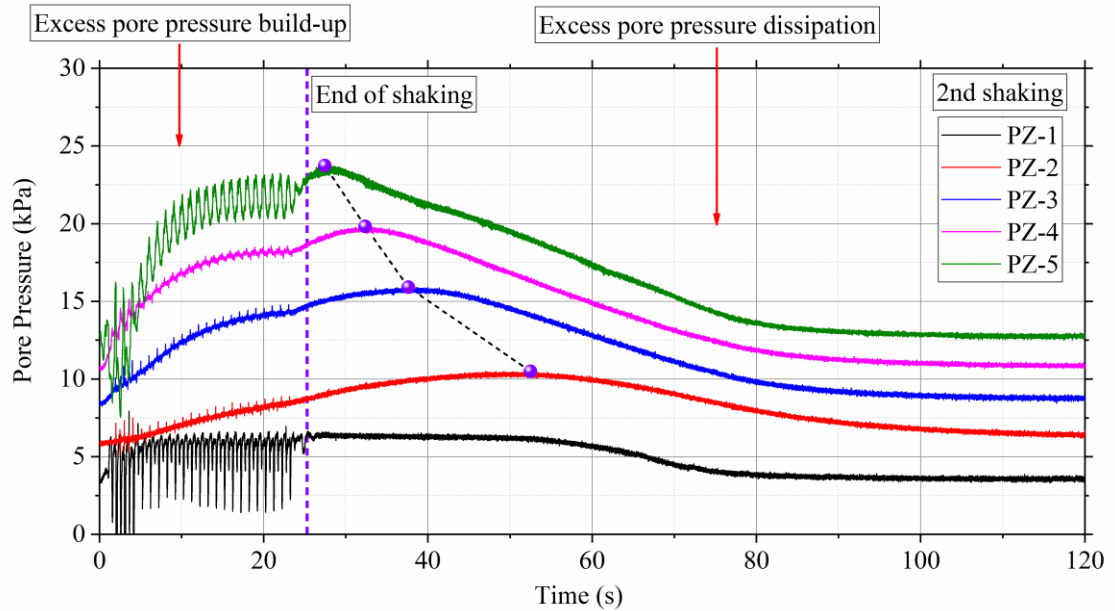


Figure 5-8. Pore pressure readings of the 2nd shaking at different depths

Figure 5-9 presents the excess pore pressure generation during the shaking event. The dash lines represent the target pore pressure readings if liquefaction occurs (i.e., $r_u = 1$). The readings from PZ-1 suggest that the sand at this depth was close to liquefaction. Most of the sand, represented by PZ-2 to PZ-5, did not liquefy. For example, at the end of the shaking, the pore pressure at PZ-3 reached 14.7 kPa. The sand at this depth would liquefy if the pore pressure reaches 17.4 kPa. The pore pressure ratio was 0.7 at the end of shaking.

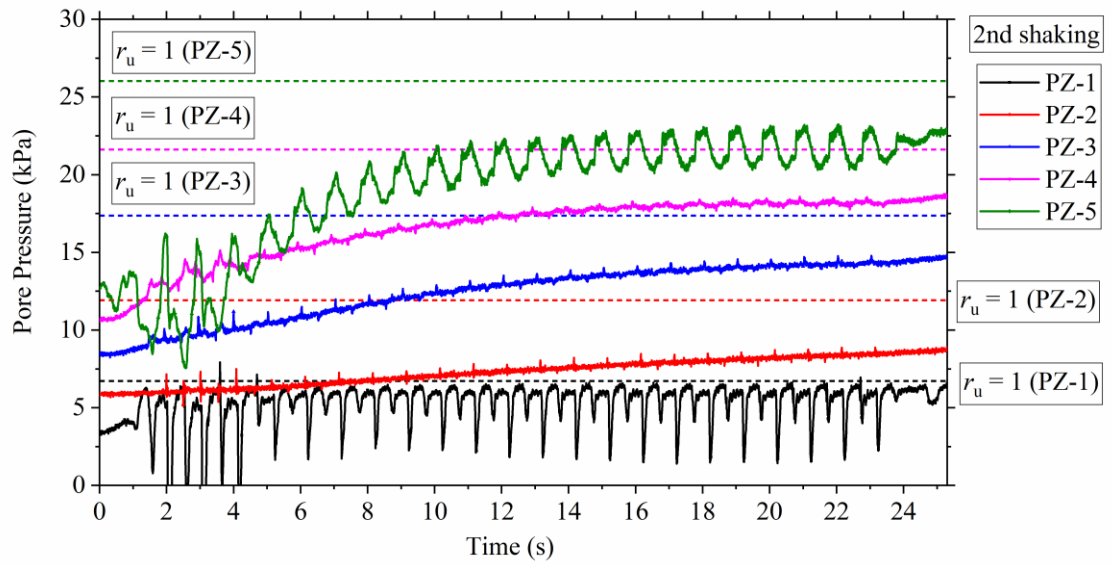


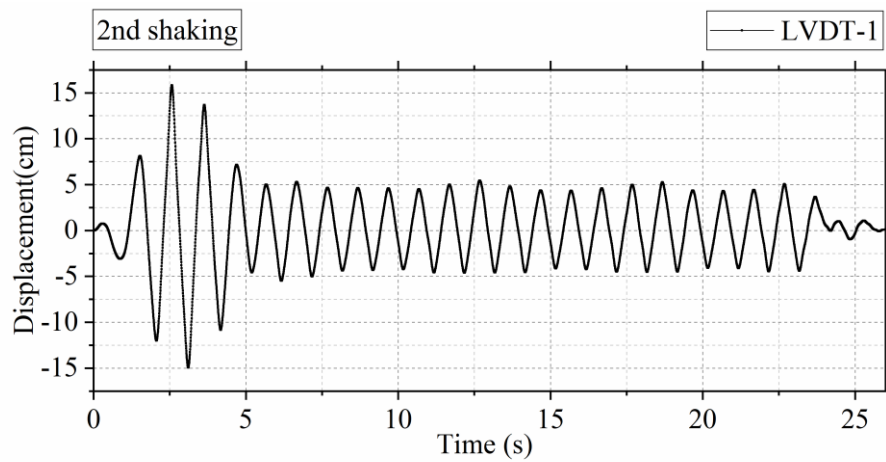
Figure 5-9. Excess pore pressure generation during the 2nd shaking at different depths

Lateral displacement

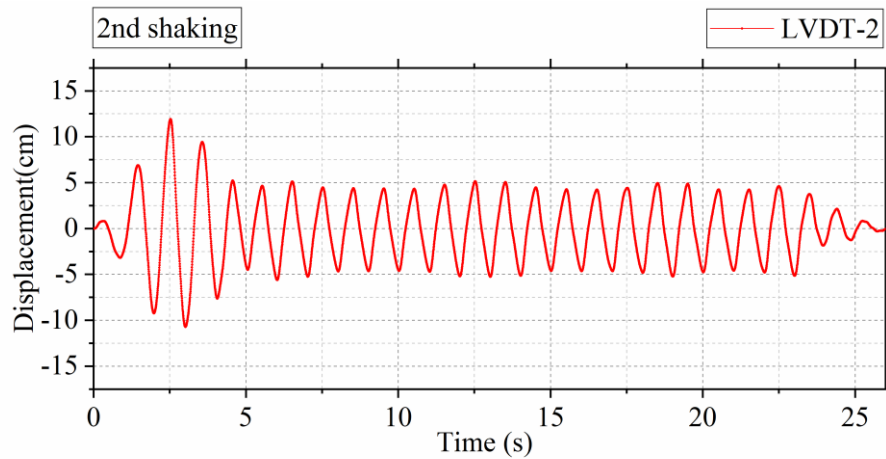
The absolute lateral movement time histories of different LSB frames are shown in Figure 5-10. The lateral movement of the 10th frame (LVDT-5) was very similar to that of the table. The 8th frame (LVDT-4) had slight amplification at the first three cycles and kept an averaged amplitude of 5.2 cm. The 6th frame (LVDT-3) had more obvious amplification at the first three cycles and kept an averaged amplitude of 5 cm. The 4th frame (LVDT-2) had obvious amplification at the first three cycles and kept an averaged amplitude of 5 cm. The 2nd frame (LVDT-1) had large amplification (15 cm) at the first three cycles and kept an averaged amplitude of 5 cm.

LSB movement of the 1st shaking clearly demonstrated both amplification and de-amplification due to liquefaction occurrence. In the 2nd shaking, amplification was indeed

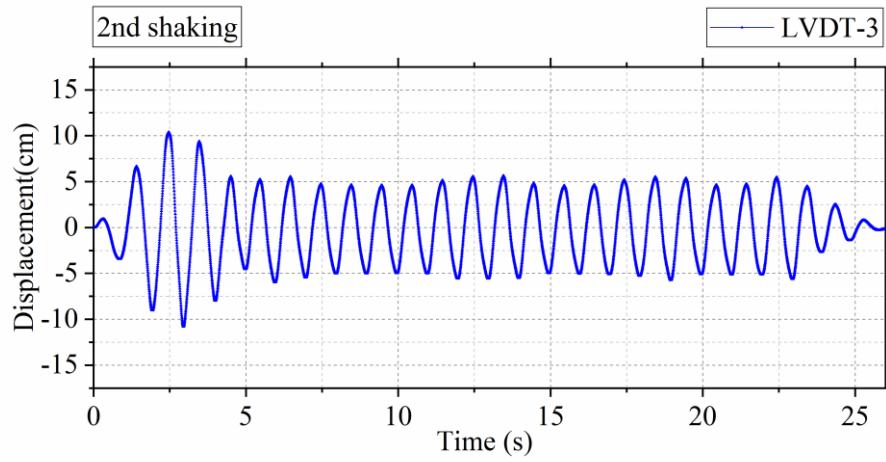
observed in the first four cycles. After that, no de-amplification was observed. All the recorded LSB frames had similar amplitude of about 5 cm. As discussed in Chapter 3, the main reason for a ground motion de-amplification is the occurrence of liquefaction. Some shear waves cannot propagate through a liquefied layer. In the 2nd shaking, liquefaction did not occur based on the pore pressure readings. The observation in lateral movement was consistent with the pore pressure readings.



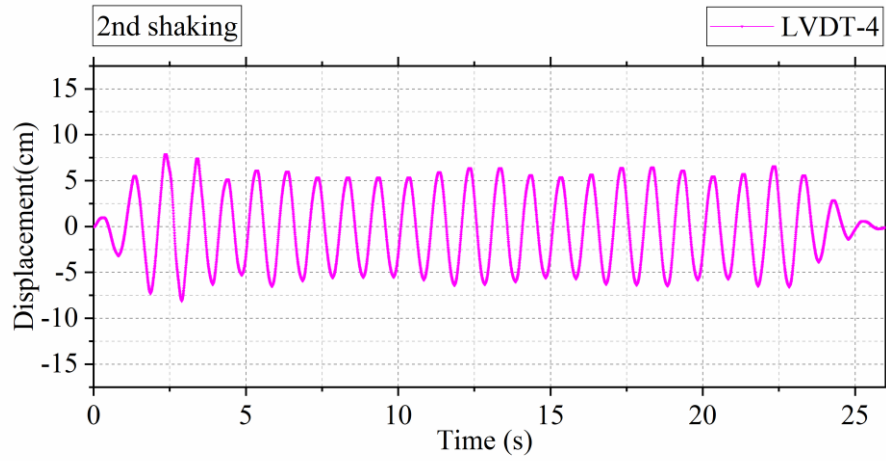
(a)



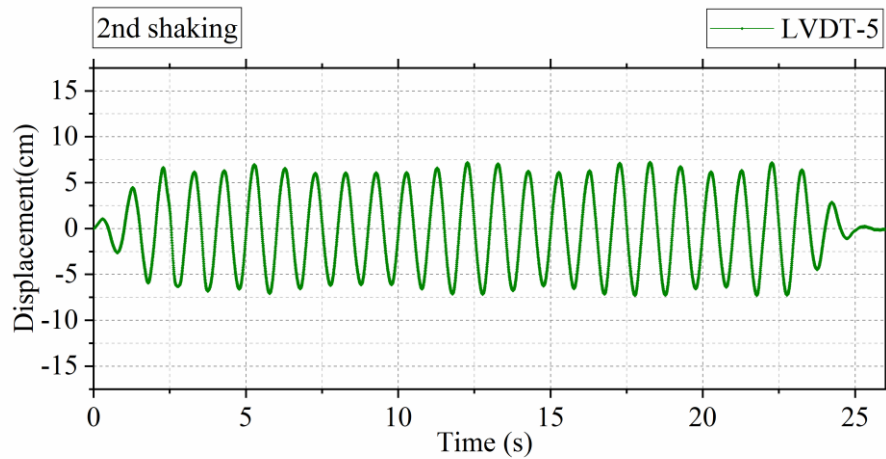
(b)



(c)



(d)



(e)

Figure 5-10. Absolute lateral movement time histories of different LSB frames for the 2nd shaking (a) 2nd frame (b) 4th frame (c) 6th frame (d) 8th frame (e) 10th frame. The elevations of the frames where LVDTs were installed are shown in Figure 3-16

5.2.2 Shake table measurement of the 3rd shaking

Pore pressure readings

Figure 5-11 presents the pore pressure readings for the 3rd shaking. Similar to what happened in the 2nd shaking, the excess pore pressure did not start to dissipate right after shaking either. PZ-5 recorded its maximum reading at $t = 61.9$ s, 1.9 s after the end of the shaking. PZ-4 recorded its maximum reading at $t = 65.5$ s. PZ-3 had the maximum reading at $t = 68.1$ s. PZ-2 recorded its maximum reading at $t = 77.2$ s. This suggests that an upward seepage was also developed in this shaking event.

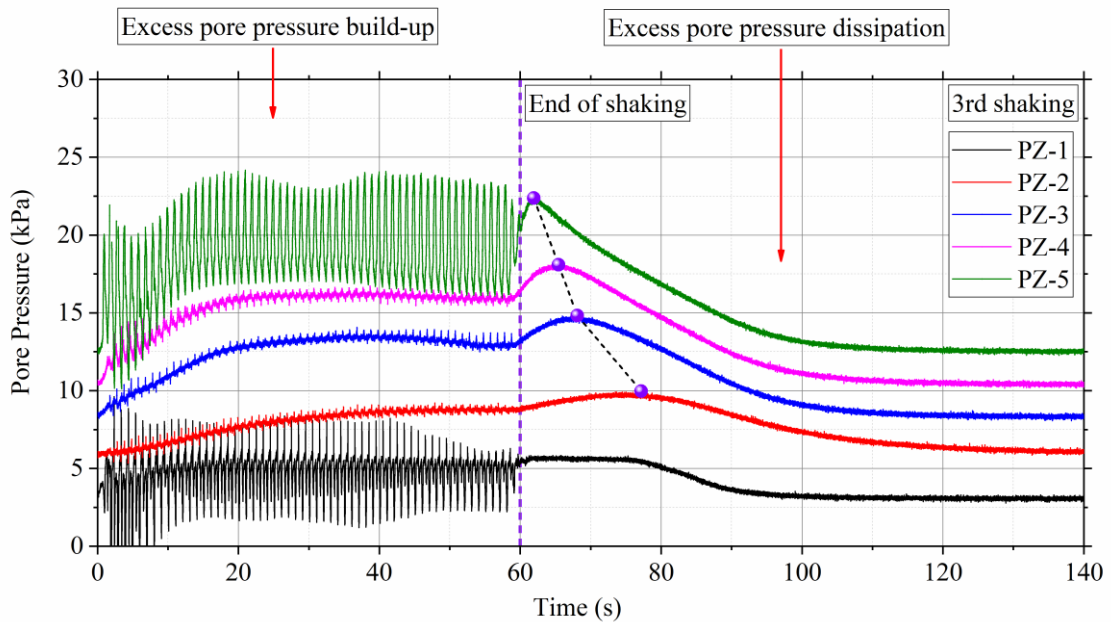


Figure 5-11. Pore pressure readings of the 3rd shaking at different depths

Figure 5-12 presents the excess pore pressure generation during the shaking event. The dash lines represent the target pore pressure readings if liquefaction occurs. The readings from all piezometers suggest that the sand deposit did not liquefy. For example,

at the end of the shaking, the pore pressure at PZ-4 reached 16.3 kPa. The sand at this depth would liquefy if the pore pressure reaches 21.7 kPa. The pore pressure ratio was 0.52 at the end of shaking. Another observation is that pore pressure increase was not sensitive to the number of cycles after a certain time. The pore pressure readings from PZ-3, PZ-4 and PZ-5 kept almost constant after 20 s. The pore pressure readings from PZ-2 stopped increasing after 40 s.

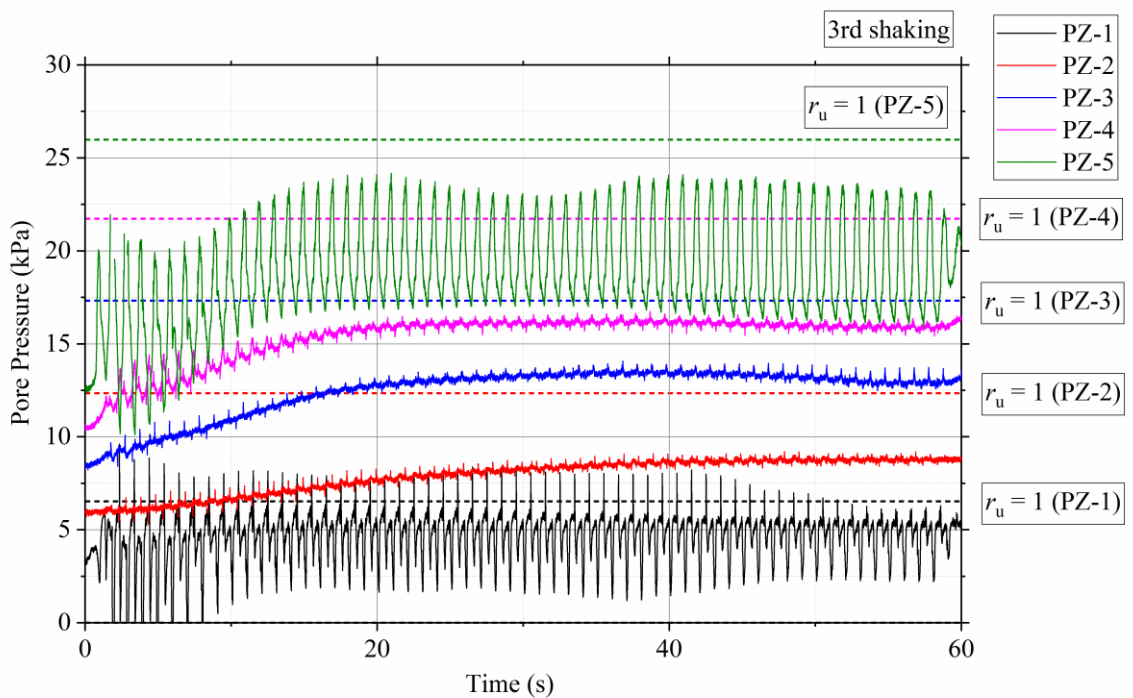
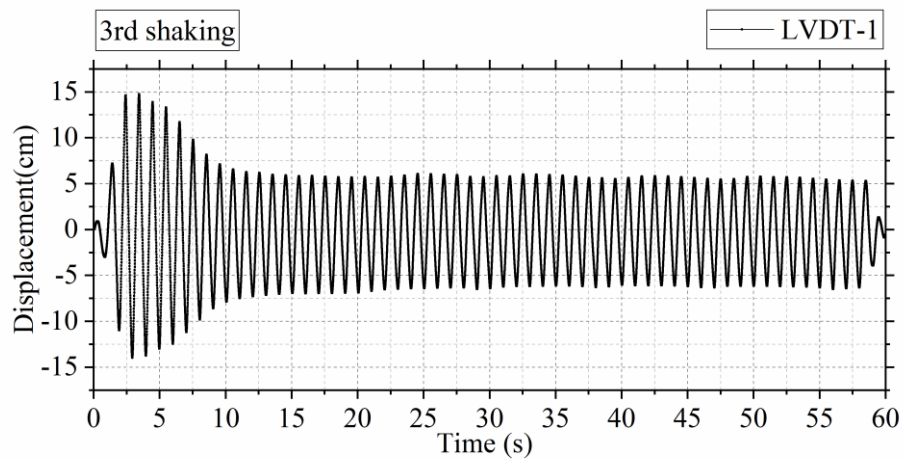


Figure 5-12. Excess pore pressure generation during the 3rd shaking at different depths

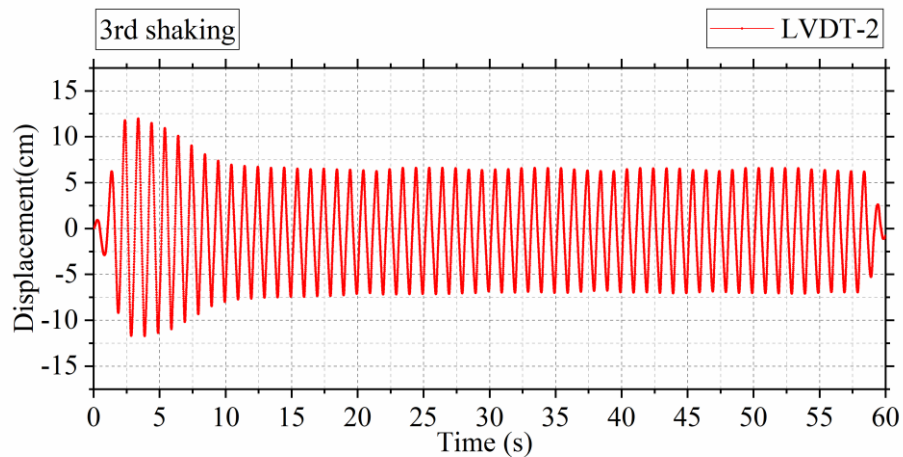
Lateral displacement

The absolute lateral movement time histories of different LSB frames are shown in Figure 5-13. From this shaking, all the LVDTs were relocated one frame down since no sand was within the 2nd frame because of the settlement. The lateral movement of 11th frame (LVDT-5) was very similar to that of the table. The 9th frame (LVDT-4) had very

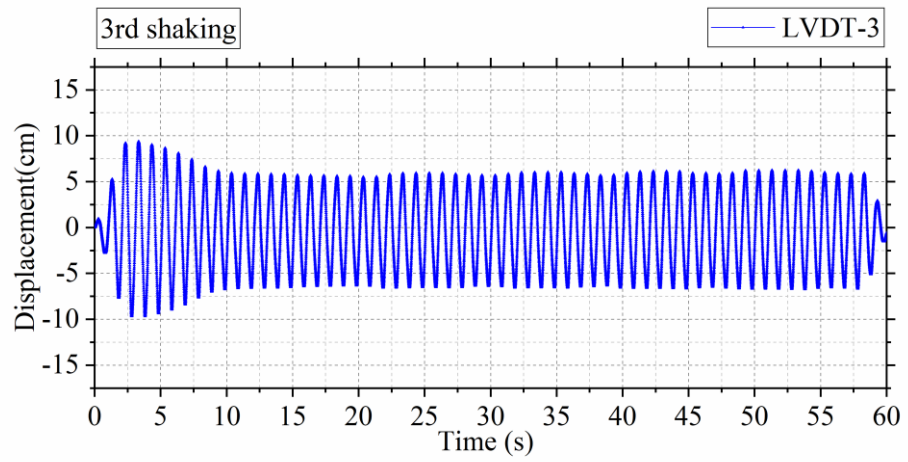
slight amplification at the first several cycles and kept an averaged amplitude of 6.2 cm. The 7th frame (LVDT-3) had more obvious amplification at the first 9 cycles and kept an averaged amplitude of 6.2 cm. The 5th frame (LVDT-2) had obvious amplification at the first 9 cycles and kept an averaged amplitude of 6.2 cm. The 3rd frame (LVDT-1) had large amplification (15 cm) at the first three cycles and kept an averaged amplitude of 6.2 cm. The general trend of LSB movement was similar to that of the 2nd shaking. After the amplification, the LSB moved almost the same as the shake table. This means the sand became very dense and little relative movement of the box was allowed.



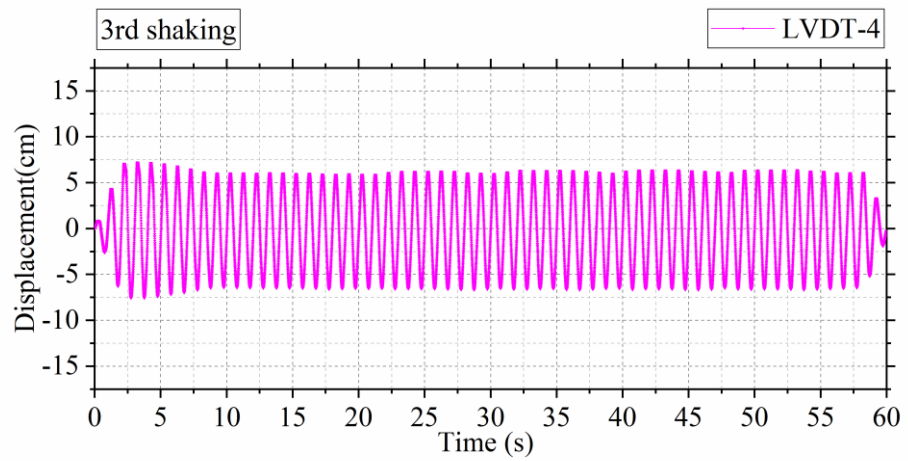
(a)



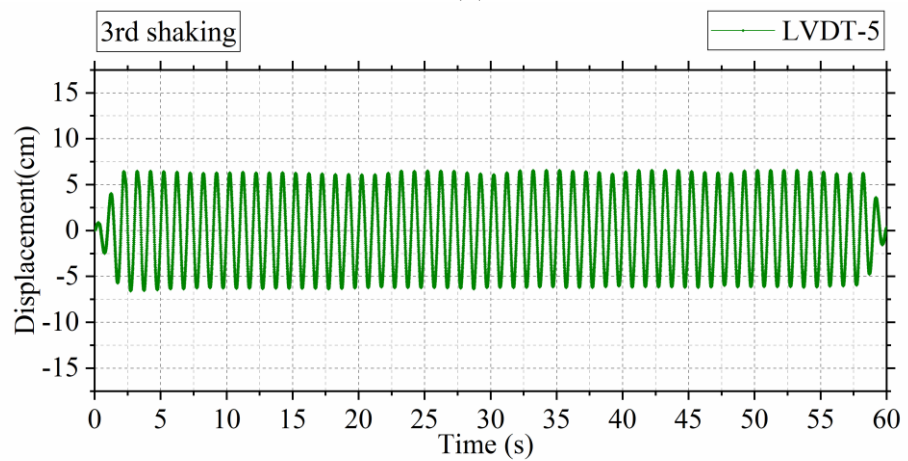
(b)



(c)



(d)



(e)

Figure 5-13. Absolute lateral movement time histories of different LSB frames for the 3rd shaking (a) 3th frame (b) 5th frame (c) 7th frame (d) 9th frame (e) 11th frame

5.2.3 Shake table measurement of the 4th shaking

Pore pressure readings

Figure 5-14 presents the pore pressure readings of the shaking event (4-1) in the 4th shaking. Similar to the performances in the 2nd and 3rd shaking, the excess pore pressure did not start to dissipate right after the shaking. PZ-5 recorded its maximum reading at $t = 30.6$ s, 5.6 s after the end of shaking. PZ-4 recorded its maximum reading at $t = 33.5$ s. PZ-3 had the maximum reading at $t = 36.7$ s. PZ-2 recorded its maximum reading at $t = 45.5$ s. This suggests that an upward seepage also occurred in this shaking event.

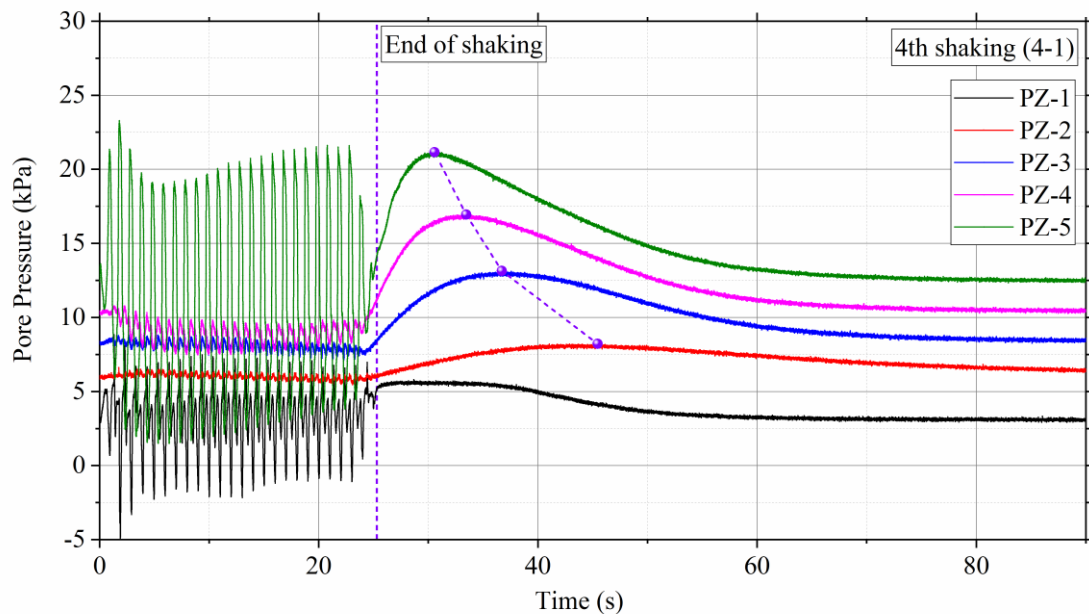


Figure 5-14. Pore pressure readings of 4th shaking (4-1) at different depths

Figure 5-15 presents the excess pore pressure generation during the shaking event. Very limited amount of excess pore pressure was generated during this shaking event.

Apart from the large fluctuations of PZ-5 and PZ-1, the pore pressure at the end of the shaking was almost the same as that at the beginning of the shaking.

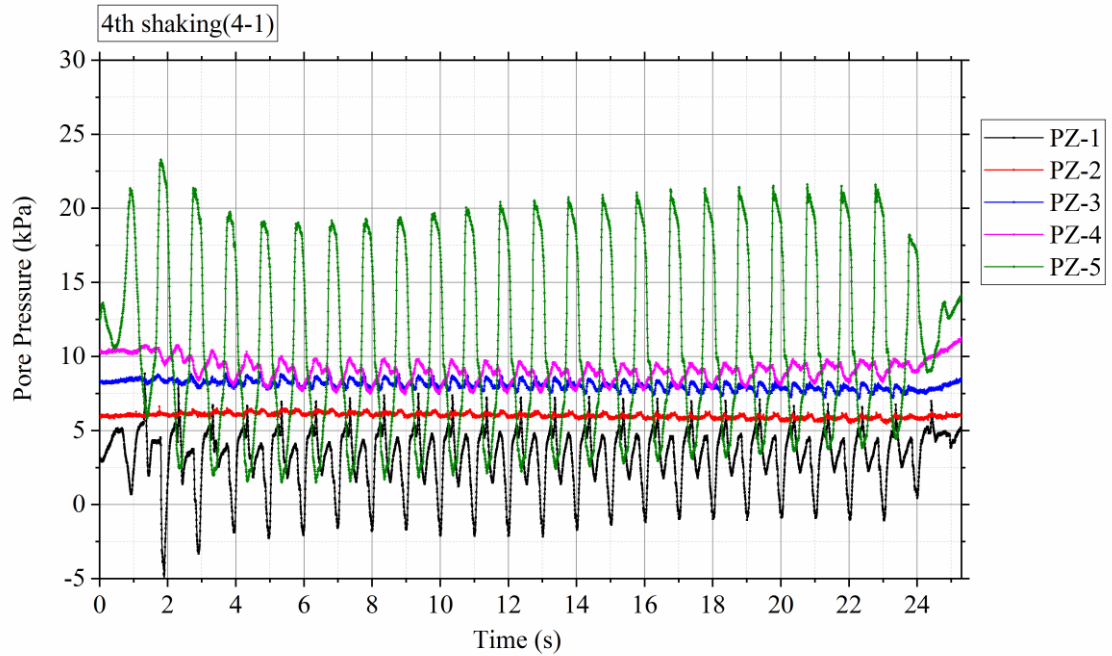
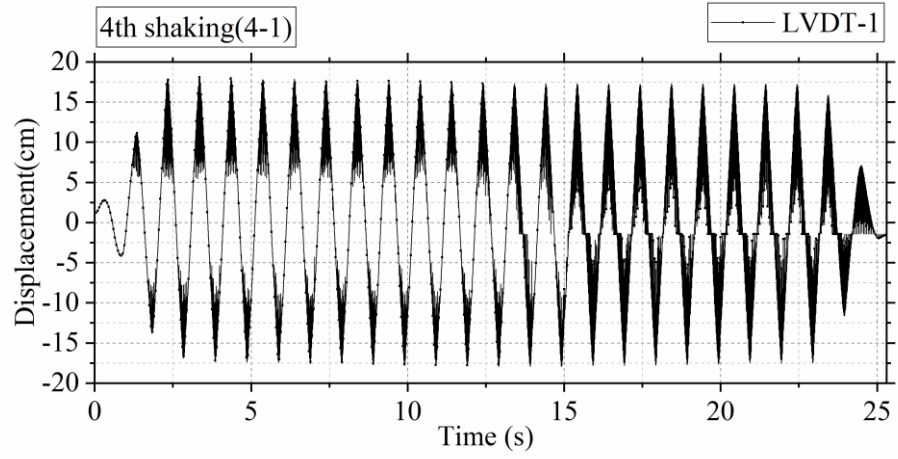


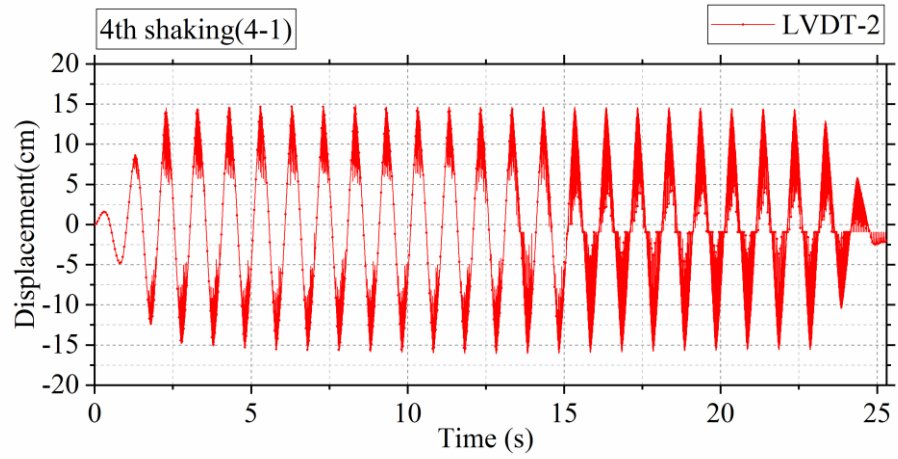
Figure 5-15. Excess pore pressure generation during the 4th shaking event (4-1) at different depths

Lateral displacement

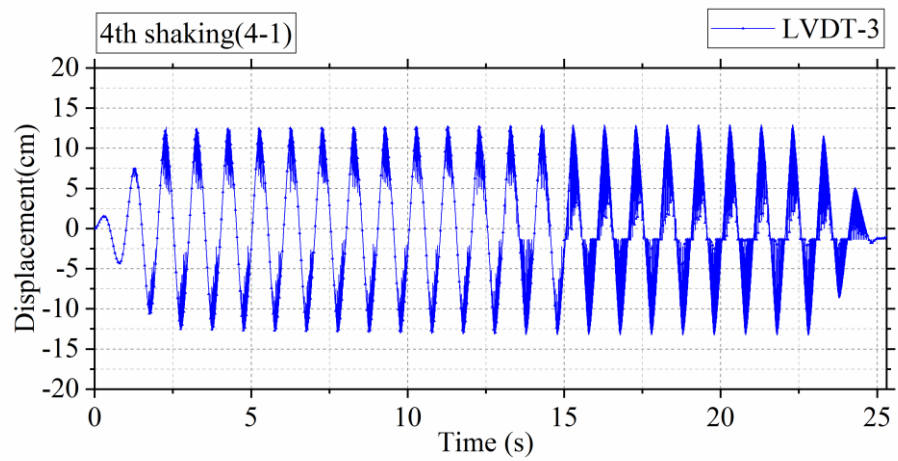
The absolute lateral movement time histories of different LSB frames are shown in Figure 5-16. The response of the LSB to this shaking was different from that of previous shakings. All the LVDTs kept a uniform amplitude during the shaking. The amplitudes of LVDT-1 to LVDT-5 (from the top to the bottom of the LSB) are 17.5 cm, 15 cm, 12.5 cm, 11 cm and 10.5 cm, respectively.



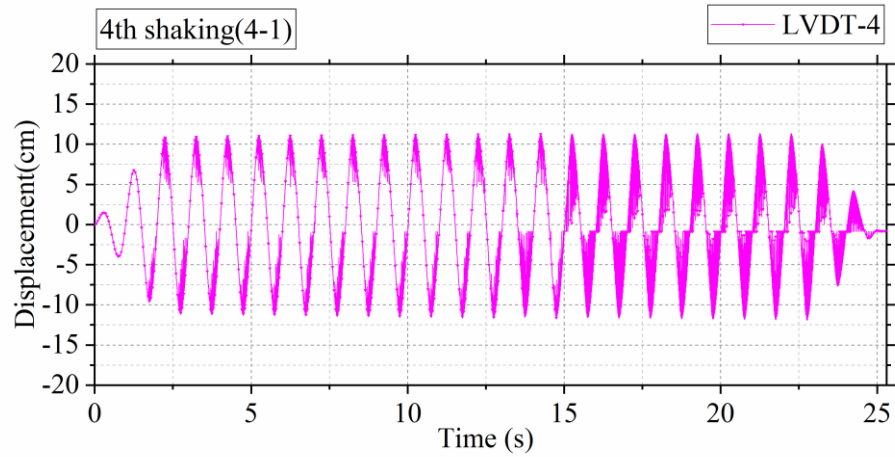
(a)



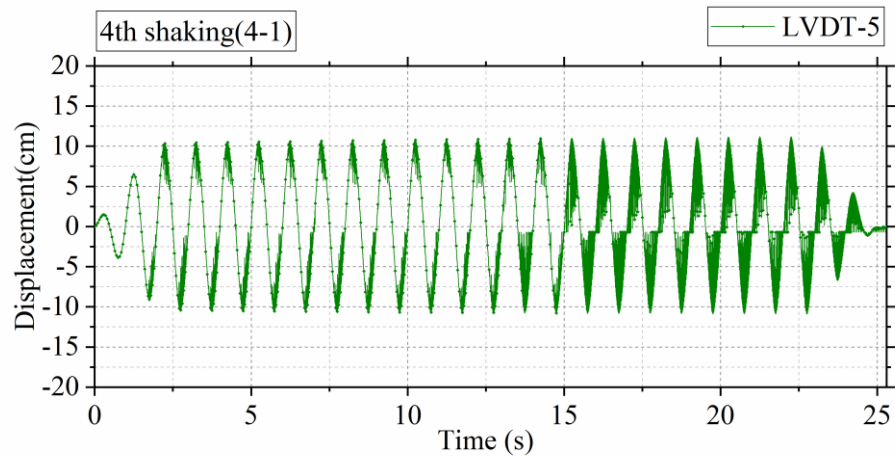
(b)



(c)



(d)



(e)

Figure 5-16. Absolute lateral movement time histories of different LSB frames in the 4th shaking (a) 3th frame (b) 5th frame (c) 7th frame (d) 9th frame (e) 11th frame

Figure 5-17 to Figure 5-19 present the excess pore pressure generation of the shaking events of (4-2) to (4-4) in the 4th shaking, respectively. The pore pressure generations during shaking event (4-2) and shaking event (4-4) were similar, as both shaking share the same input motion. Surprisingly, the pore pressure had more obvious increase in the shaking event (4-3) than shaking event (4-1), considering that this event was

a mild shaking. A detailed comparison of results from these four shaking events is presented in the next section.

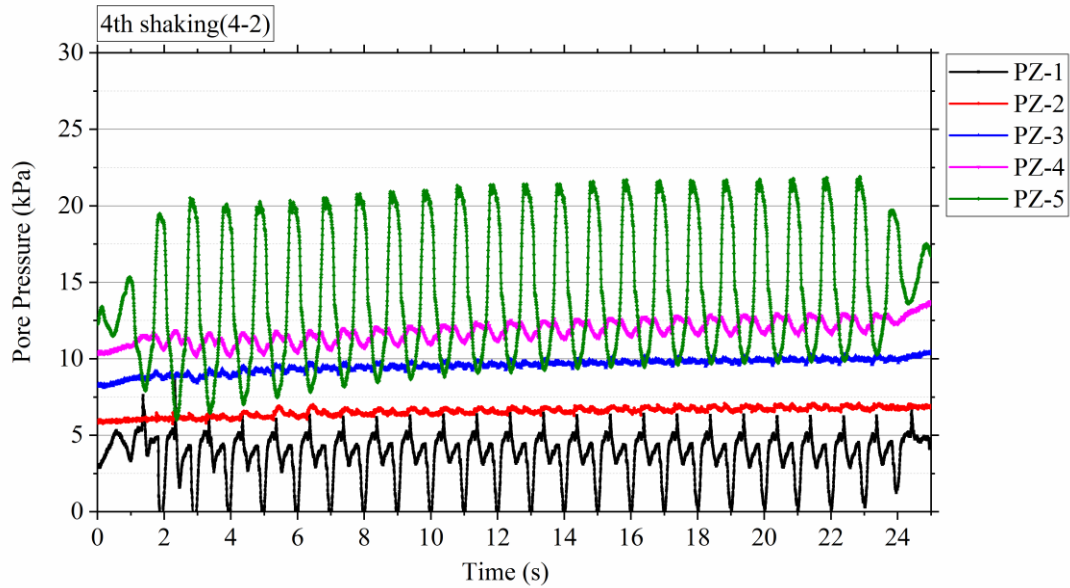


Figure 5-17. Excess pore pressure generation during the shaking event (4-2) at different depths

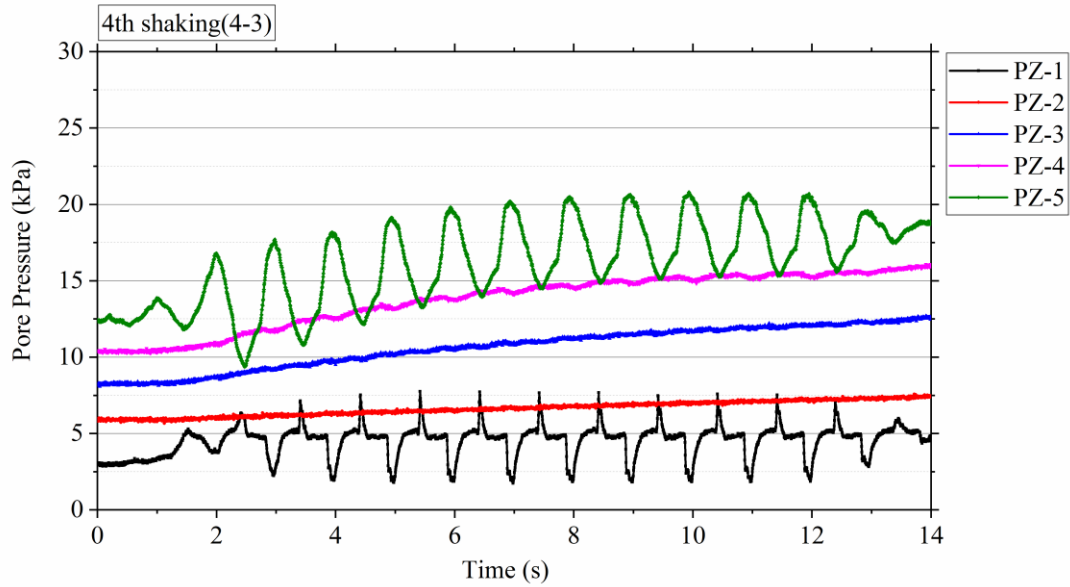


Figure 5-18. Excess pore pressure generation during the shaking event (4-3) at different depths

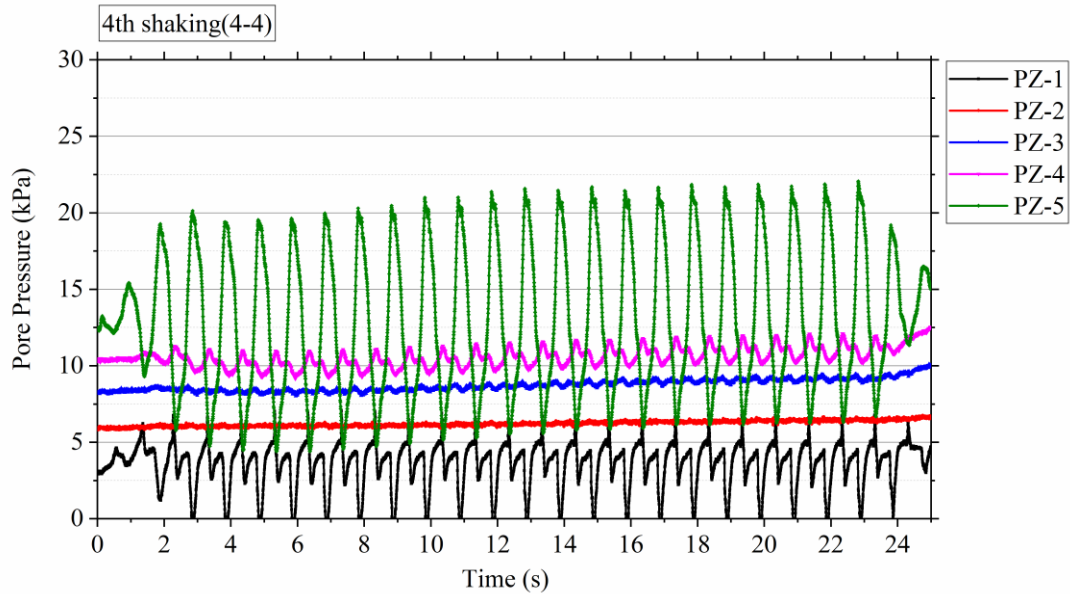


Figure 5-19. Excess pore pressure generation during the shaking event (4-4) at different depths

5.3 Discussion of the shake table test results

5.3.1 Comparison of shake table recordings in the 1st shaking and the 4th shaking

Relative density

The average relative density of the sand deposit can be calculated based on the surface settlement recordings. The surface of the sand settled 4.25 cm, 3.11 cm, 1.95 cm and 1.22 cm after the 1st, 2nd, 3rd, and 4th shaking event, respectively. The calculated average relative density of the sand deposit was approximately 70.8%, 82.3%, 89.5% and 94.1% after the 1st, 2nd, 3rd, and 4th shaking events, respectively. The sand deposit became denser with each shaking.

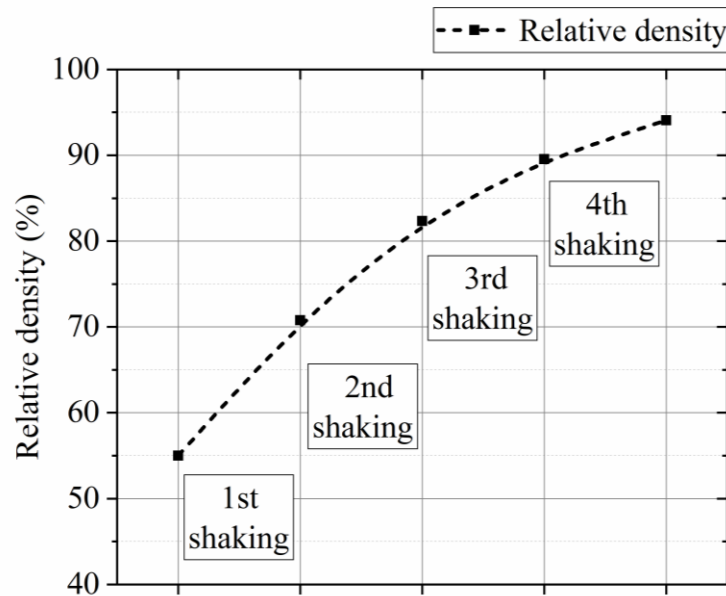


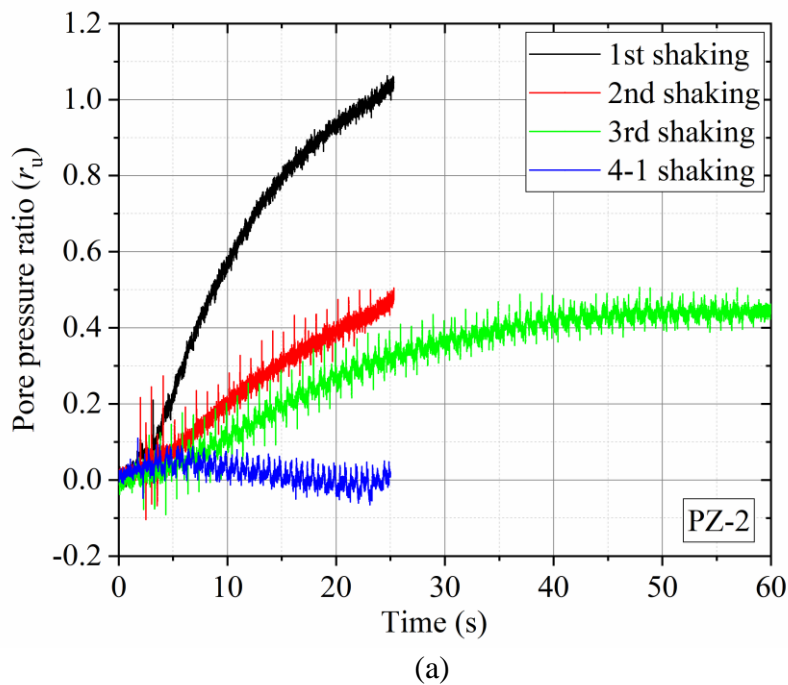
Figure 5-20. Average relative density of the sand deposit before each shaking event

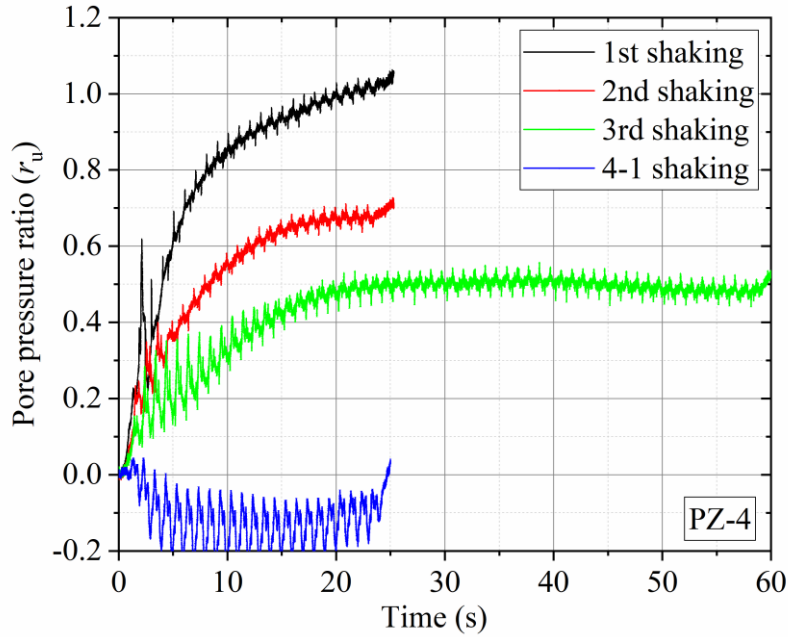
Pore pressure ratio

Figure 5-21 presents the comparison of pore pressure ratio (r_u) between the 1st, 2nd, 3rd, and (4-1) shaking. PZ-2 and PZ-4 were selected to represent the sand at depths of 0.45 m to 0.95 m. r_u at both depths had the similar trend. For PZ-2, r_u exceeded 1.0 in the 1st shaking and reached 0.5 in the 2nd shaking. In the 3rd shaking, r_u reached 0.33 after 25 s and arrived at 0.45 in the end. In the 4th shaking (4-1), r_u was less than 0.1. For PZ-4, r_u exceeded 1.0 in the 1st shaking and reached 0.72 in the 2nd shaking. In the 3rd shaking, r_u reached 0.5 after 25 s and arrived at 0.3 in the end. In the 4th shaking (4-1), r_u was less than 0.05 and even had negative values.

A comparison between the 1st and 2nd shaking suggests that the liquefaction resistance of the sand increased significantly. This has been confirmed by the CPTu results presented in Chapter 4. The liquefaction resistance increase is because of the densification

as results of the 1st shaking and the aging in the first 153 days. A comparison between the 2nd and 3rd shaking suggests that the liquefaction resistance further increased, but not as drastically as that after 1st shaking. The reason might be that the sand only “aged” for 3 weeks and the relative density was already high (82.3%) before the 3rd shaking, so that not much strength gain was obtained. For the 4th shaking (4-1), small r_u (less than 0.1) was reported. This can be explained by the high relative density (89.5%) before this shaking. The sand was classified as very dense sand. Even a very strong shaking such as 0.4g cannot generate much pore pressure.





(b)

Figure 5-21. Pore pressure ratio comparison between 1st, 2nd, 3rd, and 4-1 shaking: (a) PZ-2 (b) PZ-4

5.3.2 Comparison of shake table recordings of the 4th shaking

Figure 5-22 presents the pore pressure ratio (r_u) comparison between the shaking events of (4-2) and (4-4). Both shaking events had the same input motion. However, the sand deposit experienced different shaking events before these two shakings. Before shaking (4-2), the sand experienced a strong shaking event (0.4 g, 25 cycles), while before shaking (4-4), the sand experienced a mild shaking event (0.1g, 14 cycles). The pore pressure readings of PZ-2 and PZ-4 suggest that r_u in shaking (4-4) was slightly smaller than r_u in shaking (4-2). This means mild shaking tends to increase the liquefaction resistance while strong shaking will reduce the liquefaction resistance. This observation is in consistence with the findings of El-Sekelly et al. (2016a).

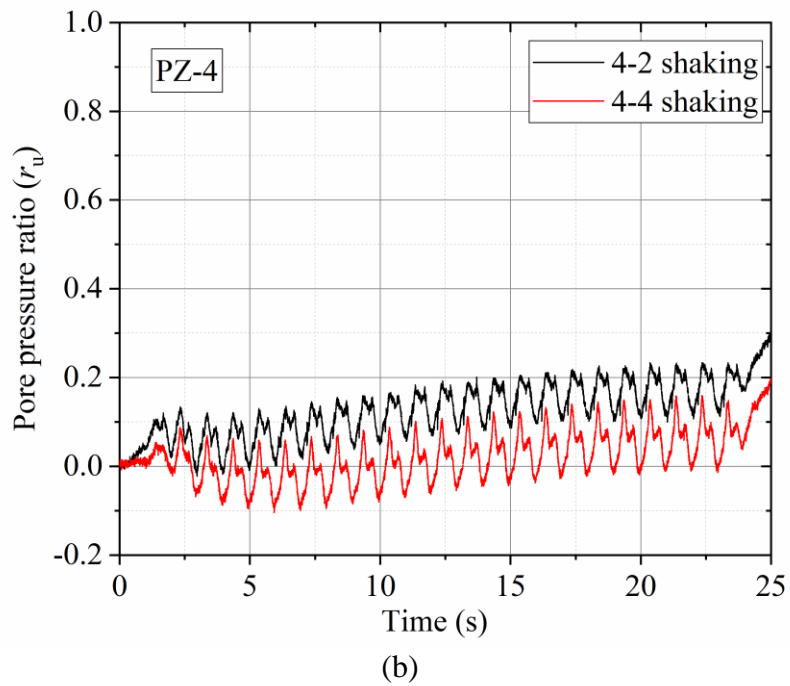
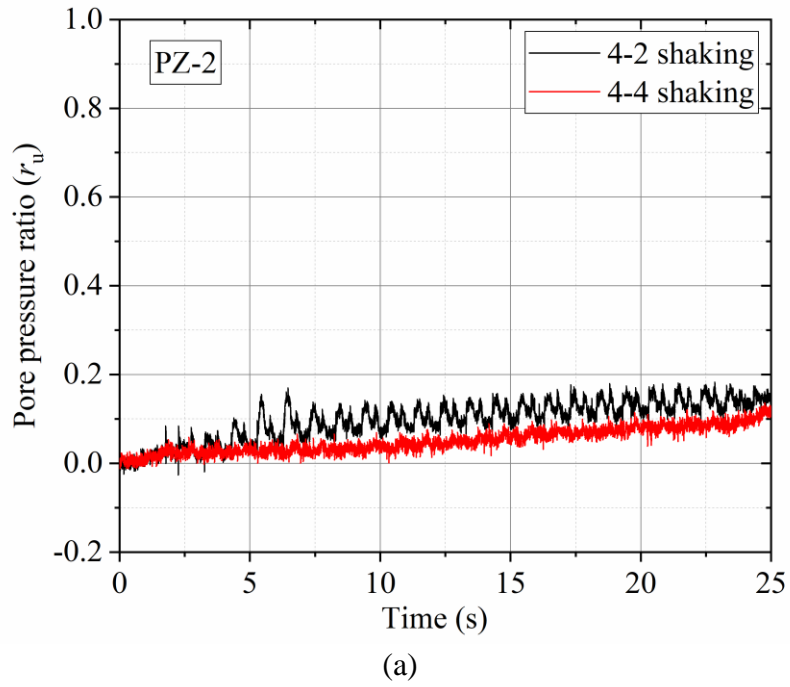


Figure 5-22. Comparison of pore pressure ratios between shaking (4-2) and (4-4): (a) PZ-2 (b) PZ-4

5.4 Conclusion and summary

The following conclusions and summary are based on the data, analysis and interpretation presented in this chapter.

(1) Along with the shaking, the sand deposit became denser and denser. The calculated the relative density of the sand deposit were 70.8%, 82.3%, 89.5% and 94.1% after the 1st, 2nd, 3rd, and 4th shaking event, respectively.

(2) A comparison between 1st and 2nd shaking suggests that the liquefaction resistance of the sand increased a lot. This is confirmed by the CPTu results presented in Chapter 4. The liquefaction resistance increase is because of the densification of 1st shaking and the aging effect in 153 days.

(3) The pore pressure increase was not sensitive to the number of cycles after a certain time. Increased number of loading cycles would not necessarily produce positive excess pore pressures.

(4) The mild shaking tended to increase the liquefaction resistance while strong shaking would reduce the liquefaction resistance.

Chapter 6

Numerical Modelling of Sand Liquefaction for Shake Table Test using PM4Sand

This chapter presents the development of a numerical model simulations of the shake table tests presented in Chapter 3. The *FLAC* algorithm and PM4Sand are introduced. A series of cyclic undrained direct simple shear tests (DSS) of the sand used in the shake table tests are conducted. The laboratory test results are used for a rigorous model calibration of PM4Sand. A numerical model is developed in *FLAC* to simulate the shake table tests. A detailed comparison of the simulation and shake table testing results is presented. In this chapter, the following questions are addressed: 1) What is the liquefaction potential for F50 Ottawa sand under relatively low confining stress levels? 2) Can the numerical simulations successfully capture key features as well as the trends and magnitudes of the shake table test recordings? 3) What are the strengths and limitations of the PM4Sand model in predicting soil response under small stress levels? Answering these questions can provide insights for further understanding of liquefaction and advance soil constitutive models for liquefaction.

6.1 Introduction of *FLAC* algorithm and PM4Sand

6.1.1 *FLAC* algorithm

The *FLAC* computer program (Fast Lagrangian Analysis of Continua) uses explicit, finite difference (FD) approach (ITASCA 2016) to perform static and dynamic, non-linear, numerical analyses of continuous media and it has been extensively used for analysis of a variety of geotechnical problems. Most importantly, the code is relatively flexible and adaptable in that it allows a user to define problem specific constitutive relationships. Detailed descriptions of the code and its capabilities are described in detail elsewhere (ITASCA 2016); therefore, only the details of the code implementation specific to the current modeling effort are addressed herein.

(1) Interface elements in *FLAC*

FLAC provides interfaces that are characterized by Coulomb sliding and/or tensile separation. Interfaces have the properties of friction, cohesion, dilation, normal and shear stiffness, and tensile strength. Although there is no restriction on the number of interfaces or the complexity of their intersections, it is generally not reasonable to model more than a few simple interfaces with *FLAC* (ITASCA 2016).

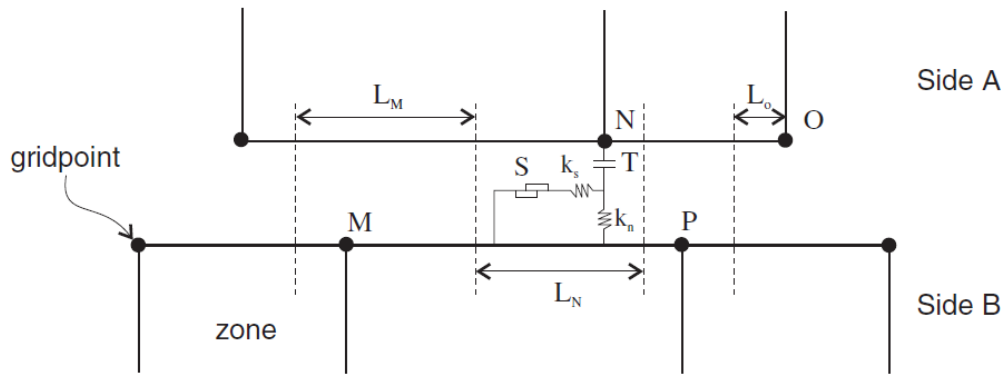


Figure 6-1 Schematic of the FLAC interface element (Itasca 2016)

A schematic of an interface in *FLAC* is represented in Figure 6-1. An interface is represented by normal and shear stiffness between two planes which may contact one another. In the figure, S represents the slider; T is the tensile strength; k_n is the normal stiffness; k_s is the shear stiffness; L_n is the length associated with gridpoint N ; L_m is the length associated with gridpoint M ; and the dashed line '-----' denotes limits for joint segments (placed halfway between adjacent gridpoints). *FLAC* uses a contact logic, which is similar in nature to that employed in the distinct element method, for either side of the interface (e.g., Cundall and Hart 1992). The code keeps a list of the grid points (i,j) that lie on each side of any particular surface. Each point is taken in turn and checked for contact with its closest neighboring point on the opposite side of the interface. Referring to Figure 6-1, grid point N is checked for contact on the segment between grid points M and P . If contact is detected, the normal vector, n , to the contact grid point, N , is computed. A “length,” L , is also defined for the contact at N along the interface. This length is equal to half the distance to the nearest grid point to the left of N plus half the distance to the nearest grid point to the right, irrespective of whether the neighboring grid point is on the same

side of the interface or on the opposite side of N . In this way, the entire interface is divided into contiguous segments, each controlled by a grid point.

(2) Dimensions of the finite difference zones

Proper dimensioning of the finite difference zones is required to avoid numerical distortion of propagating ground motions, in addition to accurate computation of model response. The *FLAC* manual (Itasca 2016) recommends that the length of the element Δl be smaller than one-tenth to one-eighth of the wavelength λ associated with the highest frequency f_{max} component of the input motion.

(3) Damping

Natural dynamic systems contain some degree of damping of the vibration energy within the system; otherwise, the system would oscillate indefinitely when subjected to driving forces. Damping is due, in part, to energy loss as a result of internal friction in the intact material and slippage along interfaces, if these are present. For a dynamic analysis, the damping in the numerical simulation should reproduce in magnitude and form the energy losses in the natural system when subjected to a dynamic loading. In soil and rock, natural damping is mainly hysteretic (i.e., independent of frequency – see Gemant and Jackson 1937, and Wegel and Walther 1935). It is difficult to reproduce this type of damping numerically, because (a) there are no laws that describe the complete material response; and (b) existing laws that capture many important aspects have many material parameters, requiring extensive calibration (ITSCA 2016).

In *FLAC 8.0* dynamic analysis, there are four types of damping model provided: Rayleigh damping, hysteretic damping, local damping and artificial viscosity. In time-domain programs, Rayleigh damping is commonly used to provide damping that is

approximately frequency-independent over a restricted range of frequencies. The hysteretic damping allows strain-dependent modulus and damping functions to be incorporated directly into the *FLAC* simulation. This makes it possible to make direct comparisons between calculations made with the equivalent-linear method and a fully nonlinear method, without making any compromises in the choice of constitutive model. Local damping in dynamic problems is useful as an approximate way to include hysteretic damping. However, it becomes increasingly unrealistic as the complexity of the waveforms increases. Artificial viscosity can be used for analyses involving sharp dynamic fronts.

6.1.2 PM4Sand constitutive model

The plasticity model for sand (PM4Sand) follows the basic framework of the stress-ratio controlled, critical state compatible, bounding surface plasticity model for sand presented by Dafalias and Manzari (2004). Modifications to the model were developed and implemented by Boulanger (2010, version 1), Boulanger and Ziotopoulou (2012, version 2), Boulanger and Ziotopoulou (2015, version 3) and Boulanger and Ziotopoulou (2017, version 3.1). The improvements were made to better approximate the stress-strain responses important to geotechnical earthquake engineering applications (Boulanger and Ziotopoulou 2017). The PM4Sand has a narrow stress-ratio based elastic cone and three other key surfaces: the bounding, dilation and critical-state surfaces. The locations of the dilation and bounding surfaces are dependent on the relative state of the soil (the difference between the relative density and the relative density at critical state for the current confining pressure), such that they both rotate when the relative state of the soil changes. As the soil

is sheared towards critical state, both surfaces approach each other until they coincide at the critical state stress ratio (Kamai 2011, Boulanger and Ziotopoulou 2017). The model was coded as a user defined material (UDM) in a dynamic link library (DLL) for use with the commercial program FLAC 8.0 (Itasca 2016).

The PM4Sand model has 22 input parameters. Out of these, three parameters are considered primary and are required as inputs. They are the sand's apparent relative density D_r , the shear modulus coefficient G_o and the contraction rate parameter h_{po} (Boulanger and Ziotopoulou 2017).

D_r is the primary variable controlling dilatancy and stress-strain response characteristics. It can be commonly estimated based on CPT or SPT penetration resistances. The following relationships by Idriss and Boulanger (2008) are often used:

$$D_r = \sqrt{\frac{(N_1)_{60}}{C_d}} \quad (6-1)$$

where $(N_1)_{60}$ is the normalized SPT blow counts, and $C_d = 46$.

$$D_r = 0.465 \left(\frac{q_{C1N}}{C_{dq}} \right)^{0.264} - 1.063 \quad (6-2)$$

Where q_{C1N} is the normalized cone penetration resistance, and $C_{dq} = 0.9$.

G_o is the shear modulus coefficient and the primary variable controlling the small strain shear modulus G_{max} as:

$$G_{max} = G_o p_A \left(\frac{p}{p_A} \right)^{1/2} \quad (6-3)$$

where p_A is the atmospheric pressure (101.3 kPa), p is the mean effective stress.

A value for G_o can be estimated on the modified correlation based on the shear wave velocity as:

$$G_o = \frac{\rho(V_{s1})^2}{p_A} / \left(\frac{1+K_o}{2}\right)^{0.5} \quad (6-4)$$

Where ρ is the dry density of the material and K_o is the coefficient of lateral earth pressure at rest.

Contraction rate parameter (h_{po}) is used to modify the contractiveness and is able to calibrate the model to specific values of the target cyclic resistance ratio (*CRR*) or cyclic strength. The *CRR* is commonly estimated based on CPT or SPT penetration resistances and liquefaction correlations. The calibration of h_{po} should be performed last because its value can depend on the values assigned to other parameters (Boulangier and Ziotopoulou 2017).

The other 19 parameters include 2 flags and 17 secondary input parameters. All the default values of these secondary input parameters have been selected to generally produce reasonable agreement with the trends in typical design, empirical and semi-empirical, relationships (Boulangier and Ziotopoulou 2017).

6.2 Numerical modeling of shake table test

6.2.1 Model construction and boundary conditions

Figure 6-2 shows the model construction and boundary conditions in *FLAC*. Each layer of the laminar shear box was modeled by two blocks of elastic elements. The sand was modeled by advanced constitutive model PM4Sand Version 3.1. The gravel was modeled using elastic elements. The geomembrane bag was simulated by two thin layers of elastic elements. The parameters for PM4Sand were summarized in Table 6-1. The

parameters were all calibrated based on a series of direct simple shear tests (that is presented in section 6.2.2) and resonant column tests. The parameters for elastic elements were summarized in Table 6-2. As suggested by FLAC manual (Itasca 2016), the elastic properties of the laminar shear box elements were reduced to speed up the calculation. No obvious deformation of the LSB blocks was observed. The shear modulus of the geomembrane bag was only a quarter of that of the sand, so that the bag was flexible enough compared with the sand.

The boundary of left block of the LSB was rigidly attached to that of right block of LSB at the same level to simulate a rigid LSB frame during shaking. The sliding of LSB frames relative to the frames immediately above and below was achieved by using interface settings between adjacent blocks. The interface between LSB frames has a small friction angle and a large tensile strength in normal direction. Based on the measurement of the friction coefficient between the LSB frames, a 5° friction angle was used for the interface setting. The tensile strength in normal direction was set to be 5×10^7 kPa/m to make sure that no separation was allowed between the slider and rail. For the interfaces between the geomembrane bag and the box, a $2/3$ of the sand friction angle was used. There was no tensile strength so that the separation between the box and the bag was allowed. K_n and K_s values were picked based on *FLAC* suggestions and the simulation results are not sensitive to those two values, based on parametric study. The detailed setting of interface parameters is summarized in Table 6-2.

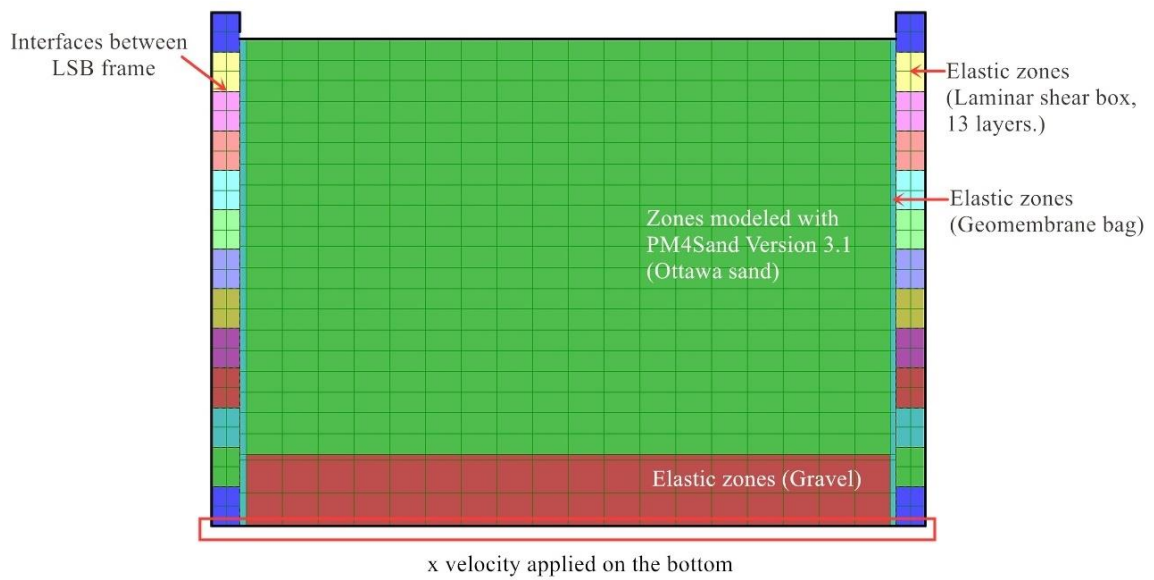


Figure 6-2 *FLAC* meshing with boundary conditions

Table 6-1 Soil properties for PM4Sand elements

Parameter	Ottawa sand	Source of measurements
D_r (%)	55	Controlled by pluviation
e_{min}	0.48	Measured by Kramer (2013)
e_{max}	0.78	Measured by Kramer (2013)
V_s (m/sec)	160	Resonant column test
h_{p0}	0.15	DSS calibration
G_0	619.0	Based on V_s

Table 6-2 Properties for elastic elements

Parameter	For gravel	For laminar shear box	For geomembrane bag
Density (kg/m^3)	2000	1600	940
Shear modulus (Pa)	2×10^8	2×10^9	1×10^7
Bulk modulus (Pa)	3.3×10^8	4.3×10^9	2×10^7

Table 6-3 Interface parameters and their values

Parameters	Interfaces between laminae	Interfaces between bag and box
K_n (kPa/m)	1×10^9	1×10^9
K_s (kPa/m)	1×10^9	1×10^9
Friction angle (°)	5	20
Tensile strength (kPa/m)	5×10^7	0

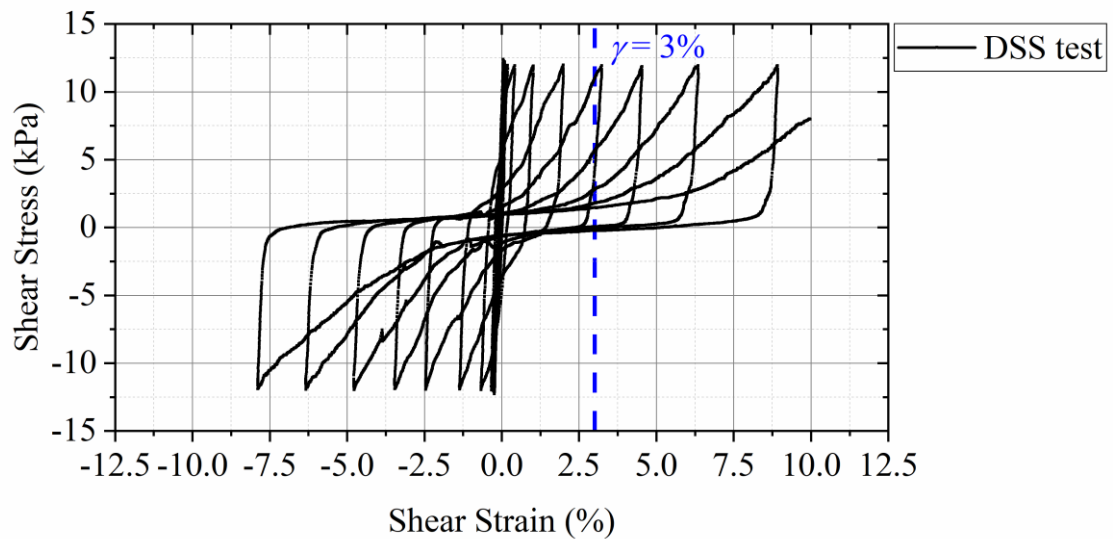
6.2.2 Model calibration

Cyclic DSS tests

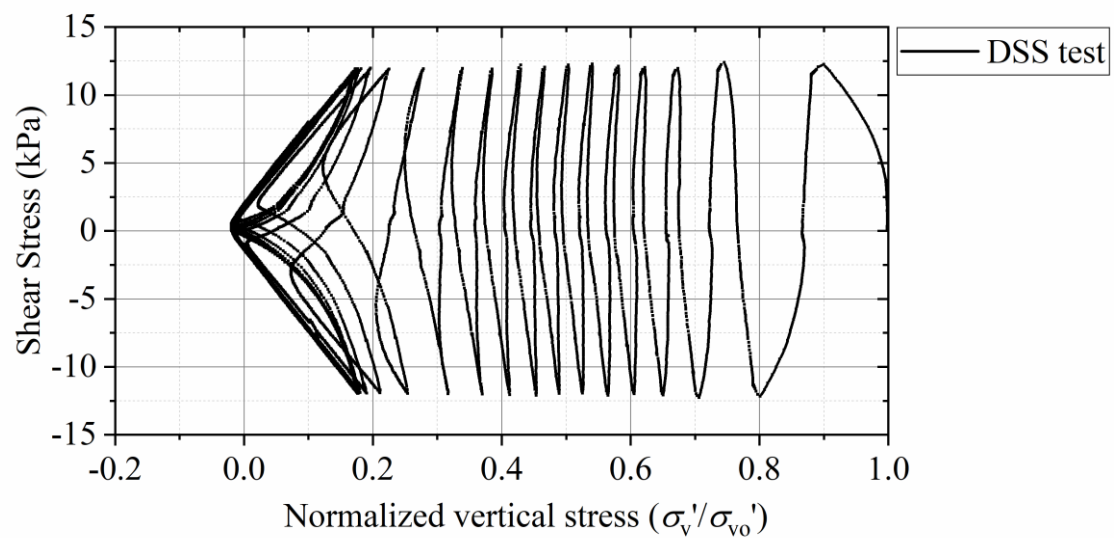
A series of cyclic DSS were performed on the Ottawa Sand. The sand was shipped to the University of California, Davis and the DSS tests on the sand were performed by Dr. Ziotopoulo's research team. The cyclic DSS tests were run under a deformation-controlled mode using stress-controlled criteria for reversal of loading directions. The specimens were consolidated to vertical confining stress (σ'_{vo}) of 100 kPa prior to shear. The tests were performed at different cyclic stress ratios (CSRs).

The cyclic loading responses of the sand ($\sigma'_{vo} = 100$ kPa, $CSR = 0.12$) are shown in Figure 6-3. Figure 6-3(a) shows the shear stress (τ) vs. shear strain (γ) relationship, τ vs. normalized vertical effective stress (σ'_v/σ'_{vo}), σ'_v/σ'_{vo} vs. γ , γ vs. number of loading cycles (N), and pore pressure ratio (r_u) vs. N . The peak shear strain γ exceeds 1% after 13 loading cycles and exceeds 3% after 14 loading cycles. The peak r_u exceeds 0.95 after 13 loading cycles and reaches 1.0 after 14 loading cycles. From the shear stress vs. strain loop, in the first 12 cycles, the shear strain accumulation rate is very low and seems constant. Starting

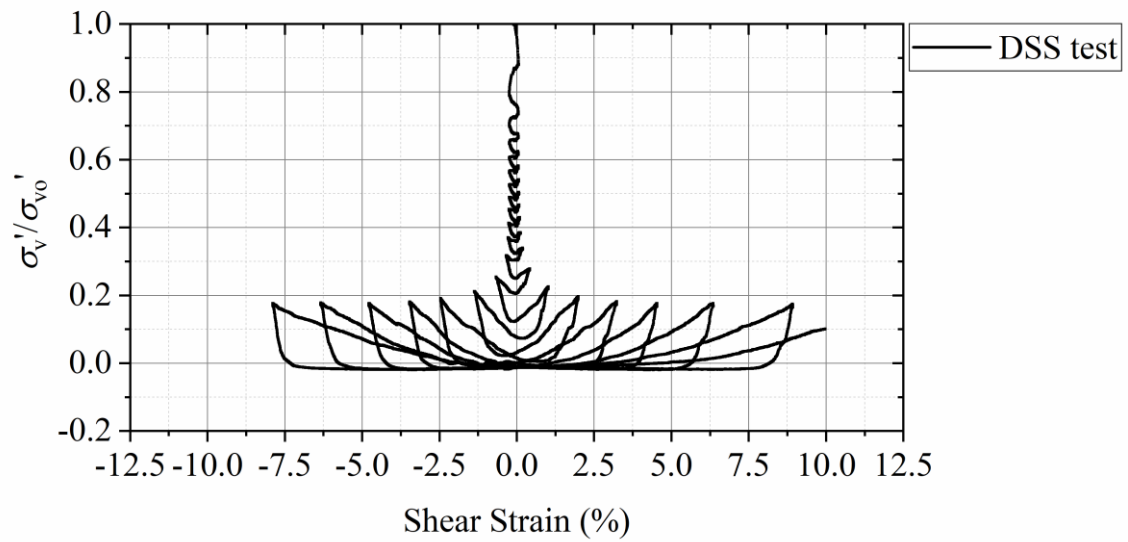
from the 13th cycle, the shear strain accumulation rate increases rapidly with every cycle of loading because the specimen had lost a significant amount of vertical effective stress. The value of σ'_v/σ'_{v0} reduces to about 0.75 during the first loading cycle, to about 0.3 in the 8 following loading cycles, and to about 0.21 in the 12th cycle. The values of σ'_v/σ'_{v0} then show transient increases and decreases with each loading cycle, forming loops in the stress path plot.



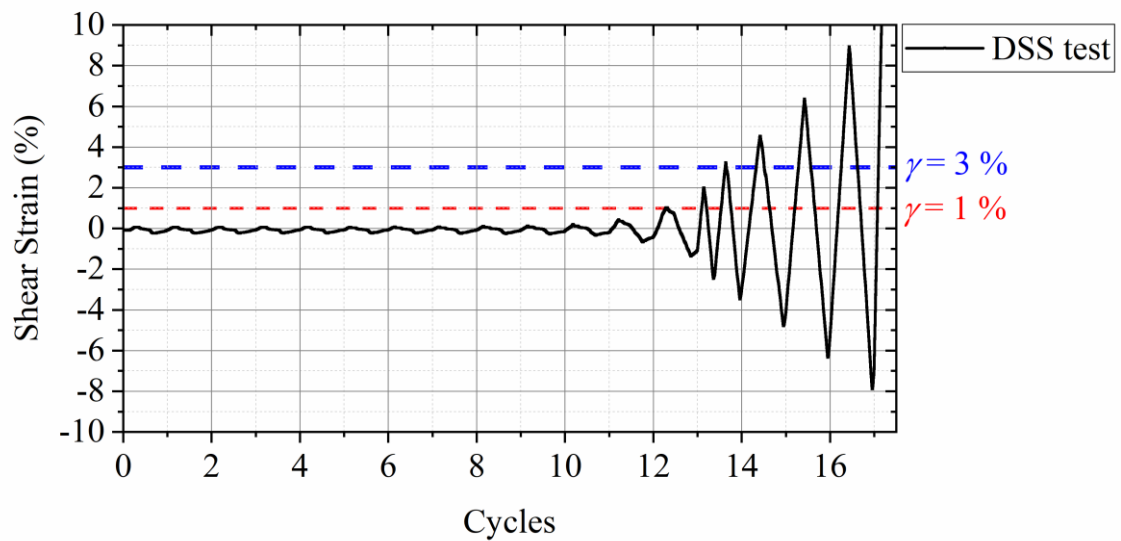
(a) Stress and strain loop



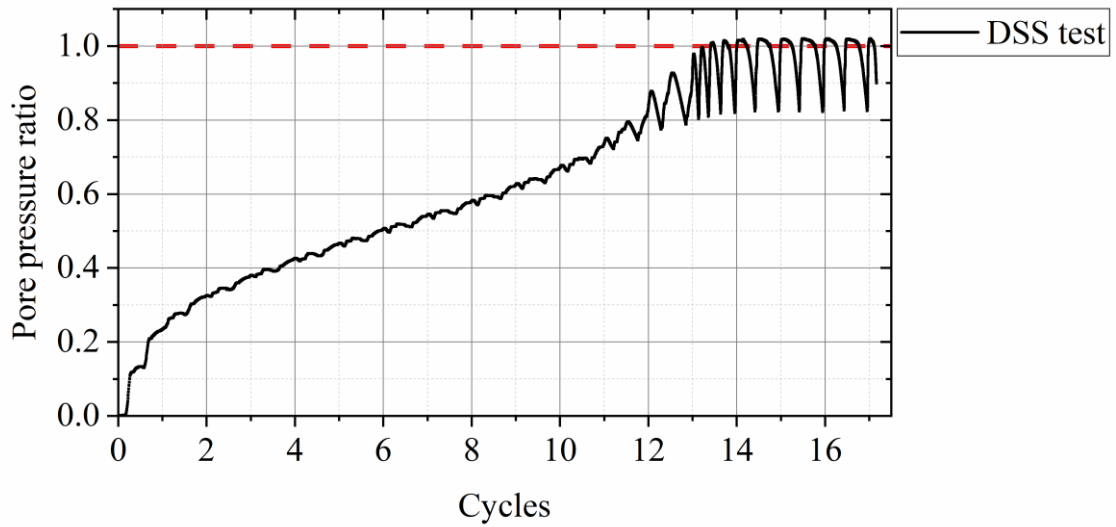
(b) Stress path



(c) Normalized vertical stress vs. strain



(d) shear strain vs. number of cycles



(e) Pore pressure ratio vs. number of cycles

Figure 6-3 Cyclic loading responses of sand of $D_r = 55\%$ ($\sigma'_{vo} = 100$ kPa, $CSR = 0.12$) sheared up to shear strain peak = 10% (DSS test)

The cyclic stress ratio (CSR) vs. number of loading cycles (N) to reach several failure criteria was evaluated for sand specimen with D_r of about 55% consolidated to 100 kPa. The CSR vs. number of loading cycles to reach 3% peak shear strain ($N_\gamma = 3\%$) is shown in Figure 6-4 for consolidation effective stresses of 100 kPa. A total of six CSR s were selected in the tests: 0.08, 0.1, 0.12, 0.13, 0.14 and 0.15. As the CSR increases, it takes less number of loading cycles for the sand to reach 3% peak shear strain. A power relationship can be established between CSR and N as:

$$CSR = 0.244N^{-0.271} \quad (6-5)$$

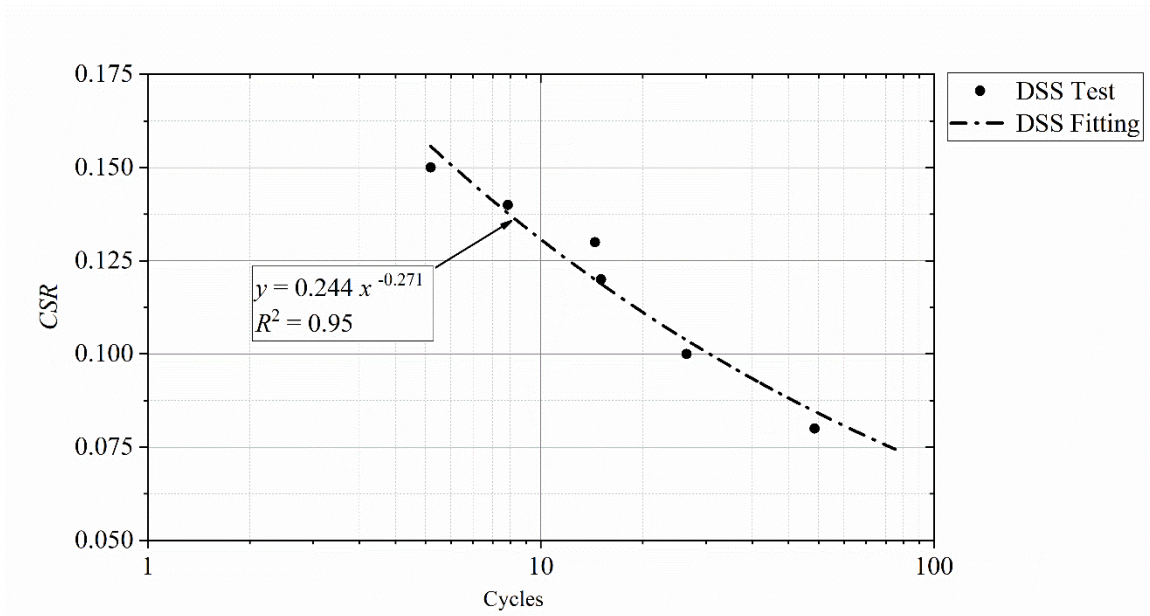


Figure 6-4 CSR vs. $N_{\gamma=3\%}$ curves from DSS tests

Single element test in FLAC using PM4Sand

A series of undrained single element test simulations were performed in *FLAC* to simulate the cyclic DSS tests. As the average relative density of the sand in the shake table test is 55%, D_r of PM4Sand remains 0.55 in the simulation. The resonant column test suggests a normalized shear wave velocity of 160 m/s, which was directly used as an input parameter. The elastic shear modulus at one atmosphere, G_{max} , is derived from the normalized shear wave velocity, V_{s1} , such that:

$$G_{max} = \rho(V_{s1})^2 \quad (6-6)$$

where ρ is the dry density of the material. The shear modulus constant (G_o) can then be found using equation (6-3).

The parameter h_{p0} is obtained in an iterative process, by matching single-element, undrained, cyclic DSS simulations to the target liquefaction triggering curve shown in

Figure 6-4. The model is calibrated to the cyclic stress ratio required to reach 3% shear strain in 14 cycles and then inherently captures the response under a range of other stress ratios. Undrained DSS simulation results of the calibrated model, for a range of cyclic stress ratios are presented in Figure 6-5. All the activated PM4Sand parameters in calibration are summarized in Table 6-4. Figure 6-5 suggests a satisfactory calibration of PM4Sand for the triggering curve.

Table 6-4 Activated PM4Sand parameters in calibration

Parameters	D_r	V_s (m/s)	h_{p0}
Values	55 %	160	0.15

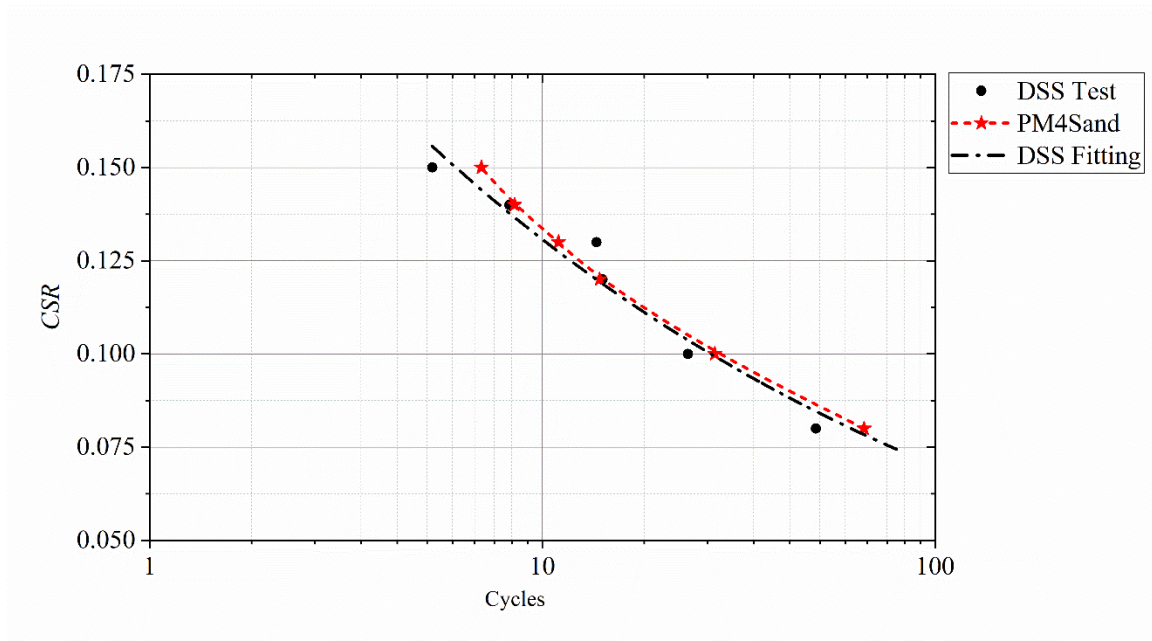
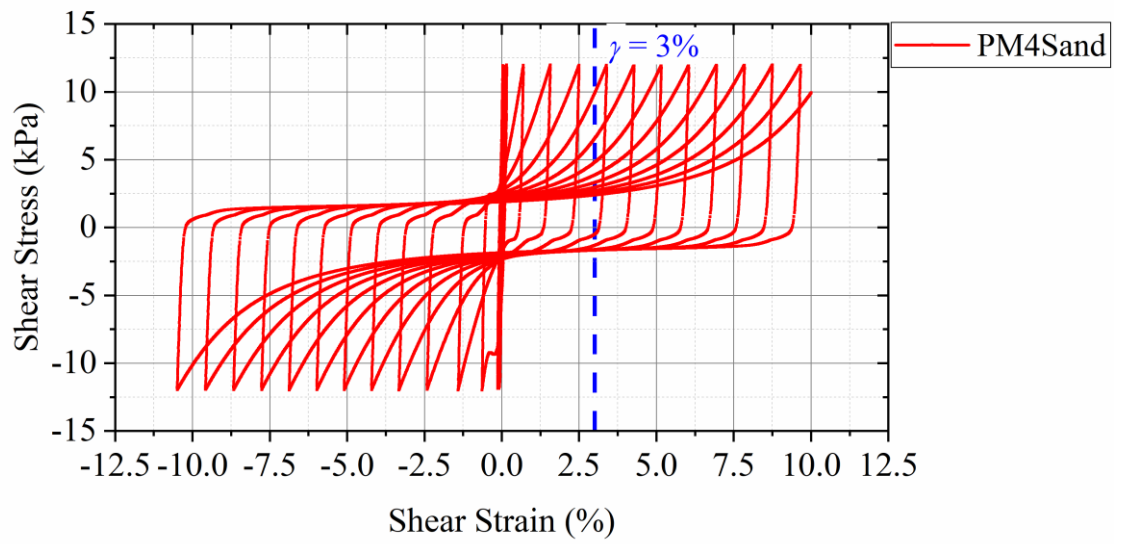
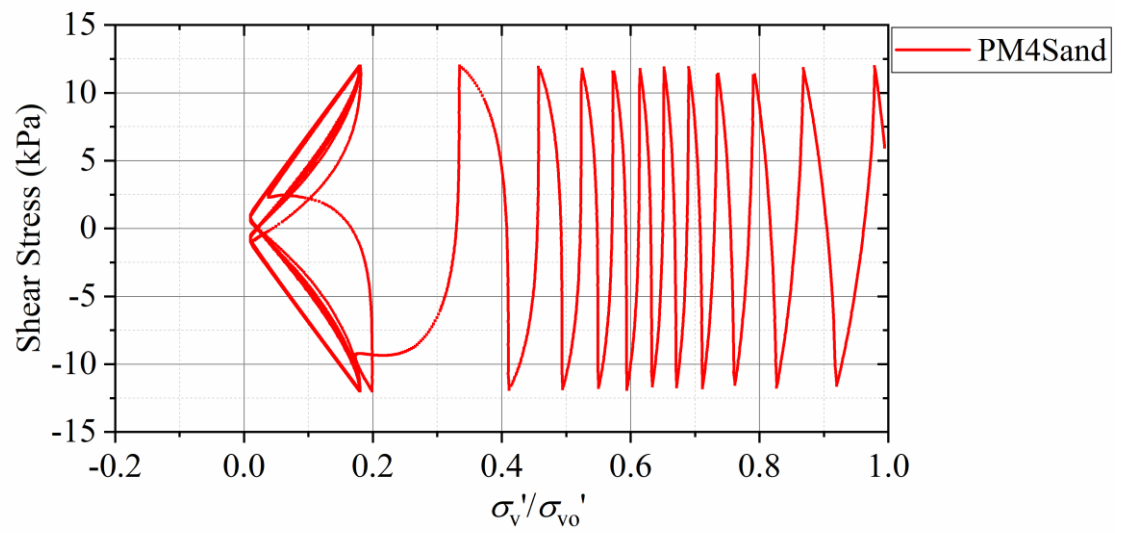


Figure 6-5 Triggering calibration for PM4Sand

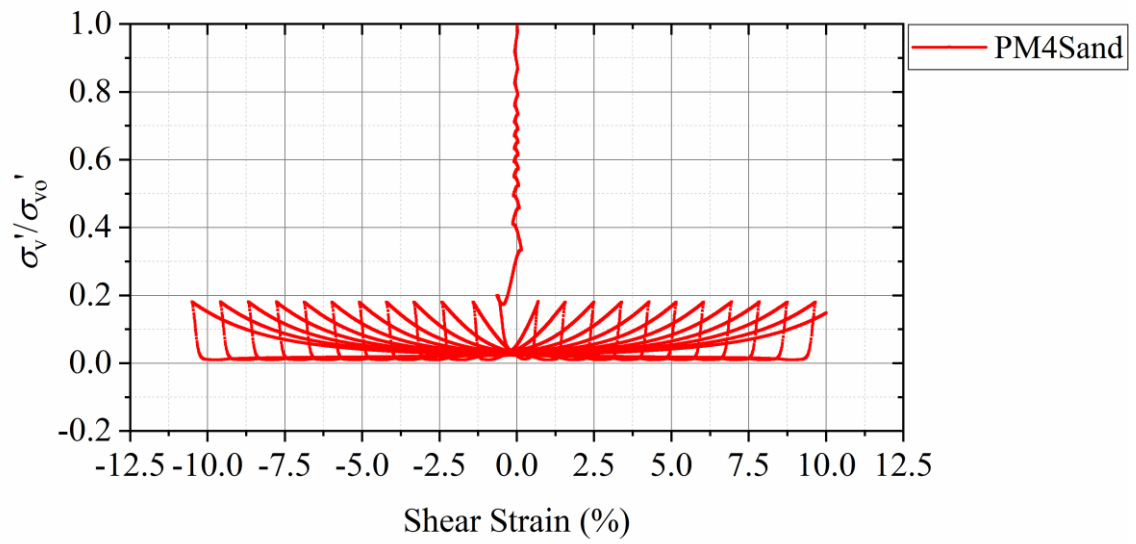
In order to compare the detailed behavior of the PM4Sand with the DSS test, one *CSR* is selected and the cyclic loading responses of the sand (at $\sigma'_{vo} = 100$ kPa, $CSR = 0.12$) are shown in Figure 6-6. Similar to the DSS results at this *CSR*, shear stress (τ) vs. shear strain (γ), τ vs. normalized vertical effective stress (σ'_v/σ'_{vo}), σ'_v/σ'_{vo} vs. γ , γ vs. number of loading cycles (N) and pore pressure ratio (r_u) vs. N are shown in the figure. The peak shear strain γ exceeds 1% at 11th loading cycles and exceeds 3% at 14th loading cycles. The peak r_u exceeds 0.95 at 11th loading cycles and reaches 1.0 at 12th loading cycles. From the stress and strain loop, in the first 10 cycles, the shear strain accumulation rate is very low and seems constant. Starting from the 11th cycle, the shear strain accumulation rate increases rapidly with every cycle of loading because the specimen had lost a significant amount of vertical effective stress. The value of σ'_v/σ'_{vo} reduces to about 0.9 during the first loading cycle, to about 0.31 in the 10 following loading cycles, and to about 0.2 in the 12th cycle. The values of σ'_v/σ'_{vo} then show transient increases and decreases with each loading cycle, forming loops in the stress path plot. A comparison between Figure 6-3 and Figure 6-6 suggests that the element-level behavior of PM4Sand is close to the sand response in DSS test.



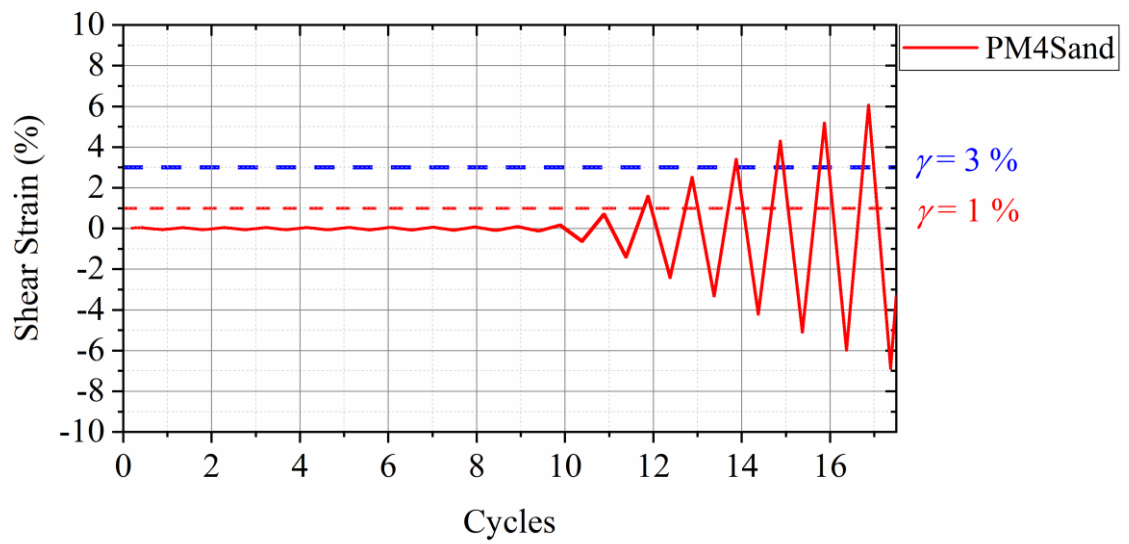
(a) Stress and strain loop



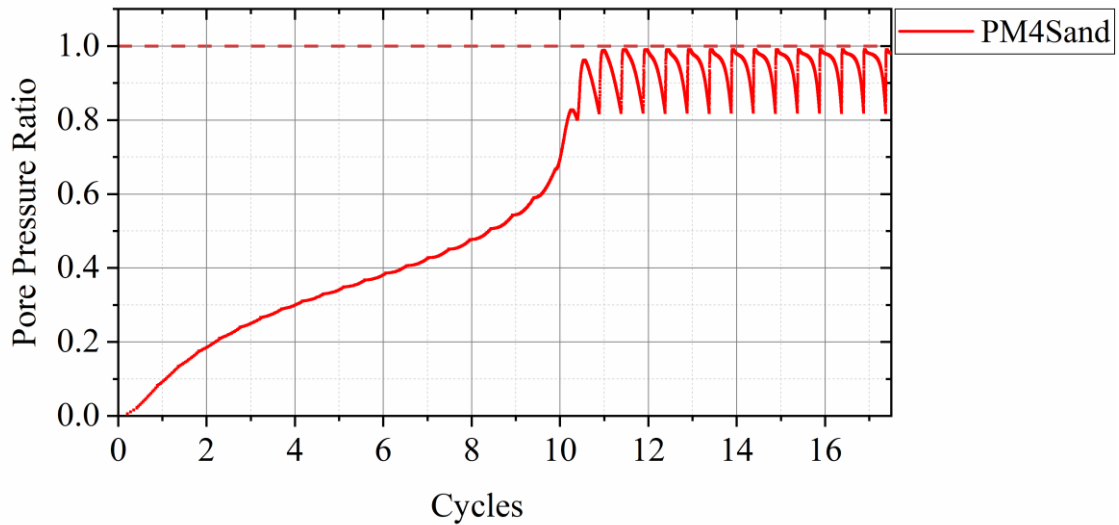
(b) Stress path



(c) Normalized vertical stress vs. strain



(d) shear strain vs. number of cycles



(e) Pore pressure ratio vs. number of cycles

Figure 6-6 Cyclic loading responses of sand at $Dr = 55\%$ ($\sigma'_{vo} = 100$ kPa, $CSR = 0.12$) sheared up to shear strain peak = 10% (PM4Sand)

6.3 Comparison of simulation and shake table test results

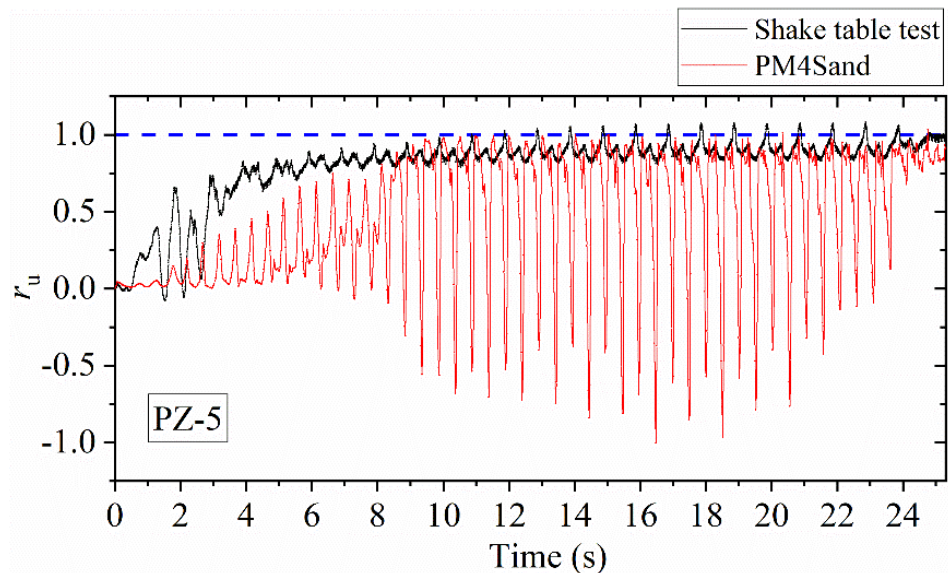
Comparison of simulation results with observations and measurements from the shake table test are presented in the following section. Numerical results are reported for the same locations of the instruments in the shake table model.

6.3.1 Excess pore pressure generation during shaking

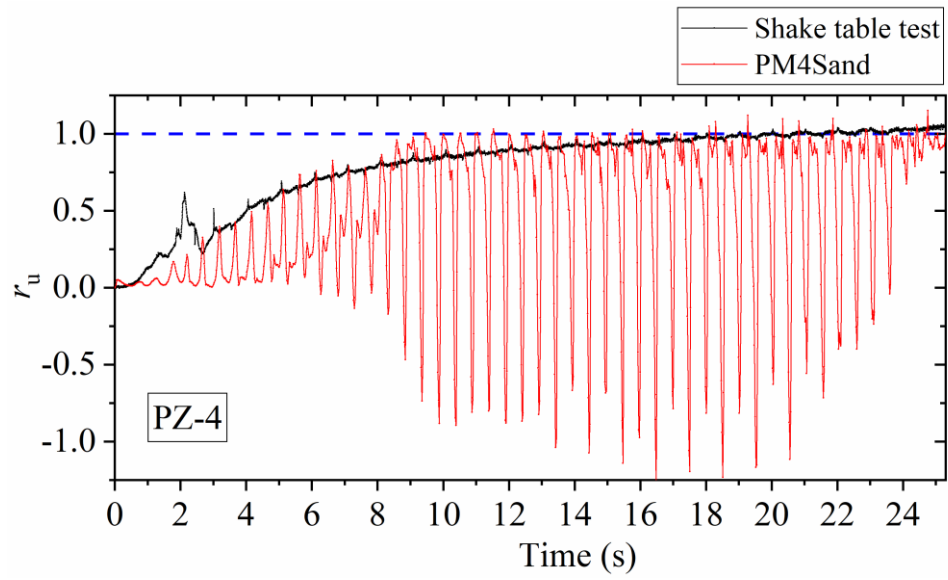
Figure 6-7 presents the pore pressure ratio comparison of the shake table test (the 1st shaking) with simulations. For PZ-5 (depth = 1.2 m), the computed response is under-predicted for the first 8 seconds. The peak r_u reaches 1.0 at $t = 10$ s. After that, the r_u from simulation has large fluctuations towards the end of shaking. For PZ-4 (depth = 0.95 m), the simulation results have a good match with the shake table test results in the first 8

seconds. The peak r_u reaches 1.0 at $t = 10$ s. For PZ-3 (depth = 0.70 m), the computed response is slightly over-predicted for the first 8 seconds. The peak r_u reaches 1.0 at $t = 9$ s. For PZ-2 (depth = 0.45 m), the computed response is over-predicted for the first 8 seconds. The peak r_u reaches 1.0 at $t = 9$ s. For PZ-1 (depth = 0.20 m), the computed response is under-predicted compared with the shake table tests. The piezometer reading from shake table test at this depth might be affected by sensor settlement during shaking.

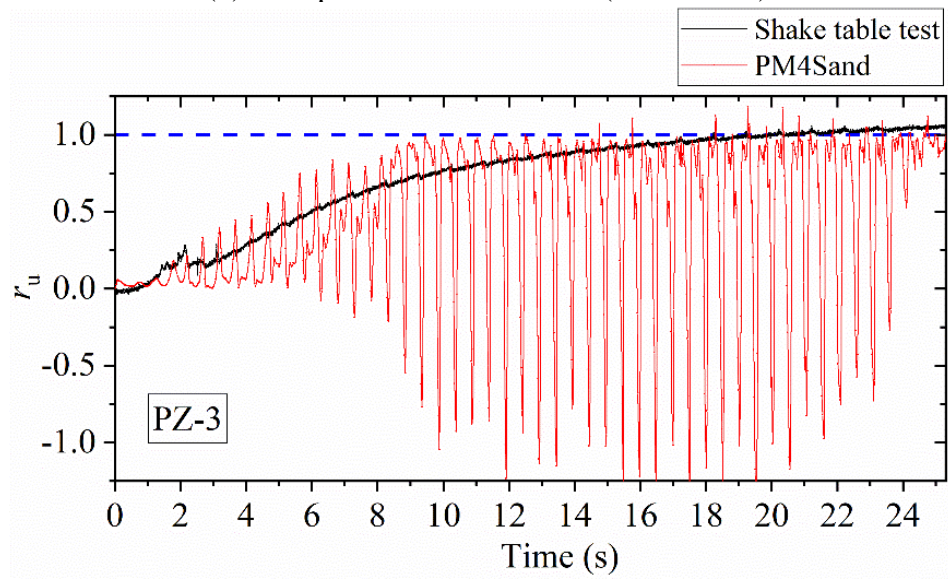
In general, the simulation results over-predict the liquefaction occurrence for most of the sand deposit. The PM4Sand model results suggest that liquefaction happens from 9s to 10s. The model is conservative in liquefaction occurrence prediction.



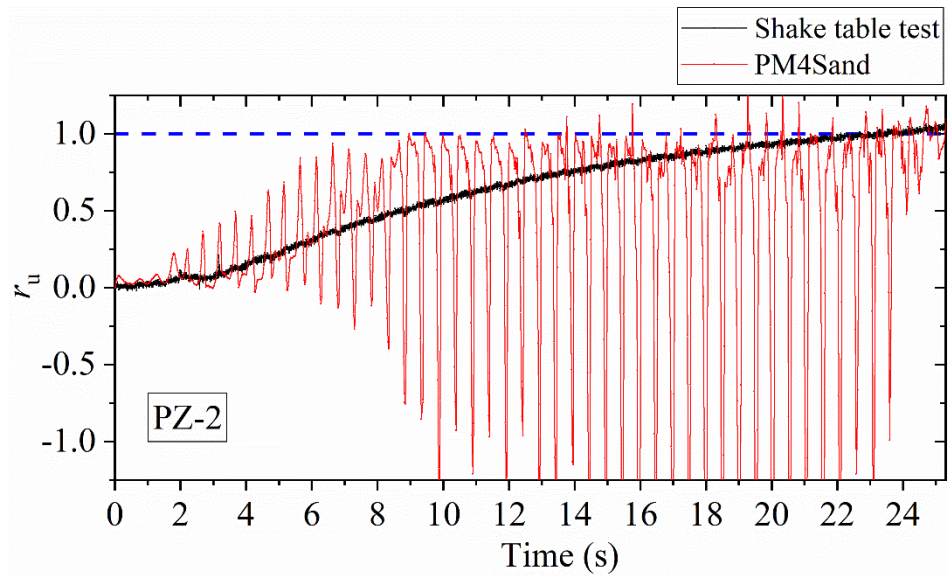
(a) Pore pressure ratio at PZ-5 ($D = 1.2$ m)



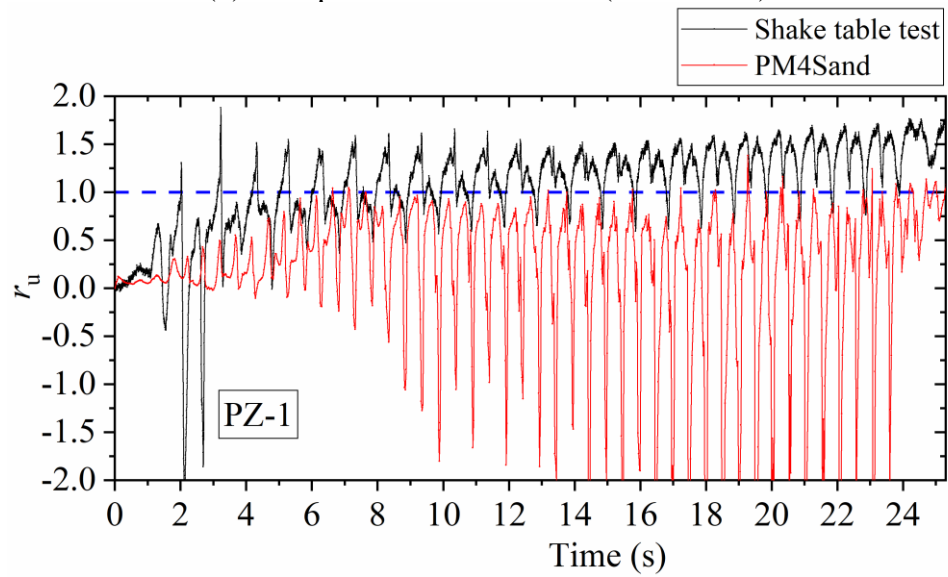
(b) Pore pressure ratio at PZ-4 ($D = 0.95$ m)



(c) Pore pressure ratio at PZ-3 ($D = 0.70$ m)



(d) Pore pressure ratio at PZ-2 ($D = 0.45$ m)



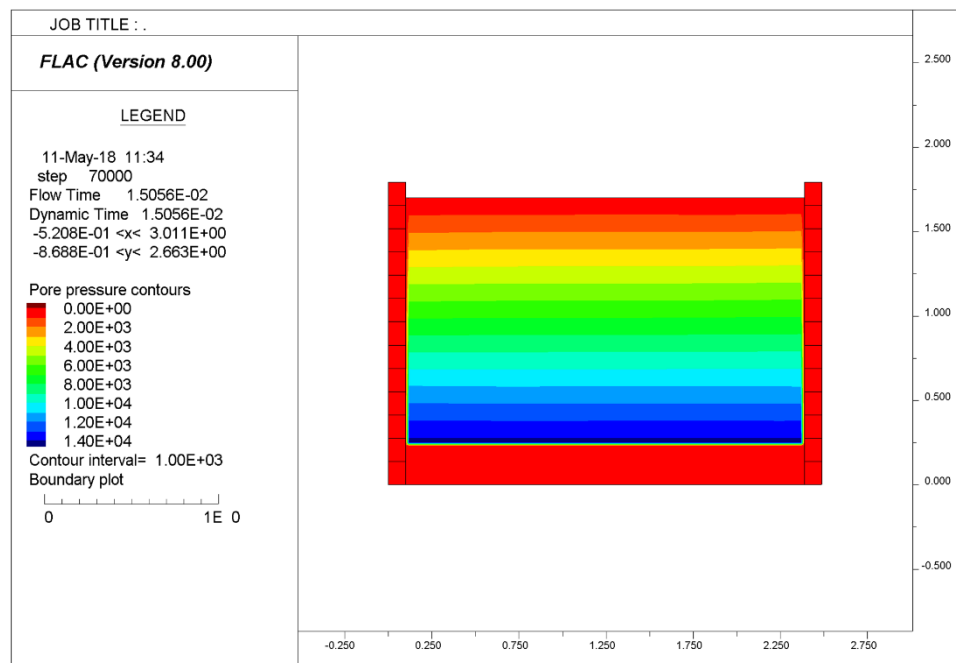
(e) Pore pressure ratio at PZ-1 ($D = 0.20$ m)

Figure 6-7 Pore pressure ratio time histories at five different depths: comparison of the shake table test (1st shaking) with simulations

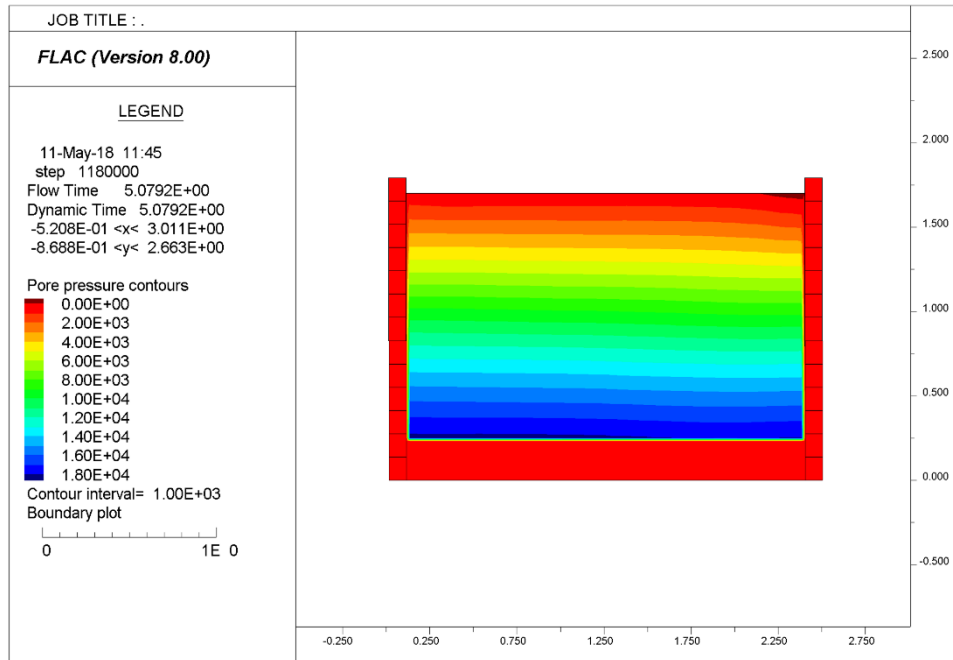
6.3.2 Pore pressure contour at different time

Figure 6-8 shows the contour plots of pore pressures during shaking at selected time ($t = 0.015$ s, 5.08 s, 10.00 s, 15.55 s, 20.19 s and 25.32 s). Figure 6-8 (a) shows the pore

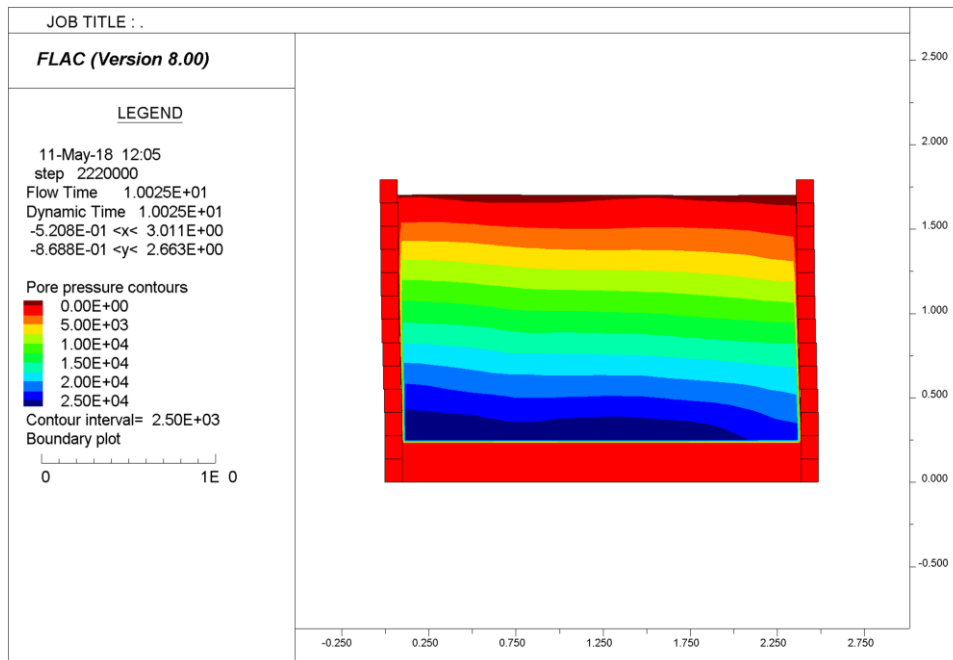
pressure contour at the beginning of the shaking with no excess pore pressure generation. The pore pressure increases as shaking starts. At $t = 10$ s, relative displacement of the LSB is observed. The reason is the sand deposit has liquefied based on the r_u readings from 6.3.1. The sand has lost most of its strength. More obvious deformation of the LSB can also be observed at $t = 15.55$ s and 20.19 s. After the shaking stops ($t = 25.32$ s), the LSB resumes to its original shape. This observation is consistent with the shake table test.



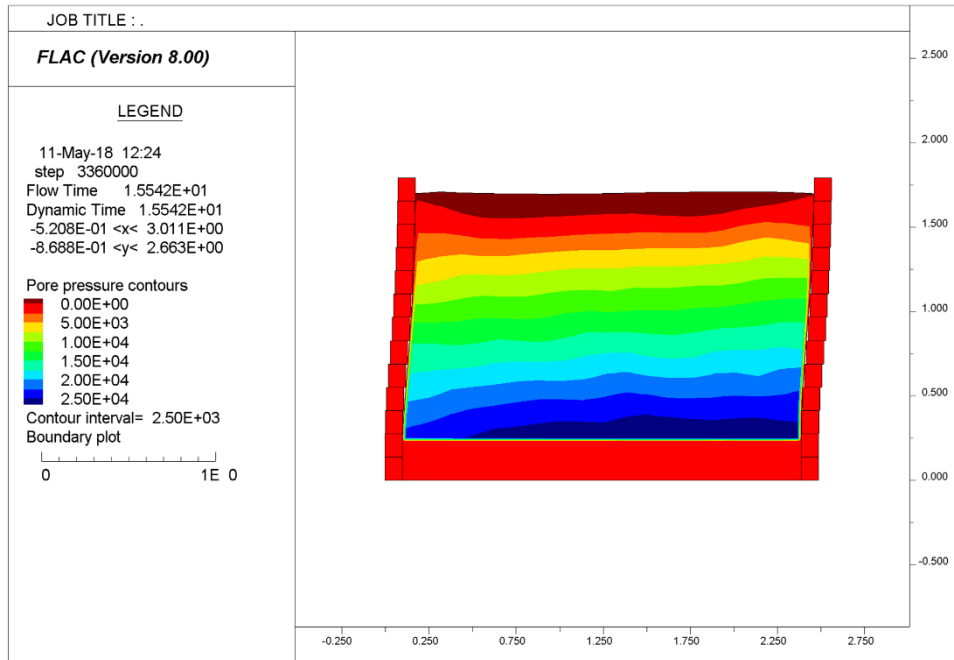
(a) Pore pressure contour at $t = 0.015$ s



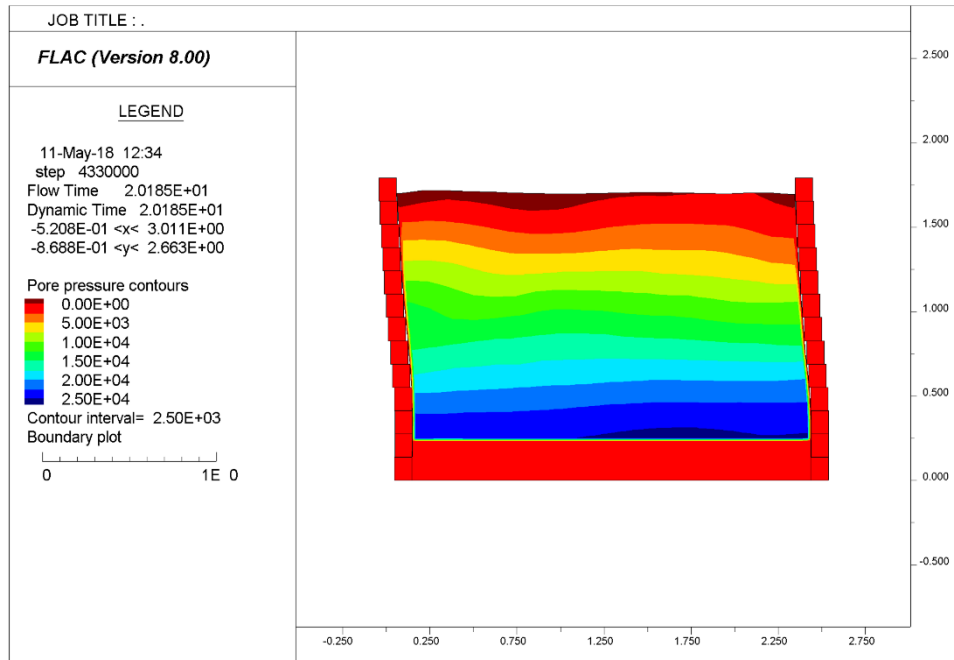
(b) Pore pressure contour at $t = 5.08$ s



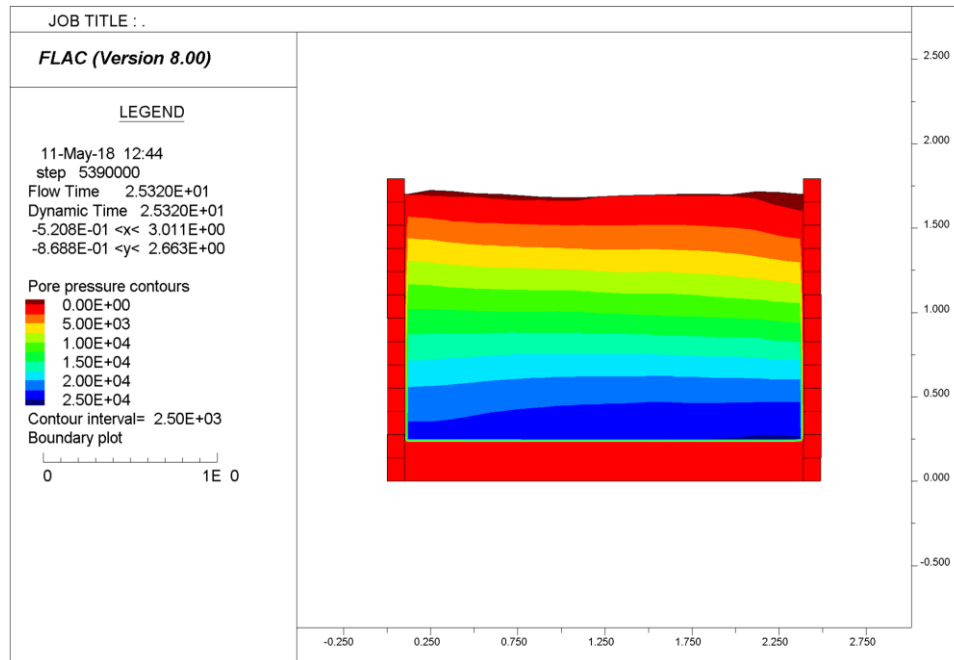
(c) Pore pressure contour at $t = 10.00$ s



(d) Pore pressure contour at $t = 15.55$ s



(e) Pore pressure contour at $t = 20.19$ s



(f) Pore pressure contour at $t = 25.32$ s

Figure 6-8 Contour plots of pore pressures during shaking at different time (units: Pa)

6.3.3 Shear strain

Figure 6-9 presents the shear strain comparison of the shake table test (1st shaking) with simulations. The simulation results from both depths ($D = 0.7$ m and 1.2 m) show a similar variation pattern with time. The accumulation rate of the shear strain is small in the first 8 seconds. After that, accumulation rate of shear strain increases rapidly with cycle of loading. This observation is consistent with the cyclic DSS and PM4Sand single element simulations. The maximum peak to peak shear strain values for $D = 0.7$ m and 1.2 m are 22.9% and 16.6%, respectively.

In the shake table test, the sudden change of accumulation rate of shear strain near liquefaction point was not observed. For both depths shown in Figure 6-9, the shear strains increased rapidly as the shaking started and kept relatively constant amplitudes after 4

seconds. The maximum peak to peak shear strain values after 4 seconds for $D = 0.7$ m and 1.2 m are 15% and 8%, respectively. The simulation results tend to over-predict the shear strains after liquefaction.

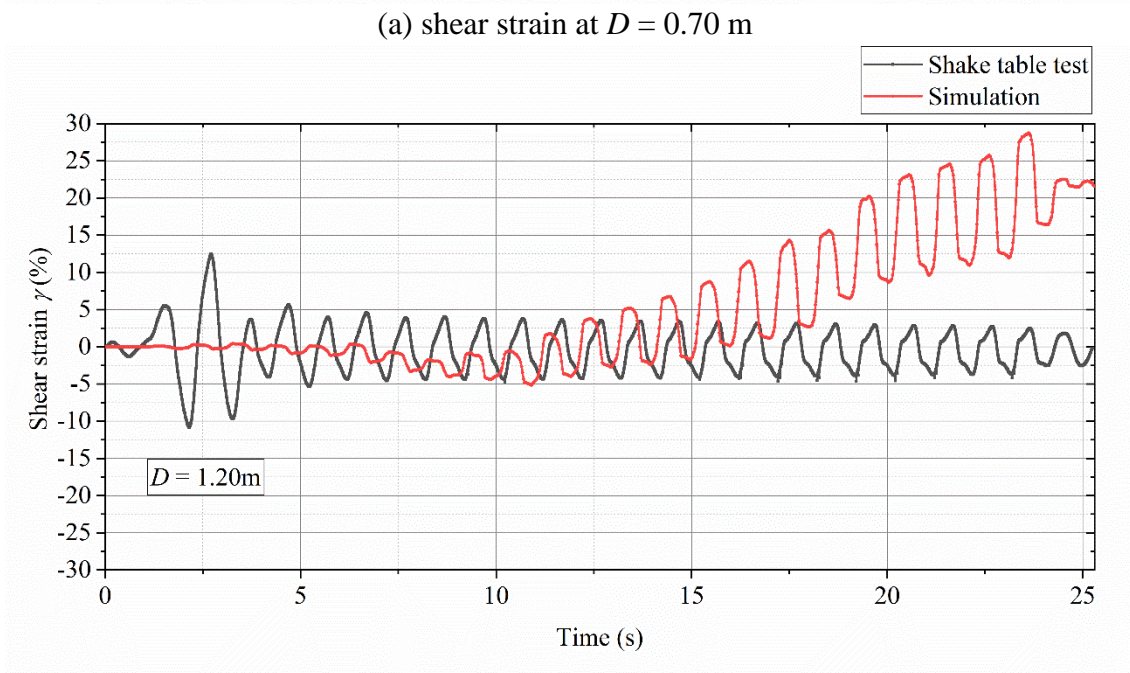
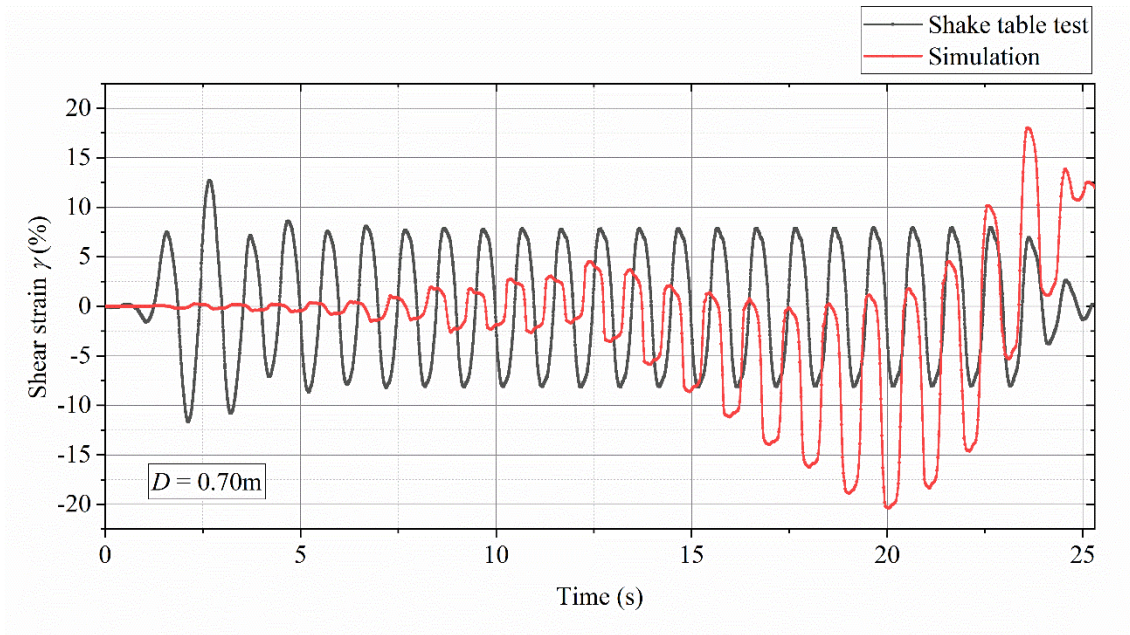


Figure 6-9 Shear strain time histories at two different depths: comparison of the shake table test (1st shaking) with simulations

6.3.4 Surface settlement

Figure 6-10 presents the surface settlement comparison of the shake table test (1st shaking) with simulations. The simulation results show little surface settlement in the first 12 seconds. Starting from 13 s, the settlement rate increases, and the final surface settlement is 1.96 cm. In the shake table test, the surface did not settle in the first two seconds. After that, the settlement rate increased, and a final settlement of 4.25 cm was observed. A larger fluctuation was observed in the shake table test compared with the simulation. This might be due to the plastic plate which was placed between the top LVDT rod and sand surface in the shake table test. The rocking of the plate during shaking may result in significant fluctuation in LVDT measurement. In general, the simulation results tend to under-predict the final surface settlement.

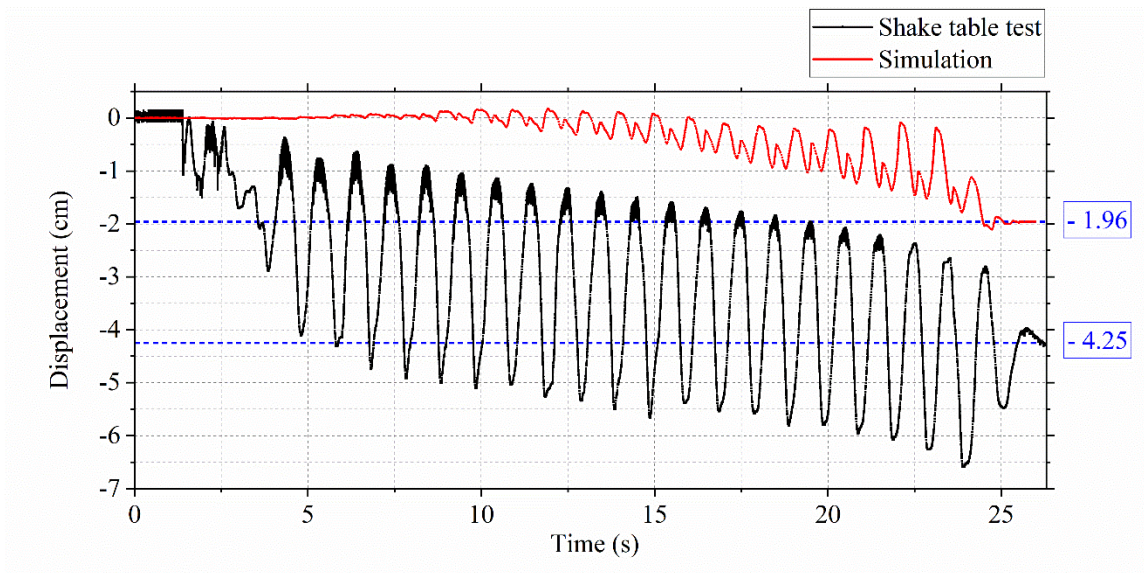


Figure 6-10 Surface settlement time histories: comparison of the shake table test (1st shaking) with simulations

6.4 Conclusion and summary

Numerical simulations of a shake table test, in which sand liquefaction was observed, are presented using PM4Sand constitutive model. A series of cyclic DSS tests are presented to provide the laboratory data for model calibration. The PM4Sand model is calibrated using the liquefaction triggering curve. The simulation results are compared with the observations and measurements from the shake table test, including pore pressures, lateral deformation profiles, shear strains, and surface settlement. The following conclusions are based on the data, analysis and interpretation presented in this chapter.

1. The PM4Sand in single element simulation can well capture the sand performance in cyclic DSS test using the calibrated parameters. The process of PM4Sand calibration is simple. Only one parameter (h_{p0}) needs to be calibrated using iterative process. The relatively simple calibration makes PM4Sand an appropriate and effective tool for liquefaction evaluations.

2. The simulation results over-predict the liquefaction occurrence for most of the sand deposit. The simulation results suggest that liquefaction happens around 10 to 15 seconds earlier than the case in shake table test. The PM4Sand model seems to be conservative in liquefaction occurrence prediction.

3. The simulations results tend to under-predict the shear strains of the sand deposit before liquefaction and over-predict the shear strains after liquefaction. The computed surface settlement is 46% of the measurement settlement in the shake table test.

A limitation of the numerical modeling must be pointed out. The performance of geomembrane bag used in the shake table test cannot be fully simulated by the elastic

models. In the simulation, the bag is set to be as a thin and flexible layer. The geomembrane bag in the test, however, could exhibit some degree of rigidity when subjected to large deformation. The bag might inhibit the deformation of the sand deposit during shaking.

Chapter 7 Summary and Conclusions

7.1 Summary

This dissertation presents a series of shake table tests conducted on a uniform sand deposit. The sand deposit was subjected to a liquefying shaking event (1st shaking) in the laminar shear box. The test recordings from piezometers, accelerometers and LVDTs were presented and discussed. Three subsequent major shaking events were designed and performed on the same sand deposit after the first shaking. The shake table test results from different shaking events were compared to investigate the seismic response of the sand deposit under multiple shaking events. The time-dependent liquefaction resistance of a post-liquefaction sand deposit was studied using piezo-cone penetration testing (CPTu) after 1st shaking event. A series of CPTu tests were conducted to measure the cone penetration resistance, friction resistance, and pore water pressure throughout the depth of the post-liquefaction sand deposit. To capture the sand aging effect after liquefaction, CPTu tests were done at different locations over a total elapsed time of 135 days. To evaluate the predictive capabilities of the PM4Sand model, a numerical simulation of the shake table test was developed. The model was first calibrated using cyclic direct simple shear tests. The calibrated model was then used to simulate the seismic performance of the uniform soil deposit under sinusoidal seismic motions. Further insight into the strengths and limitations of the PM4Sand model gained from this research was presented.

7.2 Conclusions

The following conclusions are based on the data, analysis and interpretation presented in this dissertation.

(1) The shake table has a satisfactory performance for all the employed shaking input motions.

(2) In the 1st shaking event, the pore pressure readings indicate the occurrence of liquefaction for the whole sand deposit. The sand near the top liquefies first and the sand near the bottom liquefies last. The sand in between liquefies between 20.5 s to 23 s.

(3) A correlation can be found between pore pressure ratio and cyclic shear strain in the 1st shaking event. The sand that liquefies first shows the largest shear strain amplitude. The sand that liquefies last has the smallest shear strain amplitude.

(4) Liquefaction can reduce the cone penetration resistance of a sand deposit significantly immediately after the liquefaction event. For a sand deposit from 0.2 m to 1.0 m depth, the cone penetration resistance can reduce by 50% on average due to liquefaction.

(5) After liquefaction, the cone penetration resistance of a sand deposit increases with aging time. In an aging span of 4.5 months after liquefaction, an average of 113% gain in cone penetration resistance was observed. An equation relating the cone penetration resistance, effective stress and time is proposed and compared with results from the literature. The equation may under-predict strength gain at long time.

(6) After the liquefaction, the normalized cone penetration resistance increases with time. In 4.5 months, a 101% gain of normalized cone penetration resistance is observed. The normalized cone penetration resistance has a linear relationship with the logarithm of

time. The cyclic resistance ratio for earthquake with magnitude of 7.5 increases with time after liquefaction. A 17.6% increase in $CRR_{7.5}$ is observed in the testing time span. The $CRR_{7.5}$ has a linear relationship with the logarithm of time.

(7) Along with the shaking, the sand deposit became denser and denser. The calculated the relative density of the sand deposit were 70.8%, 82.3%, 89.5% and 94.1% after the 1st, 2nd, 3rd, and 4th shaking event, respectively.

(8) A comparison between 1st and 2nd shaking suggests that the liquefaction resistance of the sand increased a lot. This is confirmed by the CPTu results presented in Chapter 4. The liquefaction resistance increase is because of the densification of 1st shaking and the aging effect in 153 days.

(9) The PM4Sand in single element simulation can well capture the sand performance in cyclic DSS test using the calibrated parameters. The process of PM4Sand calibration is simple. Only one parameter (h_{p0}) needs to be calibrated using iterative process. The relatively simple calibration makes PM4Sand an appropriate and effective tool for liquefaction evaluations.

(10) The simulation results over-predict the liquefaction occurrence for most of the sand deposit. The simulation results suggest that liquefaction happens around 10 to 15 seconds earlier than the case in shake table test. The PM4Sand model seems to be conservative in liquefaction occurrence prediction.

7.3 Limitations of this research

The limitation of the experimental part of this research is only the sand at relatively shallow depths were investigated. The effective stress levels of the sand are relatively low as is typical in shake table test. Further examination of the proposed equations is needed for different soil types and effective stress levels.

The limitation of the numerical modeling is that the performance of geomembrane bag used in the shake table test cannot be fully simulated by the elastic models. In the simulation, the bag is set to be a thin and flexible layer. The geomembrane bag in the test, however, could exhibit some degree of rigidity when subjected to large deformation. The bag might inhibit the deformation of the sand deposit during shaking.

Tap water was used to saturate the sand deposit. Bacteria may grow in in the total test period of 217 days from saturation to the completion of the 4th shaking event. The growth of bacteria may introduce air bubbles in the soil causing delayed reading of the piezometers. Biocide (a chemical intended to prevent bacteria growth) may be used in future shaking table testing of prolonged durations.

7.4 Recommendations for future work

The following are recommended for future study:

(1) The current study can extend to different soil types. Factors such as initial relative density and fine content can be investigated.

(2) A series of centrifuge tests can be conducted to investigate the sand aging effect under relatively high effect stress levels.

(3) The numerical model can include more advanced constitutive models for liquefaction, such as UBCSAND model and PDMY02 model. Using the cyclic DSS test and available shake table tests results, the predictive capability of different models can be compared.

REFERENCES

- Abdoun, T., et al. (2013). "Centrifuge and large-scale modeling of seismic pore pressures in sands: Cyclic strain interpretation." *J. Geotech. Geoenviron. Eng.*, 10.1061/(ASCE)GT.1943-5606.0000821, 1215–1234.
- Adalier, K., and Elgamal, A. W. (2002). "Seismic response of adjacent dense and loose saturated sand columns". *Soil Dynamics and Earthquake Engineering*, 22(2), 115-127.
- Anderson, D. G., and Stokoe, K.H. (1978). "Shear modulus, a time-dependent soil property" *Dynamic Geotechnical Testing, ASTM STP 654*, 66–90.
- Andrus, R. D., and Stokoe, K. H., II (2000). "Liquefaction resistance of soils from shear-wave velocity." *J. Geotech. and Geoenviron. Engrg.*, ASCE, 126(11), 1015–1025.
- Andrus, R. D., Stokoe, K. H., II, and Juang, C. H. (2004). "Guide for shear wave-based liquefaction potential evaluation." *Earthquake Spectra*, 20(2), 285-308.
- Andrus, R. D., Hayati, H., and Mohanan, N. P. (2009). "Correcting liquefaction resistance of aged sands using measured to estimated velocity ratio." *J. Geotech. Geoenviron. Eng.*, 135(6), 735–744.10.1061/(ASCE)GT.1943-5606.0000025
- Antonellis, G., Gavras, A. G., Panagiotou, M., Kutter, B. L., Guerrini, G., Sander, A. C., and Fox, P. J. (2015). "Shake Table Test of Large-Scale Bridge Columns Supported on Rocking Shallow Foundations." *Journal of Geotechnical and Geoenvironmental Engineering*, 141(5).
- Arango, I., Lewis, M. R., and Kramer, C. (2000). "Updated liquefaction potential analysis eliminates foundation retrofitting of two critical structures." *Soil Dyn. Earthquake Eng.*, 20, 17-25.
- Beaty, M.H. and Byrne, P.M. (2011). UBCSAND constitutive model version 904aR. Documentation Report: UBCSAND Constitutive Model on Itasca UDM Web Site.
- Boulanger, R.W., and Idriss, I. M. (2011). "Cyclic failure and liquefaction: Current issues. State-of-the-art lecture." *Proc., 5th Int. Conf. on Earthquake Geotechnical Engineering*, Chilean Geotechnical Society, Santiago, Chile, 137–159.
- Boulanger, R. W., and Idriss, I. M. (2014). "CPT and SPT based liquefaction triggering procedures." Rep. No. UCD/CGM-14/01, Univ. of California, Davis, CA.
- Boulanger, R. W., and Idriss, I. M. (2015). "CPT-based liquefaction triggering procedure." *J. Geotech. Geoenviron. Eng.*, 142(2), 04015065.

- Boulanger, R. W., Kamai, R., and Ziotopoulou, K. (2014). "Liquefaction induced strength loss and deformation: simulation and design". *Bulletin of Earthquake Engineering*, 12(3), 1107-1128.
- Boulanger, R. W. and Ziotopoulou, K. (2015). "PM4Sand (Version 3): A sand plasticity model for earthquake engineering applications." Report No. UCD/CGM-15/01, Center for Geotechnical Modeling, University of California, Davis, CA; 112 pp.
- Boulanger, R. W., Khosravi, M., Khosravi, A., and Wilson, D. W. (2017). "Remediation of liquefaction effects for an embankment using soil-cement walls: Centrifuge and numerical modeling." Proc., Performance-based Design in Earthquake Geotechnical Engineering, PBD-III Vancouver, M. Taiebat et al., eds., ISSMGE Technical Committee TC203, paper 537.
- Brandenberg, S. J., Boulanger, R. W., Kutter, B. L., and Chang, D. (2005). "Behavior of pile foundations in laterally spreading ground during centrifuge tests". *Journal of Geotechnical and Geoenvironmental Engineering*, 131(11), 1378-1391.
- Bray, J., and Boulanger, R., (2016). U.S.–New Zealand–Japan International Workshop.
- Byrne, P. M., Park, S.-S., Beaty, M., Sharp, M., Gonzalez, L., and Abdoun, T. (2004). "Numerical modeling of liquefaction and comparison with centrifuge tests." *Canadian Geotechnical Journal*, 41(2), 193-211.
- Campanella, R.G., Gillespie, D., and Robertson, P.K., (1982). "Pore pressures during cone penetration testing." *In Proceedings of the 2nd European Symposium on Penetration Testing*, ESPOT II. Amsterdam. A.A. Balkema, 507-512.
- Cetin, K. O., Seed, R. B., Der Kiureghian, A., Tokimatsu, K., Harder, L. F., Jr., Kayen, R. E., and Moss, R. E. S. (2004). "Standard penetration test-based probabilistic and deterministic assessment of seismic soil liquefaction potential." *J. Geotech. Geoenviron. Eng.*, 130(12), 1314–1340.
- Charlie, W. A., Rwebyogo, M. F., and Doehring, D. O. (1992). "Time-dependent cone penetration resistance due to blasting." *Journal of Geotechnical Engineering*, 118(8), 1200-1215.
- Chian, S. C., Tokimatsu, K., and Madabhushi, S. P. G. (2014). "Soil Liquefaction–Induced Uplift of Underground Structures: Physical and Numerical Modeling." *Journal of Geotechnical and Geoenvironmental Engineering*, 140(10), 04014057.
- Cubrinovski, M., and McCahon, I. (2012). "Short term recovery project 7: CBD foundation damage." Natural Hazards Research Platform, Univ. of Canterbury, Christchurch, New Zealand.
- Dafalias, Y. F., and Manzari, M. T. (2004). "Simple plasticity sand model accounting for fabric change." *Journal of Engineering Mechanics*, 130(6), 622-634.

- Dashti, S., and Bray, J. D. (2012). "Numerical simulation of building response on liquefiable sand". *Journal of Geotechnical and Geoenvironmental Engineering*, 139(8), 1235-1249.
- Dobry, R., Abdoun, T., Stokoe, K., II, Moss, R., Hatton, M., and El Ganainy, H. (2015). "Liquefaction potential of recent fills versus natural sands located in high-seismicity regions using shear-wave velocity." *J. Geotech. Geoenviron. Eng.*, 10.1061/(ASCE)GT.1943-5606.0001239, 04014112.
- Ecemis, N. (2013). "Simulation of seismic liquefaction: 1-g model testing system and shaking table tests." *European Journal of Environmental and Civil Engineering*, 17(10), 899-919.
- El-Sekelly, W. (2014). "The effect of seismic pre-shaking history on the liquefaction resistance of granular soil deposits." Ph.D. dissertation, Rensselaer Polytechnic Institute, Troy, NY.
- El-Sekelly, W., Dobry, R., Abdoun, T., and Steidl, J. H. (2016a). "Centrifuge modeling of the effect of preshaking on the liquefaction resistance of silty sand deposits." *J. Geotech. Geoenviron. Eng.*, 10.1061/(ASCE)GT.1943-5606.0001430.
- El-Sekelly, W., Abdoun, T., and Dobry, R. (2016b). "Liquefaction resistance of a silty sand deposit subjected to preshaking followed by extensive liquefaction." *J. Geotech. Geoenviron. Eng.*, 10.1061/(ASCE)GT.1943-5606.0001444.
- Ekstrom, L. T., and Ziotopoulou, K. (2017). "Seismic Response of Liquefiable Sloping Ground Validation of Class B Predictions against the LEAP Centrifuge Tests." *Geotechnical Frontiers 2017 GSP 281* Orlando, FL.
- Elgamal, A. Yang, Z. and Parra, E. (2002). "Computational modeling of cyclic mobility and post liquefaction site response". *Soil Dynamic and Earthquake Engineering* 22, 259-271.
- Finn, W. D. L., Bransby, P. L., and Pickering, D. J. (1970). "Effect of strain history on liquefaction of sand." *J. Soil Mech. Found. Div.*, 96(SM6), 1917–1934.
- Fretti C., Lo Presti D. C. E. and Pedroni S. (1995). A Pluvial Deposition Method to Reconstitute Well-Graded Sand Specimens. *Geotechnical Testing Journal*, 18(2), 31-37.
- Gade, V. K. and Dasaka, S. M. (2016): "Development of a mechanized travelling pluviator to prepare reconstituted uniform sand specimens." *J. Mater. Civ. Eng.*, 10.1061/(ASCE)MT.1943-5533.0001396, .
- Ha, I.S., Olson, S. M., Seo, M. W., and Kim, M. M. (2011). "Evaluation of reliquefaction resistance using shaking table tests." *Soil Dyn Earthq Eng* 31(4):682–691.

- Haeri, S. M., Kavand, A., Rahmani, I., and Torabi, H. (2012). "Response of a group of piles to liquefaction-induced lateral spreading by large scale shake table testing". *Soil Dynamics and Earthquake Engineering*, 38, 25-45.
- Hayati, H., Andrus, R. D., Gassman, S. L., Hasek, M., Camp, W. M., and Talwani, P. (2008). "Characterizing the liquefaction resistance of aged soils". In *Geotechnical Earthquake Engineering and Soil Dynamics IV* (pp. 1-10).
- Heidari, T., and Andrus, R. D. (2012). "Liquefaction potential assessment of Pleistocene beach sands near Charleston, South Carolina." *J. Geotech. Geoenviron. Eng.*, 10.1061/(ASCE)GT.1943-5606.0000686, 1196–1208.
- Hushmand, B., Scott, R. F., and Crouse, C. B. (1988). "Centrifuge liquefaction tests in a laminar box". *Geotechnique*, 38(2), 253-262.
- Hu, X., and Wang, J. (2014). "Recovery of cooling water circulation tunnel collapse: construction of permanent bulkhead by ground freezing." *In Tunneling and Underground Construction*: 829-835.
- Hu, X., Guo, W., Zhang, L., and Wang, J. (2013). "Application of liquid nitrogen freezing to recovery of a collapsed shield tunnel." *Journal of Performance of Constructed Facilities*, 28(4), 04014002.
- Hu, X. D., Yu, J. Z., Ren, H., Wang, Y., and Wang, J. T. (2017). "Analytical solution to steady-state temperature field for straight-row-piped freezing based on superposition of thermal potential". *Applied Thermal Engineering*, 111, 223-231.
- Hu, X. D., Wang, J. T., and Yu, R. Z. (2013). "Uniaxial compressive and splitting tensile tests of artificially frozen soils in tunnel construction of Hong Kong." *Journal of Shanghai Jiaotong University (Science)*, 18(6), 688-692.
- Idriss, I. M., and Boulanger, R. W. (2006). "Semi-empirical procedures for evaluating liquefaction potential during earthquakes." *Soil Dynamics and Earthquake Engineering* 26: 115–130.
- Idriss, I. M., and Boulanger, R. W. (2008). "Soil liquefaction during earthquakes." *Monograph MNO-12*, Earthquake Engineering Research Institute, Oakland, CA.
- Ishihara, K. (1993). "Liquefaction and flow failure during earthquakes." *Géotechnique*, 43(3), 351-415.
- Ishihara, K., Araki, K., and Bradley, B. A. (2011). "Characteristics of liquefaction-induced damage in the 2011 great east Japan earthquake." *Proc., Int. Conf. Geotechnics for Sustainable Development*, Univ. of Canterbury, Christchurch, New Zealand.
- Itasca (2016). *FLAC – Fast Lagrangian Analysis of Continua*, Version 8.0, Itasca Consulting Group, Inc., Minneapolis, Minnesota.

- Jafarzadeh, B. (2004). "Design and evaluation concepts of laminar shear box for 1g shaking table tests". In *Proceedings of the 13th world conference on earthquake engineering, Vancouver, paper* (No. 1391).
- Joshi, R. C., Achari, A., Kaniraj, S.R., and Wijeweera, H. (1995). "Effect of aging on the Penetration Resistance of Sands." *Canadian Geotechnical Journal*, 32(5), 767-782.
- Kamai, R., and Boulanger, R. W. (2012). "Simulations of a centrifuge test with lateral spreading and void redistribution effects". *Journal of Geotechnical and Geoenvironmental Engineering*, 139(8), 1250-1261.
- Kayen, R. R., et al. (2013). "Shear wave velocity-based probabilistic and deterministic assessment of seismic soil liquefaction potential." *J. Geotech. Geoenviron. Eng.*, 10.1061/(ASCE)GT.1943-5606.0000743, 407–419.
- Kagawa, K., Sato, M., Minowa, C., Abe, A. and Tazon, T. (2004). "Centrifuge Simulations of Large-Scale Shaking Table Tests: Case Studies." *J. Geotech. Geoenviron. Eng.*, 130(7): 663-672.
- Karimi, Z., and Dashti, S. (2016). "Numerical and Centrifuge Modeling of Seismic Soil–Foundation–Structure Interaction on Liquefiable Ground." *Journal of Geotechnical and Geoenvironmental Engineering*, 142(1), 04015061.
- Kramer, C. (2013). An experimental investigation on performance of a model geothermal pile in sand. The Pennsylvania State University. USA.
- Kramer, S. L. (1996). Geotechnical earthquake engineering. Prentice Hall, Upper Saddle River, N.J
- Kramer, C., and Arango, I. (1998). "Aging effects on the liquefaction resistance of sand deposits: A review and update." *Proc., Eleventh European Conf. on Earthquake Engineering*, A.A. Balkema, CD-ROM, Bisch, Philippe, Pierre Labbe, and Alain Pecker, eds., Paris, Abstract Vol. 184.
- Kulasingam, R., Malvick, E. J., Boulanger, R. W., and Kutter, B. L. (2004). "Strength loss and localization at silt interlayers in slopes of liquefied sand". *Journal of Geotechnical and Geoenvironmental Engineering*, 130(11), 1192-1202.
- Lewis, M. R., McHood, M. D., and Arango, I. (2004). "Liquefaction evaluations at the Savannah River Site, a case history." *Proc., Fifth Int. Conf. on Case Histories in Geotechnical Engineering*, Univ. of Missouri, Rolla, Mo., 1–10.
- Li, P., Dashti, S., Badanagki, M., and Kirkwood, P. (2018). "Evaluating 2D numerical simulations of granular columns in level and gently sloping liquefiable sites using centrifuge experiments". *Soil Dynamics and Earthquake Engineering*, 110, 232-243.

- Liao, S. S. C., and Whitman, R. V. (1986). "Catalogue of liquefaction and non-liquefaction occurrences during earthquakes." Res. Rep., Dept. of Civ. Engrg., Massachusetts Institute of Technology, Cambridge, Mass.
- Lin, M. L., and Wang, K. L. (2006). "Seismic slope behavior in a large-scale shaking table model test". *Engineering Geology*, 86(2-3), 118-133.
- Mesri, G., Feng, T. W., and Benak, J. M. (1990). "Postdensification penetration resistance of clean sands." *J. Geotech. Engrg.*, ASCE, 116(7), 1095–1115.
- Mitchell, J. K., and Solymar, Z. V. (1984). "Time-dependent strength gain in freshly deposited or densified sand." *J. Geotech. Engrg.*, ASCE, 110(11), 1159–1576.
- Mitchell, J.K. (2008). "Aging of sand – a continuing enigma?" *Proceedings of the 6th Int. Conf. on Case Histories in Geotechnical Engineering*. Arlington, VA, Aug. 11-16, 2008, 1-21.
- Moss, R. E. S., Seed, R. B., Kayen, R. E., Stewart, J. P., Der Kiureghian, A., and Cetin, K. O. (2006). "CPT-based probabilistic and deterministic assessment of in situ seismic soil liquefaction potential." *J. Geotech. Geoenviron. Eng.*, 132(8), 1032–1051.
- Ng, C. W., Li, X. S., Van Laak, P. A., and Hou, D. Y. (2004). "Centrifuge modeling of loose fill embankment subjected to uni-axial and bi-axial earthquakes". *Soil Dynamics and Earthquake Engineering*, 24(4), 305-318.
- Oda, M., Kawamoto, K., Suzuki, K., Fujimori, H., and Sato, J. (2001). "Microstructural interpretation on reliquefaction of saturated granular soils under cyclic loading." *J. Geotech. Geoenviron. Eng.*, 10.1061/ (ASCE)1090-0241(2001)127(5), 416–423.
- Okamura, M., and Teraoka, T. (2006). "Shaking table tests to investigate soil desaturation as a liquefaction countermeasure". In *Seismic Performance and Simulation of Pile Foundations in Liquefied and Laterally Spreading Ground* (pp. 282-293).
- Otsubo, M., Towhata, I., Hayashida, T., Shimura, M., Uchimura, T., Liu, B., ... and Rattetz, H. (2016). "Shaking table tests on mitigation of liquefaction vulnerability for existing embedded lifelines". *Soils and Foundations*, 56(3), 348-364.
- Pamuk, A., Gallagher, P. M., and Zimmie, T. F. (2007). "Remediation of piled foundations against lateral spreading by passive site stabilization technique". *Soil Dynamics and Earthquake Engineering*, 27(9), 864-874.
- Paolucci, R., Shirato, M., and Yilmaz, M. T. (2008). "Seismic behavior of shallow foundations: shaking table experiments vs numerical modeling." *Earthquake Eng. Struct. Dyn.*, 37, 577.
- Robertson, P. K., and Cabal, K. L. (2015). "Guide to cone penetration testing for geotechnical engineering." 6th edition, Gregg Drilling & Testing, Inc. Signal Hill, California.

- Robertson, P.K. (1990). "Soil classification using the cone penetration test." *Canadian Geotechnical Journal*, 27(1), 151–158.
- Robertson, P. K., and C. E. Wride. (1998). "Evaluating cyclic liquefaction potential using the cone penetration test." *Canadian Geotechnical Journal* 35(3), 442-459.
- Rad, N. & M. Tumay. 1987. Factors affecting sand specimen preparation by raining. *Geotechnical Testing Journal* 10(1), 31–37.
- Ramirez, J., Badanagki, M., Abkenar, M. R., ElGhoraiby, M. A., Manzari, M. T., Dashti, S., Barrero, A., Taiebat, M., Ziotopoulou, K., and Liel, A. (2017). "Seismic Performance of a Layered Liquefiable Site Validation of Numerical Simulations Using Centrifuge Modeling." *Geotechnical Frontiers 2017*, GSP 281: 332-341.
- Sasaki, Y., and Taniguchi, E. (1982). "Shaking table tests on gravel drains to prevent liquefaction of sand deposits". *Soils and Foundations*, 22(3), 1-14.
- Schmertmann, J.H. (1991) "The mechanical aging of soils." *Journal of Geotechnical Engineering*, ASCE, 117(9), 1288-1330.
- Seed, H. B. (1979). "Soil liquefaction and cyclic mobility evaluation for level ground during earthquakes." *J. Geotech. Eng. Div.*, 105(GT2), 201–255.
- Seed, H. B., Mori, K., and Chan, C. K. (1977). "Influence of seismic history on liquefaction of sands." *J. Geotech. Eng. Div.*, 103(GT4), 257–270.
- Seed, H.B. and Idriss, I.M. (1970). A simplified procedure for evaluation soil liquefaction potential. Report EERC 70-9, Earthquake Engineering Research Center, University of California, Berkeley.
- Seed, H. B., and Idriss, I. M. (1971). "Simplified procedure for evaluating soil liquefaction potential." *J. Geotech. Engrg. Div.*, ASCE, 97(9), 1249–1273.
- Sharp, M. K., Dobry, R., and Abdoun, T. (2003). "Liquefaction centrifuge modeling of sands of different permeability". *Journal of geotechnical and geoenvironmental engineering*, 129(12), 1083-1091.
- Shen, C. K. (1998). Development of a geotechnical centrifuge in Hong Kong. In *Proc. Int. Conf. Centrifuge 98*.
- Suzuki, Y., Tokimatsu, K., Taya, Y., and Kubota, Y. (1995). "Correlation between CPT data and dynamic properties of in situ frozen samples." in *Proceedings, 3rd International Conference on Recent Advances in Geotechnical Earthquake Engineering and Soil Dynamics*, Vol. I, St. Louis, MO.
- Stark, T. D., and Olson, S. M. (1995). "Liquefaction resistance using CPT and field case histories." *J. Geotechnical Eng.*, ASCE 121(12), 856–69.
- Stringer, M.E., Pedersen, L., Nuss B.D. and Wilson D.W. Design and use of a rotating spiral pluviator for creating large sand models. *Physical Modelling in Geotechnics*

- Turan, A., Hinchberger, S. D., and El Naggar, H. (2009). "Design and commissioning of a laminar soil container for use on small shaking tables". *Soil Dynamics and Earthquake Engineering*, 29(2), 404-414.
- Ueng, T. S., Wang, M. H., Chen, M. H., Chen, C. H., and Peng, L. H. (2005). "A large biaxial shear box for shaking table test on saturated sand". *Geotechnical Testing Journal*, 29(1), 1-8.
- Mesri, G., Feng, T.W., and Benak, J.M. (1990). "Postdensification penetration resistance of clean sands". *Journal of Geotechnical Engineering*, ASCE, 116(7), 1095-1115.
- Van Laak, P. A., Taboada, V. M., Dobry, R., and Elgamal, A. W. (1994). "Earthquake centrifuge modeling using a laminar box". In *Dynamic geotechnical testing II*. ASTM International.
- Vaid, Y.P. and Negussey, D. (1984). Relative density of pluviated sand samples. *Soils and foundations*, Vol. 24, No.2, 101-105.
- Wartman, J., Seed, R., and Bray, J. (2005). "Shaking Table Modeling of Seismically Induced Deformations in Slopes." *J. Geotech. Geoenviron. Eng.*, 131(5), 610–622.
- Whitman, R. V., and Lambe, P. C. (1986). "Effect of boundary conditions upon centrifuge experiments using ground motion simulation". *Geotechnical Testing Journal*, 9(2), 61-71.
- Wilson, D. W., Boulanger, R. W., and Kutter, B. L. (2000). "Observed seismic lateral resistance of liquefying sand". *Journal of Geotechnical and Geoenvironmental Engineering*, 126(10), 898-906.
- Xiao, M., Ledezma, M., and Wang, J. (2015). "Reduced-Scale Shake Table Testing of Seismic Behaviors of Slurry Cutoff Walls." *Journal of Performance of Constructed Facilities*, 30(3), 04015057.
- Yamada, S., Takamori, T., and Sato, K. (2010). "Effects on reliquefaction resistance produced by changes in anisotropy during liquefaction. *Soils and Foundations*, 50(1), 9-25.
- Yamaguchi, A., Mori, T., Kazama, M., and Yoshida, N. (2012). "Liquefaction in Tohoku district during the 2011 off the Pacific Coast of Tohoku Earthquake". *Soils and Foundations*, 52(5), 811-829.
- Yang, J. (2006). "Influence zone for end bearing of piles in sand." *J. Geotech. Geoenviron. Eng.*, 132(9), 1229-1237.
- Yang, Z., Lu, J. and Elgamal, A. (2008). "OpenSees soil models and solid-fluid fully coupled elements: User's manual." Dept. of Structural Engineering, Univ. of California, San Diego.

- Yao, S., Kobayashi, K., Yoshida, N., and Matsuo, H. (2004). "Interactive behavior of soil–pile-superstructure system in transient state to liquefaction by means of large shake table tests". *Soil Dynamics and Earthquake Engineering*, 24(5), 397-409.
- Youd, T. L., Idriss, I. M., Andrus, R. D., Arango, I., Castro, G., Christian, J. T., Dobry, R., Finn, W. D. L., Harder, L. F., Hynes, M. E., Ishihara, K., Koester, J. P., Liao, S. S. C., Marcuson, W. F., Martin, G. R., Mitchell, J. K., Moriwaki, Y., Power, M. S., Robertson, P. K., Seed, R. B., and Stokoe, K. H. (2001). "Liquefaction resistance of soils: summary report from the 1996 NCEER and 1998 NCEER/NSF workshops on evaluation of liquefaction resistance of soils." *J. Geotechnical and Geoenvironmental Eng.*, ASCE 127(10), 817–33.
- Ziotopoulou, K., and Boulanger, R. W. (2016). "Plasticity modeling of liquefaction effects under sloping ground and irregular cyclic loading conditions." *Soil Dynamics and Earthquake Engineering*, 84 (2016), 269-283, 10.1016/j.soildyn.2016.02.013.
- Ziotopoulou, K. (2017). "Seismic response of liquefiable sloping ground: Class A and C numerical predictions of centrifuge model responses." *Soil dynamics and earthquake engineering*.

Appendix A

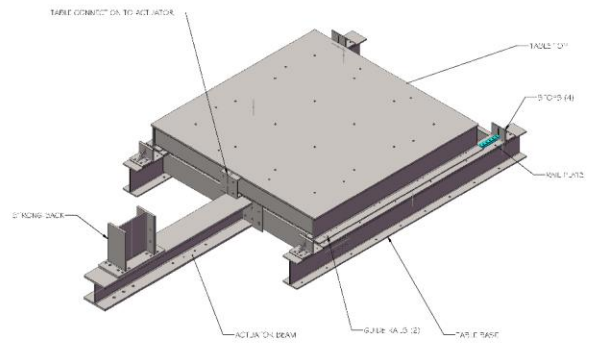
Design drawings of shake table

GENERAL NOTES:

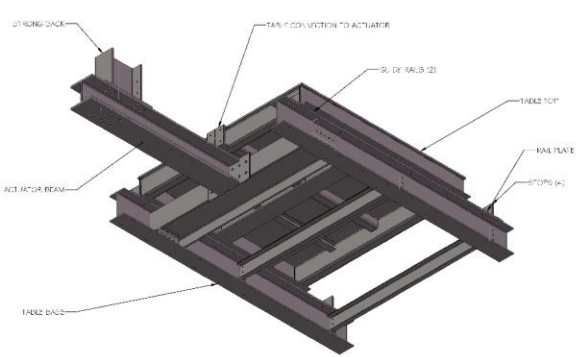
1. ALL DIMENSIONS AND EXISTING CONDITIONS SHALL BE CHECKED AND VERIFIED BY THE CONTRACTOR AT THE SITE. IMMEDIATELY REPORT TO PENN STATE ANY POTENTIAL CONDITION THAT MAY AFFECT THE PROJECT, PRIOR TO THE SUBMISSION OF BIDS AND COMMENCING CONSTRUCTION.
2. CONTRACTOR SHALL BE RESPONSIBLE FOR THE DAILY REGULAR REMOVAL AND OFF-SITE DISPOSAL OF CONSTRUCTION DEBRIS. THE PROJECT AREA SHALL BE KEPT CLEAN AT ALL TIMES.
3. CONTRACTOR IS RESPONSIBLE FOR PROTECTING THE PROJECT AREA. PROVIDE ADEQUATE FENCING, BARRICADES, WARNING SIGNS AND LIGHTS AS WARRANTED AND THESE ITEMS SHALL REMAIN IN PLACE UNTIL PROJECT IS COMPLETED.
4. CITE IN A WORKING LABORATORY. CONTRACTOR SHALL COORDINATE ALL ACTIVITIES, SCHEDULES, ETC. WITH FACILITY MANAGER.
5. A PRE-BID MEETING WILL BE CONDUCTED PRIOR TO SUBMISSION OF BIDS. DATE, TIME AND LOCATION WILL BE DETERMINED BY PENN STATE.
6. A PRE-CONSTRUCTION MEETING WILL BE HELD BETWEEN CONTRACTOR AND PENN STATE REPRESENTATIVES PRIOR TO COMMENCING CONSTRUCTION.
7. ALL EXISTING CONSTRUCTION FINISHES AND/OR FACILITIES DAMAGED DURING CONSTRUCTION ARE TO BE REPAIRED/REPLACED TO MATCH EXISTING TO THE SATISFACTION OF PENN STATE, UTILIZING LIKE MATERIALS AND INSTALLATION METHODS.
8. PRIOR TO SUBMITTING BID, CONTRACTORS SHOULD VISIT THE SITE AND FAMILIARIZE THEMSELVES WITH THE PROPOSED PROJECT AREA, VERIFY APPLICABLE DIMENSIONS, THE QUANTITIES, TYPES AND CONDITIONS OF MATERIALS BEING SUPPLIED BY PENN STATE TO BE INSTALLED BY CONTRACTOR, AND THE WORK THAT WILL BE CONDUCTED BY PENN STATE. NOTIFY PENN STATE OF ANY DISCREPANCIES.
9. ALL PRODUCTS, MATERIALS AND WORKMANSHIP SHALL BE IN STRICT COMPLIANCE WITH THE APPLICABLE INSTITUTIONS' REQUIREMENTS (I.E. AMERICAN INSTITUTE OF STEEL CONSTRUCTION (AISC), AMERICAN WELDING SOCIETY (AWS), ETC.).
10. PRODUCTS SUPPLIED UNDER THIS CONTRACT SHALL NOT CONTAIN ANY LEAD BASED PAINT, ASBESTOS CONTAINING MATERIALS OR OTHER HAZARDOUS MATERIALS.
11. NEW STRUCTURAL STEEL FOR HOT ROLLED SHAPES SHALL BE ASTM A992 AND SMALL SHAPES SHALL BE ASTM A36.
12. STRUCTURAL STEEL BEING PROVIDED BY PENN STATE MUST BE TAKEN TO CONTRACTOR'S FABRICATION LOCATION, MODIFIED ACCORDINGLY TO MEET PROJECT REQUIREMENTS, CLEANED AND SHOP PRIMED.
13. THE FOLLOWING ITEMS WILL BE PROVIDED BY PENN STATE AND INSTALLED BY THE CONTRACTOR:
 - A. ITEM 3 SHOWN IN SHEET 3.
 - B. ITEMS 10, 11, AND 15 SHOWN IN SHEET 4.
 - C. ITEM 8 SHOWN IN SHEET 5.
 - D. ITEM 20 SHOWN IN SHEET 6.
 - E. ITEM 25 SHOWN IN SHEET 8.
14. ALL BOLTS AND CORRESPONDING NUTS AND WASHERS WILL BE PROVIDED BY THE CONTRACTOR AND WILL BE OF A490 STEEL.
15. GUIDE RAILS WILL BE PURCHASED BY PENN STATE AND INSTALLED BY THE CONTRACTOR.
16. CONCRETE ANCHORS WILL BE PROVIDED AND INSTALLED BY PENN STATE PRIOR TO THE INSTALLATION OF THE SHAKE TABLE.
17. THE ACTUATOR SHOWN IN ASSEMBLY DRAWING WILL BE FURNISHED AND INSTALLED BY PENN STATE.
18. CONNECTIONS FOR THE ACTUATOR REQUIRE PRECISION OF 1/16".
19. THE SHAKE TABLE WILL BE MOUNTED TO THE CONCRETE FLOOR USING RESINIC CONCRETE ANCHOR BOLTS.
20. CONNECTION OF THE FUNCTIONING ACTUATOR WILL BE PERFORMED BY CTEE, IF POSSIBLE.
21. CONTRACTOR SHALL HAVE A MINIMUM OF FIVE (5) YEARS EXPERIENCE IN STRUCTURAL STEEL FABRICATION AND CONSTRUCTION.
22. WELDING INSPECTOR AND WELDING INSPECTOR QUALIFICATIONS FOR STRUCTURAL STEEL SHALL BE IN ACCORDANCE WITH AWS D1.1 - "STRUCTURAL WELDING CODE - STEEL" - LATEST EDITION.
23. ALL WELDING SHALL BE DONE BY CERTIFIED WELDERS USING TYPE E70XX ELECTRODES AND SHALL CONFORM TO THE CODE FOR WELDING IN BUILDING CONSTRUCTION OF THE AWS D1.1.
24. CONTRACTOR SHALL PROVIDE ONE (1) COAT OF METAL PRIMER ON ALL STRUCTURAL STEEL. PENN STATE WILL PROVIDE INTERMEDIATE AND FINAL TOP COATS OF PAINT. CONTRACTOR TO VERIFY PAINT BEING USED BY PENN STATE FOR COMPATIBILITY WITH METAL SHOP PRIMER.
25. STRUCTURAL STEEL PAINTING SHALL ADHERE TO THE FOLLOWING:
 - A. PRIMES, ALVEX, ANTI-CORROSIVE FOR METAL, 100%Zn.
 - B. VERIFY SUITABILITY OF STEEL BEING FURNISHED BY PENN STATE, INCLUDING SURFACE CONDITIONS FOR COMPATIBILITY OF PRIMER AND EVENTUAL INTERMEDIATE AND TOP COATS.
 - C. COMPLY WITH PAINT MANUFACTURER'S WRITTEN INSTRUCTIONS AND RECOMMENDATIONS.
 - D. CLEAN SUBSTRATES OF SUBSTANCES THAT COULD IMPAIR BOND OF PAINTS, INCLUDING DUST, DIRT, OIL, GREASE AND INCOMPATIBLE PAINTS.
 - E. REMOVE RUST, LOGS, MILL SCALE AND OTHER PAINTS, IF ANY.
 - F. PROCEED WITH PRIMER APPLICATION ONLY AFTER UNSATISFACTORY CONDITIONS HAVE BEEN CORRECTED.
 - G. CLEAN FIELD WELDS, BOLTED CONNECTIONS, AND BRAGGED AREAS OF SHOP PAINT, AND PAINT EXPOSED AREAS WITH THE SAME MATERIAL AS USED FOR SHOP PRIMING TO COMPLY WITH SSPC-PA 1 FOR TOUCHING UP SHOP PRIMED SURFACES.
 - H. APPLY PAINTS TO PRODUCE SURFACE FILMS WITHOUT CLOUDINESS, SPOTTING, HOLIDAYS, LAPS, BRUSH MARKS, ROLLER TRACKING, RUNS, SAGS, XOPNESS, OR OTHER SURFACE IMPERFECTIONS.

SolidWorks Student Edition.
For Academic Use Only.

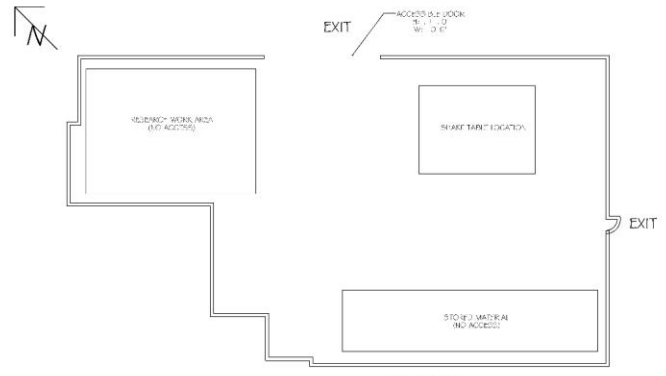
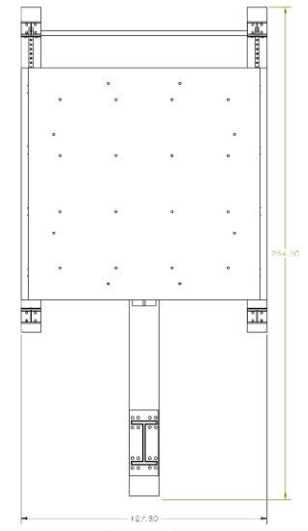




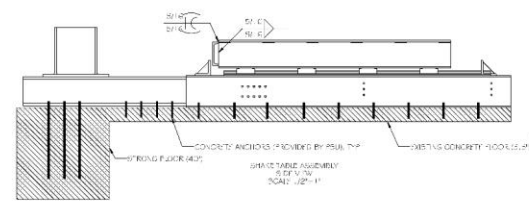
ENTIRE SHAKE TABLE ASSEMBLY
ISOMETRIC VIEW
SCALE: 1/2\"/>



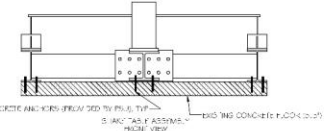
BY THE DRINKS TABLE ASSEMBLY
ISOMETRIC VIEW
SCALE: 1/2\"/>



GENERAL SITE LOCATION ON
STREET MAP (AIR PARK V. 2)
SCALE: 1/2\"/>



SHAKE TABLE ASSEMBLY
SECTION VIEW
SCALE: 1/2\"/>

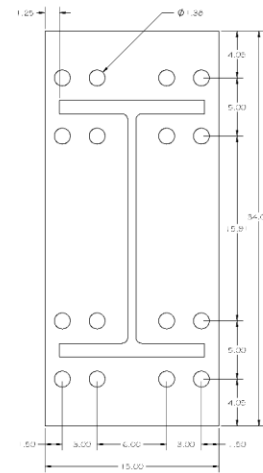
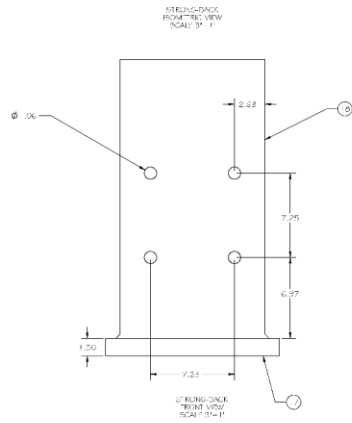
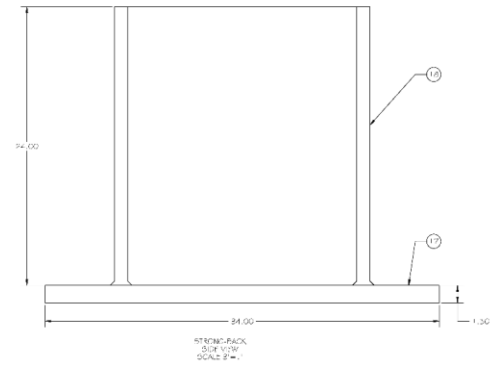
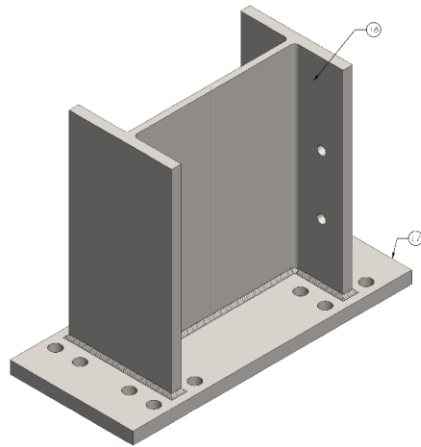


SLIDING RAIL ASSEMBLY
SECTION VIEW
SCALE: 1/2\"/>

**SolidWorks Student Edition.
For Academic Use Only.**

	PROJECT INFORMATION PROJECT NAME: NEW SHAKE TABLE PROJECT NUMBER: 12-11-12 PROJECT LOCATION: STATE COLLEGE, PA 16801 PROJECT DATE: 12-11-12	SHEET INFORMATION SHEET NUMBER: 13-11-12 SHEET TOTAL: 13-11-12
	PENNSYLVANIA STATE UNIVERSITY 3127 RESEARCH DRIVE STATE COLLEGE, PA 16801 TEL: 814/863-1000 FAX: 814/863-1000 WWW.PSU.EDU	PROJECT INFORMATION PROJECT NAME: NEW SHAKE TABLE PROJECT NUMBER: 12-11-12 PROJECT LOCATION: STATE COLLEGE, PA 16801 PROJECT DATE: 12-11-12

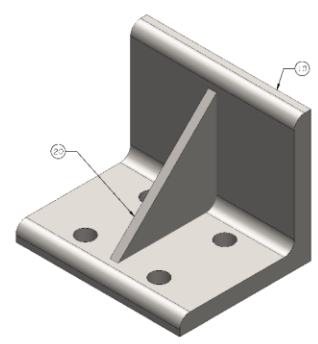
ITEM NO.	QTY	DESCRIPTION	PROV. BY (SPL. NO.)
17	1	REF. PART 14.1 PL. ST	N
18	1	182.14.17	N



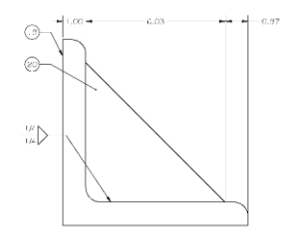
**SolidWorks Student Edition.
For Academic Use Only.**

	UNIVERSITY OF PENNSYLVANIA ENGINEERING CENTER 3127 RESEARCH DRIVE STATE COLLEGE, PA 16803	PENNSYLVANIA STATE UNIVERSITY ENGINEERING CENTER 3127 RESEARCH DRIVE STATE COLLEGE, PA 16803	PENNSYLVANIA STATE UNIVERSITY ENGINEERING CENTER 3127 RESEARCH DRIVE STATE COLLEGE, PA 16803
	PROJECT NO. 182.14.17 PROJECT NAME: NEW SHAKE TABLE SHEET NO. 182.14.17.1 DATE: 10/10/17	PROJECT NO. 182.14.17 PROJECT NAME: NEW SHAKE TABLE SHEET NO. 182.14.17.1 DATE: 10/10/17	PROJECT NO. 182.14.17 PROJECT NAME: NEW SHAKE TABLE SHEET NO. 182.14.17.1 DATE: 10/10/17

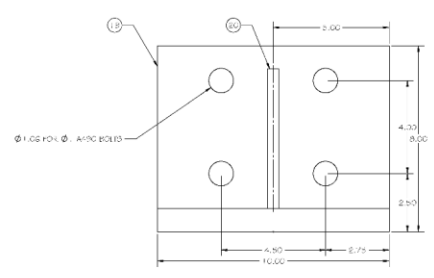
ITEM NO.	QTY.	DESCRIPTION	PROV. BY
10	1	ENDS	N
20	4	STEEL PLATE, 0.125" THICK	N



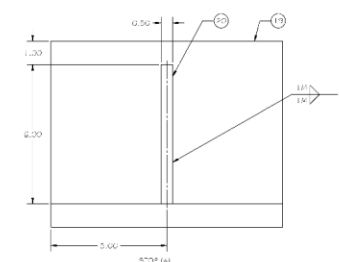
3-D (1)
ISOMETRIC VIEW
SCALE: 1"=1"



SECTION A-A
SECTION VIEW
SCALE: 1"=1"



SECTION B-B
SECTION VIEW
SCALE: 1"=1"



SECTION C-C
SECTION VIEW
SCALE: 1"=1"

**SolidWorks Student Edition.
For Academic Use Only.**

	UNIVERSITY OF PENNSYLVANIA COLLEGE OF ENGINEERING ENGINEERING CENTER 3127 RESEARCH DRIVE STATE COLLEGE, PA 16801 TEL: (814) 863-1000 FAX: (814) 863-1000 WWW: WWW.PENNSYLVANIA.EDU	PENNSYLVANIA STATE UNIVERSITY COLLEGE OF ENGINEERING ENGINEERING CENTER 3127 RESEARCH DRIVE STATE COLLEGE, PA 16801 TEL: (814) 863-1000 FAX: (814) 863-1000 WWW: WWW.PENNSYLVANIA.EDU	PENNSYLVANIA STATE UNIVERSITY COLLEGE OF ENGINEERING ENGINEERING CENTER 3127 RESEARCH DRIVE STATE COLLEGE, PA 16801 TEL: (814) 863-1000 FAX: (814) 863-1000 WWW: WWW.PENNSYLVANIA.EDU
	UNIVERSITY OF PENNSYLVANIA COLLEGE OF ENGINEERING ENGINEERING CENTER 3127 RESEARCH DRIVE STATE COLLEGE, PA 16801 TEL: (814) 863-1000 FAX: (814) 863-1000 WWW: WWW.PENNSYLVANIA.EDU	UNIVERSITY OF PENNSYLVANIA COLLEGE OF ENGINEERING ENGINEERING CENTER 3127 RESEARCH DRIVE STATE COLLEGE, PA 16801 TEL: (814) 863-1000 FAX: (814) 863-1000 WWW: WWW.PENNSYLVANIA.EDU	UNIVERSITY OF PENNSYLVANIA COLLEGE OF ENGINEERING ENGINEERING CENTER 3127 RESEARCH DRIVE STATE COLLEGE, PA 16801 TEL: (814) 863-1000 FAX: (814) 863-1000 WWW: WWW.PENNSYLVANIA.EDU

ITEM NO.	QTY	DESCRIPTION	PROV'D BY
24	1	VC_BRO	N
25	1	STK_FAC_11-CC	N

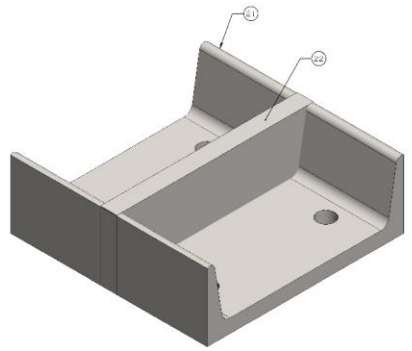


TABLE CONNECTION TO ACTUATOR
EDGE VIEW
SCALE 0.75"

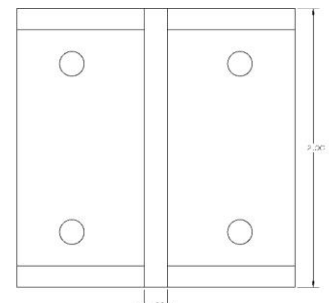


TABLE CONNECTION TO ACTUATOR
SIDE VIEW
SCALE 0.75"

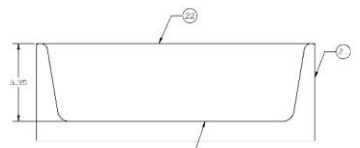


TABLE CONNECTION TO ACTUATOR
SECTION VIEW
SCALE 1.0:1"

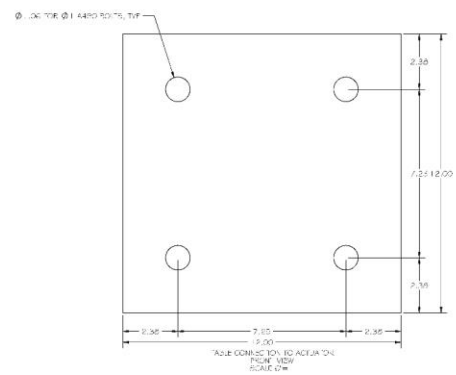


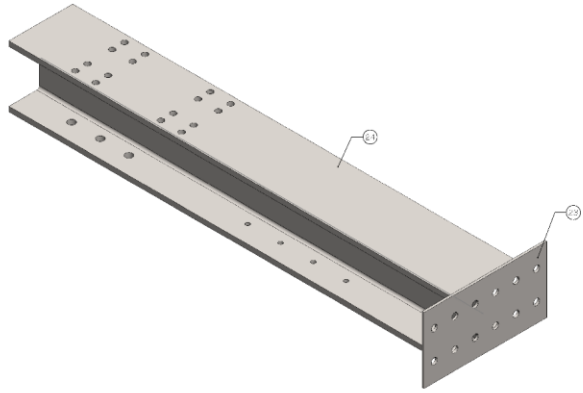
TABLE CONNECTION TO ACTUATOR
TOP VIEW
SCALE 0.75"

**SolidWorks Student Edition.
For Academic Use Only.**

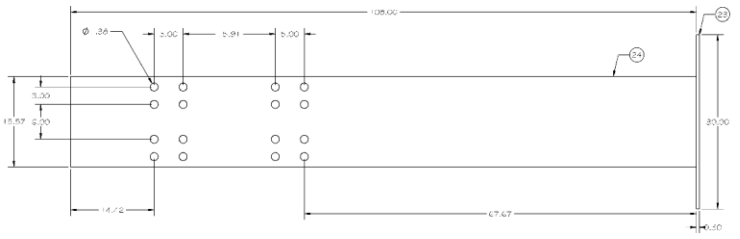
	UNIVERSITY OF PENNSYLVANIA COLLEGE OF ENGINEERING ENGINEERING DESIGN CENTER 3127 RESEARCH DRIVE STATE COLLEGE, PA 16801	PROJECT NO. 11-000	DATE 07-25-07	DRAWN BY JACOB HORN	CHECKED BY JACOB HORN	APPROVED BY JACOB HORN	TITLE NEW SHAKE TABLE QTEEL 3127 RESEARCH DRIVE STATE COLLEGE, PA 16801
	PROJECT NAME NEW SHAKE TABLE QTEEL	PROJECT NO. 11-000	DATE 07-25-07	DRAWN BY JACOB HORN	CHECKED BY JACOB HORN	APPROVED BY JACOB HORN	TITLE NEW SHAKE TABLE QTEEL 3127 RESEARCH DRIVE STATE COLLEGE, PA 16801

SCALE: 1/32"=1'-0" (AS SHOWN) 1/4"=1'-0" (OTHER VIEWS)

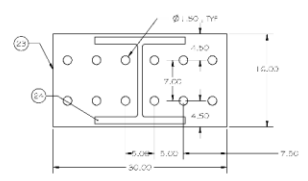
ITEM NO.	QTY.	DESCRIPTION	REMARKS
25	-	STEEL PLATE, 0.75" THICK	\
26	-	W 4x12.8	Y



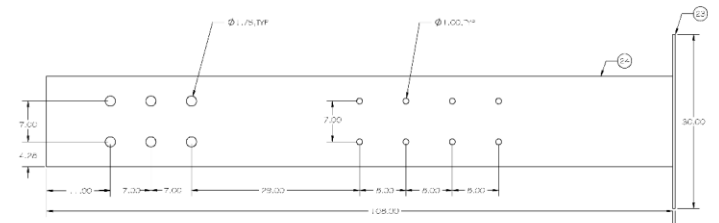
ACT UNDR B2AM
ISOM VIEW
SCALE: 1/2"=1"



ACT UNDR B2AM
FRONT VIEW
SCALE: 1/2"=1"



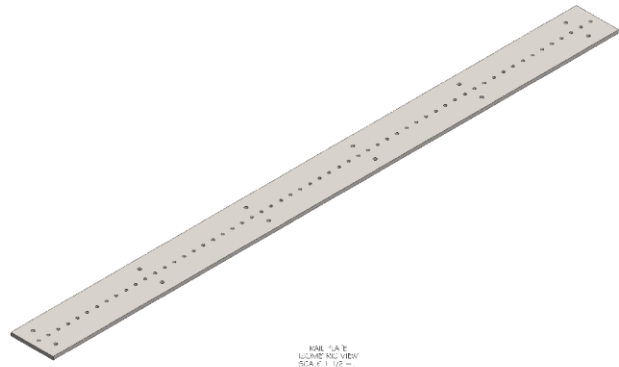
ACT UNDR B2AM
TOP VIEW
SCALE: 1/2"=1"



ACT UNDR B2AM
BOTTOM VIEW
SCALE: 1/2"=1"

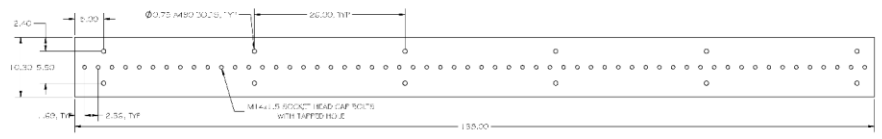
**SolidWorks Student Edition.
For Academic Use Only.**

	PROJECT NO. 1000000000 PROJECT NAME PROJECT LOCATION PROJECT START DATE PROJECT END DATE PROJECT MANAGER PROJECT ENGINEER	DATE: 10/1/2010 TIME: 10:00 AM USER: [Name] CANCELED BY: [Name]	Pennsylvania State University 3127 RESEARCH DRIVE STATE COLLEGE, PA 16801 817 (800) 462-3800 www.psu.edu
	NEW SHAKE TABLE QTEL DTABLEPLANS REV 01 SCALE: 1/2"=1" (1/2"=1" OF 10)		



RAW ISVT
ISOMETRIC VIEW
SCALE 1:100

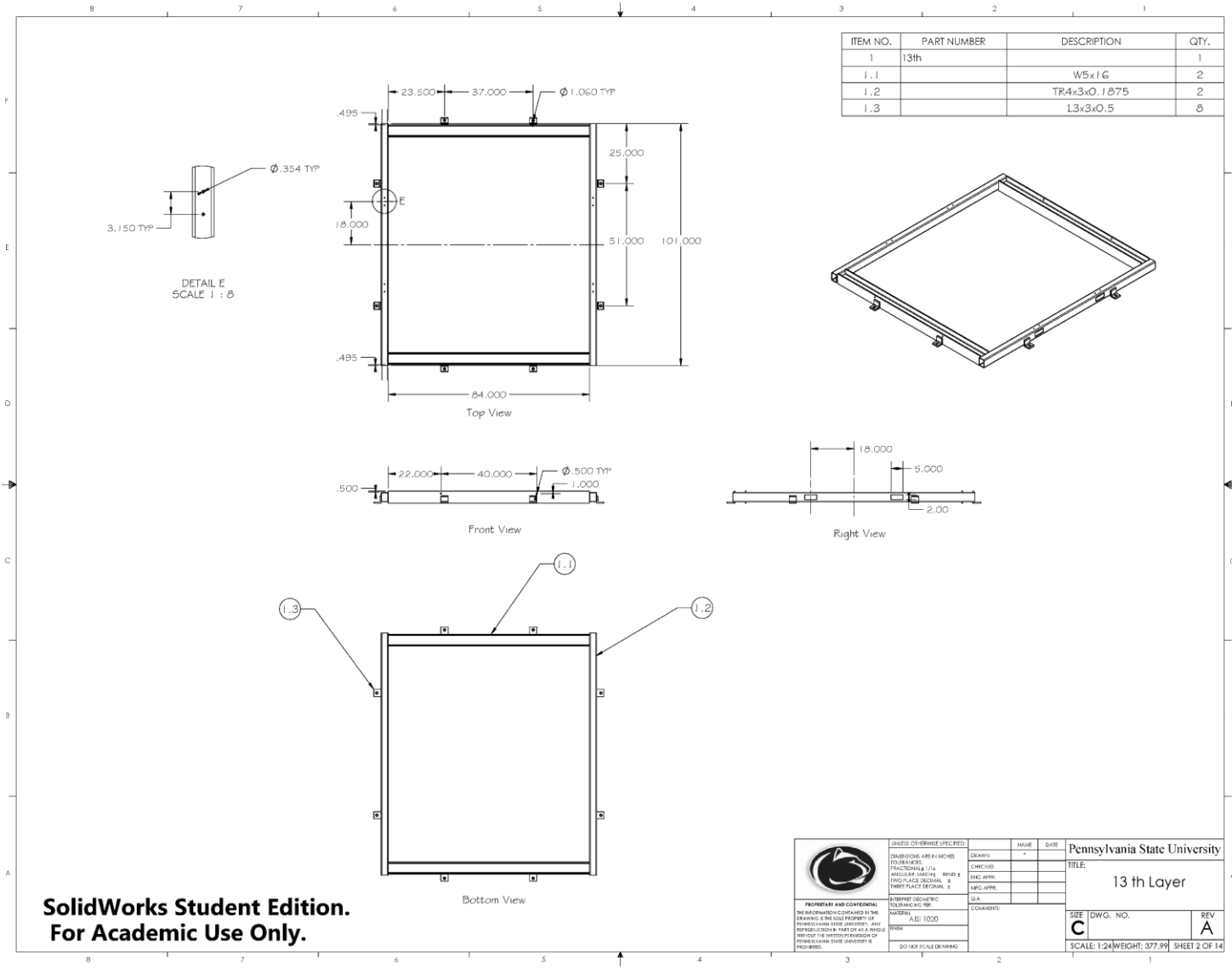
ITEM NO.	QTY.	DESCRIPTION	PROVISED BY
26	2	STEEL PLATE 0.75" THICK	A



RAW ISVT
PLAN VIEW
SCALE 1:100

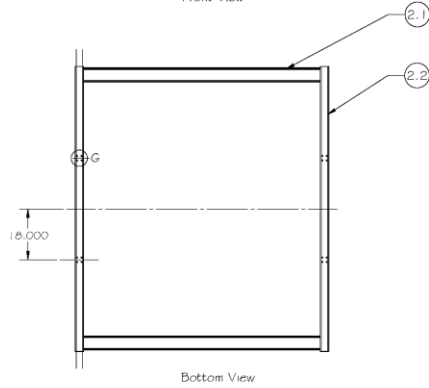
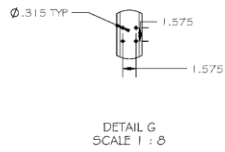
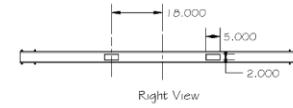
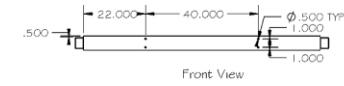
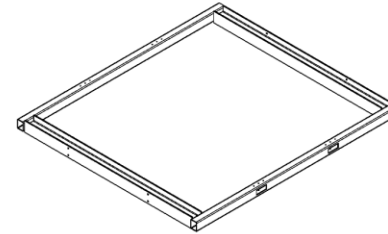
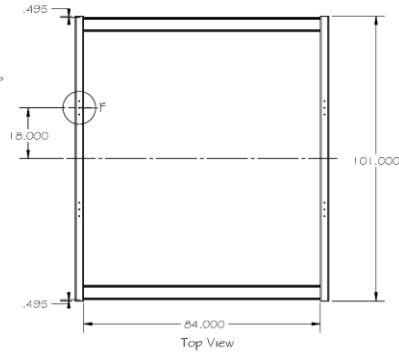
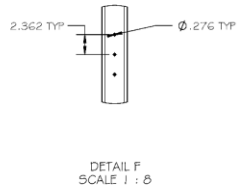
**SolidWorks Student Edition.
For Academic Use Only.**

	UNIVERSITY OF PENNSYLVANIA PENNSYLVANIA STATE UNIVERSITY COLLEGE OF ENGINEERING ENGINEERING DESIGN CENTER 3127 RESEARCH DRIVE STATE COLLEGE, PA 16801 814/863-1000 WWW.PENNSYLVANIASTATE.EDU	PROJECT NO. 1000000000 DRAWING NO. 1000000000 SHEET NO. 1000000000 DATE 10/10/10	PENNSYLVANIA STATE UNIVERSITY NEW SHAKE TABLE CFEEL TABLEPLANS REV SCALE 1:3 (WIDTH: 39.1, 5-481) P OF 10
	PROJECT TITLE PROJECT LOCATION PROJECT NUMBER PROJECT DATE	PROJECT MANAGER PROJECT ENGINEER PROJECT CHECKER PROJECT APPROVER	PROJECT STATUS PROJECT PHASE PROJECT BUDGET PROJECT RISK



**SolidWorks Student Edition.
For Academic Use Only.**

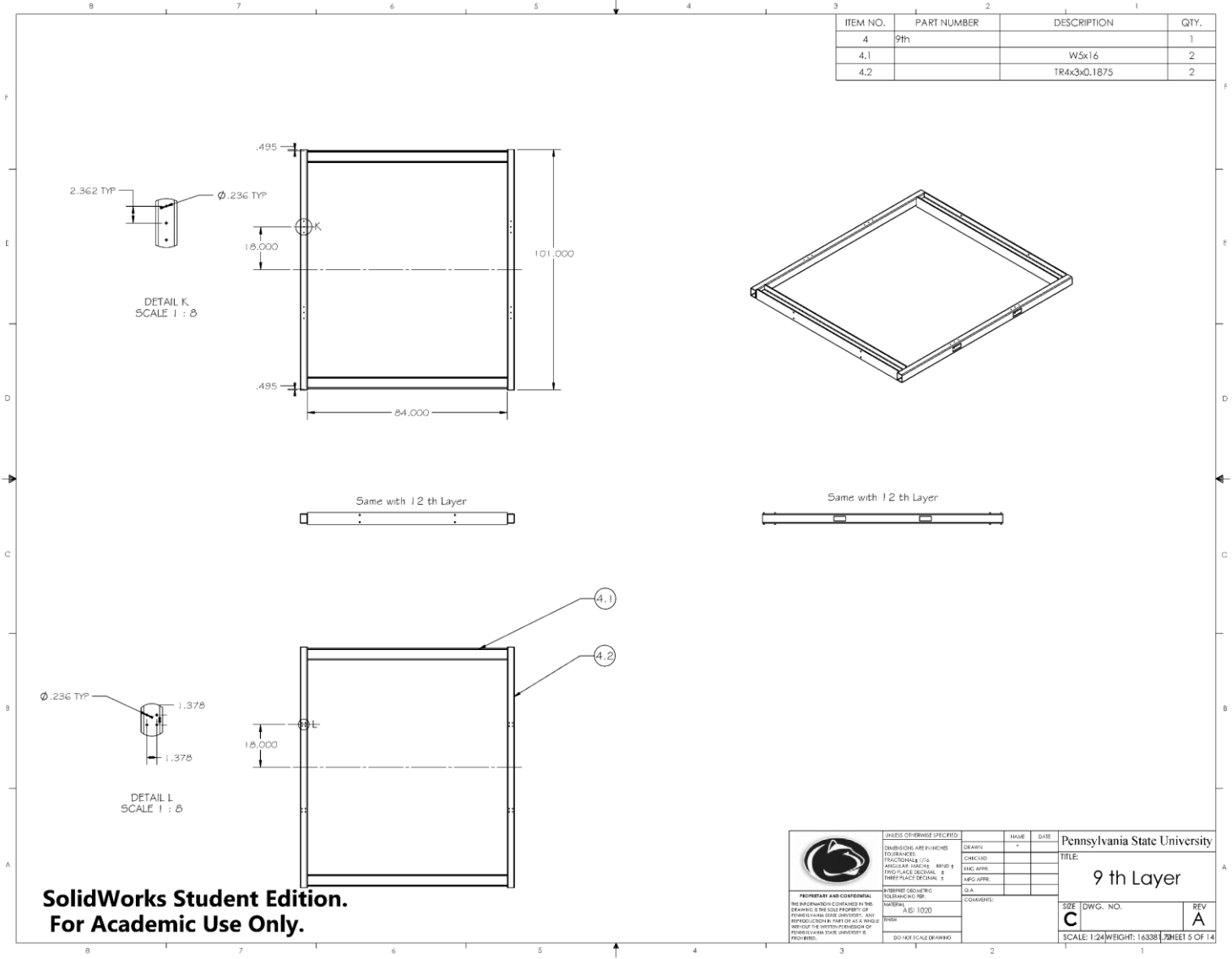
ITEM NO.	PART NUMBER	DESCRIPTION	QTY.
2	12th		1
2.1		W5x16	2
2.2		TR4x3x0.1875	2



	UNLESS OTHERWISE SPECIFIED:	UNITS: INCHES	SCALE: AS SHOWN	DATE: _____	Pennsylvania State University 12 th Layer
	DIMENSIONS ARE FRACTIONS DECIMALS TO FIFTH PLACE ANGULAR DIMENSIONS TO TWO PLACE DECIMALS HOLE DIMENSIONS TO THREE PLACE DECIMALS	DIMENSIONS ARE FRACTIONS DECIMALS TO FIFTH PLACE ANGULAR DIMENSIONS TO TWO PLACE DECIMALS HOLE DIMENSIONS TO THREE PLACE DECIMALS	DIMENSIONS ARE FRACTIONS DECIMALS TO FIFTH PLACE ANGULAR DIMENSIONS TO TWO PLACE DECIMALS HOLE DIMENSIONS TO THREE PLACE DECIMALS	DIMENSIONS ARE FRACTIONS DECIMALS TO FIFTH PLACE ANGULAR DIMENSIONS TO TWO PLACE DECIMALS HOLE DIMENSIONS TO THREE PLACE DECIMALS	
PROPRIETARY AND CONFIDENTIAL THE INFORMATION CONTAINED IN THIS DRAWING IS THE SOLE PROPERTY OF PENNSYLVANIA STATE UNIVERSITY. ANY REPRODUCTION IN PART OR AS A WHOLE WITHOUT THE WRITTEN PERMISSION OF PENNSYLVANIA STATE UNIVERSITY IS PROHIBITED.	INTERPRET GEOMETRIC TOLERANCING PER MATERIAL: AS 1000 FINISH:	COMMENTS:	SIZE: C DWG. NO.: 1-24-16336	REV: A SHEET 3 OF 14	SCALE: 1:24 WEIGHT: 1.6336 SHEET 3 OF 14

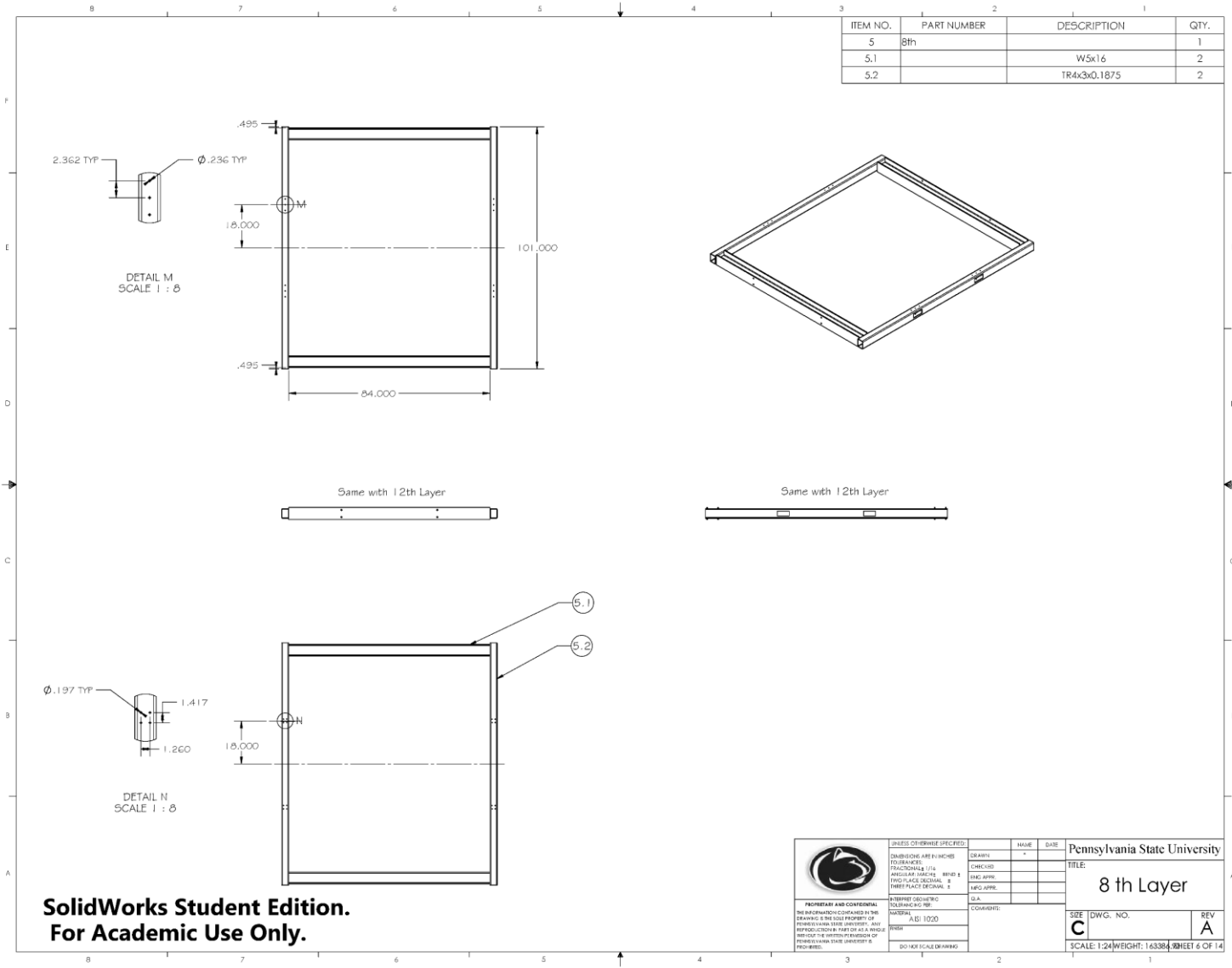
**SolidWorks Student Edition.
For Academic Use Only.**

ITEM NO.	PART NUMBER	DESCRIPTION	QTY.
4	9th		1
4.1		W5x16	2
4.2		TR4x3x0.1875	2



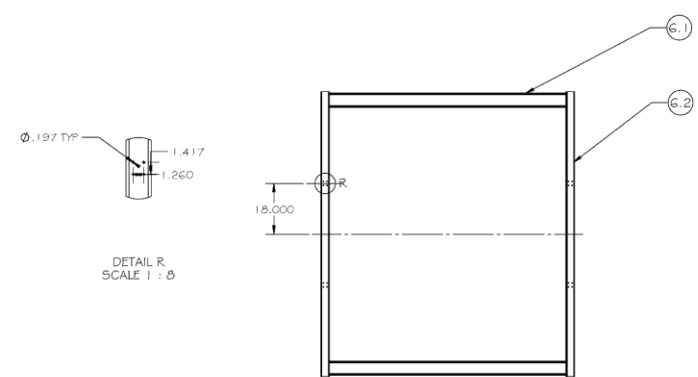
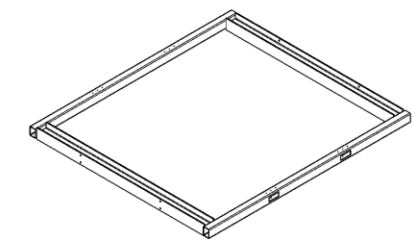
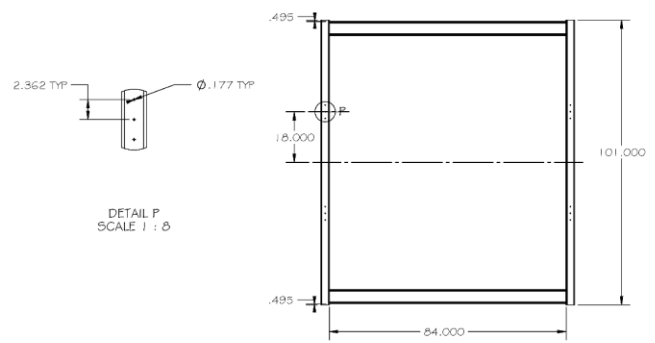
**SolidWorks Student Edition.
For Academic Use Only.**

	UNLESS OTHERWISE SPECIFIED: DIMENSIONS ARE IN INCHES TOLERANCES: FRACTIONAL ± 1/16 DECIMAL ± 0.005 ANGULAR DIMENSIONS ± 0.005 HOLE DIMENSIONS ± 0.005 HOLE LOCATIONS ± 0.005	DRAWN: _____ CHECKED: _____ ENG APPR: _____ MFG APPR: _____ QA: _____ COMMENTS: _____	NAME: _____ DATE: _____	Pennsylvania State University TITLE: 9 th Layer
	PROPRIETARY AND CONFIDENTIAL THE INFORMATION CONTAINED IN THIS DRAWING IS THE SOLE PROPERTY OF PENNSYLVANIA STATE UNIVERSITY. ANY REPRODUCTION IN PART OR AS A WHOLE WITHOUT THE WRITTEN PERMISSION OF PENNSYLVANIA STATE UNIVERSITY IS PROHIBITED.	INTERPRET GEOMETRIC TOLERANCING PER: MATERIAL: AS 1020 FINISH: _____ DO NOT SCALE DRAWING	SIZE: DWG. NO. C SCALE: 1:24 WEIGHT: 16338 SHEET 5 OF 14	REV: A



**SolidWorks Student Edition.
For Academic Use Only.**

ITEM NO.	PART NUMBER	DESCRIPTION	QTY.
6	7th		1
6.1		W5x16	2
6.2		TR4x3@.1875	2

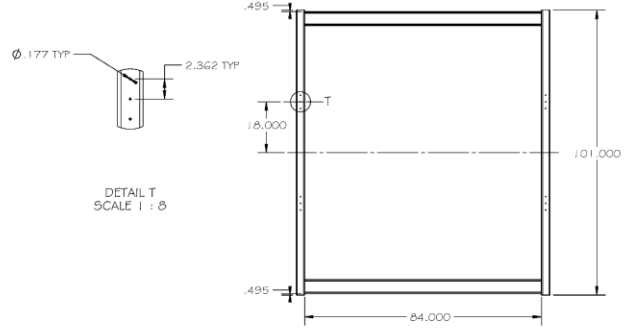


	UNLESS OTHERWISE SPECIFIED:	UNITS: INCHES	SCALE: AS SHOWN	DATE: _____	Pennsylvania State University 7 th Layer
	DIMENSIONS ARE FRACTIONS DECIMALS TO 3 PLACES ANGULAR DIMENSIONS TO 2 PLACES HOLE DIMENSIONS TO 3 PLACES	DIMENSIONS ARE FRACTIONS DECIMALS TO 3 PLACES ANGULAR DIMENSIONS TO 2 PLACES HOLE DIMENSIONS TO 3 PLACES	DIMENSIONS ARE FRACTIONS DECIMALS TO 3 PLACES ANGULAR DIMENSIONS TO 2 PLACES HOLE DIMENSIONS TO 3 PLACES	DIMENSIONS ARE FRACTIONS DECIMALS TO 3 PLACES ANGULAR DIMENSIONS TO 2 PLACES HOLE DIMENSIONS TO 3 PLACES	
PROPRIETARY AND CONFIDENTIAL THE INFORMATION CONTAINED IN THIS DRAWING IS THE SOLE PROPERTY OF PENNSYLVANIA STATE UNIVERSITY. ANY REPRODUCTION IN PART OR AS A WHOLE WITHOUT THE WRITTEN PERMISSION OF PENNSYLVANIA STATE UNIVERSITY IS PROHIBITED.	INTERPRET GEOMETRIC TOLERANCING PER MATERIAL: AS 1020 FINISH: _____	COMMENTS: _____	SIZE: DWG. NO. C	REV: A	SCALE: 1:24 WEIGHT: 16339 SHEET 7 OF 14

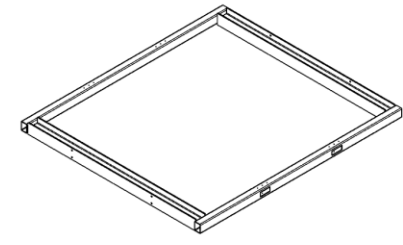
**SolidWorks Student Edition.
For Academic Use Only.**

ITEM NO.	PART NUMBER	DESCRIPTION	QTY.
7	2nd-6th		5
7.1		W5x16	10
7.2		TR4x3x0.1875	10

Layer Duplicates: 5



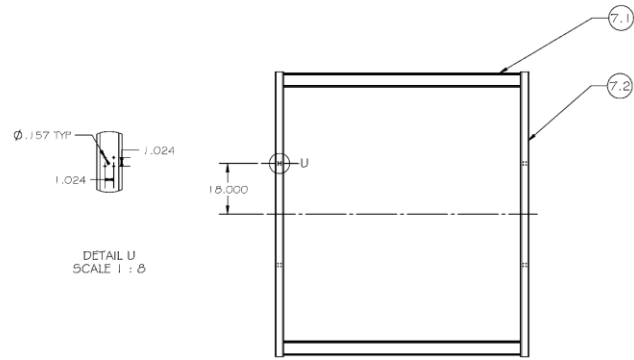
DETAIL T
SCALE 1 : 8



Same with 1 2 th Layer



Same with 1 2 th Layer

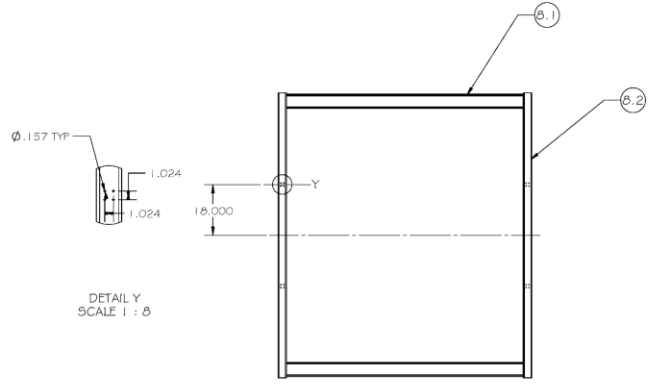
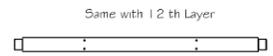
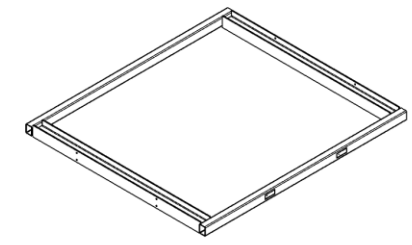
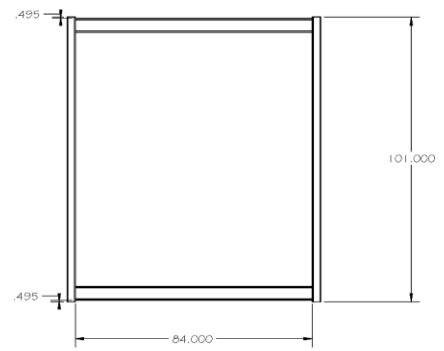


DETAIL U
SCALE 1 : 8

**SolidWorks Student Edition.
For Academic Use Only.**

	UNLESS OTHERWISE SPECIFIED: DIMENSIONS ARE IN INCHES TOLERANCES: FRACTIONAL ± .015 DECIMAL ± .005 ANGULAR DIMENSIONS ± .01 HOLE LOCATIONS ± .015 HOLE DRILLING ± .015	DRAWN: _____ CHECKED: _____ ENG APPR: _____ MFG APPR: _____ QA: _____ COMMENTS: _____	NAME: _____ DATE: _____	Pennsylvania State University TITLE: 2nd- 6th Layer
	PROPRIETARY AND CONFIDENTIAL THE INFORMATION CONTAINED IN THIS DRAWING IS THE SOLE PROPERTY OF PENNSYLVANIA STATE UNIVERSITY. ANY REPRODUCTION IN PART OR AS A WHOLE WITHOUT THE WRITTEN PERMISSION OF PENNSYLVANIA STATE UNIVERSITY IS PROHIBITED.	INTERPRET GEOMETRIC TOLERANCING PER: MATERIAL: AS 1020 FINISH: _____	DO NOT SCALE DRAWING	SIZE: DWG. NO. C SCALE: 1:24 WEIGHT: 1.63394 SHEET 8 OF 14

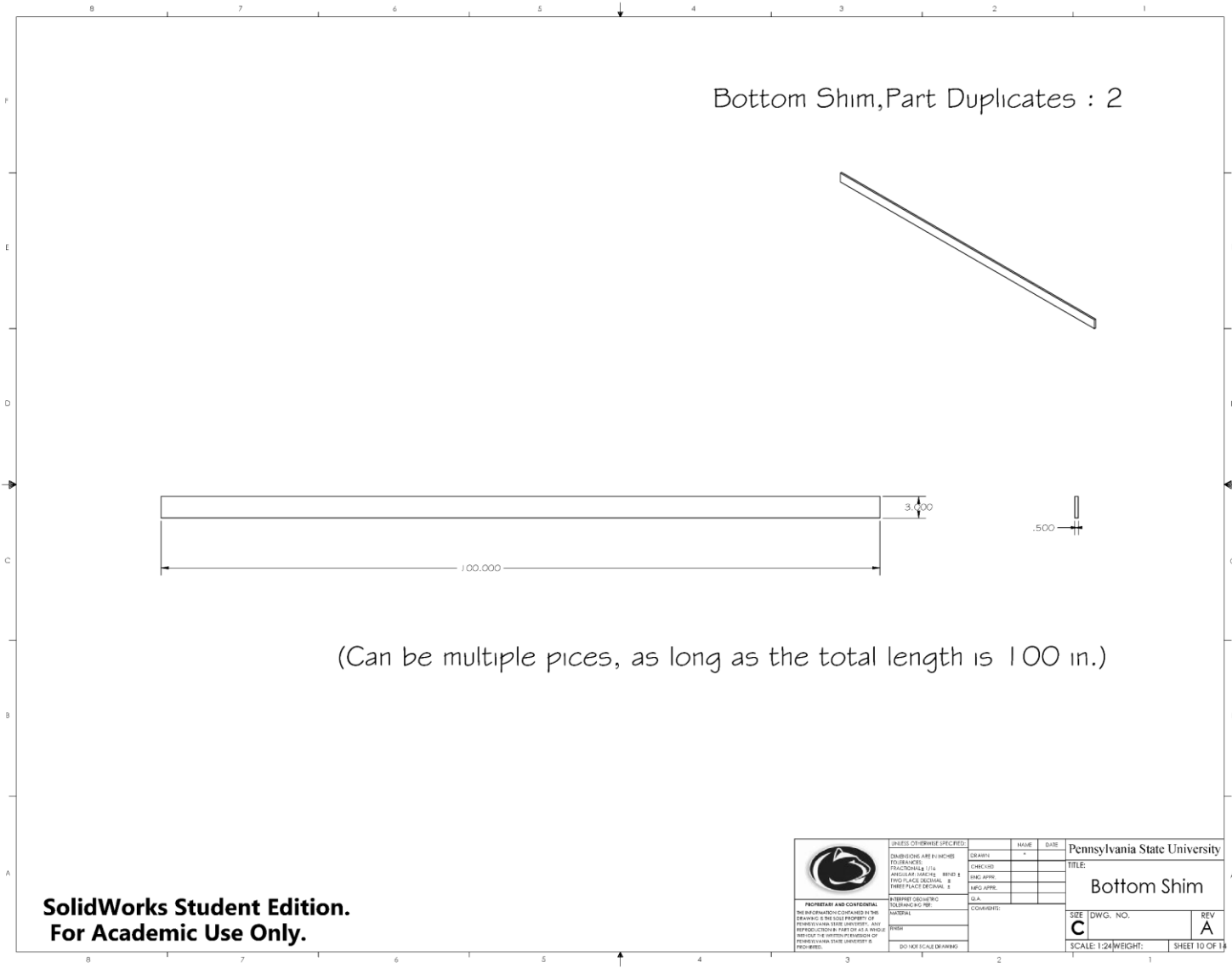
ITEM NO.	PART NUMBER	DESCRIPTION	QTY.
8	1st		1
8.1		W5x16	2
8.2		TR4x3x0.1875	2



DETAIL Y
SCALE 1 : 8

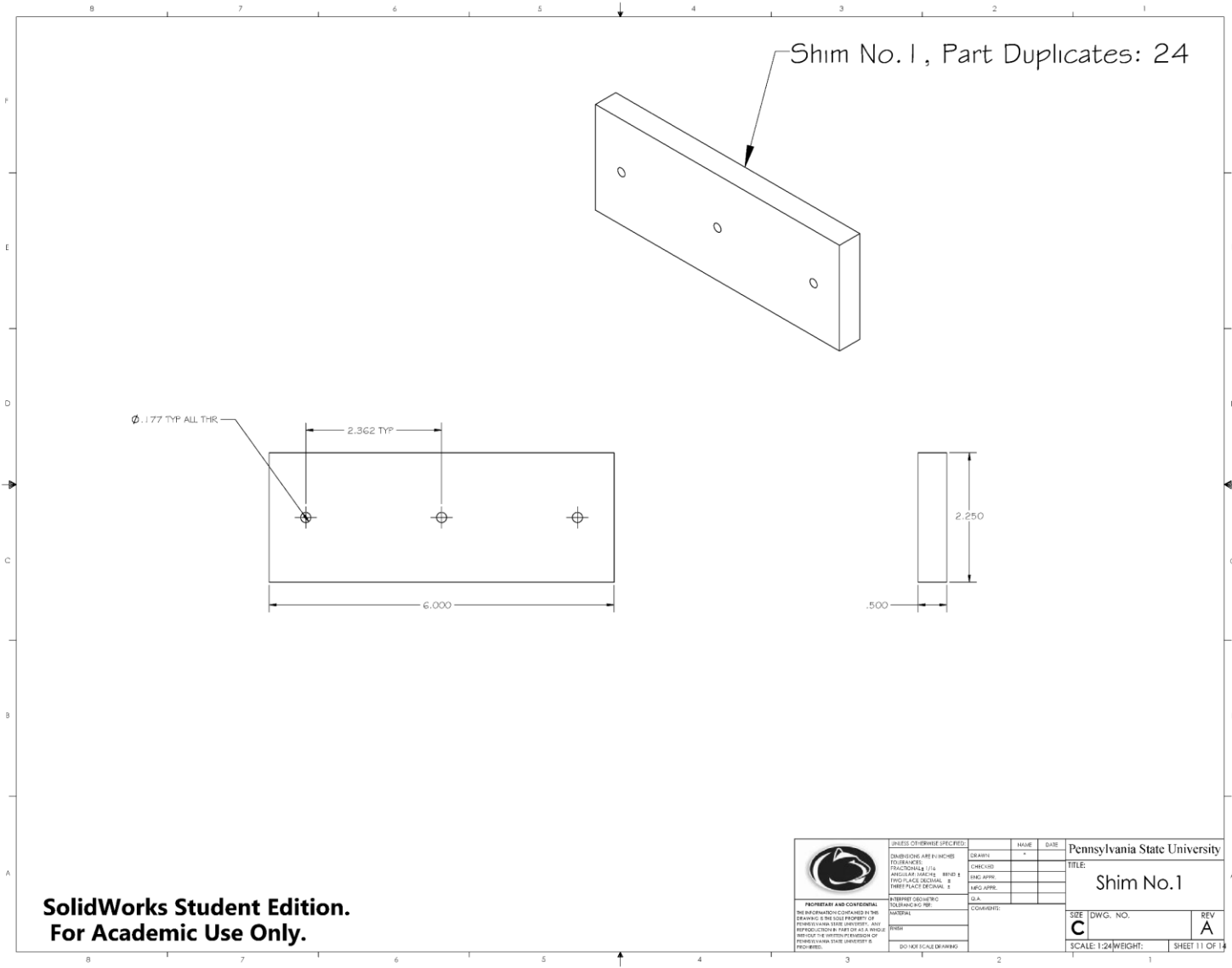
**SolidWorks Student Edition.
For Academic Use Only.**

	UNLESS OTHERWISE SPECIFIED: DIMENSIONS ARE IN INCHES DECIMALS TO FIVE ANGULAR DIMENSIONS TO TWO PLACE DECIMALS HOLE DIMENSIONS TO THREE PLACE DECIMALS	DESIGNED BY: _____ CHECKED BY: _____ ENG. APPROVED BY: _____ MFG. APPROVED BY: _____ DATE: _____	Pennsylvania State University TITLE: 1st Layer
	INTERPRET GEOMETRIC TOLERANCING PER: MATERIAL: AS 1020 FINISH: _____ COMMENTS: _____ DO NOT SCALE DRAWING	SIZE: C DWG. NO.: _____ SCALE: 1:24 WEIGHT: 1.63403 SHEET 9 OF 14	REV: A



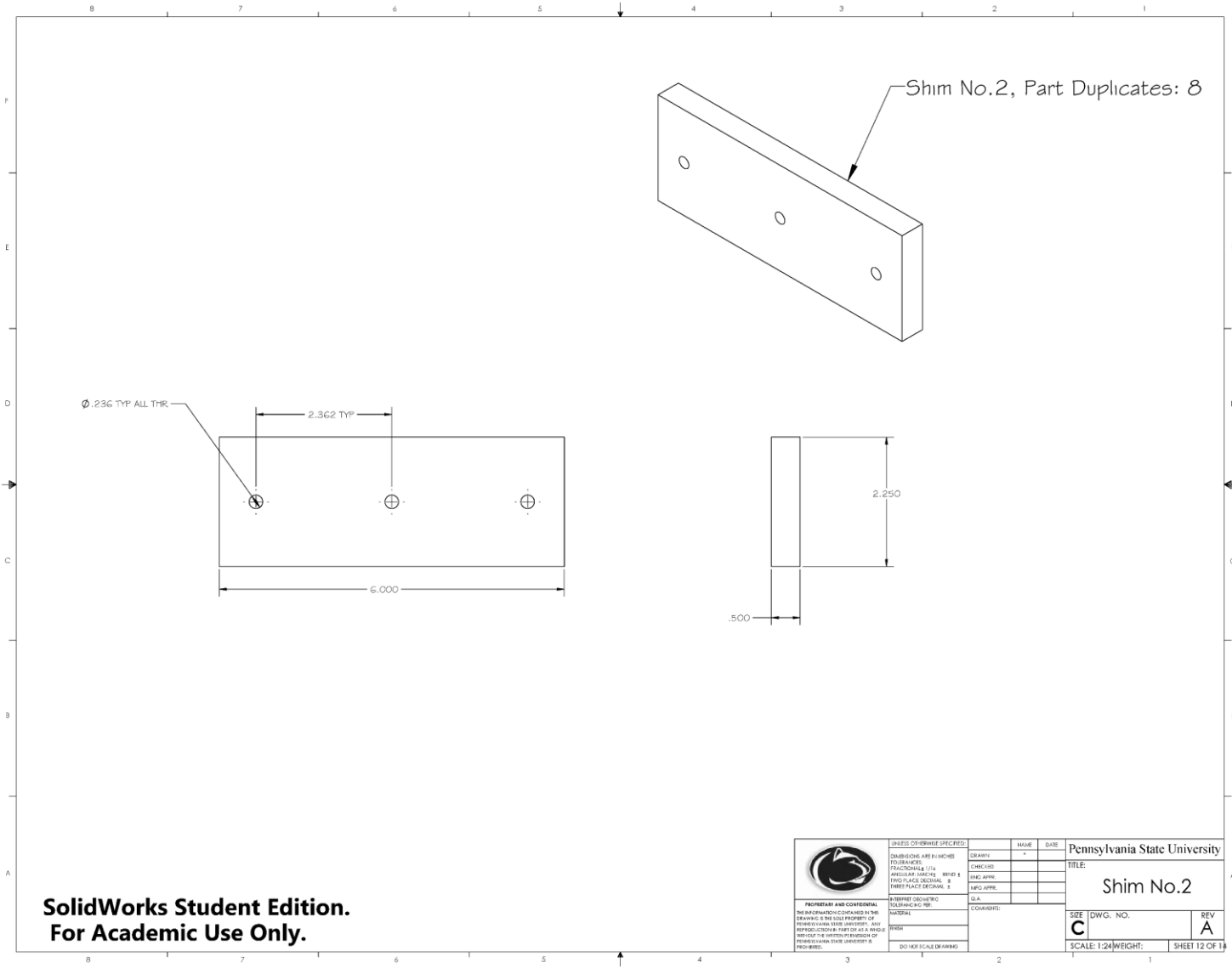
**SolidWorks Student Edition.
For Academic Use Only.**

	UNLESS OTHERWISE SPECIFIED:	DESIGN:	NAME:	DATE:	Pennsylvania State University TITLE: Bottom Shim
	TOLERANCES:	CONCAD:			
	FRACTIONAL: 1/16	ENG APPR:			
	ANGULAR: DECIMALS: 10	ENG APPR:			
	THREE PLACE DECIMAL: 3	ENG APPR:			SIZE: DWG. NO. REV C 1 A
PROPRIETARY AND CONFIDENTIAL THE INFORMATION CONTAINED IN THIS DRAWING IS THE SOLE PROPERTY OF PENNSYLVANIA STATE UNIVERSITY. ANY REPRODUCTION IN PART OR AS A WHOLE WITHOUT THE WRITTEN PERMISSION OF PENNSYLVANIA STATE UNIVERSITY IS PROHIBITED.	INTERPRET GEOMETRIC TOLERANCING PER: MATERIAL: FINISH: DO NOT SCALE DRAWING	COMMENTS:			SCALE: 1:24 WEIGHT: SHEET 10 OF 11



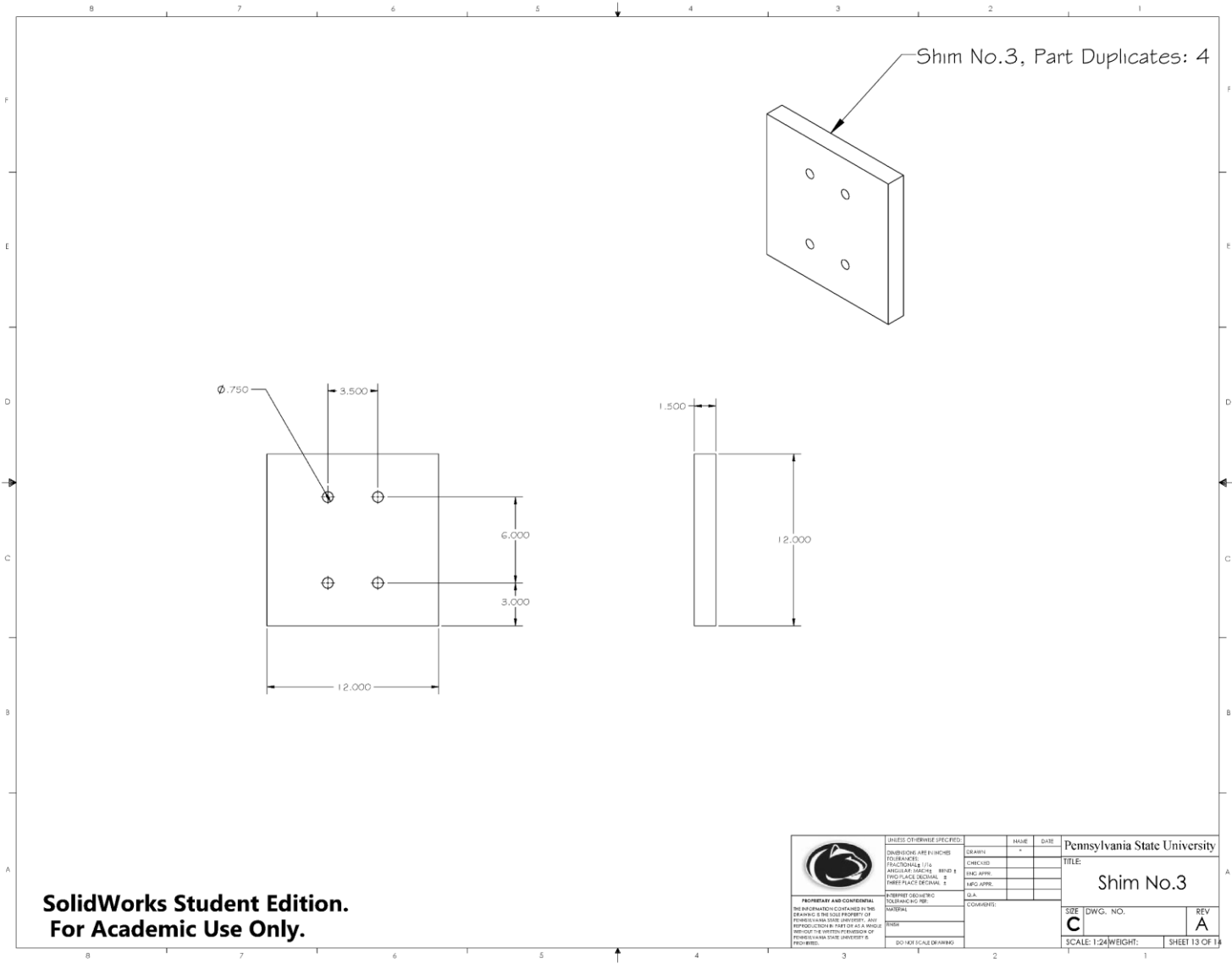
**SolidWorks Student Edition.
For Academic Use Only.**

	UNLESS OTHERWISE SPECIFIED: DIMENSIONS ARE IN INCHES DECIMALS TO 1/16 ANGULAR DIMENSIONS TO NEAREST 5 MINUTES HOLE DIMENSIONS TO NEAREST 0.0005 INCHES	DESIGNED BY: _____ CHECKED BY: _____ ENG. APPR. _____ MFG. APPR. _____ D.A. _____	NAME: _____ DATE: _____	Pennsylvania State University TITLE: Shim No.1
	PROPRIETARY AND CONFIDENTIAL THE INFORMATION CONTAINED IN THIS DRAWING IS THE SOLE PROPERTY OF PENNSYLVANIA STATE UNIVERSITY. ANY REPRODUCTION IN PART OR AS A WHOLE WITHOUT THE WRITTEN PERMISSION OF PENNSYLVANIA STATE UNIVERSITY IS PROHIBITED.	INTERPRET GEOMETRIC TOLERANCING PER ASME Y14.5-2009 MATERIAL: _____ FINISH: _____ DO NOT SCALE DRAWING	COMMENTS: _____	SIZE: C DWG. NO.: _____ SCALE: 1:24 WEIGHT: _____ SHEET 11 OF 14



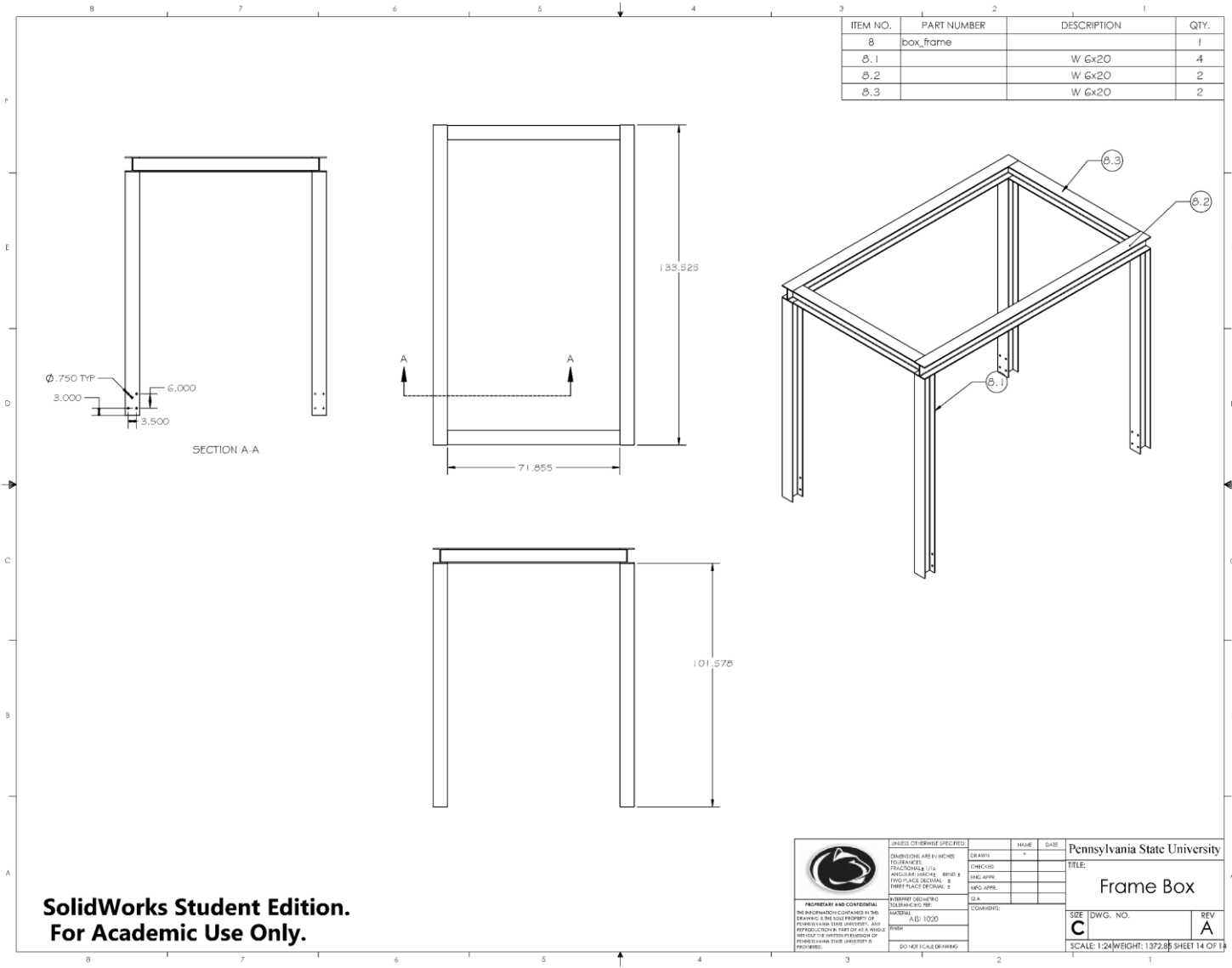
**SolidWorks Student Edition.
For Academic Use Only.**

	UNLESS OTHERWISE SPECIFIED:	DESIGN:	NAME:	DATE:	Pennsylvania State University TITLE: Shim No.2
	DIMENSIONS ARE IN INCHES	CONC/APP:			
	TOLERANCES UNLESS OTHERWISE SPECIFIED:	ENG APPR:			
	FRACTIONAL: 1/16	MFG APPR:			
DECIMAL: .005					
ANGULAR: DECIMAL: .1					
THREE PLACE DECIMAL: .005					
FOOTNOTES:					
PROPERTY AND CONFIDENTIAL	INTERPRET GEOMETRIC TOLERANCING PER:				
THE INFORMATION CONTAINED IN THIS DRAWING IS THE SOLE PROPERTY OF PENNSYLVANIA STATE UNIVERSITY. ANY REPRODUCTION IN PART OR AS A WHOLE WITHOUT THE WRITTEN PERMISSION OF PENNSYLVANIA STATE UNIVERSITY IS PROHIBITED.	MATERIAL:				
	FINISH:				
	DO NOT SCALE DRAWING				
		SIZE:	DWG. NO.:	REV:	
		C		A	
		SCALE: 1:24	WEIGHT:	SHEET 12 OF 14	



**SolidWorks Student Edition.
For Academic Use Only.**

	UNLESS OTHERWISE SPECIFIED:	DESIGN:	NAME:	DATE:	Pennsylvania State University TITLE: Shim No.3
	DIMENSIONS ARE IN INCHES TOLERANCES: FRACTIONAL: 1/16 DECIMAL: .0005 ANGULAR: 30 MIN HOLE: .0015 HOLE: .0015 HOLE: .0015	CHECKED:			
PROPRIETARY AND CONFIDENTIAL THE INFORMATION CONTAINED IN THIS DRAWING IS THE SOLE PROPERTY OF PENNSYLVANIA STATE UNIVERSITY. ANY REPRODUCTION IN PART OR AS A WHOLE WITHOUT THE WRITTEN PERMISSION OF PENNSYLVANIA STATE UNIVERSITY IS PROHIBITED.	INTERPRET GEOMETRIC TOLERANCING PER ASME Y14.5-2009	MATERIAL:	ISSUE:	COMMENTS:	SIZE DWG. NO. C SCALE: 1:24 WEIGHT: SHEET 13 OF 14

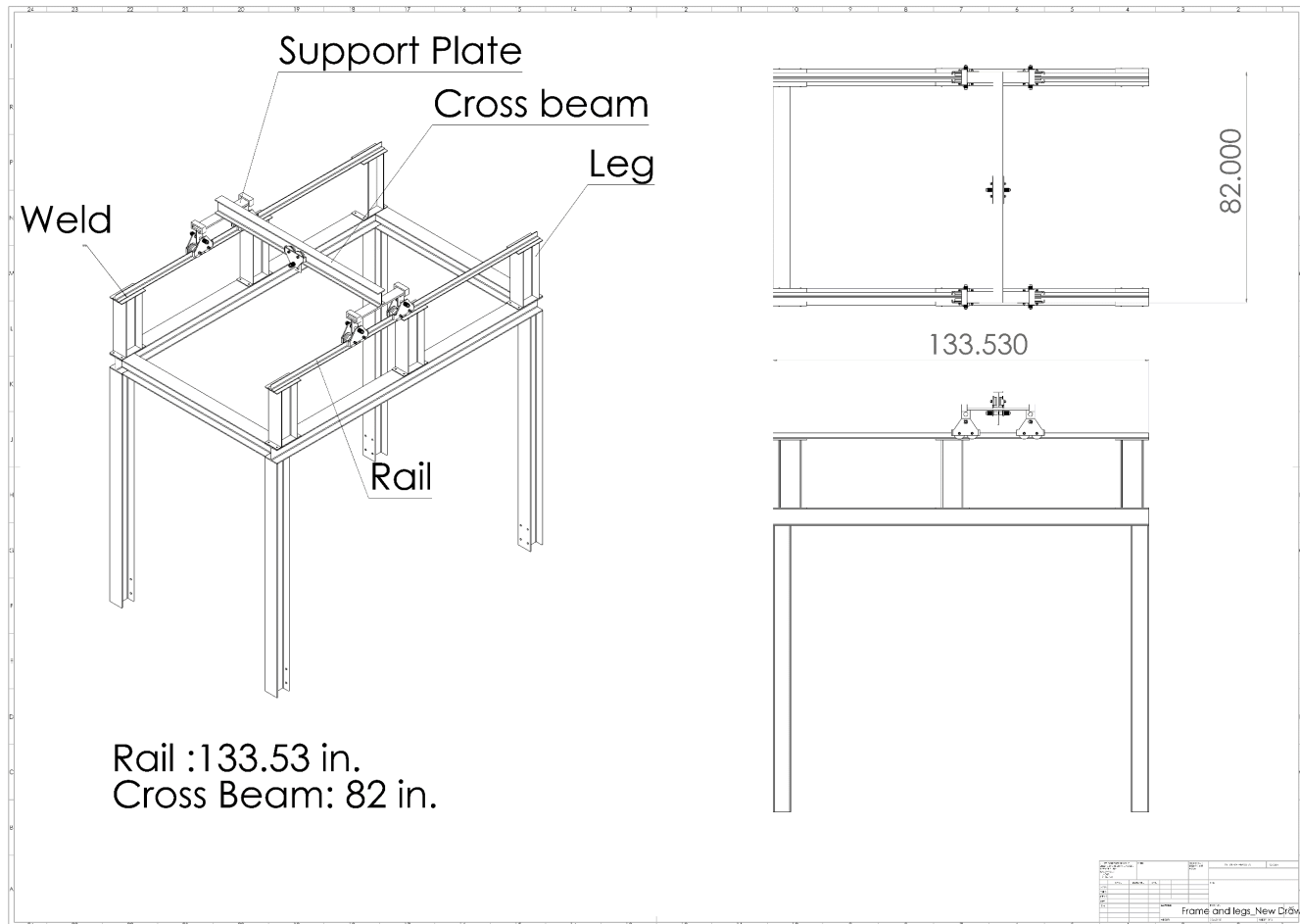


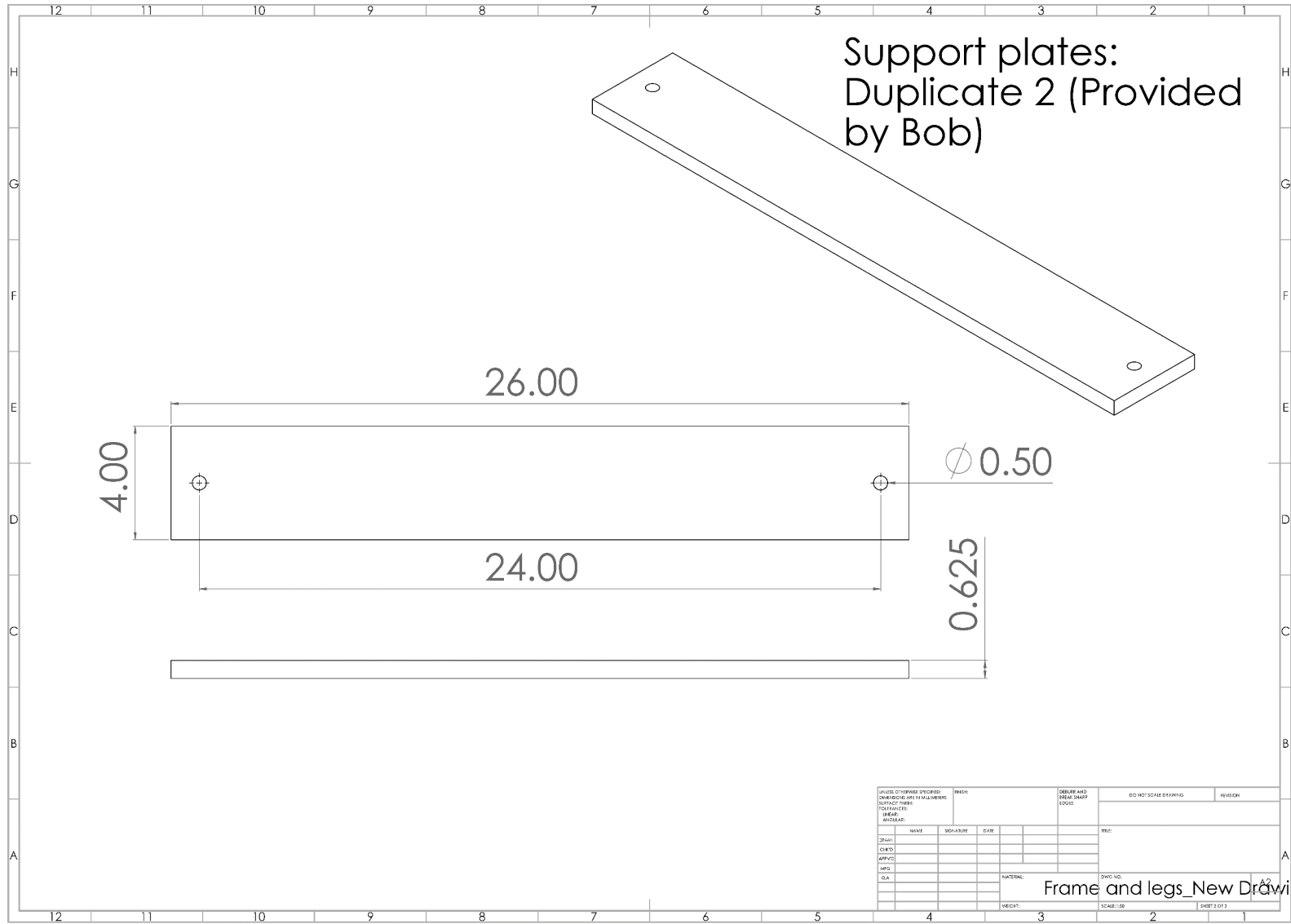
**SolidWorks Student Edition.
For Academic Use Only.**

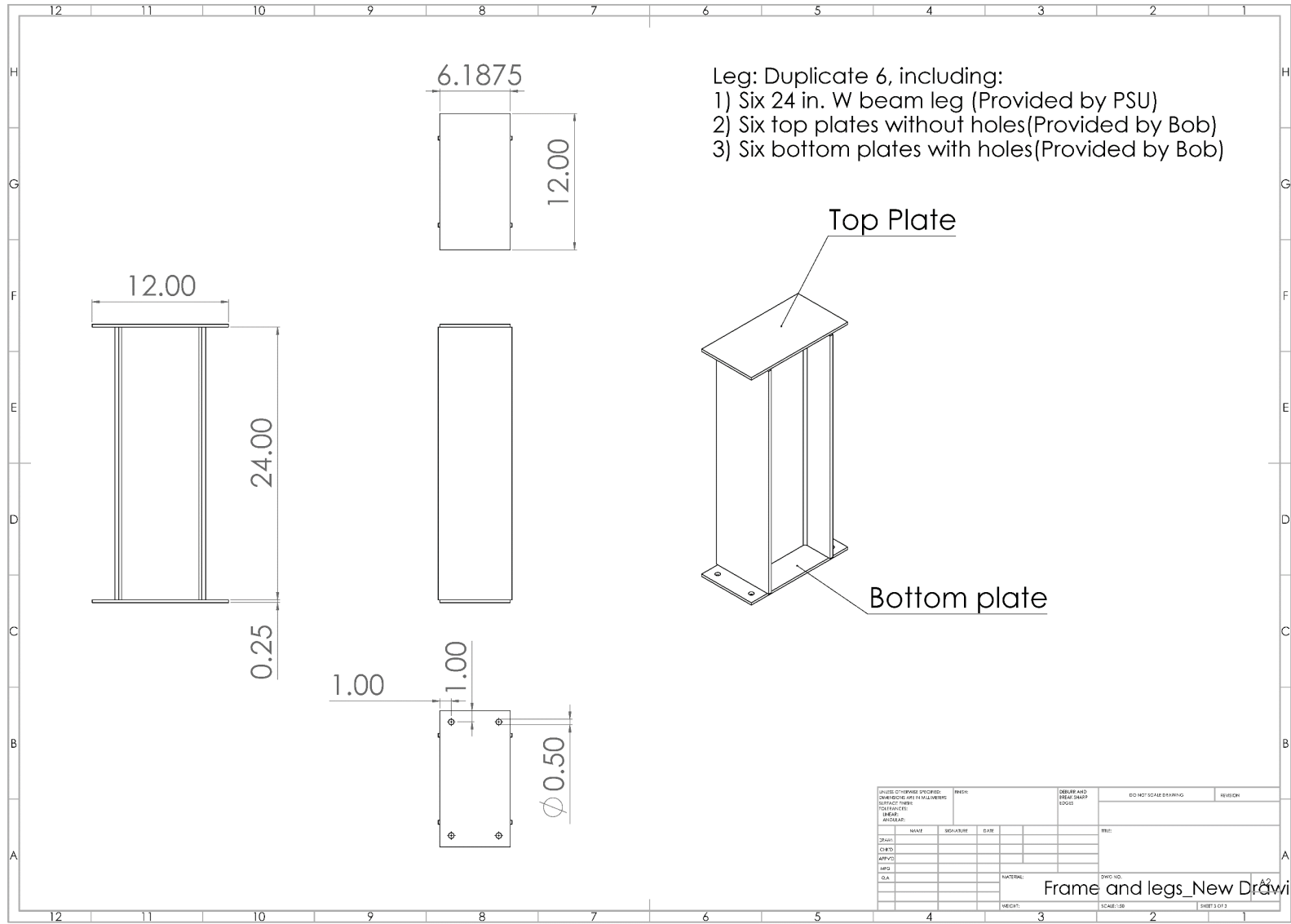
	DIMENSIONS ARE IN INCHES TOLERANCES UNLESS OTHERWISE SPECIFIED: FRACTIONAL ± .005 DECIMAL ± .001 ANGULAR DIMENSIONS ± .01 HOLE LOCATIONS ± .005 HOLE DIAMETERS ± .001	NAME: _____ DATE: _____	Pennsylvania State University TITLE: Frame Box
	INTERPRET GEOMETRIC TOLERANCING PER AS Y14.5 MATERIAL: AISI 1020 FINISH: _____ COMMENTS: _____	DRAWN BY: _____ CHECKED BY: _____ ENG. APPR. _____ MFG. APPR. _____ Q.A. _____ FOUNDATIONS: _____	SIZE: C DWG. NO. _____ SCALE: 1:24 WEIGHT: 1372.8 SHEET 14 OF 14

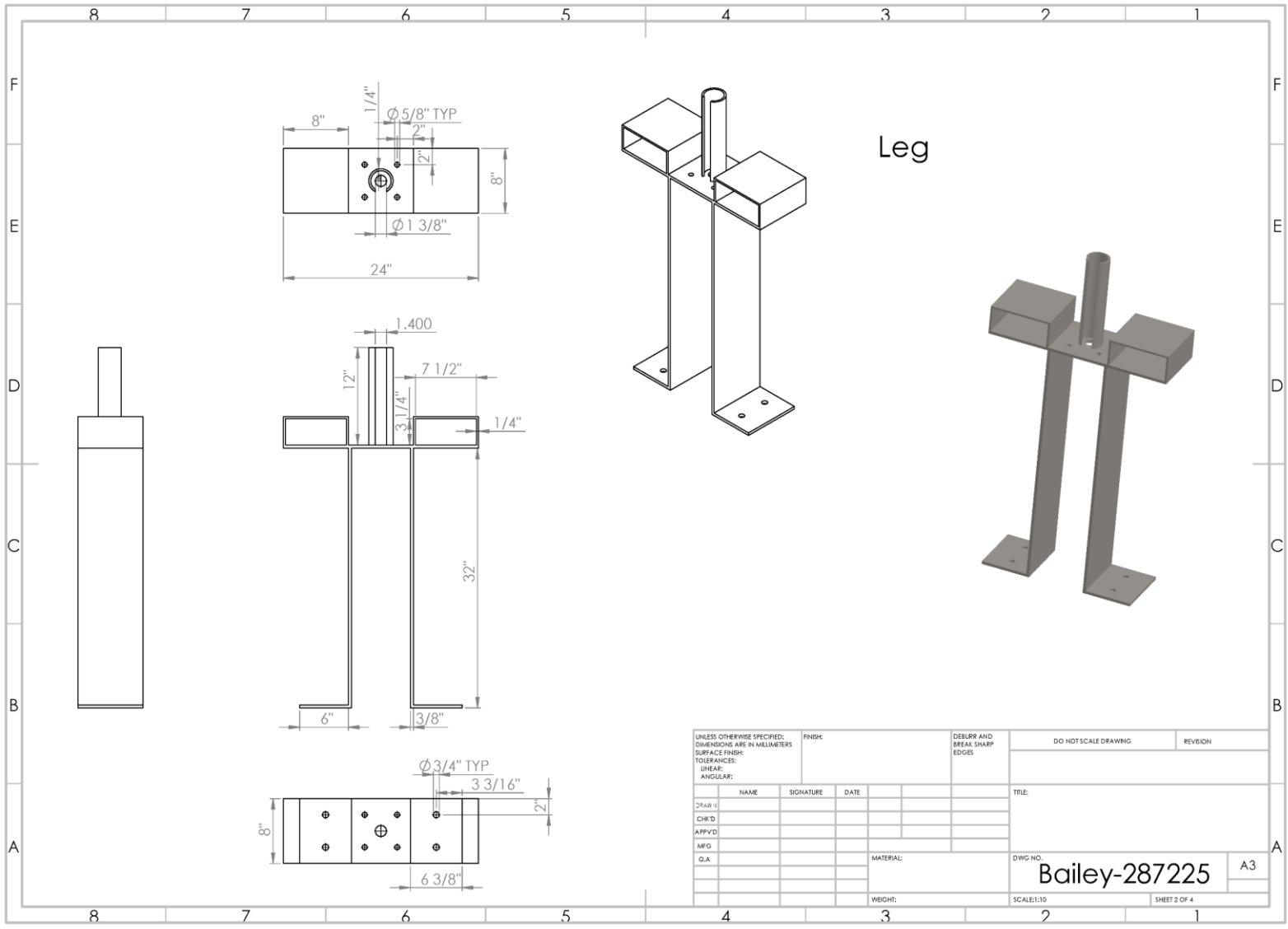
Appendix C

Design drawings of pluviation system



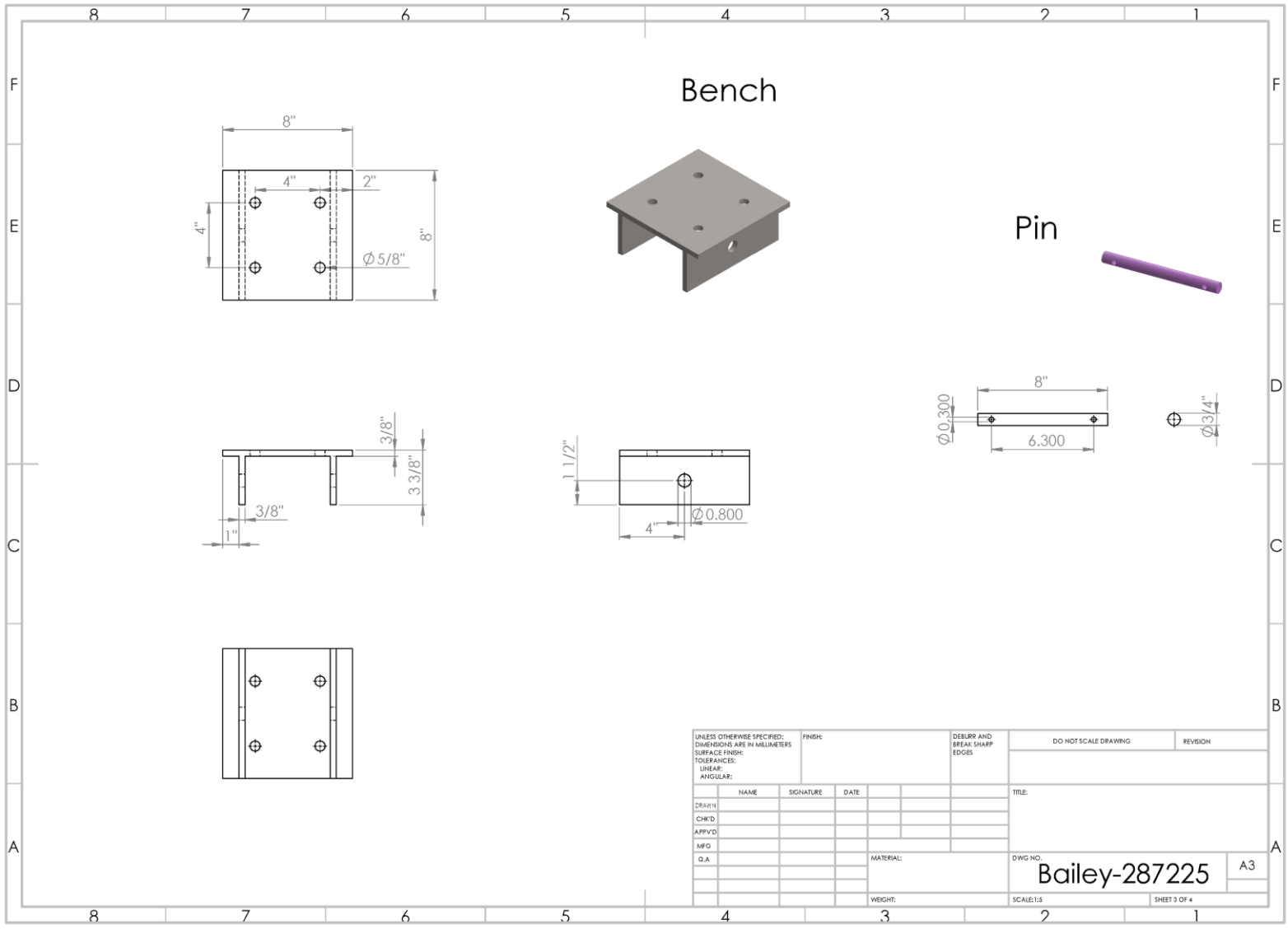




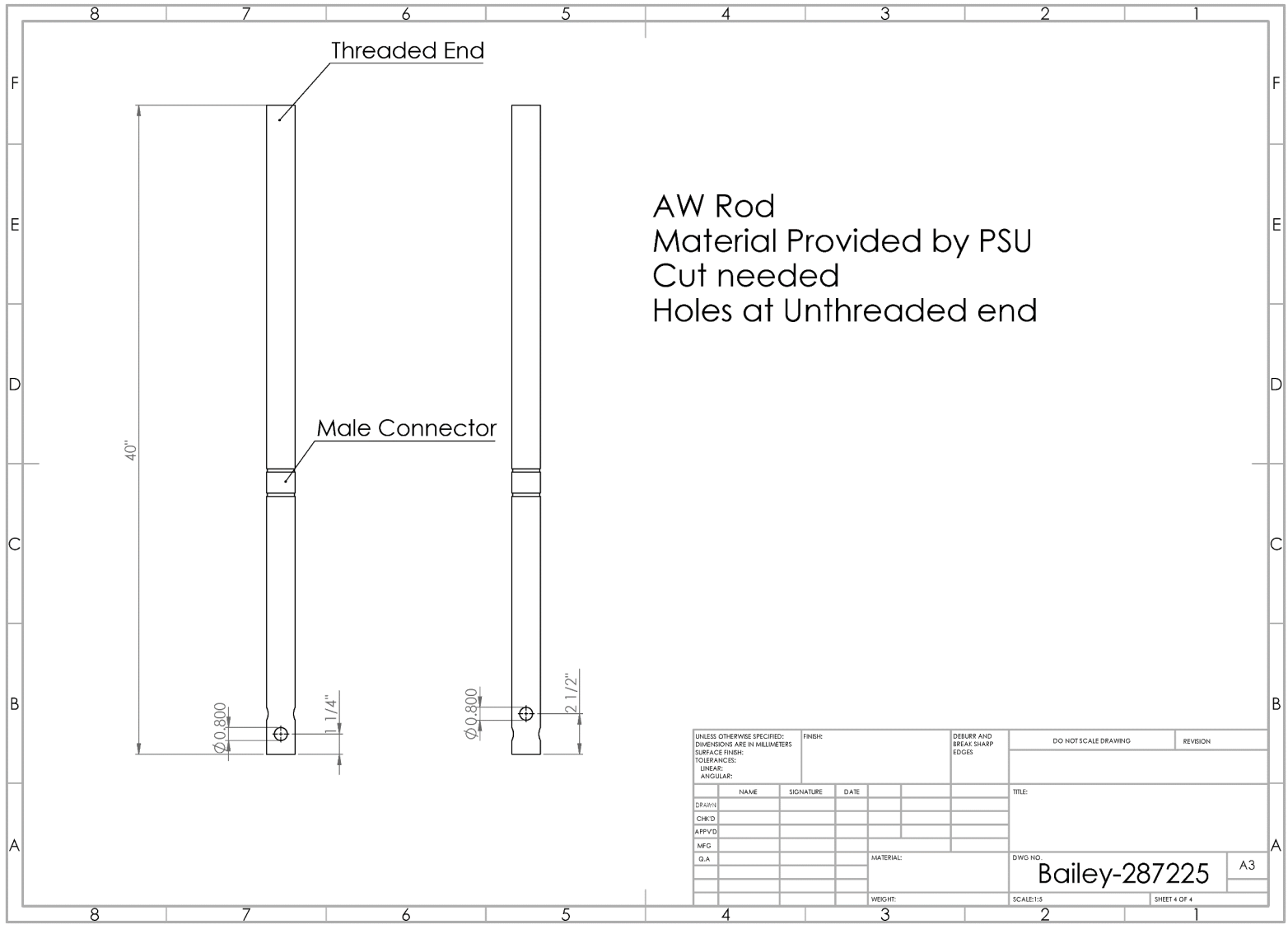


Leg

UNLESS OTHERWISE SPECIFIED: DIMENSIONS ARE IN MILLIMETERS		FINISH:	DEBURR AND BREAK SHARP EDGES	DO NOT SCALE DRAWING	REVISION
SURFACE FINISH:					
TOLERANCES:					
LINEAR:					
ANGULAR:					
DESIGN'D	NAME	SIGNATURE	DATE	TITLE:	
CHK'D					
APP'VD					
MFG					
D.A.					
			MATERIAL:	DWG. NO. Bailey-287225 A3	
			WEIGHT:	SCALE:1:10 SHEET 2 OF 4	



UNLESS OTHERWISE SPECIFIED: DIMENSIONS ARE IN MILLIMETERS			FINISH:		DEBURR AND BREAK SHARP EDGES		DO NOT SCALE DRAWING		REVISION	
SURFACE FINISH:										
TOLERANCES:										
LINEAR:										
ANGULAR:										
NAME					SIGNATURE		DATE		TITLE:	
DRAWN					CHK'D		APPR'D		MFG	
G.A.					MATERIAL:		DWG NO.		A3	
WEIGHT:					SCALE:1:5		SHEET 3 OF 4		Bailey-287225	



VITA

Jintai Wang

EDUCATION

Ph.D., The Pennsylvania State University, University Park. 07/2018

Master of Engineering in Civil Engineering, Tongji University, Shanghai, China. 07/2014

Bachelor of Science in Civil Engineering, Tongji University, Shanghai, China. 07/2010

PUBLICATIONS

Wang, J., Xiao, M., Evans, J., Tong, Q., and Salam, S. “Time-Dependent Cone Penetration Resistance Variation of a Post-Liquefaction Sand Deposit at Shallow Depth.” *Journal of Geotechnical and Geoenvironmental Engineering*. (Submitted).

Wang, J., Salam, S. and Xiao, M. “The Effect of Shaking History on Liquefaction Resistance of Sand Deposit Using Shake Table Testing and CPTu.” *Geo-Congress 2019*. (Submitted).

Wang, J., Xiao, M., and Ziotopoulou, K. “Seismic Performance of Liquefiable Ground: Validation of Numerical Simulations Using Shake Table Test.” *Soil Dynamics and Earthquake Engineering*. (In draft).

Xiao, M., Ledezma, M., and **Wang, J.** (2015). “Reduced-Scale Shake Table Testing of Seismic Behaviors of Slurry Cutoff Walls.” *Journal of Performance of Constructed Facilities*, 30(3), 04015057.

Wang, C., Qiu, T., Xiao, M., and **Wang, J.** (2017). “Utility Trench Backfill Compaction Using Vibratory Plate Compactor versus Excavator-Mounted Hydraulic Plate Compactor.” *Journal of Pipeline Systems Engineering and Practice*, 8(4), 04017021.

Hu, X., and **Wang, J.** (2014). “Recovery of cooling water circulation tunnel collapse: construction of permanent bulkhead by ground freezing.” *In Tunneling and Underground Construction*: 829-835.

Hu, X., Guo, W., Zhang, L., and **Wang, J.** (2013). “Application of liquid nitrogen freezing to recovery of a collapsed shield tunnel.” *Journal of Performance of Constructed Facilities*, 28(4), 04014002.

Hu, X. D., Yu, J. Z., Ren, H., Wang, Y., and **Wang, J. T.** (2017). Analytical solution to steady-state temperature field for straight-row-piped freezing based on superposition of thermal potential. *Applied Thermal Engineering*, 111, 223-231.